Interface Engineering of Functional Oxides: A Photoemission Study

Dissertation zur Erlangung des
naturwissenschaftlichen Doktorgrades
der Julius-Maximilians-Universität Würzburg

vorgelegt von
Judith Gabel
aus Bad Mergentheim

Würzburg 2019

Eingereicht am: 29.04.2019

bei der Fakultät für Physik und Astronomie

1. Gutachter: Prof. Dr. Ralph Claessen

2. Gutachter: Prof. Dr. Mark Golden

3. Gutachter: Prof. Dr. Matthias Bode

der Dissertation

Vorsitzender: Prof. Dr. Jens Pflaum

1. Prüfer: Prof. Dr. Ralph Claessen

2. Prüfer: Prof. Dr. Mark Golden

3. Prüfer: Prof. Dr. Matthias Bode

4. Prüfer: Prof. Dr. Fakher Assaad

im Promotionskolloquium

Tag des Promotionskolloquiums: 08.11.2019

Doktorurkunde ausgehändigt am:

In memoriam

Klara Seubert
(1933–2018)

Abstract

Due to their complex chemical structure transition metal oxides display many fascinating properties which conventional semiconductors lack. For this reason transition metal oxides hold a lot of promise for novel electronic functionalities. Just as in conventional semiconductor heterostructures, the interfaces between different materials play a key role in oxide electronics. The textbook example is the (001) interface between the band insulators $LaAlO_3$ and $SrTiO_3$ at which a two-dimensional electron system (2DES) forms. In order to utilize such a 2DES in prospective electronic devices, it is vital that the electronic properties of the interface can be controlled and manipulated at will. Employing photoelectron spectroscopy as well as electronic transport measurements, this thesis examines how such interface engineering can be realized in the case of the $LaAlO_3/SrTiO_3$ heterostructure:

By photoemission we manage to unambiguously distinguish the different mechanisms by which $SrTiO_3$ can be doped with electrons. An electronic reconstruction is identified as the driving mechanism to render stoichiometric $LaAlO_3/SrTiO_3$ interfaces metallic. The doping of the $LaAlO_3/SrTiO_3$ heterointerface can furthermore be finely adjusted by changing the oxygen vacancy (V_O) concentration in the heterostructure. Combining intense x-ray irradiation with oxygen dosing, we even achieve control over the V_O concentration and, consequently, the doping in the photoemission experiment itself.

Exploiting this method, we investigate how the band diagram of $SrTiO_3$-based heterostructures changes as a function of the V_O concentration and temperature by hard x-ray photoemission spectroscopy. With the band bending in the $SrTiO_3$ substrate changing as a function of the V_O concentration, the interfacial band alignment is found to vary as well. The relative permittivity of the $SrTiO_3$ substrate and, in particular, its dependence on temperature and electric field is identified as one of the essential parameters determining the electronic interface properties. That is also why the sample temperature affects the charge carrier distribution. The mobile charge carriers are shown to shift toward the $SrTiO_3$ bulk when the sample temperature is lowered. This effect is, however, only pronounced if the total charge carrier concentration is small. At high charge carrier concentrations the charge carriers are always confined to the interface, independent of the sample temperature.

The dependence of the electronic interface properties on the V_O concentration is also investigated by a complementary method, viz. by electronic transport measurements. These experiments confirm that the mobile charge carrier concentration increases concomitantly to the V_O concentration. The mobility of the charge carriers changes as well depending on the V_O concentration. Comparing spectroscopy and transport results, we are able to draw conclusions about the processes limiting the mobility in electronic transport. We furthermore build a memristor device from our $LaAlO_3/SrTiO_3$ heterostructures and demonstrate how interface engineering is used in practice in such novel electronic applications.

This thesis furthermore investigates how the electronic structure of the 2DES is affected by the interface topology: We show that, akin to the (001) $LaAlO_3/SrTiO_3$ heterointerface, an electronic reconstruction also renders the (111) interface between $LaAlO_3$ and $SrTiO_3$ metallic. The change in interface topology becomes evident in the Fermi surface of the buried 2DES which is probed by soft x-ray photoemission. Based on the asymmetry in the Fermi surface, we estimate the extension of the conductive layer in the (111)-oriented $LaAlO_3/SrTiO_3$ heterostructure. The spectral function measured furthermore identifies the charge carriers at the interface as large polarons.

Zusammenfassung

Aufgrund ihrer komplexen chemischen Struktur weisen Übergangsmetalloxide viele faszinierende Eigenschaften auf, die konventionelle Halbleitermaterialien entbehren und die Potenzial für neuartige elektronische Funktionalitäten bergen. Genauso wie in konventionellen Halbleiterstrukturen kommt dabei den Grenzflächen zwischen den Materialien besondere Bedeutung zu. In der Oxid-Elektronik ist ein Paradebeispiel hierfür die (001)-Grenzfläche zwischen den Bandisolatoren $LaAlO_3$ und $SrTiO_3$, an der sich ein zweidimensionales Elektronensystem (2DES) ausbildet. Um solche Elektronensysteme zukünftig in elektronischen Anwendungen zu nutzen, ist es jedoch unabdingbar, dass die elektronischen Eigenschaften der Grenzfläche gezielt kontrolliert und manipuliert werden können. Mittels Photoelektronenspektroskopie sowie Transportmessungen untersucht diese Arbeit am Beispiel der $LaAlO_3/SrTiO_3$-Grenzfläche, wie eine derartige Kontrolle realisiert werden kann.

Mithilfe von Photoemissionsexperimenten gelingt es, verschiedene Mechanismen zu unterscheiden, mit denen $SrTiO_3$ dotiert werden kann. In stöchiometrischen $LaAlO_3/SrTiO_3$-Heterostrukturen kann so die elektronische Rekonstruktion als treibender Mechanismus identifiziert werden, der zur Ausbildung der leitfähigen Grenzschicht führt. Die Dotierung der $LaAlO_3/SrTiO_3$-Heterostruktur kann weiterhin auch durch die kontrollierte Erzeugung von Sauerstofffehlstellen (V_O) gezielt gesteuert werden. Die V_O-Konzentration kann sogar während der Photoemissionsexperimente zielgerichtet variiert werden, wenn die Bestrahlung mit intensivem Röntgenlicht mit einer Sauerstoffbehandlung kombiniert wird.

Diese Methode nutzen wir in Folge aus, um in Photoemissionsmessungen mit harter Röntgenstrahlung systematisch zu untersuchen, wie sich das Banddiagramm von $SrTiO_3$-basierten Heterostrukturen als Funktion der V_O-Konzentration und Temperatur ändert. Wir zeigen, dass sich parallel zur Bandverbiegung im $SrTiO_3$-Substrat auch die Bandanordnung an der Grenzfläche als Funktion der V_O-Konzentration ändert. Dabei stellt sich heraus, dass die dielektrische Funktion des $SrTiO_3$-Substrats – insbesondere durch ihre starke Abhängigkeit vom elektrischen Feld und Temperatur – maßgeblich die elektronischen Eigenschaften der Grenzfläche bestimmt. Aus diesem Grund hat die Temperatur der Probe Einfluss auf die Ladungsträgerverteilung. Die mobilen Ladungsträger verschieben sich weg von der Grenzfläche tiefer in das Substrat, je niedriger die Temperatur gewählt wird. Dieser Effekt ist jedoch nur bei niedriger Dotierung zu beobachten. Bei hoher Dotierung ist das zweidimensionale Elektronensystem unabhängig von der Temperatur nahe der Grenzfläche lokalisiert.

Die Abhängigkeit der elektronischen Eigenschaften von der V_O-Konzentration wird auch komplementär im elektronischen Transport untersucht. Auch hier steigt die Ladungsträgerdichte simultan zur V_O-Konzentration. Zugleich ändert sich auch die Mobilität der Ladungsträger. Der direkte Vergleich von Spektroskopie- und Transportmessungen erlaubt Rückschlüsse auf die Prozesse, die die Ladungsträgermobilität begrenzen. Am Beispiel eines $LaAlO_3/SrTiO_3$-basierten Memristors wird darüber hinaus praktisch demonstriert, wie die Kontrolle über die Grenzfläche in neuartigen elektronischen Anwendungen tatsächlich eingesetzt werden kann.

Ferner untersucht diese Arbeit, wie die Topologie der Grenzfläche die elektronische Struktur des 2DES beeinflusst: Wir weisen nach, dass analog zur (001)-Grenzfläche auch die (111)-Grenzfläche zwischen $LaAlO_3$ und $SrTiO_3$ durch eine elektronische Rekonstruktion dotiert wird. Die Änderung in der Grenzflächentopologie zeigt sich deutlich in der Fermifläche des vergrabenen 2DES, die mittels resonanter Photoemission untersucht wird. Anhand der Asymmetrie der Fermifläche wird überdies die Ausdehnung des Elektronensystems abgeschätzt, wohingegen die Spektralfunktion Hinweise auf die Elektron-Phonon-Kopplung an der Grenzfläche liefert.

Contents

Chapter 1

Introduction

Since the dawn of humankind civilizations have been defined by the materials in use. The materials lay the ground for progress – on the one hand they may boost technologies with their assets, yet on the other hand they may also restrict technological advances with their drawbacks. The impact of materials on human development has been so substantial that archaeologists even categorize the prehistoric age into periods named after the material of choice in that era, and also in modern times this impact is not to diminished. The present-day information and communication age is, for example, deeply rooted in the ever-advancing semiconductor technology.

To utilize a material, it is, however, not sufficient that the respective material is at the disposal of humankind or can be synthesized. Beyond that, it is indispensable that one can also control and manipulate the properties of the material. In ancient times this meant that the materials in question could be manufactured into tools as, e.g., arrowheads or knives. In the modern-day semiconductor fabrication materials can be even controlled and manipulated on the nanometer scale, adapting the material properties to specific needs: Sophisticated deposition techniques such as molecular beam epitaxy allow to deliberately change the atomic composition of a material or to stack different materials directly on top of each other, retaining crystalline order throughout the structure.

Such combinations of different materials are an integral component of modern-day electronic devices. A particular important role play the interfaces between the materials, at which entirely new effects may arise as a result of the broken symmetry. This inspired Nobel laureate Herbert Kroemer to begin his Nobel lecture with the statement, 'Often it may be said that the interface is the device.'[1] Solar cells, LEDs, laser diodes and transistors are all devices which draw upon interfacial phenomena – to name just a few examples from the semiconductor technology which one encounters in everyday life.

Nevertheless, not every functionality can be realized based on traditional semiconductors alone. Even in this advanced field the material properties limit the range of applications. To discover novel properties which may be exploited for new functionalities, it is thus promising to venture beyond the traditional semiconductor materials. Nowadays one cannot only fabricate semiconductor heterostructures with unprecedented control and quality but can also synthesize other, more complex materials like transition metal oxides. This opens up a phase space of new and exotic material properties which is not accessible to traditional semiconductor materials.[A2,2] Just as in the case of semiconductors, one can furthermore also build multilayer structures and exploit interfacial phenomena in such oxide materials.[A12,3,4]

This becomes apparent in the flagship heterostructure of the oxide electronics community, the $LaAlO_3/SrTiO_3$ heterointerface (in short LAO/STO), which is also the main focus of this thesis: When crystalline $LaAlO_3$ is deposited on top of a $SrTiO_3$ substrate, a two-dimensional electron system forms at the interface between the two band insulators.[3] The $LaAlO_3/SrTiO_3$ heterointerface has been furthermore reported to exhibit a plethora of remarkable properties, among them high mobility conduction,[3] Rashba spin-orbit interaction,[5] superconductivity[6] and ferromagnetism.[4] Superconductivity and ferromagnetism have even been claimed to coexist in this material system.[7,8] The heterostructure is thus interesting from the point of view of fundamental research but holds potentials for applications alike: The resistance of the 2DES can be tuned by applying a gate voltage which is essential for potential transistor functionality.[9,10] Other publications show that nanoscale $LaAlO_3/SrTiO_3$ based devices can, i.a., be employed as memristors[A7] or in spintronic devices.[11,12]

For fundamental research as well as for potential applications it is of utmost importance that the $LaAlO_3/SrTiO_3$ interface can be precisely controlled and manipulated. This thesis sets out to address this issue in various ways: We demonstrate that the electronic interface properties can be tailored by using substrates with different crystal orientations. Another essential tuning parameter in oxide heterostructures is the oxygen vacancy concentration. By taming the oxygen vacancy concentration in photoemission experiments, we are able to answer the long-standing question about the origin of the 2DES in $LaAlO_3/SrTiO_3$ heterostructures. By means of spectroscopy as well as transport experiments, we furthermore investigate in detail how to tailor the charge carrier distribution, the band bending and the band alignment at the $LaAlO_3/SrTiO_3$ heterostructure by virtue of the oxygen vacancy concentration. By the example of memristors we also discuss how this control over the oxygen vacancy concentration can be harnessed in practical devices.

The thesis is structured as follows:

The experimental methods which are most relevant in this thesis are described in chapter 2. The following chapter gives an introduction into $SrTiO_3$-based heterostructures. By the use of photoemission spectroscopy we disentangle the various doping mechanisms at work in such heterostructures. In chapter 4 the band bending and band alignment at the crystalline $LaAlO_3/SrTiO_3$ heterointerface are analyzed in detail. We focus, in particular, on the question how the electronic interface properties change as a function of the oxygen vacancy concentration, whereas the temperature dependence of the electronic interface properties in $SrTiO_3$ is scrutinized in chapter 5. Transport experiments on $SrTiO_3$-based heterostructures with a differing oxygen vacancy concentration are discussed in chapter 6. Special emphasis is placed on the comparison between the results of transport and spectroscopic measurements. Chapter 7 is concerned with $LaAlO_3/SrTiO_3$ heterostructures in (111) orientation. The thesis ends with a conclusion and an outlook on ongoing and future work.

Chapter 2

Experimental methods

In the next chapter the experimental methods most relevant to this thesis are introduced. We will shortly describe pulsed laser deposition, the method of choice with which most thin film samples in the following have been fabricated. Furthermore we will address the methods we employ to characterize the electronic structure of our samples, viz. photoemission spectroscopy as well as electronic transport measurements.

2.1 Pulsed laser deposition of complex oxides

To explore novel phases of a specific material, one can deposit it as a crystalline thin film on a substrate material: This way one can, e.g., artificially impose a lattice constant or break the symmetry at the interface between the materials, paving the way to new properties and potentially functionalities. To achieve such heterostructures, a simple and flexible yet well-controlled synthesis technique is required. One such method is pulsed laser deposition (in short PLD). With this widely popular method one can fabricate high-quality thin films of materials which may even be characterized by complex stoichiometries.[13,14] PLD is thus also ideally suited for the deposition of oxide heterostructures which contain multiple elements.

A typical PLD setup is sketched in Fig. 2.1 (a). Employing PLD, one does not evaporate every constituent element separately but uses single- or polycrystalline targets which are already made up of the desired film material. A high power excimer laser is focused on the ablation target which is mounted inside a vacuum chamber. Short laser pulses evaporate material which subsequently forms a transient plasma plume [cf. photography in Fig. 2.1 (b)]. The plasma plume contains ions, electrons as well as neutral atoms and molecules of high kinetic energy which all propagate toward the substrate material of choice mounted opposite the ablation target. The evaporated material recondenses on the substrate which is heated to promote the crystallization of the film material.

Typically, only a fraction of a monolayer (ML) of the target material is deposited on the substrate per laser pulse. In the ideal case, a single-phased film grows layer-by-layer, i.e., film material accumulates and rearranges on the substrate until a closed layer is formed, only after which the next layer is built up. The formation of the single layers in such a growth mode can be monitored live during the deposition process by reflection high energy electron diffraction (RHEED) which enables us to fabricate thin films with a precisely defined number of atomic layers.

The deposition as well as the substrate heating are generally not performed in vacuum but in a background atmosphere of, e.g., oxygen. The effects of the background atmosphere are manifold and depend strongly on the pressure range and the gas in use: Working in an oxygen background

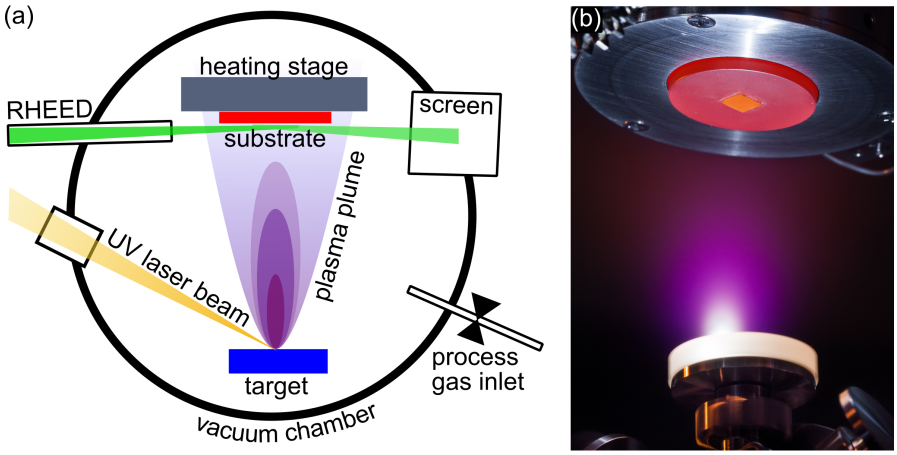

Fig. 2.1: (a) Sketch of a pulsed laser deposition system. A pulsed UV laser beam impinges on the target and ablates material creating a plasma plume. The ejected material propagates toward the substrate where it recondenses. (b) Photography of the plasma plume taken during ablation of Al_2O_3.[15]

atmosphere one may forestall that the substrate is reduced at elevated temperatures. At high pressures the particles in the plasma plume might furthermore collide and scatter with the oxygen in the background atmosphere which alters the kinetics as well as the composition of the plasma plume and subsequently the deposited film material.

Optimizing the growth conditions, stoichiometric films, i.e., films with the same elemental composition as the original target material can be fabricated. It is, in particular, hard to ensure the correct oxygen stoichiometry in the growing film. The oxygen stoichiometry of a sample can, however, be adjusted in a post-growth treatment as well. By a post-oxidation, i.e., by heating the sample in a high oxygen partial pressure, oxygen vacancies present in the substrate and film material can, e.g., be filled up.

Employing pulsed laser deposition, one is able to deposit thin films of complex stoichiometry layer-by-layer, in the best case. The simple growth technique thus offers great potential which may be harnessed to build well-defined interfaces between different materials or to deposit superlattices consisting of various constituents. However, PLD is at the same time a complex process which is depending on many parameters (the laser fluence, the oxygen partial pressure, the substrate temperature, the post-growth treatment etc.). One thus has to monitor and check the film growth as well as the sample quality carefully.

Having discussed our sample preparation technique, we are going to address the methods with which we probe the samples in the next sections.

2.2 Photoelectron spectroscopy

Photoelectron or photoemission spectroscopy is a powerful method allowing insight into the electronic structure of materials. It relies on the photoelectric effect which was first discovered at the end of the 19th century by Hertz,[16] Hallwachs[17] and Lenard[18] and explained by Einstein in the year 1905.[19] Half a century later Siegbahn *et al.*[20] established photoemission spectroscopy as a routine experimental technique and described the merits of the new method by naming it ESCA, i.e., electron spectroscopy for chemical analysis. Photoelectron spectroscopy has since turned into a well-established and widely used experimental technique.

A typical photoemission setup is sketched in Fig. 2.2 (a). A monochromatized photon beam impinges on the sample and excites electrons. At high enough photon energy the ejected electrons

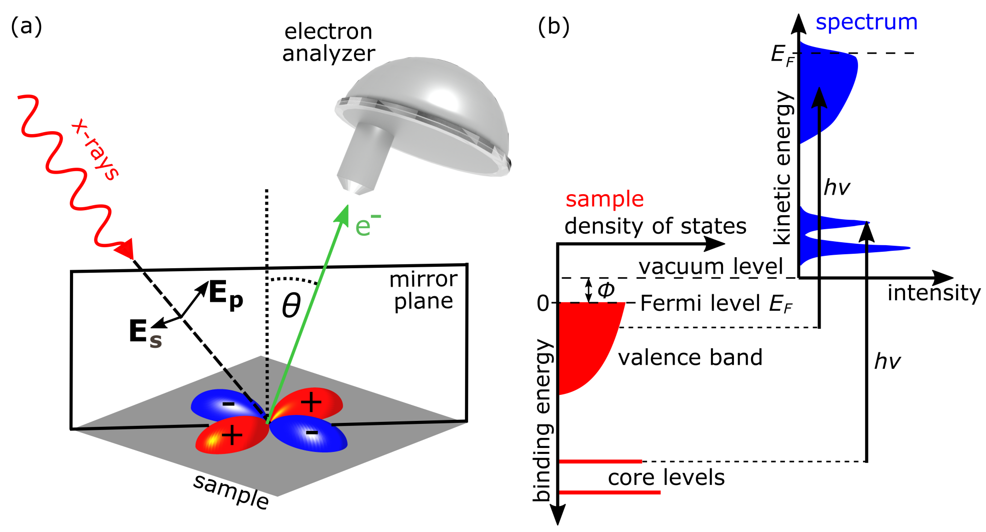

Fig. 2.2: (a) Sketch of the measurement geometry in photoemission experiments. The vector of the incoming light and the outgoing photon define the mirror plane of the experiment. Using linearly polarized light, contributions of different orbitals can be enhanced or suppressed. (b) Correspondence between the electronic structure of a sample and the photoemission spectra recorded. Figure adapted from ref. [21].

can escape the sample and are collected and detected by a hemispherical analyzer. Based on the kinetic energy as well as the emission angle θ under which the electrons escape from the sample, one can subsequently draw conclusions about the electronic structure of the sample. The basic equation which relates the kinetic energy of the photoelectrons E_{kin} and the photon energy $h\nu$ to the binding energy E_{B} of the electrons in the solid reads[19]

$$h\nu = E_{\mathrm{kin}} + E_{\mathrm{B}} + \phi, \tag{2.1}$$

where ϕ denotes the work function of the sample. This relation is also illustrated in Fig. 2.2 (b).

The figure furthermore clarifies how the electronic structure of the solid (marked in red) translates into the experimentally measured spectra (marked in blue) in an independent electron picture.[21] In the spectra the core electrons show up as Voigt-like peaks centered around the respective binding energies. From the shape and the intensity of the core level lines one can, i.a., infer the elemental composition as well as the chemical structure of the sample. If one analyzes core level lines as a function electron emission angle, one can, in addition, draw conclusions about the depth distribution of specific elements or chemical states in the sample.

The valence electrons form bands and appear in emission-angle-integrated spectra as broad features near the Fermi level which, in essence, reflect the density of states. Probing the electron emission angle dependence in valence band photoemission, the momentum-resolved electronic band structure $E(\mathbf{k})$ can be investigated.

In the next section we describe the measurement methods mentioned above in detail: We first develop a theoretical description for valence band photoemission. In the second part of the section, we adapt the description to core level photoemission spectroscopy. The introduction into photoemission is based on refs. [21, 22].

2.2.1 Valence band photoemission

The photoemission process should be modeled as one single step from excitation to the detection of the photoelectron. In an approximation one can, however, divide it into three distinct and independent steps:[23] (i) excitation of the photoelectron, (ii) photoelectron transport to the surface, and (iii) escape of the photoelectron to vacuum. This phenomenological model describes the photoemission process in most instances surprisingly well and yields, in particular, a more intuitive description which helps to understand and interpret the measured spectra. That is why we discuss the photoemission process in the framework of the three step model in the following.

The photoexcitation process

We first have to describe the excitation of the photoelectron by the incident light, i.e., the photon field. Assuming that the interaction between light and matter is weak, the photoexcitation is treated by first-order perturbation theory. In this process the solid is represented by the N electron wave function $|\psi^N\rangle$. The transition probability $w_{i\rightarrow f}$ between the initial state $|\psi_i^N\rangle$ and the final state $|\psi_f^N\rangle$ can then be described by Fermi's Golden Rule

$$w_{i\rightarrow f} = \frac{2\pi}{\hbar}|\langle\psi_f^N|H'|\psi_i^N\rangle|^2\delta\left(E_f^N - E_i^N - h\nu\right), \tag{2.2}$$

where E_f^N and E_i^N denote the energy of the final and initial N electron state and H' describes the perturbing Hamiltonian. For the light-matter interaction the perturbation H' reads

$$H' = \sum_{i=1}^{N} \frac{e}{2m}\left(-\mathbf{p}_i\mathbf{A}(\mathbf{r}_i) - \mathbf{A}(\mathbf{r}_i)\mathbf{p}_i\right) + \frac{e^2}{2m}\mathbf{A}^2(\mathbf{r}_i), \tag{2.3}$$

where $\mathbf{A}(\mathbf{r})$ describes the vector potential of the light field. As every electron may interact with the light field, we have to sum over the electrons which are numbered by i. $\mathbf{p}_i$ and $\mathbf{r}_i$ denote the momentum and position operator of the electron i in the solid. To simplify the expression for H', we neglect any two-photon processes and assume $\mathbf{A}^2(\mathbf{r}_i) \approx 0$. We furthermore exploit that light waves are transverse waves, set $\nabla\mathbf{A}(\mathbf{r}_i)=0$[1] and rewrite the Hamiltonian H'

$$H' \approx \sum_{i=1}^{N} \frac{e}{m}\mathbf{A}(\mathbf{r}_i)\cdot\mathbf{p}_i. \tag{2.4}$$

In second quantization the Hamiltonian H' above becomes

$$H' = \sum_{\mathbf{k}_f,\mathbf{k}} M_{\mathbf{k}_f\mathbf{k}} c^\dagger_{\mathbf{k}_f} c_{\mathbf{k}}, \tag{2.5}$$

where the operator $c_{\mathbf{k}}$ annihilates the electron described by the Bloch state $|\phi_{\kappa\mathbf{k}}\rangle$ with momentum $\mathbf{k}$ and band index κ. In contrast, the operator $c^\dagger_{\mathbf{k}_f}$ creates a photoelectron in the Bloch state $|\phi_{\kappa_f\mathbf{k}_f}\rangle$ with momentum $\mathbf{k}_f$ and band index κ_f. In second quantization the sum over the electron number i is replaced by the sum over the momenta $\mathbf{k}$ in the first Brillouin zone. As the electrons can be excited in an arbitrary state by the perturbation, one furthermore sums about the photoelectron momenta $\mathbf{k}_f$. The one-electron matrix element $M_{\mathbf{k}_f\mathbf{k}}$ in equation (2.5) is defined as

$$M_{\mathbf{k}_f\mathbf{k}} = \frac{e}{m}\left\langle\phi_{\kappa\mathbf{k}}|\mathbf{A}(\mathbf{r})\cdot\mathbf{p}|\phi_{\kappa_f\mathbf{k}_f}\right\rangle. \tag{2.6}$$

If the photoelectron has a sufficiently high kinetic energy, we can furthermore make use of the sudden approximation: The photoelectron is assumed to be excited and removed from the remaining $N-1$ electron system instantaneously. In other words, the escaping photoelectron does not interact with the remaining $N-1$ electron system after the photoexcitation. The final

---

[1] This equation holds in the solid as well as in vacuum but is possibly not met at the solid's surface.

state $|\Psi_f^N\rangle$ can thus be factorized and described by $|\Psi_f^N\rangle = c^\dagger_{\mathbf{k}_f}|\Psi_f^{N-1}\rangle$ where $c^\dagger_{\mathbf{k}_f}$ represents the photoelectron and $|\Psi_f^{N-1}\rangle$ the remaining $N-1$ electron system. The final state energy of the N electron system E_f^N can similarly be split up into the kinetic energy of the photoelectron E_{kin}, the work function ϕ and the energy of the $N-1$ electron system E_f^{N-1}. The transition probability $w_{i\to f}$ in equation (2.2) can then be rewritten

$$w_{i\to f} = \frac{2\pi}{\hbar}|\langle\psi_f^{N-1}|c_{\mathbf{k}_f}\sum_{\mathbf{k}'_f,\mathbf{k}} M_{\mathbf{k}'_f\mathbf{k}}c^\dagger_{\mathbf{k}'_f}c_{\mathbf{k}}|\psi_i^N\rangle|^2\delta\left(E_f^{N-1} + E_{\text{kin}} + \phi - E_i^N - h\nu\right). \tag{2.7}$$

Using momentum conservation and operator algebra, we simplify this equation

$$w_{i\to f} = \frac{2\pi}{\hbar}|\sum_{\mathbf{k}} M_{\mathbf{k}_f\mathbf{k}}\langle\psi_f^{N-1}|c_{\mathbf{k}}|\psi_i^N\rangle|^2\delta\left(E_f^{N-1} + E_{\text{kin}} + \phi - E_i^N - h\nu\right). \tag{2.8}$$

To compute the probability $I(\mathbf{k}_f, E_{\text{kin}})$ to excite a photoelectron with momentum $\mathbf{k}_f$ and energy E_{kin}, we have to sum over all final states f and arrive at the following expression

$$I(\mathbf{k}_f, E_{\text{kin}}) \propto \sum_{\mathbf{k}}|M_{\mathbf{k}_f\mathbf{k}}|^2 \underbrace{\sum_f |\langle\psi_f^{N-1}|c_{\mathbf{k}}|\psi_i^N\rangle|^2\delta\left(E_f^{N-1} + E_{\text{kin}} + \phi - E_i^N - h\nu\right)}_{A^-(\mathbf{k},\omega=h\nu-E_{\text{kin}})}. \tag{2.9}$$

The one-electron removal spectral function $A^-(\mathbf{k},\omega)$ describes the probability of removing an electron with momentum $\mathbf{k}$ and energy ω from the ground state $|\psi_i^N\rangle$ of the system. $A^-(\mathbf{k},\omega)$ encompasses all many-body effects and may, i.a., shift and broaden the photoemission lines and give rise to satellite peaks. In contrast, the one-electron matrix element $|M_{\mathbf{k}_f\mathbf{k}}|^2$ captures the photoexcitation process as well as the experimental geometry.

Photoemission for non-interacting electron systems

If one assumes that the electrons in the solid are non-interacting, one can further simplify equation (2.9). In this case, the initial state can be factorized into the electron in the orbital $|\phi_j\rangle$ which is to be excited and the remaining $N-1$ electron system $|\psi_i^{N-1}\rangle$

$$|\psi_i^N\rangle = |\phi_j\rangle|\psi_i^{N-1}\rangle. \tag{2.10}$$

Similarly, the energy E_i^N of the initial state can be expressed as the sum over the binding energy, i.e., the Hartree-Fock orbital energy, of the prospective photoelectron ϵ_j and the binding energy of the remaining $N-1$ electrons E_i^{N-1}

$$E_i^N = \epsilon_j + E_i^{N-1}. \tag{2.11}$$

Within the frozen-orbital approximation we furthermore assume that the remaining $N-1$ electrons do not react to the photoexcitation and remain in their initial state $|\psi_i^{N-1}\rangle$ which is consequently also the only admissible final state $|\psi_f^{N-1}\rangle$:

$$c_{\mathbf{k}}|\psi_i^N\rangle = |\psi_i^{N-1}\rangle = |\psi_f^{N-1}\rangle. \tag{2.12}$$

In the energy analysis $E_i^{N-1} = E_f^{N-1}$ holds accordingly. Equation (2.9) can thus be rewritten

$$I(\mathbf{k}_f, E_{\text{kin}}) \propto \sum_{\mathbf{k}}|M_{\mathbf{k}_f\mathbf{k}}|^2\delta\left(E_{\text{kin}} + \phi - \epsilon_j - h\nu\right). \tag{2.13}$$

The argument of the δ-function closely resembles the basic equation (2.1) describing the photoeffect. However, the previously loosely defined term E_B is now replaced by $-\epsilon_j$, the negative orbital energy of the prospective photoelectron. We can thus conclude that in the case of non-interacting electron systems the Hartree-Fock orbital energies are probed. The measurement results are additionally modulated by the one-electron matrix element $M_{\mathbf{k}_f\mathbf{k}}$.

Describing angle-integrated valence band measurements, the $\mathbf{k}_f$ dependence in the one-electron matrix element can be ignored. If one furthermore neglects the energy as well as orbital dependence of the one-electron matrix element, one can simplify equation (2.13)

$$I(E_{\text{kin}}) \propto \delta\left(E_{\text{kin}} + \phi - \epsilon_j - h\nu\right). \tag{2.14}$$

In the case of non-interacting electron systems angle-integrated valence band spectra thus roughly map the density of states. We note in passing that, employing angle-resolved photoemission spectroscopy (ARPES), the *momentum-resolved* valence and conduction band structure can also be inferred, as discussed later on.

The one-electron matrix element is ignored in the approximations, above. It can, however, bring about additional modulations in the measurements which can be exploited to infer the orbital character of the band structure, as described in the next section.

Symmetry in the one-electron matrix element

The one-electron matrix element has been defined before as

$$M_{\mathbf{k}_f\mathbf{k}} = \frac{e}{m}\left\langle \phi_{\kappa\mathbf{k}} | \mathbf{A}(\mathbf{r}) \cdot \mathbf{p} | \phi_{\kappa_f\mathbf{k}_f} \right\rangle. \tag{2.15}$$

Within the dipole approximation[2] we set the vector potential of the photon field to a constant $\mathbf{A}(\mathbf{r})=\mathbf{A}_0$. Using the commutation relation $\frac{\hbar\mathbf{p}}{m}=-i[\mathbf{r},H]$, $M_{\mathbf{k}_f\mathbf{k}}$ can be rewritten

$$M_{\mathbf{k}_f\mathbf{k}} \propto \left\langle \phi_{\kappa\mathbf{k}} | \mathbf{A}_0 \cdot \mathbf{r} | \phi_{\kappa_f\mathbf{k}_f} \right\rangle = \int d^3r \phi_{\kappa\mathbf{k}}(\mathbf{r}) \cdot \mathbf{A}_0 \cdot \mathbf{r} \cdot \phi_{\kappa_f\mathbf{k}_f}(\mathbf{r}). \tag{2.16}$$

In specific experimental geometries one can exploit symmetry considerations to distinguish between the contributions of different orbitals:[24] The matrix element $M_{\mathbf{k}_f\mathbf{k}}$ and the photoemission intensity is only non-vanishing if the integrand in equation (2.16) has even parity with respect to the mirror plane of the photoemission experiment.

Let us thus consider the symmetry of the different terms in equation (2.16). The mirror plane of the photoemission experiment is defined by the incoming photon beam and the outgoing photoelectron [see Fig. 2.2 (a)]. Let us consider the symmetry of the different terms in equation (2.16) under reflection at this mirror plane. Wave functions with odd parity vanish on the mirror plane itself and, in particular, also at the analyzer. We can thus conclude that the wave function $\phi_{\kappa_f\mathbf{k}_f}$ describing the outgoing photoelectron has to be even with respect to the experimental mirror plane. Working with linearly polarized light, one can choose the light polarization such that the term $\mathbf{A}_0 \cdot \mathbf{r}$ has a defined parity under reflection at the mirror plane. When $\mathbf{A}_0$ is oriented parallel (perpendicular) to the mirror plane, $\mathbf{A}_0 \cdot \mathbf{r}$ has even (odd) parity with respect to the mirror plane. Depending on the experimental geometry, the initial state wave functions $\phi_{\kappa\mathbf{k}}$ can also have a defined even or odd parity. Following these considerations, we compute the parity of the integrand in equation (2.16), i.e., the product $\phi_{\kappa\mathbf{k}}(\mathbf{r}) \cdot (\mathbf{A}_0 \cdot \mathbf{r}) \cdot \phi_{\kappa_f\mathbf{k}_f}(\mathbf{r})$ and summarize the symmetry-allowed transitions:

$\mathbf{A}_0$ oriented parallel to mirror plane → initial states $\phi_{\kappa\mathbf{k}}$ with even parity are observed
$\mathbf{A}_0$ oriented perpendicular to mirror plane → initial states $\phi_{\kappa\mathbf{k}}$ with odd parity are observed

---

[2] The dipole approximation only works well for low photon energies where the wave length of the light is large compared to the typical atomic length scales.

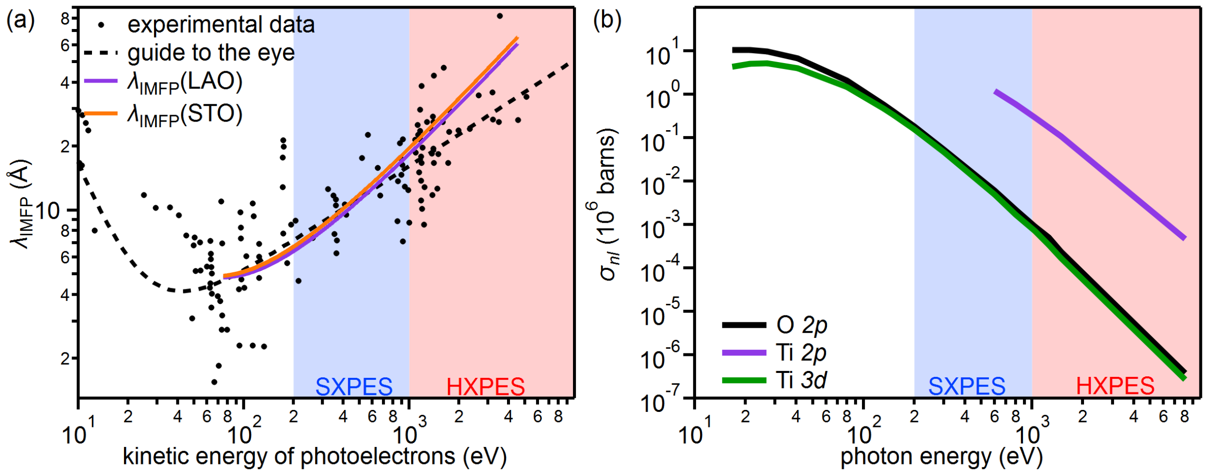

Fig. 2.3: (a) Inelastic mean free path λ_{IMFP} of electrons as a function of the kinetic energy of the electrons. The inelastic mean free path follows a characteristic, universal curve (see dashed line). Data adopted from ref. [25]. (b) Subshell photoionization cross sections σ_{nl} for exemplary orbitals as a function of the photon energy. Data adopted from ref. [26].

The inelastic mean free path of the photoelectrons

After the photoexcitation the photoelectron has to travel to the sample surface. On its way it might scatter inelastically with phonons or other electrons exciting electron-hole pairs or plasmons. The inelastic mean free path (in short λ_{IMFP}) describes the mean distance the photoelectron travels before it loses energy in such an inelastic scattering event. Figure 2.3 (a) depicts the inelastic mean free paths in different materials which is depending on the kinetic energy of the electrons. We note that, independent of the specific material, λ_{IMFP} follows a characteristic curve as a function of the kinetic energy which is called universal curve. This behavior is a result of the predominant scattering mechanism at work for photoelectrons which have kinetic energies above 50 eV. In this kinetic energy range the electrons mainly lose energy when exciting plasmons, i.e., collective oscillations of the electron gas in the solid. The mean free path of the electrons scales inversely to the mean electron-electron distance in the electron gas, which is a function of the valence electron density.[3] This quantity is, in turn, similar for many materials.

Based on similar considerations, λ_{IMFP} of the photoelectrons can be estimated for different materials as a function of the kinetic energy E_{kin} by the TPP–2M formula which has been proposed by Tanuma, Powell, and Penn[27,28]

$$\lambda_{\mathrm{IMFP}}(E_{\mathrm{kin}}) = \frac{E_{\mathrm{kin}}}{E_p^2[\beta \ln(\gamma E_{\mathrm{kin}}) - (C/E_{\mathrm{kin}}) + (D/E_{\mathrm{kin}}^2)]}. \tag{2.17}$$

Here E_p=28.8$(N_V \rho/M)^{1/2}$ denotes the plasmon energy which can be determined from the density ρ, the atomic mass M and the number of valence electrons N_V in the compound. β, γ, C and D are material-specific parameters which can be looked up in the NIST database.[29] For the materials studied in this thesis the λ_{IMFP} computed with the TPP–2M formula is plotted in Fig. 2.3 (a).

In the case of valence band photoemission, the kinetic energy of the photoelectrons can be roughly equated to the photon energy in use. We can thus also classify the λ_{IMFP} according to the photon energy, as shown in Fig. 2.3 (a). Using typical laboratory light sources as gas discharge lamps,

---

[3] From the point of view of the photoelectrons the conduction as well as the valence band electrons can be described as a free electron gas, as the bonding parameters of the valence band electrons are no longer important (valence band binding energy $\approx$10 eV $<$ kinetic energy of the photoelectrons).

λ_{IMFP} of the photoelectrons is short. In such experiments one thus only records signal from the sample surface. To probe buried interfaces, one has to increase λ_{IMFP} of the photoelectrons. This can be achieved by using higher photon energies in the soft or hard x-ray regime, which are accessible at synchrotron beamlines.

Momentum conservation

Employing photoelectron spectroscopy, one can not only measure binding energies but also infer information about the **k**-resolved valence and conduction band structure. Such measurements rely on the fact the photoelectron momentum is conserved in the measurement process as described in the following.[4] The photoelectron momentum in vacuum $|\mathbf{k}_f|$ is computed from the kinetic energy E_{kin} of the photoelectron

$$\hbar|\mathbf{k}_f| = \sqrt{2mE_{\mathrm{kin}}}. \tag{2.18}$$

The photoelectron momentum can be divided into a component oriented parallel to the sample surface $k_{f,||}$ and a component oriented perpendicular to the sample surface $k_{f,\perp}$

$$\hbar k_{f,||} = \sqrt{2mE_{\mathrm{kin}}}\sin\theta, \tag{2.19}$$

$$\hbar k_{f,\perp} = \sqrt{2mE_{\mathrm{kin}}}\cos\theta, \tag{2.20}$$

where θ describes the electron emission angle with respect to the sample surface normal [see Fig. 2.2 (a)]. Exploiting the quasi-momentum conservation in a periodic crystal lattice, the photoelectron momentum $\mathbf{k}_f$ can be expressed as the sum of the electron momentum in the initial state $\mathbf{k}_i$, the photon momentum $\mathbf{k}_{ph}$ and a crystal momentum $\mathbf{G}$

$$\mathbf{k}_f = \mathbf{k}_i + \mathbf{k}_{ph} + \mathbf{G}. \tag{2.21}$$

At low photon energies $h\nu$ we can neglect the contribution of the photon momentum, which scales with $\hbar|\mathbf{k}_{ph}| = \frac{h\nu}{c}$. Based on the identity in equation (2.21) one can directly compute the parallel component of the electron momentum in the initial state $k_{i,||}$

$$k_{f,||} = k_{i,||} + k_{ph,||} + G_{||}. \tag{2.22}$$

As the symmetry of the crystal lattice is broken at the sample surface, the quasi-momentum conservation in equation (2.21) does not apply for the momentum component oriented perpendicular to the sample surface. One can circumvent this complication by measuring two-dimensional electron systems, which show no dependence on $k_{i,\perp}$. Probing three-dimensional electron systems, one can model the surface as a potential step of size V_0 which the electron has to overcome. Employing a free electron approximation for the photoelectron final states, $k_{i,\perp}$ is given by

$$\hbar k_{i,\perp} = \sqrt{2m(E_{\mathrm{kin}}\cos^2\theta + V_0)}. \tag{2.23}$$

The so-called inner potential V_0 is typically treated as an empirical parameter which is adapted to the experimental spectra.

Having presented the theoretical description for valence band photoemission, we now adapt the description to the case of core level spectroscopy.

---

[4] Incidentally, the momentum conservation is contained in the one-electron matrix element

2.2.2 Core level photoemission

In core level photoemission localized orbitals are probed. The wave vector $\mathbf{k}$ as well as the band index κ are thus no longer good quantum numbers and are not suited to describe the core level electrons. We thus need to change the basis sets employed in the second quantization: c_l ($c_l^\dagger$) annihilates (creates) a core electron in the orbital $|\phi_l\rangle$, while c_K ($c_K^\dagger$) annihilates (creates) a photoelectron with kinetic energy E_{kin}. Analogously to the case of valence band photoemission, we derive the probability I to excite a photoelectron $|\phi_{E_{\text{kin}}}\rangle$ with kinetic energy E_{kin}

$$I \propto \sum_l |M_{Kl}|^2 \underbrace{\sum_f |\langle\psi_f^{N-1}|c_l|\psi_i^N\rangle|^2 \delta\left(E_f^{N-1} + E_{\text{kin}} + \phi - E_i^N - h\nu\right)}_{A^-(\omega = h\nu - E_{\text{kin}} - \phi)} . \tag{2.24}$$

We can once again separate the one-electron removal spectral function $A^-(\omega)$ capturing all many-body effects and the one-electron matrix element M_{Kl} describing the photoexcitation process.

Photoionization cross section

For the case of core level spectroscopy the one-electron matrix element M_{Kl} reads

$$M_{Kl} = \frac{e}{m} \langle\phi_{E_{\text{kin}}}|\mathbf{A}(\mathbf{r}) \cdot \mathbf{p}|\phi_l\rangle . \tag{2.25}$$

The matrix element describes the likelihood that the incoming light excites an electron in the subshell $|\phi_l\rangle$ to a state $|\phi_{E_{\text{kin}}}\rangle$ above the vacuum level. This probability is also referred to as photoionization cross section.

Photoionization cross sections are typically estimated for isolated atoms employing a frozen core approximation:[26] To this end, the initial as well as the final state wave function are expanded in spherical harmonics. Within the dipole approximation the operator $\mathbf{A}(\mathbf{r}) \cdot \mathbf{p}$ is also expressed in spherical harmonics.

The resulting photoionization cross section contains a term which is independent of the electron emission angle θ. This term is called the atomic subshell photoionization cross sections σ_{nl} where n and l denote the quantum numbers of the subshell from which the electron originates. In Fig. 2.3 (b) σ_{nl} is plotted for some exemplary orbitals.[26] The atomic subshell photoionization cross sections differ widely for the various orbitals and also depend strongly on photon energy.

The photoionization cross sections are furthermore modulated over the electron emission angle θ. The exact functions describing the angular asymmetry of the photoionization cross sections depend on the polarization of the photon beam as well as on the emitting atomic subshell and are listed elsewhere.[26,30,31] Suffice it to say that the asymmetry is depending on the angle between the photoelectron momentum and the polarization vector of the incoming light (the photon momentum in the case of unpolarized light).

We note in passing that the photoionization cross section also appears in the one-electron matrix element describing valence band photoemission (cf. equation (2.15)) and modulates the signal intensity of the valence and conduction band.

Quantitative analysis of core level spectra

Employing core level photoemission, one can infer the stoichiometry and chemical composition of a sample: In a homogeneous sample the intensity I_A of a core level line scales proportionally to the density N_A of the corresponding element/chemical state A in the sample. Analyzing core level intensities, information about the elemental and chemical composition of the sample can thus be gained. However, the intensity I_A also depends on further factors as, e.g., the photon flux

J as well as the transmission T and detection efficiency D of the analyzer.[32] The photoionization cross section σ_A of the orbitals also enters into the calculation

$$I_A \propto N_A \cdot J \cdot T \cdot D \cdot \sigma_A. \tag{2.26}$$

To determine the density of different elements in a sample, one thus needs to resort to the tabulated atomic photoionization cross sections whose accuracy is limited. Other quantities in equation (2.26) may furthermore be unknown or change depending on the exact experimental setup, e.g., as a function of the analyzer settings. By just comparing the peak areas of the core level lines, it may thus prove challenging to determine the composition of a sample. In a pragmatic solution one can, however, determine the abundance of different elements by comparing to the spectra of a reference sample whose stoichiometry is well established. When one measures the single core levels of the sample in question using identical experimental settings, the changes in stoichiometry can be reliably determined.

Depth profiling experiments

From core level spectra one cannot only probe the stoichiometry in homogeneous samples but may also analyze the depth distribution of an element or of a chemical state. This way one can, e.g., draw conclusions about the band bending or the charge carrier distribution in the sample volume probed. In depth profiling experiments, the same core level spectra are recorded several times under different experimental conditions: Changing the surface sensitivity of the photoemission experiment, i.e., the sample volume probed, one can easily tell if a specific signal originates from the surface or the bulk of the sample.

For a quantitative analysis of the depth profile one needs to model the measured spectra: The photoelectron is assumed to travel in a straight line to the sample surface. On its way to the surface it might, however, scatter inelastically and lose its energy information. As a result the signal I_0 emitted from a layer at a distance z from the surface is exponentially damped and one only detects a signal of intensity $I(z)$ from this very layer in photoemission experiments

$$I(z) = I_0 \exp\left(-\frac{z}{\lambda_{\mathrm{IMFP}}}\right), \tag{2.27}$$

where λ_{IMFP} describes the effective inelastic mean free path of the photoelectrons. Core level spectra are made up of the contributions $I(z)$ from all the single layers. When λ_{IMFP} is altered, the relative contributions of the different layers to the aggregate signal vary.

The surface sensitivity of the photoemission experiment is also conveniently described by the concept of the probing depth: The probing depth is defined as the sample volume from which 95% of the photoelectrons originate and amounts to $3\lambda_{\mathrm{IMFP}}$.

Since λ_{IMFP} is depending on the kinetic energy of the photoelectrons and, in consequence, on the photon energy in use, one can vary the photon energy to alter the surface sensitivity of the experiment. However, as a function the photon energy the experimental resolution might vary as well which complicates the analysis of the core level spectra.

This problem can be avoided if the core level spectra are measured at constant photon energy but at different electron emission angles. When an electron is emitted along an angle θ with respect to the surface normal (also abbreviated: along an angle θ off NE/normal emission), its path to the surface effectively elongates by the factor $\frac{1}{\cos(\theta)}$. The surface sensitivity of the measurement changes accordingly, as is illustrated in Fig. 2.4. We replace λ_{IMFP} by $\lambda_{\mathrm{eff}} = \lambda_{\mathrm{IMFP}} \cos(\theta)$ and can calculate the contribution $I(z)$ of layer z to the spectrum measured at emission angle θ by

$$I(z) = I_0 \exp\left(-\frac{z}{\lambda_{\mathrm{IMFP}} \cdot \cos(\theta)}\right). \tag{2.28}$$

With this ansatz we subsequently model the depth dependence in the angular-dependent core level photoemission spectra.

The core level intensity measured at different electron emission angles might be modulated by further effects. In crystalline samples the photoelectrons might, e.g., be diffracted at the lattice which causes an additional variation in the photoemission intensity over the electron emission angle.[33] However, if one does not compare the total areas of the core level lines but their line shapes as a function of the electron emission angle, these effects cease to be relevant.

In depth profiling experiments the photon energy has to be selected carefully: On the one hand, one has to ensure that one is sensitive to the interface and not only to the substrate bulk. On the other hand, one has to strive for a high count rate which may be limited due to the cross sections, the light source and a possible capping layer covering the sample.

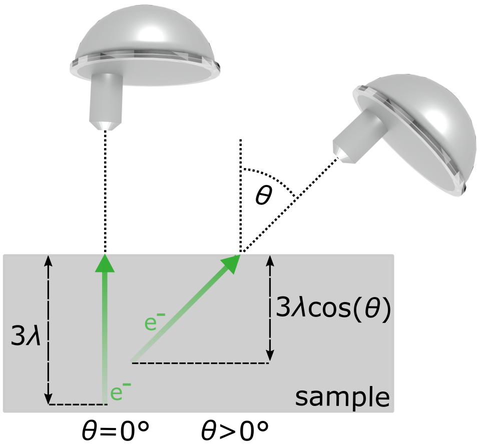

Fig. 2.4: Principle of depth profiling experiments. The probing depth changes as a function of the electron emission angle θ.

Background modeling

The inelastic scattering of photoelectrons is not only the reason for the surface sensitivity of photoemission spectroscopy but can also give rise to spurious background signals, as the electrons lose their energy and momentum information in the scattering process. The background signal has to be subtracted when the line shapes or the integrated intensity of core levels are analyzed. Shirley[34] proposed a method to correct the background signal from inelastically scattered electrons which is also used in this thesis: He assumed that the inelastic background signal at a kinetic energy E is proportional to the integral number of photoelectrons with a kinetic energy $E' > E$. The background signal I_{BG} can thus be computed by the following equation

$$I_{\mathrm{BG}}(E) \propto \int_{E}^{E_f} dE' I_0(E'), \tag{2.29}$$

where I_0 denotes the intrinsic spectrum. In the experiment we measure the spectrum I_{meas} that is a superposition of the intrinsic spectrum I_0 and the background signal I_{BG}. Employing an iterative scheme one can, however, separate the measured data into the intrinsic spectrum and the inelastic background. The Shirley background correction is illustrated with a concrete example later in Fig. 4.7.

Spectral line shape

In order to analyze the depth dependence of the core level spectra quantitatively, we need to fit the spectral lines. The single core level lines in the photoemission spectra are not infinitely sharp δ-functions appearing at the respective binding energies but are broadened by different processes:[35] As the lifetime of the photoemission final state is finite, its energy is not precisely defined according to Heisenberg's uncertainty principle. This intrinsic lifetime broadening results in a Lorentzian peak profile. In contrast, the instrumental energy resolution[5] gives rise to a Gaussian broadening of the core level lines. The ensuing core level line shape is obtained by convoluting the Gaussian and Lorentzian functions which yields a Voigt profile.

---

[5] The instrumental resolution is comprised of the spectrometer resolution and the beamline resolution, i.e., the monochromaticity of the x-ray beam.

2.2.3 Resonantly enhanced processes

Due to the inherent surface sensitivity of photoelectron spectroscopy, it is challenging to probe the buried interfaces we would like to take a look at in this thesis: Increasing the photon energy and therewith the kinetic energy of the photoelectrons, one can boost the inelastic mean free path of the photoelectrons and enhance the signal from the interface [see Fig. 2.3 (a)]. However, at the same time the photoionization cross sections are sharply decreasing [see Fig. 2.3 (b)] which, in turn, reduces the overall photoemission signal. Yet, at specific photon energies near absorption edges of core levels, the photoemission signal is resonantly enhanced which we utilize in this thesis to probe the buried interfaces.

This so-called resonant photoemission (ResPES) technique is introduced in the following by the example of Ti $3d$ core level measurements. In the direct photoemission process the Ti $3d$ electrons are excited by the photon beam and escape the solid as photoelectrons [see Fig. 2.5 (a)]. When the photon energy is tuned through the Ti L absorption edge, an additional photoexcitation channels open up [see Fig. 2.5 (b)]. A Ti $2p$ core electron might be excited to a Ti $3d$ level. The excited state may subsequently decay to the ground state by direct recombination which is accompanied by the emission of an Auger electron. In the case of a Ti $3d^1$ electron configuration the two photoexcitation processes are

$$2p^6 3d^1 + h\nu \rightarrow 2p^6 3d^0 + e^-, \tag{2.30}$$

$$2p^6 3d^1 + h\nu \rightarrow 2p^5 3d^2 \rightarrow 2p^6 3d^0 + e^-, \tag{2.31}$$

where e^- denotes the photoelectron. One notes that the final states of both channels are identical and the escaping electrons also have the same kinetic energy, in particular. Thus, the final state wave functions superimpose and interfere constructively or destructively giving rise to a Fano-resonance:[36] Depending on the exact photon energy, the Ti $3d$ signal intensity is suppressed or enhanced. If the photon energy is increased above the absorption threshold, the Auger decay becomes incoherent. The two channels do no longer interfere quantum-mechanically and the resonance effect is lost.

Beside the resonant enhancement, ResPES measurements have another advantage: The processes described above are element-specific. In our case, only the Ti $3d$ related signal is, e.g., resonantly enhanced. In general, one can thus analyze the partial density of states employing ResPES and selecting appropriate absorption edges.

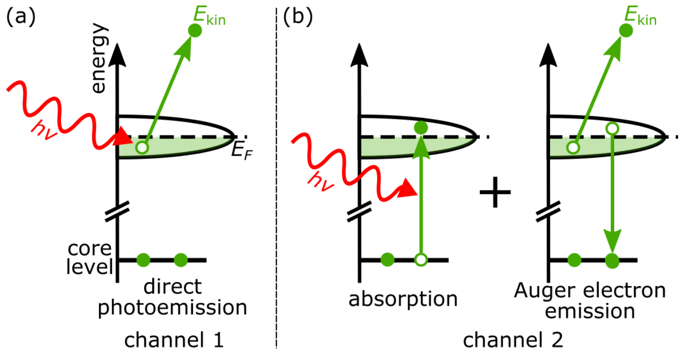

Fig. 2.5: Photoexcitation channels in resonant photoemission measurements. (a) Direct photoemission of a $3d$ electron. (b) $2p \rightarrow 3d$ absorption and subsequent Auger electron emission. The final state is identical in both channels. Accordingly, the two processes interfere quantum-mechanically.

2.3 Electronic transport measurements

In this thesis the properties of electrons at the Fermi edge are not only probed by photoemission spectroscopy but also by transport experiments. In the next section we give a short overview over the transport measurement techniques employed.

In order to perform such measurements, one first needs to establish electrical contacts to the conducting channel, i.e., the buried $LaAlO_3/SrTiO_3$ interface, which can be achieved by ultrasonic wire bonding. In this process a thin Al wire is welded to the sample and right through to the interface by an ultrasonic pulse.[37]

In the most simple transport experiment a current is then passed through the same electrode pair at which the voltage drop is measured. In such a setup, the measured resistance is, however, dominated by the large contact resistance between the sample and the wiring and not by the resistance of the sample itself. To cancel out the effect of the contact resistances, we make use of four-terminal sensing in which current and voltage are measured at separate contact pairs. We perform transport experiments in two different contact and sample geometries which are addressed in the following.

2.3.1 Measurements in van der Pauw geometry

Van der Pauw[38] described a method to measure the sheet resistance R_s of a lamella of arbitrary shape. The sheet resistance is defined as $R_s = \rho/t$ where ρ denotes the specific resistivity of the material and t describes the thickness of the conducting layer. For the technique to work, several conditions have to be met: The contacts should be point-like and have to be placed at the very periphery of the sample. The conducting layer must furthermore be homogeneous in thickness and must not have any isolated holes.

A typical contact geometry we use in experiments is displayed in the left panel of Fig. 2.6 (a). (Due to experimental limitations this contact configuration does not fulfill all the requirements listed above which will be discussed in detail shortly.) In this contact geometry one measures a value for the resistance R_1. The contact assignment is then rotated by 90° [see top right panel in Fig. 2.6 (a)]. The resistance is recorded once again and denoted as R_2. According to ref. [38] the sheet resistance can then be computed using the following formula

$$R_s = \frac{R_1 + R_2}{2} \frac{\pi}{\ln 2} f\left(\frac{R_1}{R_2}\right) , \qquad (2.32)$$

where $f\left(\frac{R_1}{R_2}\right)$ denotes a correction factor which is only depending on the ratio $\frac{R_1}{R_2}$ and which is tabulated, e.g., in ref. [39]. If the sample is homogeneous and the contact geometry is symmetric such as in Fig. 2.6 (a), $R_1 = R_2$ holds and the correction factor f becomes 1. Indeed, as long as the resistances R_1 and R_2 differ by no more than 40%, the correction factor f is still reasonably close to 1 ($0.99 < f < 1.01$).

Beside the sheet resistance, the Hall coefficient and the charge carrier concentration as well as mobility can also be determined employing the van der Pauw contact geometry.[6] If a magnetic field B is applied at right angle to the sample surface, the Lorentz force deflects the electrons perpendicular to the magnetic field and the current direction. Consequently, an electric field E_H builds up perpendicular to the current field lines which compensates the Lorentz force.

With the contact assignment depicted in the bottom right panel of Fig. 2.6 (a) the resulting voltage drop can be measured in the van der Pauw geometry: A current I is passed through two opposing contacts, while the voltage V_H is sensed at the other two opposing contacts. Note that we do not measure voltages but always record resistances in our measurement setup. The

---

[6] The electrons near the Fermi edge are described by the Drude model[40] in the following considerations.

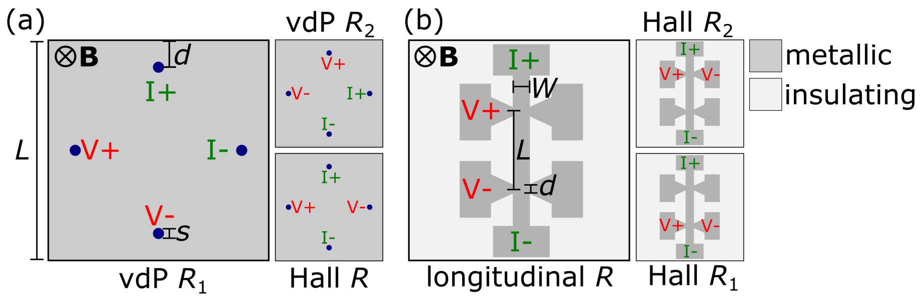

Fig. 2.6: (a) Illustration of contact geometry used for van der Pauw measurements: The figure on the right and the top figure on the left illustrate the contact configuration employed for measurements of the sheet resistance. The bottom figure on the right show the contact assignment for measurements of the Hall coefficient.
(b) Sketch of a sample patterned in a Hall bar configuration: The left figure depicts the contact configuration applied for measurements of the longitudinal resistance. For the Hall effect measurements (figures on the right) the Hall voltage is tapped between different contact pairs. For reasons of clarity the contacts themselves are not shown here. The figures are not drawn to scale.

transverse resistance $R_t = V_H/I$ is determined first at zero magnetic field. When a magnetic field B is applied at right angle to the sample surface, the resistance R_t changes by ΔR_t and the Hall coefficient R_H can be computed by[38]

$$R_H = \frac{\Delta R_t}{B}. \tag{2.33}$$

Within the Drude model[40] the sheet charge carrier concentration n_s and mobility μ can then be determined by the following equations

$$n_s = \frac{1}{R_H e}, \tag{2.34}$$

$$\mu = \frac{R_H}{R_s}. \tag{2.35}$$

All the equations above are derived for the case of only *one* charge carrier species contributing to the transport. If two species of charge carriers with, e.g., different band mass are involved in the conductivity, the equations (2.34) and (2.35) relating R_s and R_H to μ and n_s become more complex[41,42]

$$\sigma_s = \frac{1}{R_s} = e n_1 \mu_1 + e n_2 \mu_2, \tag{2.36}$$

$$R_H = -\frac{1}{e} \frac{\frac{n_1\mu_1^2}{1+\mu_1^2 B^2} + \frac{n_2\mu_2^2}{1+\mu_2^2 B^2}}{\left(\frac{n_1\mu_1}{1+\mu_1^2 B^2} + \frac{n_2\mu_2}{1+\mu_2^2 B^2}\right)^2 + \left(\frac{n_1\mu_1^2}{1+\mu_1^2 B^2} + \frac{n_2\mu_2^2}{1+\mu_2^2 B^2}\right)^2 B^2}, \tag{2.37}$$

where n_1 (μ_1) and n_2 (μ_2) denote the concentration (mobility) of the two charge carrier species.

Error estimation

One can classify the errors in transport experiments in two categories, viz. intrinsic and geometrical errors.[41] Intrinsic errors may, e.g., arise due a finite temperature gradient forming across the sample. Most of these intrinsic errors, however, cancel out when one measures at both magnetic field polarities as well as at both current polarities and averages the resulting readings.[41]

relative error	$\Delta R_s/R_s$	$\Delta R_H/R_H$
finite contact size	$-1.4\left(\frac{s}{L}\right)^2$ $\approx -0.1\%$	$-1.6\left(\frac{s}{L}\right)$ $\approx -3.2\%$
erroneous contact placement	$-2.9\left(\frac{d}{L}\right)^2$ $\approx -1.0\%$	$-2.6\left(\frac{d}{L}\right)$ $\approx -15.6\%$

Tab. 2.1: Relative measurement errors for transport experiments in van der Pauw geometry resulting from finite contact size and erroneous contact placement.[38,43] The contact geometry employed is defined in Fig. 2.6 (a). The errors are estimated for a circular sample.

The geometrical errors are more severe for our samples: The finite size of the contacts as well as the erroneous contact placement might induce measurement errors. In Tab. 2.1 we list the respective measurement errors for a sample[7] in which all four contacts have a finite size s and are displaced from the sample edge by a distance d [see contact configuration in Fig. 2.6 (a)].[38,43,44] To give a rough quantitative estimation of the errors, we furthermore plug in typical values of our contact setup.[8] While the wire-bonded contacts are small compared to the sample size, the contacts are comparably far off the sample edge, since the contacts cannot be placed at the very edge of the sample where residue of silver paste as well as significant substrate inhomogeneities are often found. That is why the erroneous contact placement dominates the measurement errors by far in our experimental setup. We furthermore note that the relative errors for the Hall coefficient $\Delta R_H/R_H$ are much larger than the relative errors for the sheet resistance $\Delta R_s/R_s$.

For transport experiments in van der Pauw geometry, the sample homogeneity is furthermore of utmost importance. Matsumara *et al.*[45] show in simulations that the charge carrier concentrations and mobilities vary from the actual values by as much as several tens of % if they introduce inhomogeneities in the samples. Bierwagen *et al.*[46] even find that sample inhomogeneities can change the sign of the Hall coefficient and can consequently lead to an incorrect identification of electron- and hole-like charge carriers. The effect of sample inhomogeneity is, however, depending sensitively on the exact shape and distribution of the inhomogeneities and can thus not be quantified.

In conclusion, the measurements in van der Pauw geometry are handy to characterize the transport characteristics of a sample 'as is', i.e., without further elaborate processing. However, in particular, the measurements of the Hall coefficient should be treated with caution, as the contact placement as well as sample inhomogeneities may distort the measurement results.

In the next section we show how these measurement errors can be reduced by probing transport on *patterned* samples.

2.3.2 Measurements in Hall bar geometry

Patterning the sample, one can create metallic and insulating areas on the sample on purpose. This way a rectangular conducting sheet, a so-called Hall bar, can be defined as exemplarily depicted in Fig. 2.6 (b). In this measurement geometry, more reliable results for the Hall coefficient are obtained, since the Hall bar geometry, contrary to the van der Pauw configuration, allows to control the geometry of the current lines and the position of the voltage probe points. Passing a current through the long side of the rectangle, we can measure the resistances along and perpendicular to the current flow which are effectively separated by the geometry of the Hall bar.

---

[7] We approximate our sample by a circle.

[8] We use $s = 0.1\,\mathrm{mm}$, $d = 0.3\,\mathrm{mm}$, $L = 5\,\mathrm{mm}$.

The left panel of Fig. 2.6 (b) shows the contact assignment employed for the measurement of the longitudinal resistance R_l. The longitudinal resistance R_l is converted to the sheet resistance R_s by[41]

$$R_s = R_l \cdot \frac{W}{L}, \tag{2.38}$$

where L and W describe the length and the width of the Hall bar (see Fig. 2.6 (b) for definition of L and W). For measurements of the Hall coefficient a different contact assignment is chosen as depicted in the right panels of Fig. 2.6 (b). The two figures show that the Hall voltage V_H can be tapped between different contact pairs. As is the case for the van der Pauw geometry, one determines the change in the transverse resistance $R_t = V_H/I$ with magnetic field B and computes the Hall coefficient according to equation (2.33). The mobility is then determined by

$$\mu = \frac{R_H}{R_l} \cdot \frac{L}{W}. \tag{2.39}$$

Error estimation

Intrinsic systematic errors also affect transport measurements in Hall bar geometry. Their effect can once again be reduced by combining measurements with different current and magnetic field polarities.

The geometrical errors are, however, reduced in the Hall bar geometry: The contacts in the Hall bar geometry are typically put at the end of arms [see Fig. 2.6 (b)]. This contact placement has been shown to curtail the error related to the finite contact size.[47] As long as the width d of the voltage probes is much smaller than the length L of the Hall bar and the ratio of Hall bar length L to Hall bar width W is larger than 3, the longitudinal and the transverse resistance R_l and R_t can be effectively separated.[48] As a consequence, one can reliably determine the magnetic field dependence of the transverse resistance $R_t(B)$ and subsequently the Hall coefficient R_H but also the magnetic field dependence of the longitudinal resistance, i.e., the magnetoresistance $R_l(B)$.

Equations (2.38) and (2.39) show that the measurement results are now scaling with the Hall bar dimensions. It is thus essential to fabricate Hall bars with an accurately defined width and length, which can, however, prove difficult for oxides. The patterning process has, e.g., been shown to damage the edges of $LaAlO_3/SrTiO_3$ nanostructures[49] and might thus reduce the effective Hall bar dimension. In ref. [49] the dimensions of the $LaAlO_3/SrTiO_3$ nanostructures do only change on the nanometer range. Yet, the impact of the patterning might depend on the exact parameters of the preparation process and might also be more pronounced for other materials which are more reactive and prone to disintegrate.

The dimensions of the Hall bar patterns are typically small compared to the sample size.[9] Several Hall bars can thus be fitted onto a single sample which allows to directly probe the homogeneity of the sample. In addition, the homogeneity can be checked by sensing the Hall voltage between different contact pairs within the same Hall bar.

In summary, transport measurements in Hall bar geometry yield more accurate results for the charge carrier concentration and mobility and can also provide a measure for the homogeneity of the sample. However, the samples have to be prepared in elaborate patterning processes[A7,50] for such transport experiments.

---

[9] Dimensions of samples in this thesis: 5 mm x 5 mm. Dimensions of Hall bars in this thesis: 600 μm x 100 μm.

Chapter 3

Disentangling generic and specific doping mechanisms in oxide heterostructures

When different materials are combined in a heterostructure, the symmetry is broken at the interface between the materials. As a result, new phases may emerge that are not present in the respective bulk components. In oxide materials, the two-dimensional electron system residing at the $LaAlO_3/SrTiO_3$ heterointerface is a prime example of such an effect: Even though both $LaAlO_3$ and $SrTiO_3$ are large-gap band insulators, the $LaAlO_3/SrTiO_3$ heterointerface is metallic.[3] The discovery of this interface conductivity has sparked tremendous research activity and led to the discovery of many fascinating properties of the 2DES.[3–8] However, the origin of the interfacial conductivity could not be clarified in experiments to date despite immense research efforts. Some publications claim that the 2DES forms as a consequence of a polar discontinuity at the $LaAlO_3/SrTiO_3$ heterointerface.[3,9,51] Other authors[52–56] challenge the idea of such a generic doping mechanism resulting from a broken symmetry at the interface. They maintain that the interface conductivity is rather induced by material-specific chemical reactions that occur during the fabrication of the heterostructure. In this chapter we aim to resolve this long-standing debate about the origin of the interfacial conductivity employing photoemission spectroscopy.

We first give an introduction to the $LaAlO_3/SrTiO_3$ heterostructure. We will, in particular, focus on the perovskite $SrTiO_3$ and its properties, as $SrTiO_3$ acts as the host material for the 2DES in the $LaAlO_3/SrTiO_3$ heterostructure and consequently determines the characteristics of the 2DES. Thereafter, we will review the different doping mechanisms that have been discussed to be at work at the $LaAlO_3/SrTiO_3$ heterointerface. We will show that valence band photoemission is able to distinguish the different doping mechanisms and unambiguously identify the doping processes in $LaAlO_3/SrTiO_3$ heterointerfaces. In the course of this discussion, we establish a method of engineering the oxygen vacancy (V_O) concentration of the $LaAlO_3/SrTiO_3$ heterostructures during the photoemission experiments at will. Exploiting this method, we finally complement our valence band measurements with core level photoemission to investigate how the electronic interface properties change as a function of the V_O concentration.

3.1 $SrTiO_3$ as host material for two-dimensional electron systems

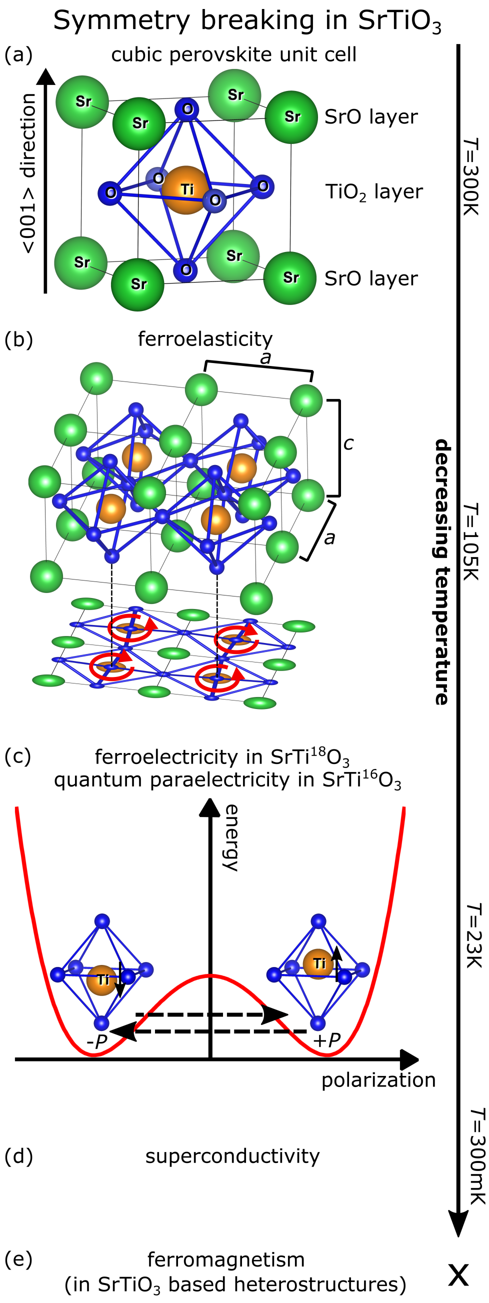

Fig. 3.1: Illustration of the phases with different symmetry which emerge in $SrTiO_3$ upon lowering the temperature. See text for details. Figure was inspired by ref. [57].

First, we introduce the substrate material of our heterostructures, viz. $SrTiO_3$ crystals. In $SrTiO_3$ intriguing phases emerge when the fundamental symmetries of the crystal are broken. Moving from room temperature to low temperature, we will discuss the symmetries of the $SrTiO_3$ crystal in the following, with an eye to the physics these (broken) symmetries entail. This paragraph was inspired by ref. [57].

3.1.1 Symmetry breaking in $SrTiO_3$

At room temperature, stoichiometric $SrTiO_3$ is a paraelectric and paramagnetic band insulator. It adopts a cubic perovskite structure (space group $Pm3m$) with a bulk lattice constant $a = 3.905\,\text{Å}$.[58] A sketch of the $SrTiO_3$ unit cell (in short uc) is shown in Fig. 3.1 (a): In the lattice of a cubic perovskite with the sum formula ABO_3 the typically larger[1] A cation sits at the corner of the unit cell while the smaller B cation is positioned at the center of the unit cell.[59] The oxygen anions in the face-centered positions of the unit cell form an octahedron surrounding the B cation. One can also picture the perovskite lattice as an alternate stacking of AO and BO_2 layers along the [001] direction.

When the temperature is lowered below 105 K, $SrTiO_3$ undergoes a structural ferroelastic phase transition to a phase in which the cubic point group symmetry is broken. In this so-called antiferrodistortive transition, the oxygen octahedra rotate around one of the cubic axes with adjacent oxygen octahedra rotating in opposite directions [cf. red arrows in Fig. 3.1 (b)].[60,61] The tilt of the oxygen octahedra is accompanied by a tetragonal distortion which deforms the unit cell into a rectangular cuboid with two shorter edges of length a and one longer edge of length c [see upper panel in Fig. 3.1 (b)]. The elongated c axis may be oriented along the [001], [010], or [100] direction, breaking up the $SrTiO_3$ crystal into orthogonal domains. The structural phase transition also affects the electronic properties: The structural deformation lifts orbital degeneracies and changes the electronic structure[62] as detailed below. Moreover, the evolution of domains leads to the formation of domain boundaries which affect the microscopic transport properties in doped $SrTiO_3$.[63]

At even lower temperatures, the inversion symmetry of the $SrTiO_3$ crystal is broken bringing about ferroelectricity: At room temperature, $SrTiO_3$ is paraelectric, as the Ti atom sits at

---

[1] with respect to its ionic radius

the center of the oxygen octahedron and the net electric dipole moment within the unit cell is zero. A non-vanishing electric dipole moment is only induced under an applied electric field which displaces the positively charged Ti atoms with respect to the negatively charged oxygen octahedron. At low temperatures, the potential landscape changes. Even in the absence of an electric field, the SrTiO$_3$ crystal starts to gain energy by displacing the Ti atom with respect to the oxygen octahedron, which induces a finite dipole moment, i.e., a finite polarization $\mathbf{P}$, within the unit cell [see the inset plots of the two polarization states in Fig. 3.1 (c)]. In the diagram of energy versus polarization, the characteristic double well potential of ferroelectric materials forms as illustrated in Fig. 3.1 (c). SrTi^{18}O$_3$, i.e., SrTiO$_3$ in which the 16 u oxygen isotope is replaced by the heavier 18 u oxygen isotope indeed becomes ferroelectric below 23 K.[64] SrTi^{16}O$_3$ thin films under small tensile strain also exhibit ferroelectricity, even up to room temperature.[65] In SrTi^{16}O$_3$ single crystals, however, the oxygen atoms are still light enough to tunnel through the potential barrier of the double well potential. The formation of a ferroelectric phase is suppressed by these quantum fluctuations and bulk SrTiO$_3$ thus remains in a paraelectric state.[66] Its proximity to a ferroelectric phase manifests itself in an exceptionally high dielectric constant of over 20,000 at low temperatures.[67,68] This behavior is coined quantum paraelectricity.

Below 300 mK the electromagnetic U(1) gauge symmetry is broken, inducing superconductivity in electron-doped SrTiO$_3$.[69] Various SrTiO$_3$-based heterostructures have as well been shown to inherit the superconducting properties from SrTiO$_3$.[6]

If rotational symmetry in spin space is broken, ferromagnetism emerges, which has been detected to date in SrTiO$_3$-based heterostructures[4,70] and in SrTiO$_3$ thin films.[71] Superconductivity and magnetism have even been observed to coexist in SrTiO$_3$-based heterostructures.[7,8,71,72]

Having touched upon the rich phase diagram of SrTiO$_3$, we will delve into the electronic structure of SrTiO$_3$ in more detail in the next section.

3.1.2 Electronic structure

SrTiO$_3$ is innately a band insulator with an optical band gap of about 3.2 to 3.4 eV.[82–84] The valence band of SrTiO$_3$ is mainly composed of O $2p$ orbitals, while its conduction band has predominantly Ti $3d$ orbital character. In stoichiometric SrTiO$_3$, Ti is in a $3d^0$ electron configuration

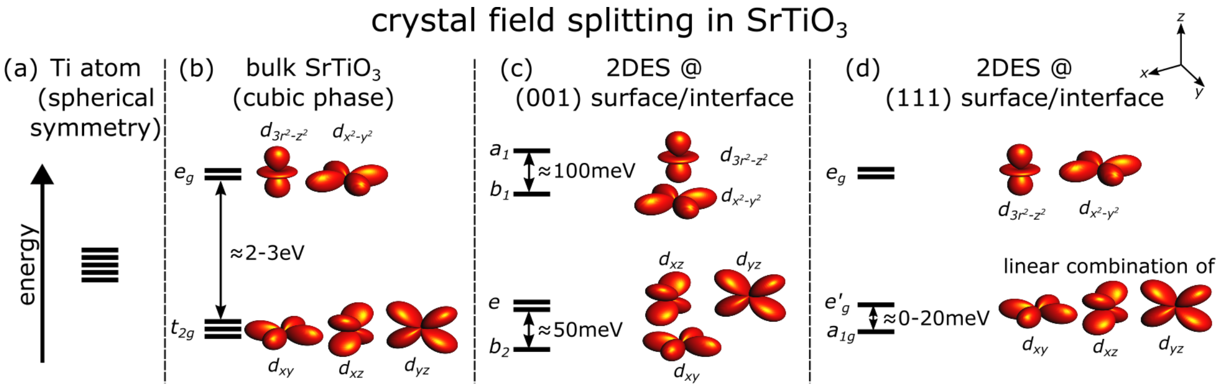

Fig. 3.2: Crystal field splitting in SrTiO$_3$: (a) In an isolated Ti atom, the Ti $3d$ energy levels are fivefold degenerate. (b) The five degenerate Ti $3d$ energy levels split into a triplet labeled t_{2g} and into a doublet labeled e_g in the cubic phase of SrTiO$_3$. (c)/(d) The confining potential present at, e.g., an surface or interface breaks the inversion symmetry of the SrTiO$_3$ crystal which further alters the energy of the Ti $3d$ orbitals. Figures (c) and (d) depict the energy level splitting which occurs at a (001) and at a (111)surface/interface, respectively. The energy separation of the single levels is not drawn to scale. Values for energy splitting from refs. [73–81].

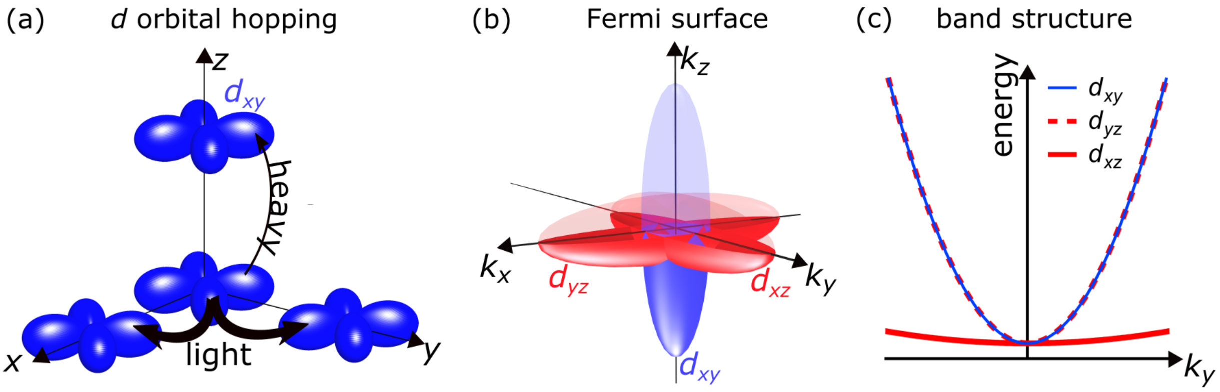

Fig. 3.3: Tight binding approach applied to $SrTiO_3$: (a) Hopping between the d_{xy} orbitals. Due to the orientation of the orbitals the probability for hopping is large (small) along the x and y direction (z direction). Figure adapted from ref. [76]. (b) Fermi surface derived from a three-dimensional the tight binding model. The Fermi surface is exemplarily cut along the (001) plane. (c) Corresponding conduction band structure along the k_y direction. The lobe/band made up of the d_{xy} orbitals is marked in blue in (b) and (c).

and the conduction band is empty. However, by oxygen depletion or by the incorporation of Nb or La in its crystal lattice, $SrTiO_3$ can be easily doped with electrons that populate the Ti 3d orbital manifold.

The Ti 3d energy levels governing the low energy physics are not five-fold degenerate in $SrTiO_3$: The oxygen octahedra surrounding the Ti atom in the $SrTiO_3$ bulk in the cubic phase give rise to an octahedral (O_h) crystal field that lifts the degeneracy of the Ti 3d energy levels:[82] The five Ti 3d orbitals split into the three energetically lowered t_{2g} orbitals (d_{xy}, d_{xz}, d_{yz}) and the two energetically raised e_g orbitals (d_{z^2}, $d_{x^2-y^2}$) as illustrated in Fig. 3.2 (b).

When the cubic symmetry of the $SrTiO_3$ crystal is broken, e.g., in the ferroelastic phase transition, the t_{2g} and e_g levels break into even more separate energy levels. Likewise, the splitting of the Ti 3d energy levels changes when the inversion symmetry of the crystal is broken at the $SrTiO_3$ surface/interface, and parity is no longer a good quantum number. Figures 3.2 (c) and (d) exemplarily show the energy level scheme at a (001) and a (111) surface, respectively. In spectroscopy experiments, the energy splitting within the t_{2g} and the e_g orbital manifold has furthermore been shown to depend on the oxidation state of the Ti cation. The intra-t_{2g} level splitting is, e.g., increasing up to 300–600 meV in $Ti^{3+}O_6$ octahedra.[A3,85]

Combining the crystal field picture with a tight binding approach, one can derive the $SrTiO_3$ band structure:[86,87] The orbitals relevant for the tight binding description of $SrTiO_3$ are the three $d_{t_{2g}}$ orbitals owing to their lower energy. We will exemplarily discuss the hopping matrix elements for the d_{xy} orbital in the nearest neighbor approximation. The d_{xy} orbitals mainly couple to adjacent d_{xy} orbitals. Hopping between d_{xy} orbitals and d_{xz} orbitals as well as hopping between d_{xy} orbitals and d_{yz} orbitals is thus neglected. With the d_{xy} orbital lobes lying in the xy plane, the electrons mainly hop between adjacent d_{xy} orbitals in x and y direction [see Fig. 3.3 (a)]. The resulting Fermi surface lobe is thus characterized by a low mass in k_x and k_y direction and a high mass in k_z direction and thus shaped like a cigar pointing in k_z direction [see the lobe marked in blue in Fig. 3.3 (b)]. Similar considerations hold for the d_{xz} and d_{yz} orbitals. The Fermi surface is thus composed of three lobes oriented along the x, y and z axes as illustrated in Fig. 3.3 (b). The Fermi surface in Fig. 3.3 (b) is exemplarily cut along the (001) plane. The corresponding band structure along the k_y axis is depicted in Fig. 3.3 (c).

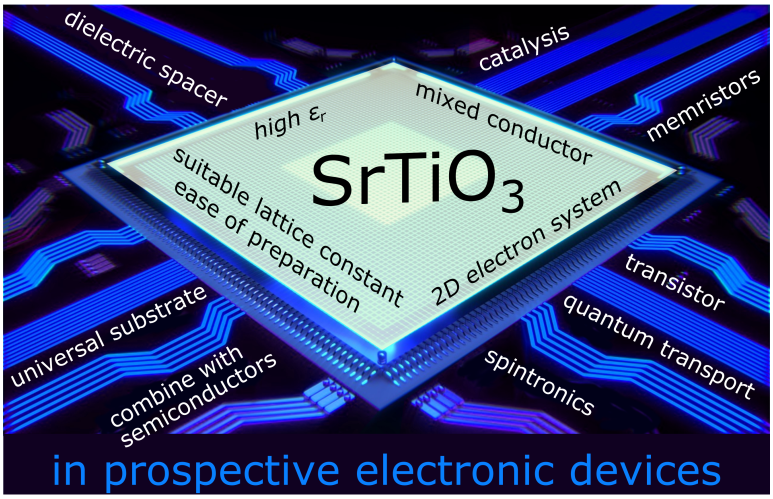

Fig. 3.4: Synopsis over the properties of SrTiO$_3$ and their potential applications in future electronic devices. Figure adapted from ref. [93].

3.1.3 SrTiO$_3$ as substrate for oxide growth

Due to the SrTiO$_3$ lattice constant nicely matching the lattice constant of other oxide materials,[88] SrTiO$_3$ crystals are the substrate material of choice for the growth of a variety of other oxide systems. To enable controlled epitaxial material growth, it is essential that the SrTiO$_3$ substrate surface is atomically flat and has a defined single termination, which can be achieved by a well-established method: For (001)-oriented SrTiO$_3$ substrates, an atomically flat and homogeneous TiO$_2$-terminated surface can be obtained applying the treatment Kawasaki *et al.*[88,89] propose. For this purpose, the substrates are successively immersed in deionized water and in a buffered HF solution, which is followed by an annealing step.

3.1.4 SrTiO$_3$ in prospective electronic applications

SrTiO$_3$ may potentially also be exploited in future electronic devices as discussed in the following. Figure 3.4 represents some essential properties of the SrTiO$_3$ crystal as well as their potential application in future electronic devices.

Due to its lattice constant and the relative ease of surface preparation, SrTiO$_3$ is ideally suited as a substrate material upon which all kinds of oxide thin films can be deposited. However, SrTiO$_3$ cannot only be interfaced with oxides but with established semiconductors as well. McKee *et al.*[90] show that SrTiO$_3$ can be grown epitaxially on the (001) face of silicon without any amorphous SiO$_2$ phase forming at the interface. This way, one could couple traditional Si-based electrical devices with SrTiO$_3$ and potentially even with more complex oxides deposited on top of the SrTiO$_3$ layer.[91,92]

One characteristic of SrTiO$_3$ which may be utilized in electronic devices is its exceptionally high dielectric constant which opens up opportunities to employ SrTiO$_3$ as an alternative gate dielectric: Hitherto, amorphous silica SiO$_2$ is used as gate dielectric in silicon-based electronics. However, SiO$_2$ is beginning to encounter its fundamental limits in the ongoing quest for miniaturization of electric circuits.[94] When the thickness of the gate oxide is further and further reduced, tunneling currents through the amorphous SiO$_2$ layer will render the devices unusable at one point. SrTiO$_3$ with its higher dielectric constant[2] might prove a feasible alternative of overcoming the current scaling limitations.[90]

---

[2] Dielectric constant of SrTiO$_3$ at 300 K: ≈300.[73,95] Dielectric constant of amorphous SiO$_2$ at 300 K: 3.9.[94]

Building devices out of oxide materials one can, however, also realize novel functionalities, as, e.g., memristors which can be used to implement artificial synapses.[96] The name memristor is a combination of the words memory and resistor and describes a device whose resistance is depending on the prior charge flow through the device. Such a memory behavior can be realized in $SrTiO_3$:[A7,97] Oxygen-deficient $SrTiO_3$ is a mixed conductor, i.e., it is prone to ionic conductivity in addition to the electronic conductivity. A bias voltage applied to oxygen-deficient $SrTiO_3$ does thus not only affect the electronic charge distribution but also the drift of charged oxygen vacancies. Concomitantly with the distribution of the oxygen vacancies, the electronic conductance of the $SrTiO_3$ is changing. This phenomenon is called resistive switching and is at the heart of the memory behavior characteristic of memristors.

The mixed conduction in $SrTiO_3$ is also exploited for catalysis.[98]

The central element of many electronic devices which are based on conventional semiconductors are two-dimensional electron gases. By interfacing $SrTiO_3$ with other oxides, $SrTiO_3$ can also be doped and a conducting layer can be induced which can be functionalized for device applications.[10–12] The textbook example for this is the two-dimensional electron system at the $LaAlO_3/SrTiO_3$ heterointerface which is also the main focus of this thesis and which is thus separately introduced in the next section.

3.2 The $LaAlO_3/SrTiO_3$ heterostructure

At room temperature, $LaAlO_3$ adopts a rhombohedrally distorted perovskite structure (space group $R\bar{3}c$).[99] The $LaAlO_3$ crystal structure can also be described in pseudocubic notation in which its lattice constant amounts to $a = 3.791\,\text{Å}$. Despite the lattice mismatch of 3% between $SrTiO_3$ and $LaAlO_3$, epitaxial $LaAlO_3$ films can be grown on a $SrTiO_3$ substrate. Just as $SrTiO_3$, $LaAlO_3$ is a band insulator (band gap $\approx 5.6\,\text{eV}$).[99] However, in 2004 Ohtomo and Hwang[3] were the first to report a high-mobility two-dimensional electron gas forming at the $LaAlO_3/SrTiO_3$ heterointerface.

This seminal finding spurred further research and many more remarkable properties of the $LaAlO_3/SrTiO_3$ heterostructure have been discovered in recent years: The interface conductivity has been shown to emerge only above a critical $LaAlO_3$ film thickness.[9] Large Rashba spin-orbit interaction has been observed at the $LaAlO_3/SrTiO_3$ interface.[5] In other publications the heterointerface has been shown to be superconducting[6] and also ferromagnetic.[4] In some samples superconductivity and ferromagnetism have even been found to coexist.[7,8]

The $LaAlO_3/SrTiO_3$ heterointerface has also proven interesting with respect to device applications:
The 2DES and its properties can effectively be tuned by the electric field effect.[5,9,100] Thiel *et al.*[9] find that the heterointerface can even be switched from a conducting to an insulating state and can be used as a field-effect transistor.[10]

The Rashba spin-orbit interaction at the interface can, in contrast, be exploited in spintronic devices to convert a charge current to a spin current and vice versa.[11,12] Notably, the Rashba spin-orbit coupling and the conversion efficiency can also be manipulated by an electric field.

Over the years, considerable effort has been spent to increase the charge carrier mobility in the $LaAlO_3/SrTiO_3$ heterostructures.[101–103] Nowadays, mobilities up to $10^4\,\text{cm}^2/(\text{Vs})$ have been achieved[103,104] and quantum conductance oscillations[101,104] as well as ballistic transport[105,106] have been observed in high-quality $LaAlO_3/SrTiO_3$ heterointerfaces as well. At enhanced quality $LaAlO_3/SrTiO_3$ heterostructures might prove a promising platform to build mesoscopic quantum devices and to explore quantum transport phenomena lying beyond the realm of the III–V semiconductor materials.[105,106]

While all these effects rely on the 2DES forming at the $LaAlO_3/SrTiO_3$ heterointerface, the discussion about the mechanisms which render the interface metallic is still ongoing. In the following, we review the various doping mechanism suggested in detail.

3.3 Doping mechanisms in oxide heterostructures

Doping mechanisms in oxide heterostructures can be classified in two categories, generic and specific doping mechanisms. Generic doping mechanisms are based on the fundamental properties of the constituent materials such as the symmetry breaking at the interface and do not depend on the specifics of the deposition process. As such, they can also be transferred to other material systems with similar properties. Specific doping mechanisms are, in contrast, based on the defect chemistry in the material and thus heavily rely on the specific material system as well as on the deposition process.

3.3.1 Generic doping mechanism – doping by electronic reconstruction

One extensively discussed *generic* doping mechanism for the $LaAlO_3/SrTiO_3$ heterostructures is the electronic reconstruction:[3,9,107,108] In an ionic picture one can describe the $SrTiO_3$ lattice as charge-neutral $(Sr^{2+}O^{2-})^0$ and $(Ti^{4+}O_2^{2-})^0$ layers alternating in [001] direction. The $LaAlO_3$ lattice is, in contrast, composed of positively charged $(La^{3+}O^{2-})^+$ and negatively charged $(Al^{3+}O_2^{2-})^-$ planes. The change in polarity at the interface triggers a potential build-up across the $LaAlO_3$ film when $LaAlO_3$ is stacked on top of a $SrTiO_3$ substrate [see Fig. 3.5 (a)]. For an infinitely thick $LaAlO_3$ film the potential would diverge, which is called polar catastrophe. However, this is energetically not favorable and in the most simple electronic reconstruction scenario, electrons are transferred from the $LaAlO_3$ surface valence band to the interfacial $SrTiO_3$ conduction band as soon as the potential build-up is exceeding the band gap of the $LaAlO_3$ film. If half an electron per surface unit cell is transferred the potential gradient in the film is compensated and a flat band situation occurs [see Fig. 3.5 (b)]. The electronic reconstruction scenario is thus characterized by a metal-insulator transition which is dependent on the film thickness. By electrostatic considerations, the critical thickness for conductivity is estimated to 3.5 $LaAlO_3$ unit cells.[107]

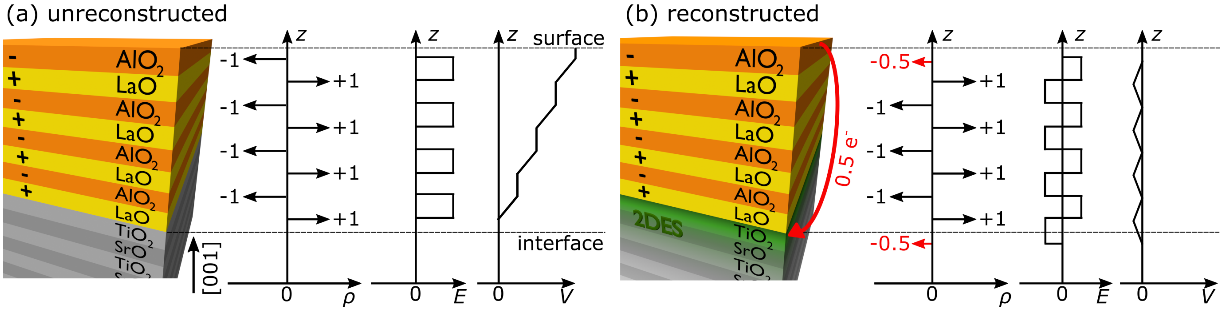

Fig. 3.5: Illustration of the electronic reconstruction scenario: (a) In [001] direction the $SrTiO_3$ lattice can be described as charge-neutral $(Sr^{2+}O^{2-})^0$ and $(Ti^{4+}O_2^{2-})^0$ layers alternating whereas the $LaAlO_3$ lattice is composed of charged $(La^{3+}O^{2-})^+$ and $(Al^{3+}O_2^{2-})^-$ planes. The change in polarity at the interface triggers a potential build-up across the $LaAlO_3$ film when stacking $LaAlO_3$ on top of $SrTiO_3$. (b) From a critical $LaAlO_3$ film thickness on, this potential build-up is energetically not longer favorable. In the most simple electronic reconstruction scenario, half an electron is transferred from the $LaAlO_3$ surface valence band (VB) to the interfacial $SrTiO_3$ conduction band (CB) which counteracts the diverging potential.

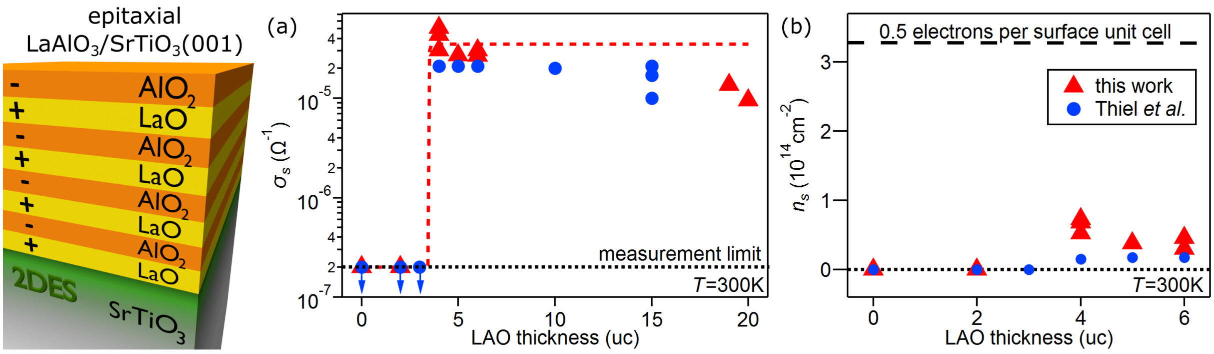

Fig. 3.6: Transport characterization of epitaxial $LaAlO_3$/$SrTiO_3$ heterostructures with varying $LaAlO_3$ film thickness. Room-temperature sheet conductance (a) and sheet carrier concentration (b) show a metal-insulator transition occurring at a $LaAlO_3$ film thickness of 4 uc. The measured sheet conductance is well below the sheet conductance estimated for an ideal electronic reconstruction scenario. The samples investigated in this work show the same characteristic transport behavior as comparable samples of Thiel *et al.*[9].

Transport experiments indeed show that $LaAlO_3$/$SrTiO_3$ heterostructures only become metallic above a critical $LaAlO_3$ film thickness of 4 unit cells[9] [see Fig. 3.6 (a)]. The critical thickness of 4 uc is observed in many laboratories and does, in particular, not depend on the exact deposition parameters in use, corroborating the polar discontinuity scenario.[9,51,107] In Figs. 3.6 (a) and (b) we also compare the transport properties of our samples (red triangles) to the data of Thiel *et al.*[9] (blue spheres) and find a good agreement.

However, other experimental observations seem to contradict the electronic reconstruction picture: In the ideal electronic reconstruction scenario the potential build-up in the $LaAlO_3$ film is compensated by half an electron that is transferred from the $LaAlO_3$ surface to the interface. Such an electron transfer would induce a sheet charge carrier concentration of $3.3{\cdot}10^{18}\,\mathrm{cm}^{-2}$ at the $LaAlO_3$/$SrTiO_3$ heterointerface. The typical sheet charge carrier concentrations measured in transport experiments on $LaAlO_3$/$SrTiO_3$ heterostructures are, however, one order of magnitude smaller as illustrated in Fig. 3.6 (b). Furthermore metallic interfaces have only been observed when the $LaAlO_3$ films are deposited on TiO_2-terminated $SrTiO_3$ crystals. Although a polar discontinuity also arises when $LaAlO_3$ is deposited on SrO-terminated $SrTiO_3$ crystals, these heterostructures remain insulating.[3]

So far the hallmarks of the standard electronic reconstruction picture have also remained elusive in spectroscopy measurements: In the standard electronic reconstruction picture the $LaAlO_3$ valence band is assumed to cross the Fermi level at the sample surface [see also band scheme colored in red in Fig. 3.9 (b)].[108] However, metallic states at the $LaAlO_3$ surface have not been observed to date.[109] Moreover, the potential build-up in the $LaAlO_3$ film in the electronic reconstruction picture should become apparent in the spectra of the film core levels: Due to the varying potential, the binding energy of the core level lines shifts across the $LaAlO_3$ film (see illustration in Fig. 3.9 (b), band scheme colored in red). As all film layers contribute to the photoemission signal, one would thus expect to measure film core level lines which are asymmetrically broadened and shifted in binding energy. However, in photoemission experiments the film core level lines are found to be sharp and symmetric, which shows that the bands in the $LaAlO_3$ film are flat [see band scheme colored in black in Fig. 3.9 (b)].[110,111]

Various authors manage to reconcile all the experimental results with the electronic reconstruction picture by introducing more elaborate models:[112–116] Instead of the $LaAlO_3$ valence band, localized defect states at the $LaAlO_3$ surface, e.g., charged oxygen vacancies have been suggested to act as a charge reservoir for the electronic reconstruction. Above the critical thickness these

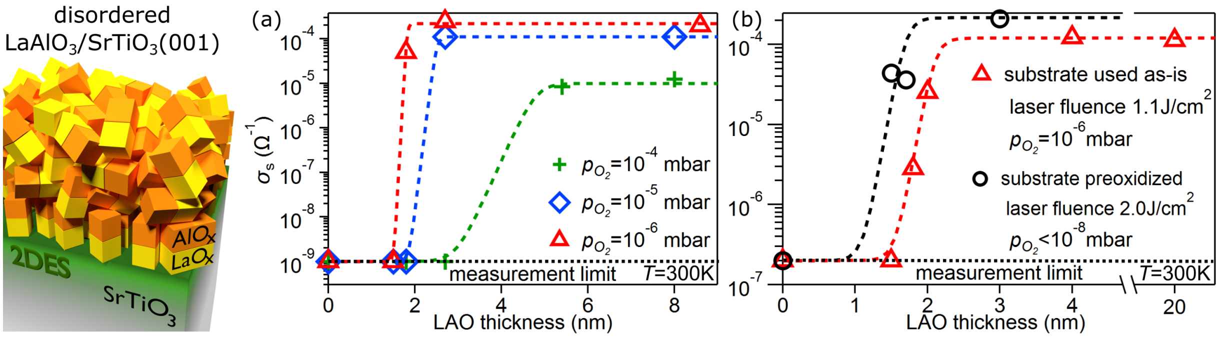

Fig. 3.7: Transport characterization of disordered $LaAlO_3/SrTiO_3$ heterostructures with varying $LaAlO_3$ overlayer thickness. (a) Room-temperature sheet conductance of samples for which the disordered $LaAlO_3$ was deposited at different oxygen background pressures. Data adopted from ref. [117]. (b) Room-temperature sheet conductance of our samples for two different sets of deposition parameters. While a metal-insulator transition is observed for all sets of samples, the critical thickness strongly depends on the deposition parameters used.

defect states form as their formation enthalpy is exceeded by the energy gained when the released charge is transferred to the interface and counteracts the potential build-up. Such refined models explain the absence of the potential gradient as well as the insulating character of the $LaAlO_3$ surface but are still driven by the polar discontinuity arising at the epitaxial $LaAlO_3/SrTiO_3$ interface, i.e., by a generic property of the constituent materials.

3.3.2 Specific doping mechanisms

Conductivity and, in particular, a critical thickness are not only observed for the epitaxial $LaAlO_3/SrTiO_3$ heterostructures but also if the $SrTiO_3$ substrate is capped by a disordered $LaAlO_3$ overlayer instead.[51,117] Albeit the disordered $LaAlO_3/SrTiO_3$ heterointerfaces do not exhibit a polar discontinuity, a clear metal-insulator transition is observed as function of the disordered $LaAlO_3$ overlayer thickness [see transport characterization of disordered $LaAlO_3/SrTiO_3$ heterostructure in Figs. 3.7 (a) and (b)]. The striking similarity of the transport properties in epitaxial and disordered $LaAlO_3/SrTiO_3$ heterostructures raises the question of a common nature of the interfacial doping mechanism. In other words, is the doping at the epitaxial $LaAlO_3/SrTiO_3$ heterointerface indeed induced by a generic property of the constituent materials, i.e., by the polar discontinuity at the interface? Or is the doping, both in the disordered and the epitaxial $LaAlO_3/SrTiO_3$ heterostructures, rather brought about by defect chemistry, i.e., by specific doping mechanisms? Such specific doping processes are discussed in detail in the following.

It has been suggested that oxygen vacancies play the crucial role in $SrTiO_3$-based heterostructures and induce interfacial conductivity:[52] For instance, it is well known that irradiation with an intense x-ray beam creates oxygen vacancies at the bare $SrTiO_3$ surface. As shallow donors the oxygen vacancies provide mobile electrons. As a result, a 2DES forms even at the bare $SrTiO_3$ surface.[A8,76,79,80,118–120]

Oxygen vacancies in $SrTiO_3$ can also be created in redox reaction when metallic Al is deposited on a $SrTiO_3$ substrate:[121,122] Since the heat of formation of AlO_x is larger than the energy which is needed to form an oxygen vacancy in $SrTiO_3$, the Al atoms oxidize upon arrival at the substrate surface scavenging oxygen from the $SrTiO_3$ surface which becomes metallic in turn. When $LaAlO_3$ is evaporated in the pulsed laser deposition process, the laser plume also contains atomic Al species which might induce oxygen vacancies and metallicity in the $SrTiO_3$ substrate.[123] Such a scenario could explain why a 2DES forms at both, epitaxial as well as disordered $LaAlO_3/SrTiO_3$ heterointerfaces.

The decisive role of oxygen vacancies in disordered $LaAlO_3/SrTiO_3$ heterostructures is substantiated by further experimental findings: The disordered $LaAlO_3/SrTiO_3$ heterostructures react sensitively to oxygen and become insulating when they are exposed to an oxygen atmosphere at elevated temperatures.[51] Moreover, the critical thickness observed for disordered $LaAlO_3/SrTiO_3$ heterostructures depends intricately on the deposition conditions. Figure 3.7 (a) shows that the critical thickness can be tuned by depositing the $LaAlO_3$ at different oxygen partial pressures.[117]

However, note that epitaxial $LaAlO_3/SrTiO_3$ heterostructures behave differently in similar experiments: Neither does their critical thickness depend on the deposition conditions, nor do the samples become insulating upon post-oxidation.[9,51,107] These findings call the crucial contribution of oxygen vacancies in epitaxial $LaAlO_3/SrTiO_3$ heterostructures in question.

Another specific doping mechanism proposed to be at work in $LaAlO_3/SrTiO_3$ heterostructures is cation intermixing: Up to now, we have always assumed that the interface between the $LaAlO_3$ film and the $SrTiO_3$ substrate is atomically abrupt. However, this does not necessarily have to be the case: As a $LaAlO_3$ film is deposited on top of a $SrTiO_3$ substrate, it might be energetically favorable for the heterostructure to form a diffuse rather than an abrupt interface, since the polar discontinuity at the interface can also be alleviated by cations intermixing at the interface.[124] The extreme growth conditions characterizing the PLD process may exacerbate and drive the cation interdiffusion: Particles arriving with a high kinetic energy at the substrate surface can, e.g., implant into the $SrTiO_3$ substrate. Since La-doped $SrTiO_3$ is metallic, cation intermixing at the interface might account for the interfacial conductivity as well.[125] Several studies employing different experimental methods have indeed found evidence for cation interdiffusion at the epitaxial $LaAlO_3/SrTiO_3$ interface.[56,126–129]

In summary, there are manifold explanations regarding the charge reservoir and transfer to the interface in the different $SrTiO_3$-based heterostructures which are sketched in Fig. 3.8. In particular, in the case of the epitaxial $LaAlO_3/SrTiO_3$ heterostructure, the prevalent doping mechanism has, however, not been identified to date.

3.4 Doping mechanisms investigated by photoemission

Even years after the discovery of the 2DES at the epitaxial $LaAlO_3/SrTiO_3$ interface no experiment hitherto succeeded in revealing unambiguous information on the origin of the interfacial charge carriers. To address this question we resort to photoemission spectroscopy probing the single-particle excitations of the valence electrons in the next section. The results presented here are published in ref. [A6].

To discriminate different doping mechanisms, we analyze samples which differ in the key parameters deemed crucial for the occurrence of interfacial conductivity: To investigate the impact of oxygen vacancies, we devise a method to systematically control the V_O concentration in the various heterostructures during the photoemission experiment. Bare $SrTiO_3$ surfaces are studied as a reference system in which the 2DES is routinely ascribed to oxygen vacancies.[A8,76,79,80,118–120,130] Samples with disordered and crystalline $LaAlO_3$ overlayers are compared to elucidate the role of the polar discontinuity. To shed light onto the effect of photoinduced carriers, we furthermore examine samples with varying thicknesses of the epitaxial $LaAlO_3$ overlayer.

3.4.1 Experimental details

To probe the valence band states originating from the buried interfaces, we employ resonant soft x-ray photoemission (in short SXPES).[109,131] The experiments below were conducted at the two-color beamline I09 at Diamond Light Source where a soft x-ray (SX) and hard x-ray (HX) beam focused onto the same spot (spot size $30\,\mu m \times 50\,\mu m$) were at our disposal.

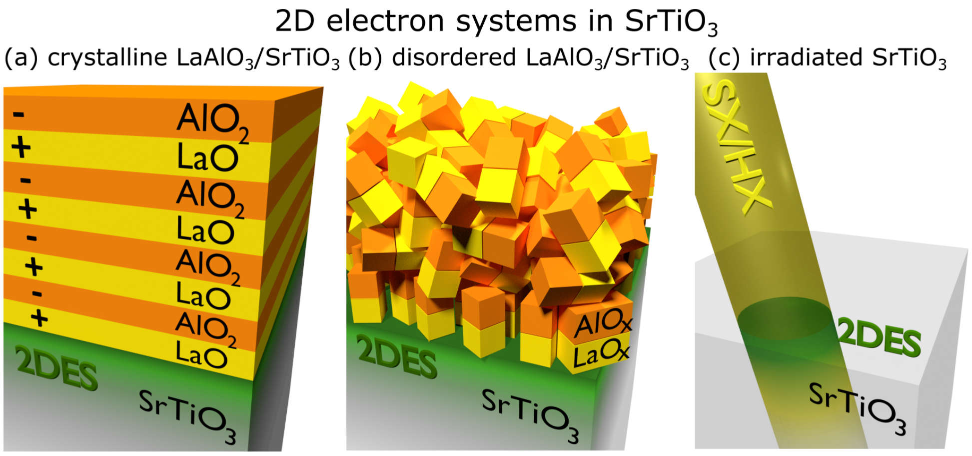

Fig. 3.8: 2DESs have been detected in numerous $SrTiO_3$-based heterostructures, e.g., at the interface between an epitaxial (a) or disordered (b) $LaAlO_3$ film and a $SrTiO_3$ substrate or at the $SrTiO_3$ surface after it has been irradiated with an intense x-ray beam (c). Various doping mechanisms are discussed to be at play in the different $SrTiO_3$-based heterostructures.

All samples were measured at a temperature of 60 K after having been exposed to air. An EW4000 photoelectron analyzer equipped with a wide angle acceptance lens (VG Scienta, Uppsala, Sweden) was used to acquire the spectroscopic data. The samples were all oriented in the exact same manner with the analyzer slit aligned parallel to the $\Gamma - X$ direction. The spectra were then integrated over the whole angular acceptance range of the analyzer (acceptance angle parallel to analyzer slit 60°, perpendicular to analyzer slit 0.3°) and normalized to the spectral contributions from second order light[3] which were subsequently subtracted in all spectra.[109]

3.4.2 Sample fabrication

The epitaxial 4 uc thick $LaAlO_3/SrTiO_3$ heterostructures were grown by pulsed laser deposition on TiO_2-terminated $SrTiO_3$ substrates at an oxygen partial pressure of $1 \cdot 10^{-3}$ mbar, a substrate temperature of 780°C, a laser fluence of $1.4\,\mathrm{J/cm^2}$ and a pulse repetition rate of 1 Hz.[A9] To eliminate oxygen vacancies created during the synthesis, the samples were cooled down after growth in a 500 mbar oxygen atmosphere with temperatures being held constant at 560°C for 1 h, at 460°C for 30 min and at 360°C for 30 min.

The disordered $LaAlO_3$ films were deposited by pulsed laser deposition at room temperature. Before the $LaAlO_3$ deposition the $SrTiO_3$ substrates were degassed for 1 h in a 500 mbar oxygen atmosphere at 500°C to avoid carbon contamination at the interface. The high oxygen background pressure prevented that oxygen vacancies form during this annealing step. The 1.7-nm-thick disordered $LaAlO_3$ films were subsequently deposited at room temperature in vacuum (base pressure $< 1 \cdot 10^{-8}$ mbar), at a laser fluence of $2.0\,\mathrm{J/cm^2}$ and 1 Hz pulse repetition rate.

The transport characterization of such epitaxial and disordered $LaAlO_3/SrTiO_3$ heterostructures with varying thickness is presented in Fig. 3.6 and Fig. 3.7 (b), respectively. Our samples show the same characteristic transport behavior as comparable samples of other groups.[9,117]

The Nb-doped $SrTiO_3$ substrates had a defined TiO_2 surface termination and measured without further surface preparation.

---

[3] Even after monochromatization the photon beam still contains some light of the photon energy $2h\nu$. When measuring at the resonance of the Ti $2p \rightarrow 3d$ transition, this second order light may excite Ti $2p$ electrons which escape from the sample with a similar kinetic energy as the valence band electrons excited by first order light and thus appear near the chemical potential in the spectra.

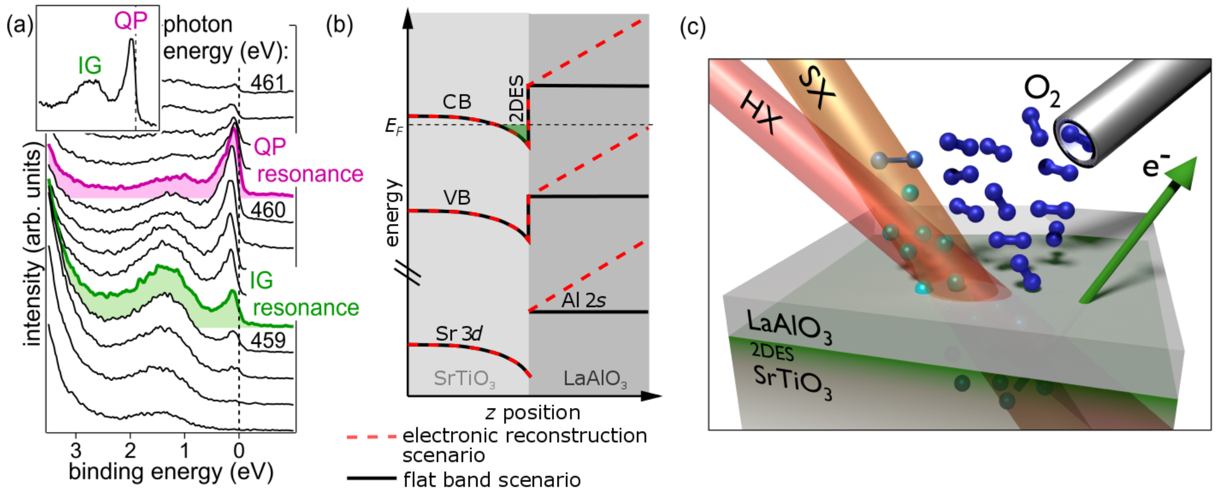

Fig. 3.9: (a) Valence band spectra of an oxygen-deficient $SrTiO_3$ surface. As the photon energy is scanned across the Ti L absorption edge, the quasiparticle (QP) state at the Fermi edge as well as an in gap (IG) feature at 1.3 eV binding energy are resonantly enhanced. (b) Scheamtic band diagram of the $LaAlO_3/SrTiO_3$ heterointerface as expected according to the standard electronic reconstruction scenario[108] and as derived from photoemission spectroscopy.[110,111] (c) Illustration of the photoemission and oxygen dosing setup at beamline I09, Diamond Light Source. Figure adapted from ref. [A6].

3.4.3 Bare $SrTiO_3$ surface: a 2DES induced by oxygen depletion

To familiarize ourselves with the experimental technique, we first study a bare $SrTiO_3$ substrate as a reference system: It is well known that the 2DES at the bare $SrTiO_3$ surface is induced by oxygen depletion and concomitant band bending.[A8,76,79,80,118–120,130] In valence band spectra of such an oxygen-depleted $SrTiO_3$ surface two prominent features are known to arise[A8,79,80,118,119,130] [see inset of Fig. 3.9 (a)]. While the so-called quasiparticle (QP) peak at the Fermi edge is ascribed to the itinerant carriers forming the 2DES, in gap (IG) states lying at ≈1.3 eV binding energy reflect the existence of localized carriers. Density functional theory studies confirm the experimental finding that electrons released by oxygen vacancies do not only populate states at the Fermi level but at the same time give rise to the distinct 1.3 eV peak ubiquitously observed in oxygen-deficient $SrTiO_3$.[132–134]

Tuning the photon energy through the Ti L absorption edge as shown in Fig. 3.9 (a), the QP and IG features are resonantly enhanced at certain photon energies (see pink- and green-colored spectra in Fig. 3.9 (a), respectively). The resonant enhancement of both the QP and the IG feature at the Ti L absorption edge shows that both states have Ti 3d character. The difference in the resonance energies of ≈ 1 eV reveals that the features originate from different types of electronic states.[109]

Being now acquainted with the signatures of oxygen vacancies in the valence band spectra of $SrTiO_3$, we establish our method of altering the oxygen vacancy concentration of the samples next. Highly intense synchrotron radiation is known to create oxygen vacancies at the bare $SrTiO_3$ surface:[A8,79,80,118,119] This becomes apparent in the series of valence band spectra recorded on the QP resonance depicted in Fig. 3.10 (a). The measurement series is started on a fresh spot and shows how the valence band spectra taken on the bare $SrTiO_3$ (001) surface evolve under continuous irradiation. The arrow in Fig. 3.10 (a) illustrates the sequence in which the measurements were recorded. The oxygen depletion is becoming apparent in a severe and fast increase in both QP and IG weight over the duration of the measurement, i.e., over irradiation time.

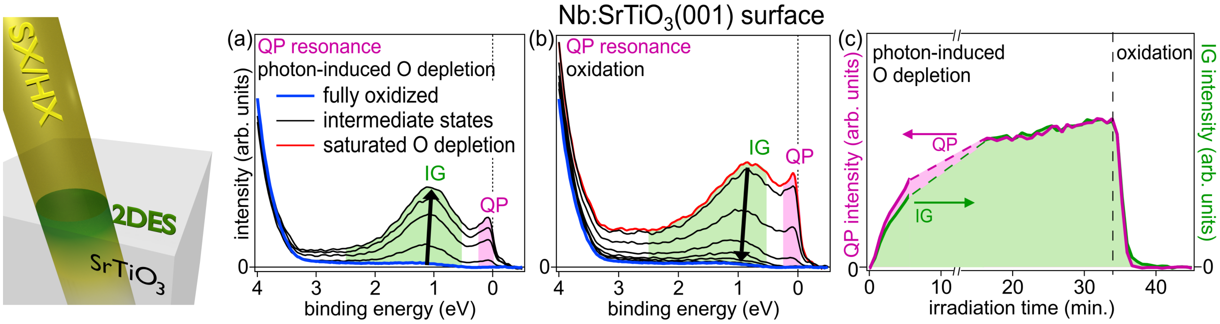

Fig. 3.10: Valence band spectra of the bare $SrTiO_3$ (001) surface recorded on the QP resonance at different V_O concentrations: (a) Series of valence band spectra recorded on a fresh spot under continuous x-ray exposure in vacuum. (b) Series of valence band spectra recorded on an oxygen-depleted spot under O dosing. The spectra are recorded on the QP resonance. The valence band spectrum of the fully oxidized state is shown in blue. The arrows illustrate in which sequence the measurements were recorded. (c) Evolution of QP and IG weight under O depletion/oxidation. Figure adapted from ref. [A6].

However, we can replenish oxygen *in situ* during x-ray exposure by dosing O_2 with an aluminum capillary directed toward the sample surface.[A8] An artistic representation of this process is shown in Fig. 3.9 (c): The intense x-ray beam continues to deplete oxygen from the sample surface. At the same time, the oxygen dosing supplies oxygen molecules at the substrate surface which the x-ray beam cracks. The more reactive O radicals diffuse back into the sample and fill up the oxygen vacancies. In consequence, a dynamic equilibrium between the oxygen depletion and the reoxidation forms. Dosing oxygen onto an already illuminated and hence oxygen-depleted spot the irradiation induced changes are indeed reversed as demonstrated in the series of spectra depicted in Fig. 3.10 (b). Under oxygen dosing, both QP and IG weight are decreasing continuously and are finally completely suppressed [see blue spectrum Fig. 3.10 (b)] indicating that the sample is fully oxidized.

In order to get a quantitative account of the oxygen depletion and the reoxidation, the QP and IG weight is furthermore integrated over the intervals highlighted in Fig. 3.10 (a) and plotted versus the irradiation time in Fig. 3.10 (c). When the $SrTiO_3$ substrate is exposed to x-rays in vacuum, the QP and IG weight rise in the same proportion, which is attributed to the beam-assisted creation of oxygen vacancies [see left part of Fig. 3.10 (c)]. However, note that we can neither estimate the (absolute) concentration of mobile and trapped charge carriers nor determine their (relative) ratio from the QP and IG weights as the cross sections for QP and IG states are different and unknown, in particular at resonance where the cross sections change rapidly with varying photon energy. Under oxygen dosing both the QP and the IG weight are completely quenched which points to the absence of oxygen vacancies in this state [see right part of Fig. 3.10 (c)]. Thus, we call this state fully oxidized.

In conclusion, synchrotron irradiation combined with oxygen dosing thus allows for reversible *in situ* control over the oxygen stoichiometry of the $SrTiO_3$ surface.

3.4.4 Epitaxial $LaAlO_3$ overlayers: a 2DES induced by electronic reconstruction?

Having established our experimental technique by the example of the $SrTiO_3$ surface, we apply this method to the epitaxial, metallic $LaAlO_3/SrTiO_3$ heterostructures.

To check for the effect of oxygen vacancies in the epitaxial $LaAlO_3/SrTiO_3$ heterostructures, we record a series of valence band spectra under continuous irradiation in vacuum and under O dosing, respectively. Figures 3.11 (a) and (b) depict how the valence band spectra of the epitaxial $LaAlO_3/SrTiO_3$ heterointerface evolve in this experiment. In contrast to before, we now tune the photon energy alternately to the resonance energies of the QP [Fig. 3.11 (a)] as well as the IG feature [Fig. 3.11 (b)] to enhance the signal intensity of both features which is now damped due to the $LaAlO_3$ overlayer. The arrows again indicate in which sequence the measurements were recorded.

Under continuous x-ray exposure, QP and IG weight increase signaling that the beam creates oxygen vacancies in the $SrTiO_3$ substrate, similar as at the bare surface [see arrows in Figs. 3.11 (a) and (b)]. However, the oxygen can also be replenished in turn by dosing oxygen *in situ* during the measurement. The inset in Fig. 3.11 (b) shows a series of spectra which are recorded on a previously irradiated and oxygen-depleted spot as the O dosing is turned on. The figure illustrates that the O depletion is indeed reversed as the light-induced QP and IG weight is quenched under oxygen dosing. This shows that, even for the heterointerface, we can control the V_O concentration fully reversibly. Henceforth, we thus do not distinguish any longer with which method we adjusted the V_O concentration and only plot the states with different V_O concentrations.

Moreover, we note a crucial difference between the spectra of the fully oxidized $LaAlO_3/SrTiO_3$ heterostructure and the fully oxidized $SrTiO_3$ substrate. Under oxygen dosing the IG weight in the $LaAlO_3/SrTiO_3$ heterostructure is completely quenched [see blue spectrum in Fig. 3.11 (b)], which shows that the $SrTiO_3$ substrate is fully oxidized. However, even in the absence of oxygen vacancies in the $SrTiO_3$ substrate, the QP weight is still finite [see blue spectrum in Fig. 3.11 (a)].

As before, we also analyze the QP and IG weight quantitatively by integrating over the areas shaded in Fig. 3.10 (a). Note that we now estimate the IG weight with the spectra taken on the IG resonance and the QP weight with the spectra recorded on the QP resonance. In the quantitative analysis depicted in Fig. 3.11 (c) the oxygen depletion under x-ray exposure becomes apparent in the simultaneous and concomitant increase in QP and IG weight in the left part of the graph. Under oxygen dosing, the IG weight is, in contrast, completely suppressed while residual QP weight is observed [see right part of Fig. 3.11 (c)]. When we subtract the remaining QP weight to match the IG weight in the fully oxidized state [see gray curve in Fig. 3.11 (c)], the curve of QP and IG weight, notably, lie on top of the other in the entire graph. This showcases that the QP peak in epitaxial $LaAlO_3/SrTiO_3$ has an intrinsic component that persists even in the absence of O defects in the $SrTiO_3$ substrate. Under oxygen depletion, electrons released by oxygen vacancies then add up to this intrinsic weight.

Experiments in which the irradiation dose is changed provide further evidence for the intrinsic residual QP weight in the fully oxidized $LaAlO_3/SrTiO_3$ heterostructure: Figure 3.12 depicts the quantitative analysis of QP and IG weight for two different measurement series. In one measurement series the sample was just irradiated by soft x-rays (see solid lines) while in the other measurement series the creation of oxygen vacancies was boosted by interjacent irradiation with the more intense hard x-ray beam (see dotted lines). The different effective irradiation doses manifest themselves in the different overall slopes by which the QP and IG weight increase upon exposure to x-rays (see left part of Fig. 3.12). In contrast, under oxygen dosing the IG weight is completely quenched while the QP weight approaches a minimal but, notably, similar finite value in both measurement series (see right part of Fig. 3.12). This observation confirms that the state under oxygen dosing indeed constitutes a limiting case, i.e., the fully oxidized state.

The residual QP weight observed for the fully oxidized heterointerface stands in sharp contrast to the quenched QP weight observed at the fully oxidized bare $SrTiO_3$ surface. This proves that the 2DES in the epitaxial $LaAlO_3/SrTiO_3$ heterostructures has an intrinsic component which is not induced by oxygen vacancies in the $SrTiO_3$ substrate and which is, in particular, not existing at the bare $SrTiO_3$ surface, pointing to the decisive role of the $LaAlO_3$ overlayer.

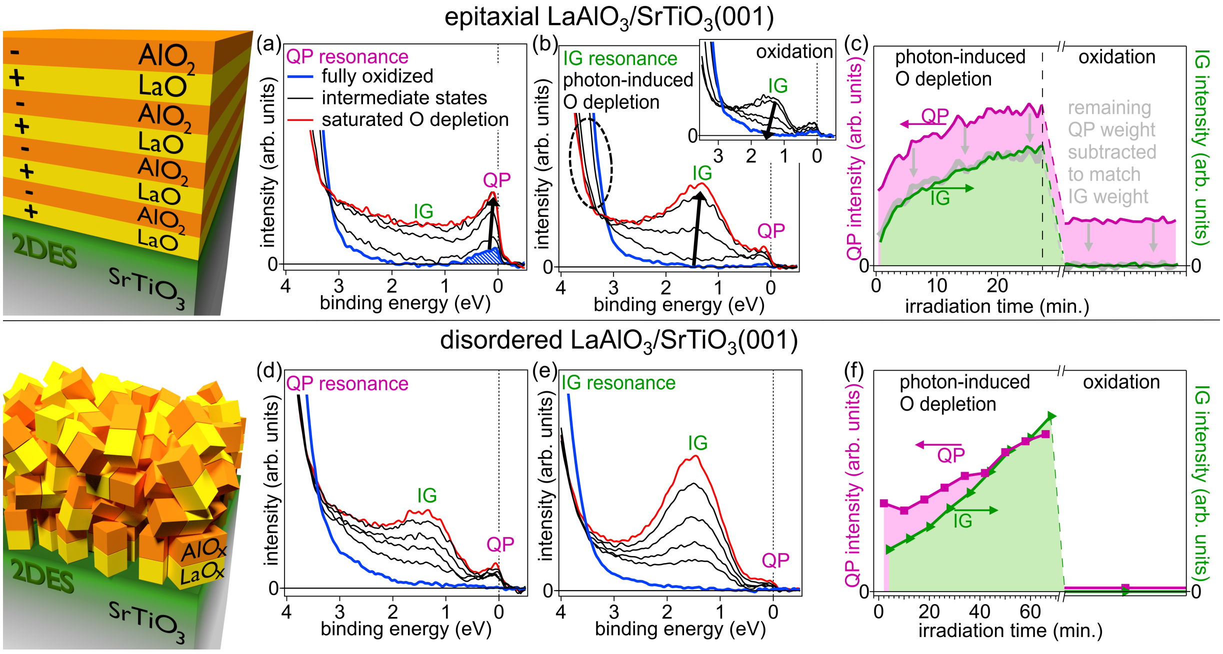

Fig. 3.11: Valence band spectra of epitaxial (a)–(c) and disordered (d)–(f) LaAlO$_3$/SrTiO$_3$ heterointerfaces at different V_{O} concentrations: The graphs (a) and (d) [(b) and (e)] show how the valence band spectra recorded on the QP [IG] resonance evolve under continuous x-ray exposure. Additionally, the valence band spectra of the fully oxidized state are shown in blue. The inset in panel (b) depicts the evolution of the valence band spectra on the IG resonance on a spot which has previously been irradiated when the oxygen dosing is switched on. The arrows show in which sequence the measurements were recorded. Panels (c) and (f) display the quantitative analysis of QP and IG weight under oxygen depletion/oxidation. Under oxygen dosing, residual QP weight is only observed at the epitaxial LaAlO$_3$/SrTiO$_3$ heterointerface. Figure adapted from ref. [A6].

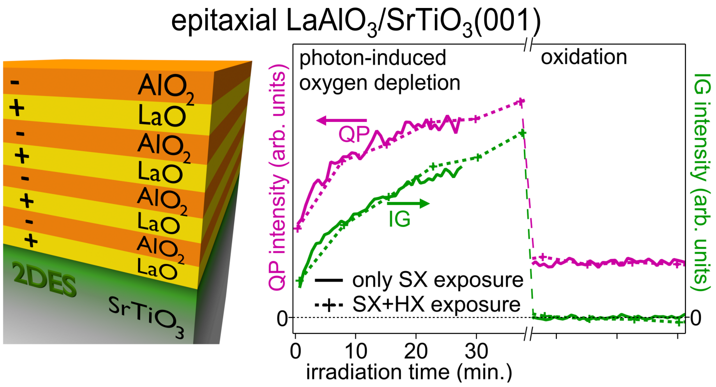

Fig. 3.12: Quantitative analysis of QP and IG weight during oxygen depletion and oxidation in two different measurement series. In one of the measurement series depicted the sample was solely exposed to the soft x-ray beam, in the other measurement series it was intermittently exposed to the hard x-ray beam to boost the creation of oxygen vacancies. Notably, the QP and IG weight approached under oxygen dosing do not depend on the measurement series, i.e., the irradiation dose. Figure adapted from ref. [A6].

However, the comparison between surface and heterointerface falls short: Going from the surface to the heterointerface, one does not only switch on the polarity inherent to the $LaAlO_3$ overlayer but also introduces a growth and deposition process which could impact the $SrTiO_3$ substrate as well. This raises the question whether the intrinsic QP weight in the fully oxidized $LaAlO_3/SrTiO_3$ heterointerface can be attributed to an electronic reconstruction induced by the polar film or whether it could also be induced by chemical reactions occurring during the deposition process. Interfacial cation intermixing[56] driven by the $LaAlO_3$ deposition process could just as well account for the intrinsic component. A La-doped $SrTiO_3$ interface layer, e.g., would also give rise to QP weight which persists even under oxidation. Instead of contrasting the epitaxial $LaAlO_3/SrTiO_3$ heterostructure to a bare surface it is thus more suitable to compare the epitaxial $LaAlO_3/SrTiO_3$ heterointerface with a disordered $LaAlO_3/SrTiO_3$ heterostructure which is fabricated in a similar deposition process but in which the polarity of the $LaAlO_3$ overlayer is switched off.

3.4.5 Epitaxial and disordered $LaAlO_3$ overlayers: toggling the polar discontinuity

Depositing a $LaAlO_3$ film at room temperature prevents that a long-range crystalline order forms in the $LaAlO_3$ overlayer. To obtain a disordered $LaAlO_3/SrTiO_3$ heterostructure which has a similar critical thickness as its epitaxial counterpart (and can thus be probed with photoemission), some of the other deposition parameters had to be adjusted as well (see Sec. 3.4.2 for the detailed deposition parameters). However, all other deposition parameters change in such a way that the deposition process should have an even major impact on the $SrTiO_3$ substrate.[4] The impact of the growth process is thus considered equally severe for the epitaxial and the disordered $LaAlO_3/SrTiO_3$ heterostructures. Comparing experiments on heterostructures with epitaxial and disordered $LaAlO_3$ overlayers, we can thus clear up the role of the deposition process.

Figures 3.11 (d)–(f) depict how heterostructures with disordered $LaAlO_3$ overlayers behave under x-ray exposure and oxygen dosing, respectively: A series of valence band spectra at different V_O concentrations recorded on the QP and IG resonance is shown in Fig. 3.11 (d) and (e), respectively. The quantitative analysis of the spectra is shown in Fig. 3.11 (f). Under oxygen depletion the QP weight is once again increasing in proportion to the IG weight.[5] However, under oxygen dosing the QP weight is clearly quenched along with the IG weight (see blue spectra in Figs. 3.11 (d) and (e), respectively). This shows that oxygen vacancies are the only electron source at the disordered $LaAlO_3/SrTiO_3$ heterointerface.

In contrast, intrinsic QP weight is observed at the fully oxidized epitaxial $LaAlO_3/SrTiO_3$ heterointerface. Since the crystalline order and the polarity of the $LaAlO_3$ overlayer is the only apparent, relevant difference between the disordered and epitaxial $LaAlO_3/SrTiO_3$ heterostructures, the finite QP weight in the fully oxidized epitaxial $LaAlO_3/SrTiO_3$ heterostructure is not a consequence of the deposition process but supplies evidence for an electronic reconstruction which is driven by the polar discontinuity at the heterointerface.

Let us also take a closer look at the more subtle differences in the spectra. When comparing the spectra recorded at the QP resonance for the different samples, one notices that the ratio of QP to IG weight differs considerably. It is particularly striking that no pronounced IG states are observed at the QP resonance for the epitaxial heterointerface, not even in the most oxygen-deficient state [see red spectrum in Fig. 3.11 (a)]. While the QP and IG intensity might be low for the heterointerfaces, we would expect that the relative ratio between the QP and the IG signal does not change as the capping layer only damps the signal intensity in total. This observation

---

[4] The laser fluence is increased and the oxygen partial pressure is decreased.

[5] In the case of the disordered heterointerface the QP signal is quite low even at the QP resonance. The error bars in the quantitative analysis of the QP weight are comparatively large as a result.

highlights that comparatively few oxygen vacancies are formed in the $SrTiO_3$ substrate when it is capped with an epitaxial $LaAlO_3$ overlayer: The spectra are scaled up to reveal the small intrinsic QP weight. On this scale the increase in QP and IG weight then appears to be quite sizable although the small IG weight at the QP resonance in the oxygen-deficient states shows that only few oxygen vacancies are created. This reasoning is confirmed by the spectra of the disordered heterostructure. In this case, there is no intrinsic QP weight which distorts the scaling of the spectra. As a result, finite IG weight is also observed in spectra measured at the QP resonance when the sample is oxygen-deficient [see red and black spectra in Fig. 3.11 (d)], just like in the spectra of the bare surface.

Let us finally comment on the O $2p$-related valence band signal in the measurements, which is, in the case of the heterostructures, dominated by the signal of the $LaAlO_3$ capping layer. We note that, independent of the V_O concentration, the valence band maximum stays far below the Fermi edge, never even approaching it [see dashed ellipse marking in Fig. 3.11 (b)]. These observations contradict the standard electronic reconstruction scenario in which the potential build-up is expected to push the $LaAlO_3$ valence band edge toward the Fermi edge across the $LaAlO_3$ film and at the critical thickness even above the Fermi edge [see band scheme colored in red in Fig. 3.9 (b)].[108] According to this model, O $2p$-related spectral weight should be observed at or near the Fermi level, which is, however, clearly not detected in the spectra of the $LaAlO_3/SrTiO_3$ heterostructure. Instead, our findings indicate that the bands in the $LaAlO_3$ film are flat as earlier photoemission studies have also shown [see band scheme colored in black in Fig. 3.9 (b)].[110,111,128,135–139]

Yet, we observe a pronounced shift in the valence band onset upon oxygen depletion and reoxidation for the epitaxial $LaAlO_3/SrTiO_3$ heterointerface [see dashed ellipse marking in Fig. 3.11 (b)]. With the valence band signal measured being dominated by the $LaAlO_3$ capping layer, this observation shows that the valence band of the $LaAlO_3$ film and the valence band alignment at the interface is changing as a function of the V_O concentration. Measurements of the $LaAlO_3$ film core levels confirm this interpretation (see Sec. 3.5). Note that, in the case of the bare surface [Fig. 3.10 (a)], the valence band onset hardly moves under oxygen depletion as the resulting doping of the Ti $3d$ conduction bands only induces small variations in the Fermi energy.

In conclusion, the observation of the finite QP peak in the fully oxidized epitaxial $LaAlO_3/SrTiO_3$ heterostructure constitutes the first spectroscopic evidence for an electronic reconstruction at the heterointerface even though other fingerprints of the standard electronic reconstruction picture have not been detected in photoemission experiments to date. To reconcile all the photoemission findings, the electronic reconstruction scenario has to be refined as several theory papers suggest:[112–116] All the photoemission results are explained by an electronic reconstruction model in which localized defect states at the $LaAlO_3$ surface or surface adsorbates act as the charge reservoir for the interface.

3.4.6 Altering the overlayer thickness: elucidating the role of photogenerated carriers

The apparent flat band behavior in photoemission has also been ascribed to a measurement artifact, resulting from electron-hole pairs, which are created during the photoemission process. The electron-hole pairs are subsequently separated by the inherent electric field in the polar $LaAlO_3$ overlayer and successively screen the potential build-up out. The electrons which are driven to the interface in this process might possibly give rise to the residual QP weight in the fully oxidized state. Preceding papers on photoemission of $LaAlO_3/SrTiO_3$ heterostructures have already extensively discussed and ruled out such a situation.[111,138] To elucidate the role of photogenerated carriers, we compare the spectra of two heterostructures with a $LaAlO_3$ overlayer above (4 uc $LaAlO_3$ film) and below the critical thickness (2 uc $LaAlO_3$ film).

If photogenerated electrons and holes were separated by the built-in potential and the electrons transferred to the interface were to give rise to the QP peak, we would expect photogenerated metallic carriers at the interface independent of the epitaxial $LaAlO_3$ overlayer thickness. The emergence of the intrinsic QP weight in the fully oxidized heterostructure should, in contrast, correlate with the emergence of metallicity at the $LaAlO_3/SrTiO_3$ heterointerface, if the intrinsic QP weight were to arise due to the electronic reconstruction.

We have to resort to Nb-doped, metallic substrates for these experiments, to prevent charging of the insulating heterostructure with an overlayer below the critical thickness. By replacing the insulating substrate with a metallic one, the electrostatics of the heterostructures change. That is why we first check that a sample with a 4 uc $LaAlO_3$ overlayer on a Nb-doped substrate behaves in the same way in the spectroscopy measurements as an otherwise identical sample on an insulating substrate. The comparison of Figs. 3.13 (a)–(c) to Figs. 3.11 (a)–(c) demonstrates that this is indeed the case. In particular, we observe residual QP weight in the fully oxidized state of both heterostructures, independent of the metallicity of the substrate [see blue-shaded QP peak in Fig. 3.13 (a) and Fig. 3.11 (a)].

Let us thus next take a closer look at the measurements on the 2 uc $LaAlO_3/SrTiO_3$ heterostructure which are summarized in Figs. 3.13 (d)–(f): Also in the 2 uc $LaAlO_3/SrTiO_3$ heterostructure the doping can be tailored by virtue of the V_O concentration in the $SrTiO_3$ substrate: Under oxygen depletion, both QP and IG weight rise [see left part of Fig. 3.13 (f)]. In the fully oxidized state the QP peak is, however, totally quenched in the 2 uc $LaAlO_3/SrTiO_3$ heterostructure [see blue spectrum in Fig. 3.13 (d)].

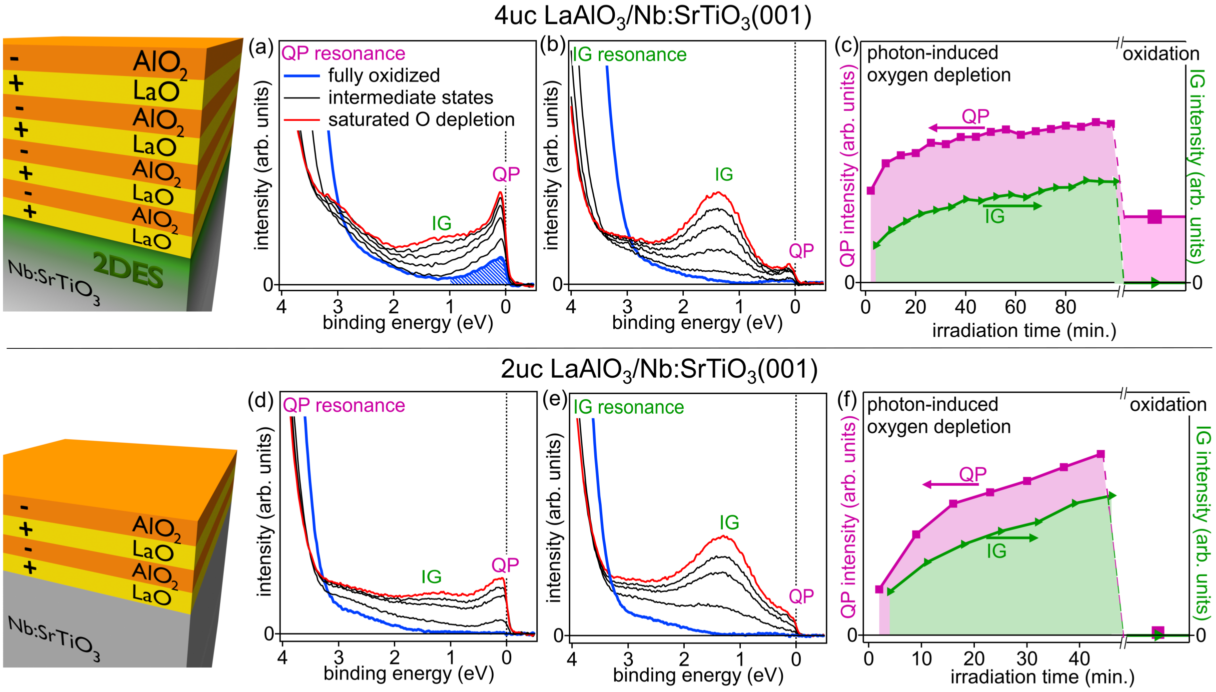

Fig. 3.13: Valence band spectra of $LaAlO_3/SrTiO_3$ heterostructures with overlayer thicknesses of 4 uc (a)–(c) and 2 uc (d)–(f) at different V_O concentrations: The graphs (a) and (d) [(b) and (e)] show how the valence band spectra recorded on the QP [IG] resonance change depending on the V_O concentration. Panels (c) and (f) depict the quantitative analysis of QP and IG weight under oxygen depletion/oxidation. In the fully oxidized state, residual QP weight is only observed for the $LaAlO_3/SrTiO_3$ heterostructure with a 4 uc $LaAlO_3$ overlayer. Figure adapted from ref. [A6].

As the intrinsic QP weight is only observed for heterostructures with a $LaAlO_3$ thickness above the critical thickness, we conclude that the non-vanishing QP weight in fully oxidized epitaxial $LaAlO_3/SrTiO_3$ heterostructures does not originate from photogenerated charge carriers, but is indeed generic and due to an electronic reconstruction which is induced by the polar discontinuity at the epitaxial $LaAlO_3/SrTiO_3$ interface.

3.5 Tracking the oxygen depletion in core level spectroscopy

In the previous section we studied the emergence of valence band states as a function of the V_O concentration. In order to get a better understanding of the microscopic mechanisms at play under oxidation and oxygen depletion, it is imperative to investigate how the core level spectra change with the V_O concentration.

3.5.1 Qualitative analysis of the SX core level spectra

To track the oxygen depletion by core level spectroscopy, we *alternately* record valence band and core level spectra on an epitaxial $LaAlO_3/SrTiO_3$ heterointerface while we continuously vary the oxygen vacancy concentration: We start the measurement series from the fully oxidized state and subsequently deplete oxygen from the sample by irradiation in vacuum.

To facilitate the interpretation of the measured spectra, we work at the same probing depth, i.e., at the same kinetic energy of the photoelectrons, throughout the entire measurement series:[6] For the core level measurements the photon energies are thus tuned in such a way that the kinetic energy of the core level photoelectrons matches the kinetic energy of the valence band photoelectrons measured at the QP/IG resonance [note the similar kinetic energy axes in Figs. 3.14 (a) to (e)].[7] In all measurements the inelastic mean free path of the photoelectrons amounts to $\lambda_{\mathrm{IMFP}} \approx 11\,\text{Å}$.[27–29]

The valence band spectra recorded on the QP and IG resonance are depicted in Figs. 3.14 (a) and (b), respectively. The QP and IG feature show the same characteristic behavior under oxidation and oxygen depletion as discussed previously: In the fully oxidized state (blue spectra), the IG weight is completely quenched, while the QP weight is decreased but finite. Under oxygen depletion (black and red spectra), the QP and IG weight increase concomitantly.

The angle-integrated spectra of film and substrate core levels are shown in Figs. 3.14 (c) to (e). The intensity of *all* spectra slightly varies over the course of the measurement series due to, i.a., changes in the light intensity. To compensate for this superimposed intensity modulation, we assume that the intensity of the substrate core levels does not change over the measurement series and normalize the core level spectra in every iteration step by the integral intensity of the Ti $2p$ core level line. A Shirley background is furthermore subtracted in all core level spectra.

Let us first take a closer look at a *substrate* core level spectrum, viz. the Ti $2p_{3/2}$ spectrum which is depicted in Fig. 3.14 (c): In the oxygen-depleted state (red spectrum) the Ti $2p_{3/2}$ spectrum is comprised of two distinct lines. The main line is attributed to Ti atoms with valence 4+, i.e., Ti atoms in a $3d^0$ configuration which characterizes the undoped $SrTiO_3$ substrate. An additional peak appears at higher kinetic energies, i.e., lower binding energies, which is ascribed to Ti atoms with valence 3+.[140] When electrons dope the otherwise empty Ti $3d$ shell in $SrTiO_3$ and the Ti oxidation state changes from Ti^{4+} to Ti^{3+}, the extra electrons aid to screen the nuclear charge.

---

[6] Note that the photon flux changes when the photon energy is varied. The time scale with which the oxygen depletion advances might thus depend on the photon energy. However, as we continuously alternate between the measurements at the different photon energies and average over the different time scales, this is of no consequence in our measurement series.

[7] The beamline setup did not allow to tune the photon energy to a value at which the O $1s$ spectra could be measured at the same photoelectron kinetic energies as the other core levels.

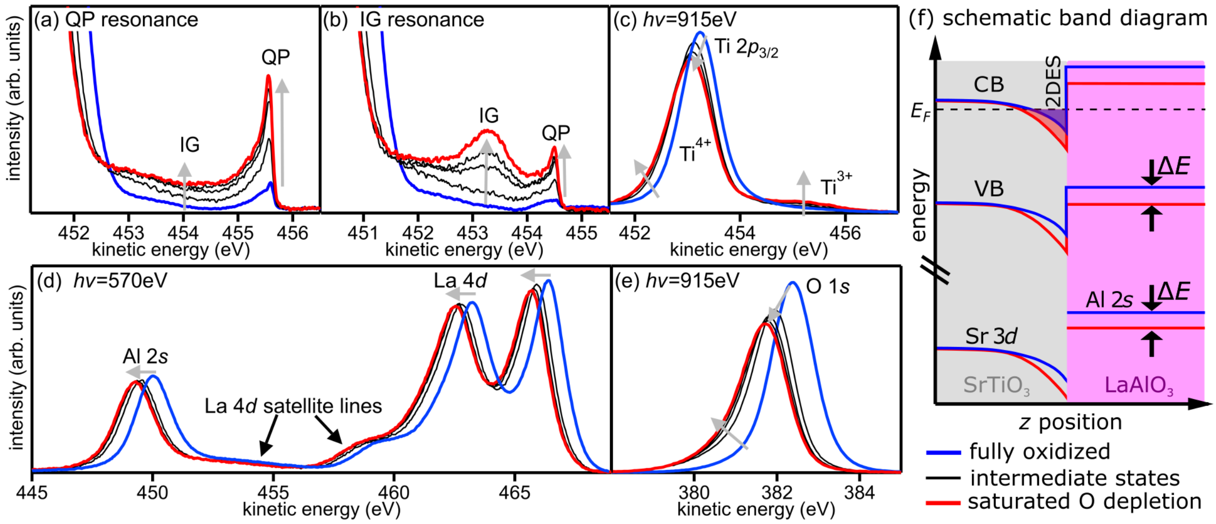

Fig. 3.14: Valence band spectra on the QP (a) and IG resonance (b), as well as Ti $2p_{3/2}$ (c), Al $2s$ and La $4d$ (d), and O $1s$ (e) core level spectra of a $LaAlO_3/SrTiO_3$ heterointerface at different V_O concentrations. All spectra are measured with soft x-rays which are tuned in energy such that the photoelectron kinetic energy amounts to ≈455 eV. The probing depth of all measurements is thus similar. (f) Band scheme at the $LaAlO_3/SrTiO_3$ interface in the fully oxidized and at saturated O depletion as inferred from the spectra in (a) to (e).

The binding energy of the Ti $2p$ orbital accordingly shifts to lower values. The observation of finite Ti^{3+} weight thus corroborates that Ti $3d$ orbitals are doped in the $LaAlO_3/SrTiO_3$ heterostructure. Under O depletion/oxidation the doping in the heterostructure varies and the intensity of the Ti^{3+} peak changes as well.

The spectral shape of the Ti^{4+} line also changes as a function of the V_O concentration: While the Ti^{4+} line is rather symmetric in the fully oxidized state (see blue spectrum), it becomes distinctly asymmetric toward lower kinetic energies, i.e., higher binding energies under oxygen depletion [see arrows in Fig. 3.14 (c)]. This asymmetry is ascribed to interfacial band bending. Concomitant to the $SrTiO_3$ conduction band bending toward the interface, the binding energy of the $SrTiO_3$ core levels varies. The photoemission spectrum is comprised of signals which originate from the single $SrTiO_3$ layers and which are weighted by an exponential function implementing the damping. With the binding energy of the Ti $2p$ core level changing toward the interface, the measured Ti $2p$ spectrum is broadened and shifted in binding energy (see Fig. 4.11 for a detailed visualization of this effect).

Based on the Ti $2p_{3/2}$ spectra, we sketch a tentative band scheme for the $SrTiO_3$ substrate in the fully oxidized state and at saturated O depletion in Fig. 3.14 (f): In the fully oxidized state the band bending and the doping is small (band scheme marked in blue), while the doping is increased and the $SrTiO_3$ bands are strongly bent toward higher binding energies at the interface at saturated O depletion (band scheme marked in red).

Next, we scrutinize the *film* core level spectra recorded in the measurement series, viz. the Al $2s$ and La $4d$ spectra which are depicted in Fig. 3.14 (d). We focus on the Al $2s$ core level line as it is more symmetric by nature and thus easier to interpret than the La $4d$ spectrum.[8] The Al $2s$ core level line is sharp and, in particular, not asymmetrically broadened. This observation contradicts the most simple electronic reconstruction scenario in which the binding energy of the film core levels is shifted across the $LaAlO_3$ film in parallel to the valence band edge. The film core level spectra are expected to broaden, in consequence. From our measurements we deduce

---

[8] Note that a La $4d$ satellite overlaps slightly with the Al $2s$ line.[141]

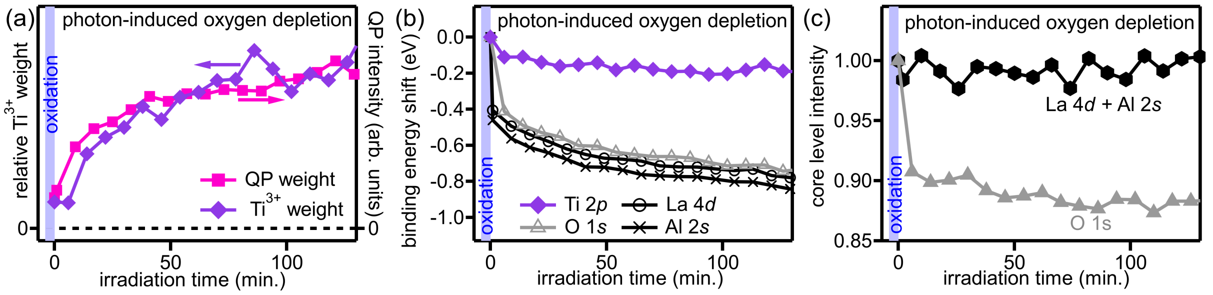

Fig. 3.15: Quantitative analysis of the SX spectra depicted in Fig. 3.14: The measurement series starts from the fully oxidized state ($t = 0$ min, blue marking). For $t > 0$ min oxygen is continuously depleted by irradiation in vacuum. (a) Analysis of the QP weight and the relative Ti^{3+} spectral weight as a function of the irradiation time. (b) Binding energy of different core level lines as a function of the irradiation time. (c) Analysis of the integral Al $2s$+La $4d$ and O $1s$ spectral weight as a function of the irradiation time. The binding energies and core level intensities are compared to the respective quantities in the fully oxidized state.

that the bands in the $LaAlO_3$ film are flat, independent of the V_O concentration, which confirms the conclusions drawn from the O $2p$ valence band onset.

Furthermore the binding energy of the film core levels is found to shift under oxygen depletion. Since the binding energies of the film core levels shift in parallel to the $LaAlO_3$ conduction and valence band edge, this finding reveals that the band alignment between the $SrTiO_3$ substrate and the $LaAlO_3$ film changes as a function of the V_O concentration. We complete our band scheme in Fig. 3.14 (f) accordingly.

Lastly, we discuss the O $1s$ spectra displayed in Fig. 3.14 (e). The O $1s$ core level also shifts in binding energy under O depletion which is also attributed to the interfacial band alignment changing as a function of the V_O concentration: At our experimental conditions the inelastic mean free path of the O $1s$ photoelectrons amounts to only 9.3 Å[27–29] while the $LaAlO_3$ overlayer of the sample is 20 Å thick. The largest part of the O $1s$ signal thus originates from the $LaAlO_3$ film and is varying in binding energy just as the La $4d$ and Al $2s$ spectra. Moreover, the O $1s$ spectral weight is noticeably decreasing upon irradiation in vacuum which reveals that the oxygen stoichiometry of the sample is indeed changed by irradiation in vacuum/under oxygen dosing.

3.5.2 Quantitative analysis of the SX core level spectra

For a more thorough examination of the band bending and band alignment we analyze the core level spectra quantitatively. Recall that the measurement series starts from the fully oxidized state at $t = 0$ min (see blue markings in Fig. 3.15) and that oxygen is continuously depleted by irradiation in vacuum for $t > 0$ min.

First we analyze the relative Ti^{3+} weight in the Ti $2p_{3/2}$ spectra, i.e., the ratio $\frac{I(\mathrm{Ti}^{3+})}{I(\mathrm{Ti}^{3+})+I(\mathrm{Ti}^{4+})}$, where $I(x)$ denotes the intensity of feature x. We estimate this intensity ratio, by fitting the Ti $2p_{3/2}$ peak with two Voigt profiles, one for the Ti^{3+} and one for the Ti^{4+} contribution.[9] In Fig. 3.15 (a) we plot the relative Ti^{3+} weight as well as the QP weight as a function of the irradiation time. For reasons of clarity the evolution of the IG weight is not shown. Remember, however, that the IG weight changes in proportion to the QP weight. The Ti^{3+} weight is changing concomitantly with the QP and IG weight, i.e., the Ti $3d$ occupation, in the measurement. This

---

[9] To fit the Ti $2p_{3/2}$ spectra and, in particular, the small Ti^{3+} feature reliably, all Ti $2p_{3/2}$ spectra of the measurement series were analyzed in a single, so-called global fit in which corresponding parameters were set to the same values for all spectra (as, e.g., the binding energy difference between the Ti^{3+} and the Ti^{4+} peaks).

observation reinforces the correspondence between the Ti^{3+} weight and the Ti 3*d* occupation.

In Fig. 3.15 (b) we depict the evolution of the binding energy of the film and substrate peaks under oxidation and oxygen depletion. The binding energy of the single core level lines is compared to the binding energy of the respective core level lines in the fully oxidized state. The binding energy of all core level lines continuously changes in proportion to the QP weight increasing under oxygen depletion [compare changes over irradiation time in Figs. 3.15 (a) and (b)]. The absolute size of the binding energy shift, however, differs for the single core levels: While the binding energies of the La 4*d*, Al 2*s* and O 1*s* core level shift by a similar amount, we observe a substantially smaller shift in the binding energy of the Ti $2p_{3/2}$ substrate core level.

These observations corroborate the band diagram sketched in Fig. 3.14 (f). The binding energy shift in the film core level lines, i.e., the La 4*d*, Al 2*s* and O 1*s* core level lines is ascribed to the band alignment at the interface changing under O depletion [see schematic band diagram in Fig. 3.14 (f)]. As a result, the binding energy is shifted in all film layers, i.e., in all layers contributing to the photoemission signal. The binding energy shift in the substrate core level lines is, in contrast, attributed to the band bending in the $SrTiO_3$ substrate varying as a function of the V_O concentration. While the spectra of the interfacial layers are affected by the change in band bending, the spectra of the bulk layers are not. The substrate core level spectra are a *superposition* of the signal originating from interfacial layers and of the signal originating from bulk layers. The observed shift in the Ti $2p_{3/2}$ binding energy is thus small and coupled with a change in peak asymmetry as described in the previous section.

Lastly, we address the evolution of the film stoichiometry under oxygen dosing and irradiation in vacuum: Owing to our normalization procedure, we can not only scrutinize the spectral shape and binding energy but can also look for changes in the integral spectral weight of the film core level lines depending on the V_O concentration and draw conclusion about variations in the film stoichiometry. For that purpose, we analyze the O 1*s* and the aggregated La 4*d*+Al 2*s* spectral weight. The O 1*s* and the La 4*d*+Al 2*s* spectral weight is always compared to the spectral weight of the respective core levels in the fully oxidized state. The results of this analysis are plotted in Fig. 3.15 (c). While the La 4*d*+Al 2*s* integral weight remains constant over the whole measurement series, the O 1*s* spectral weight declines when the sample is irradiated in vacuum. The oxygen spectral weight decreases as the Ti 3*d* spectral weight increases [compare Fig. 3.15 (c) to Fig. 3.15 (a)], confirming that the oxygen depletion and the charge carrier doping are interlinked.

3.5.3 Modeling the oxygen loss in the $LaAlO_3/SrTiO_3$ heterostructure

In the measurement series discussed above, the O 1*s* spectral weight decreases by $\approx 13\%$ under irradiation in vacuum [see Fig. 3.15 (c)]. In the next section, we estimate the oxygen depletion necessary to induce such a change in the O 1*s* spectral weight and answer the question where in the $LaAlO_3/SrTiO_3$ heterostructure oxygen is lost.

To address this issue, we construct models for the V_O concentration which are depicted in Fig. 3.16. For simplicity, the fully oxidized state [Fig. 3.16 (a)] is assumed to be fully stoichiometric. Modeling the oxygen-deficient state, we first assume that oxygen is only depleted at the $LaAlO_3$ surface [Fig. 3.16 (b)], while in the second model oxygen is only drained from the $SrTiO_3$ substrate [Fig. 3.16 (c)] and in the third model oxygen is lost in the $LaAlO_3$ film and the $SrTiO_3$ substrate [Fig. 3.16 (d)]. We adapt all models of the oxygen-depleted states in such a way that the O loss induces a $\approx 13\%$ decrease in O 1*s* spectral weight, i.e., a similar decline in O 1*s* spectral weight as observed in our measurement series .[10]

---

[10] To estimate the decrease in O 1*s* spectral weight, we build up the O 1*s* spectra of the fully oxidized state and of the oxygen-depleted states layer-by-layer, taking into account the appropriate attenuation, and analyze the resulting integral O 1*s* spectral intensity in the fully oxidized and the oxygen-depleted states.

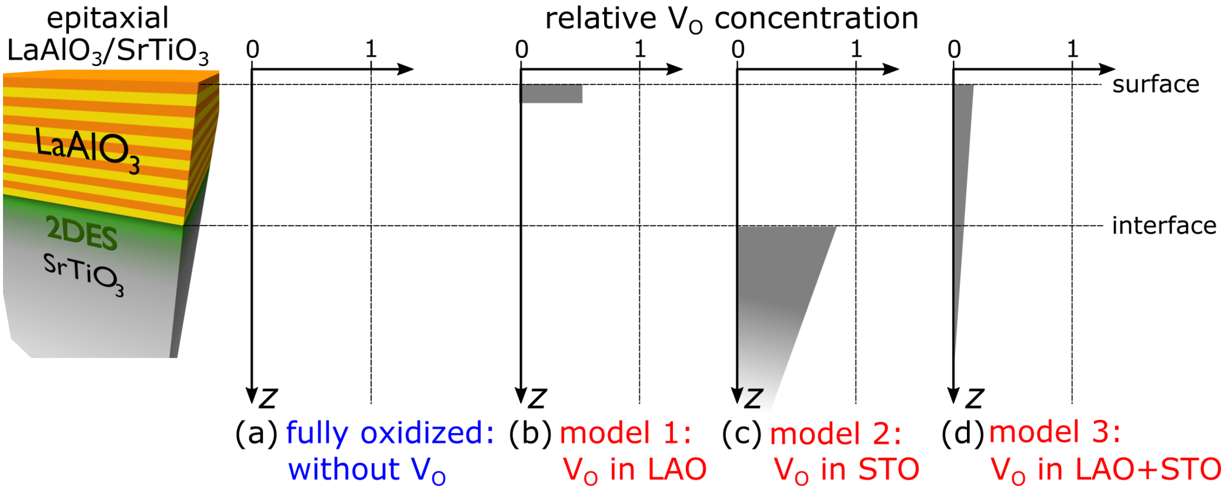

Fig. 3.16: Modeling the V_O depletion in epitaxial $\mathrm{LaAlO_3/SrTiO_3}$ heterostructures: The sample is assumed to be fully stoichiometric in the fully oxidized state (a). We construct several models for the oxygen-depleted state in which oxygen is depleted only at the $\mathrm{LaAlO_3}$ surface (b), only in the $\mathrm{SrTiO_3}$ substrate (c) and both in the $\mathrm{LaAlO_3}$ film and in the $\mathrm{SrTiO_3}$ substrate (d). All models of the V_O distribution are chosen in such a way that the estimated O loss would induce a ≈13% decrease in O 1s spectral weight.

Beware that we can only roughly estimate the O loss in our samples as our measurements at a single photon energy offer no depth resolution. In this approximation we thus deliberately only consider the order of magnitude of the different effects. Our estimates nevertheless show whether the different models of the V_O distribution are at all plausible.

In the first model we assume that oxygen vacancies are only created in the topmost $\mathrm{LaAlO_3}$ layer [see Fig. 3.16 (b)]. To achieve the ≈13% decrease in O 1s spectral intensity, more than half of the oxygen atoms in the topmost $\mathrm{LaAlO_3}$ layer have to be removed. This model does not include any oxygen vacancies in the $\mathrm{SrTiO_3}$ substrate and contradicts our earlier observations of IG states which emerge in the valence band spectra of the $\mathrm{LaAlO_3/SrTiO_3}$ heterostructures under oxygen depletion and which are unambiguously related to oxygen vacancies in the $\mathrm{SrTiO_3}$ substrate [cf. red spectrum in Fig. 3.14 (b)]. This scenario is thus discounted.

In the second model we instead assume that the oxygen vacancies reside *only* on the $\mathrm{SrTiO_3}$ side of the heterostructure. As the O 1s signal mainly originates from the $\mathrm{LaAlO_3}$ film, the oxygen content in the $\mathrm{SrTiO_3}$ substrate must dramatically decrease to induce the ≈13% decline in the O 1s spectral weight [see Fig. 3.16 (c)]. Such a high V_O concentration in the $\mathrm{SrTiO_3}$ substrate cannot be reconciled with the Ti 2p spectra recorded under oxygen depletion [see red spectrum in Fig. 3.14 (c)]: Each oxygen vacancy in $\mathrm{SrTiO_3}$ presumably dopes two electrons into Ti 3d orbitals. The oxidation state of these Ti atoms changes from $\mathrm{Ti^{4+}}$ to $\mathrm{Ti^{3+}}$ (or even $\mathrm{Ti^{2+}}$ when two electrons dope the same Ti atom). At our limited probing depth, we would thus expect Ti 2p spectra with low $\mathrm{Ti^{4+}}$ weight and sizable $\mathrm{Ti^{3+}}$ or even $\mathrm{Ti^{2+}}$ weight if the V_O concentration in the topmost $\mathrm{SrTiO_3}$ layers were as high as in Fig. 3.16 (c). However, this is obviously not the case.

In the third model we thus combine the two previous approaches: We assume that the concentration of oxygen vacancies peaks at the $\mathrm{LaAlO_3}$ surface, decreases linearly into the heterostructure and reaches zero beyond the $\mathrm{LaAlO_3/SrTiO_3}$ heterointerface. Fig. 3.16 (d) shows a V_O distribution of this kind which would yield a ≈13% decrease in O 1s spectral weight. In the model in Fig. 3.16 (d) the topmost $\mathrm{LaAlO_3}$ layer hosts ≈16% oxygen vacancies while the topmost $\mathrm{SrTiO_3}$ layer still hosts ≈8% oxygen vacancies. This V_O profile matches to the IG weight but also to the order of magnitude of the Ti^{3+} weight observed in the oxygen-depleted state. We conclude that a V_O distribution as displayed in Fig. 3.16 (d) seems the most plausible scenario describing the O depletion.

3.6 Conclusion

In this chapter we scrutinized different doping mechanisms occurring in $\mathrm{SrTiO_3}$-based heterostructures by means of photoemission spectroscopy. The microscopic insight into the interfacial electronic structure enabled us to distinguish the different doping mechanisms at play in $\mathrm{SrTiO_3}$-based heterostructures (see synopsis in Fig. 3.17) and, in particular, to resolve the long-standing debate about the origin of the 2DES at the epitaxial $\mathrm{LaAlO_3/SrTiO_3}$ (001) heterointerface: By varying key parameters of the samples, viz. the V_O concentration, the crystalline order as well as the thickness of the $\mathrm{LaAlO_3}$ overlayer, we identify a unique feature in the spectra of the epitaxial 4 uc $\mathrm{LaAlO_3/SrTiO_3}$ heterostructure: Only in this heterostructure, residual quasiparticle weight at the Fermi level persists even in the absence of oxygen vacancies. These results provide strong evidence that in epitaxial $\mathrm{LaAlO_3/SrTiO_3}$ (001) heterostructures metallicity is induced by an electronic reconstruction which is driven by the polar discontinuity arising at the interface.[11]

This generic doping mechanism relies on the fundamental properties of the constituent materials and is thus very robust, in the preparation as well as in the subsequent handling and functionalization of the heterointerfaces. Doping by electronic reconstruction can thus be readily adopted to other oxide heterointerfaces which display a similar polar discontinuity. In this way one may be able to reliably manipulate and tailor any oxide-based functionality which is controlled by charge transfer.

The doping by oxygen vacancies can also be exploited to engineer the electronic properties of oxide heterointerfaces: Complementary measurements of the core level spectra in an epitaxial $\mathrm{LaAlO_3/SrTiO_3}$ heterostructure showed that the electronic interface properties, such as the valence band alignment, can be manipulated by means of the V_O concentration.

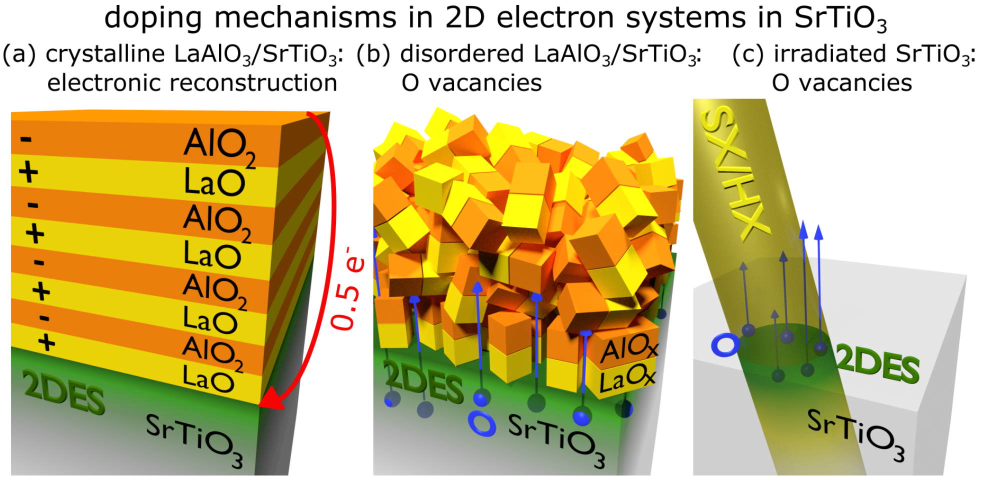

Fig. 3.17: Synopsis of the doping mechanism at work in the various $\mathrm{SrTiO_3}$-based heterostructures as identified by our photoemission experiments.

---

[11] Note that we also conducted similar oxygen dosing experiments on the (111) $\mathrm{SrTiO_3}$ surface and the (111) $\mathrm{LaAlO_3/SrTiO_3}$ heterointerface and found that the (111) $\mathrm{LaAlO_3/SrTiO_3}$ heterointerface is doped by electronic reconstruction as well. These measurements are discussed in more detail in the Appendix in Sec. A.

Chapter 4

Interface band engineering in $LaAlO_3/SrTiO_3$ heterostructures

The controllability of the electronic interface properties is a key requirement for applications of the $LaAlO_3/SrTiO_3$ heterostructure in future electronic devices. In the photoemission experiments presented in the previous chapter, we have already seen that the doping as well as the band bending and band alignment in epitaxial $LaAlO_3/SrTiO_3$ heterostructures can be engineered by virtue of the oxygen vacancy concentration. The oxygen vacancy concentration could, in turn, be changed at will during the photoemission experiment by a combination of oxygen dosing and x-ray irradiation. We can thus not only probe the electronic interface properties but also manipulate them within the same experiment and can investigate on *one and the same sample* how the band profile changes as a function of the oxygen vacancy concentration. In this way, we are furthermore able to precisely control the oxygen vacancy concentration *without changing any other parameter*. This variation in only the oxygen stoichiometry is not as easily achievable, if one endeavors to change the oxygen vacancy concentration by altering the deposition conditions in the pulsed laser deposition process.

The core level measurements in the previous chapter gave a first inkling of the band bending, band alignment and doping at the epitaxial $LaAlO_3/SrTiO_3$ interface. However, the analysis did not yield any information about the *depth dependence* of, e.g., the charge carrier concentration or the band bending. In the following chapter, we thus scrutinize how the electronic properties of (001)- and (111)-oriented $LaAlO_3/SrTiO_3$ heterointerfaces vary as a function of the oxygen vacancy concentration. By means of *angle-dependent* hard x-ray photoelectron spectroscopy (HXPES), we analyze the depth dependence of the film and substrate core level spectra and infer the band bending in the $LaAlO_3$ film and the $SrTiO_3$ substrate as well as the band alignment at the interface. It is particularly interesting to revisit the band bending and band alignment at the $LaAlO_3/SrTiO_3$ heterointerface, as many previous photoemission studies on solitary samples – possibly with ill-defined oxygen stoichiometries– arrive at widely different results.

In this chapter, we initially review the results of earlier photoemission studies to get a first insight the interfacial band profile. Then we focus on the substrate core level spectra by means of which we analyze the band profile and charge distribution in the $SrTiO_3$ substrate employing a self-consistent Poisson-Schrödinger model. The interfacial band alignment and the potential build-up in the $LaAlO_3$ film is investigated next. Subsequently, we contrast our results to the earlier photoemission studies. The results presented here are compiled in ref. [A14].

4.1 Review of previous photoemission studies

In this section we first compile the results of previous photoemission studies on the band profile across the (001) $LaAlO_3/SrTiO_3$ heterointerface. Most studies agree qualitatively with the band scheme sketched in Fig. 4.1.

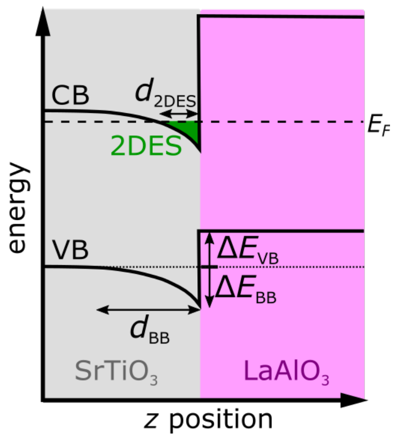

Fig. 4.1: Sketch of the band profile typically obtained in photoemission experiments.

They find flat bands in the $LaAlO_3$ film[110,111,128,135–139] while the bands on the $SrTiO_3$ side are shown to be bent downward toward the interface forming a potential trough for the electrons.[135,137,145]

Yet, the quantitative values describing the interfacial valence band offset ΔE_{VB} as well as the band profile in the $SrTiO_3$ substrate differ widely between various groups. The results of previous photoemission studies are gathered in Tab. 4.1. The interfacial valence band offsets ΔE_{VB} estimated vary even between positive and negative values [see Tab. 4.1 (a)]. Note that in our convention the interfacial valence band offset is positive (negative) if the $LaAlO_3$ valence band lies above (below) the $SrTiO_3$ valence band. This means that some groups classify the $LaAlO_3/SrTiO_3$ heterointerface as a type II interface/staggered gap heterojunction (in the case of a positive valence band offset) while others find a type I interface/straddling gap heterojunction (in the case of a negative valence band offset).

The potential trough on the $SrTiO_3$ side of the interface is estimated to be up to $\Delta E_{\mathrm{VB}} \approx 0.8\,\mathrm{eV}$ deep by some studies,[135,137] while other groups cannot find indications of a pronounced potential well at the interface[111,128] [see first column in Tab. 4.1 (b)]. The information about the spatial extent d_{BB} of the potential well and about the extension d_{2DES} of the 2DES are scarce and differ widely as well [see last column in Tab. 4.1 (b)].

(a) **valence band offset at interface**

publication	$\boldsymbol{\Delta E_{\mathrm{VB}}}$ (eV)
Susaki *et al.*[142]	+0.42
Berner *et al.*[111]	+0.36
Chambers *et al.*[128] (Augsburg sample)	+0.2
Qiao *et al.*[143,144]	+0.16
Yoshimatsu *et al.*[145]	0.0
Treske *et al.*[137]	0.0
Chambers *et al.*[128] (Tokyo sample)	–0.06
Drera *et al.*[136]	–0.1
Segal *et al.*[110]	–0.35

(b) **potential profile and 2DES extension in $SrTiO_3$**

publication	$\boldsymbol{\Delta E_{\mathrm{BB}}}$ (eV)	$\boldsymbol{d_{\mathrm{BB}}}$ (Å)
Berner *et al.*[111]	0±0.3	—
Yoshimatsu *et al.*[145]	0.25±0.07	—
Chambers *et al.*[128]	0±0.06	—
Drera *et al.*[135]	0.8±0.2	—
Treske *et al.*[137]	≥0.4	≥20

publication	$\boldsymbol{d_{\mathrm{2DES}}}$ (Å)
Sing *et al.*[140] (Augsburg samples)	4–40
Slooten *et al.*[138] (good substrate)	≥80
Sing *et al.*[140] (PSI sample)	4–12
Slooten *et al.*[138] (bad substrate)	25±15

Tab. 4.1: Band alignment and band bending at the epitaxial (001) $LaAlO_3/SrTiO_3$ heterointerface as determined by various photoemission studies. Interfacial valence band offset ΔE_{VB} (a), potential profile and 2DES extension in $SrTiO_3$ substrate (c) as estimated by different publications. The results obtained for the valence band offset at the interface as well as for the potential profile and the charge carrier distribution in the $SrTiO_3$ substrate differ widely.

Apart from the variability in the photoemission results, it is furthermore hard to find simultaneous information on the band alignment, the band bending as well as on the charge carrier profile. In summary, it can thus be said that no conclusive band scheme of the $LaAlO_3/SrTiO_3$ heterojunction can be derived from the previous investigations. For that reason, we investigate in the following in detail how the band alignment,the band bending and the charge carrier profile at the $LaAlO_3/SrTiO_3$ heterointerface varies as a function of the oxygen vacancy concentration.

4.2 Depth profiling of the two-dimensional electron system

In the experiments discussed so far we employed soft x-ray photoemission. Under these experimental conditions the inelastic mean free path of the photoelectrons amounts to only $\lambda_{\mathrm{IMFP}} \approx 11\,\text{Å}$.[27–29] The photoelectron signal from the substrate is thus rather low and dominated by the uppermost substrate layers. It is thus hard to draw conclusions about, e.g., the band bending which may extend far into the $SrTiO_3$ substrate.

To overcome this limitation, we enhance the probing depth by measuring at higher photon energies [see illustration in Fig. 4.2 (b)]. At beamline I09 at Diamond Light Source we even have the worldwide unique possibility of probing the *same* sample spot with a soft as well as a hard x-ray beam.[147] A sketch of the beamline layout is shown in Fig. 4.2 (a). Two undulators arranged in a row emit a soft and a hard x-ray beam. The two beams are subsequently directed into separate branches in which they are monochromatized and focused. In the end, the soft and hard x-ray beam are brought together again and can, in particular, be focused onto the same spot. We are thus able to prepare a sample state, say the fully oxidized state, check that the IG weight is fully quenched with the soft x-ray beam and subsequently record core level spectra of the very same sample spot at an enhanced probing depth with the hard x-ray beam.

For the following measurements with the hard x-ray beam we choose a photon energy of 3 keV, which increases the inelastic mean free path of the photoelectrons to 40 – 46 Å depending on the core level from which the photoelectrons originate.[27–29] Measuring at such a photon energy, we are able to boost the signal from the $SrTiO_3$ substrate but preserve the interface sensitivity at the same time.

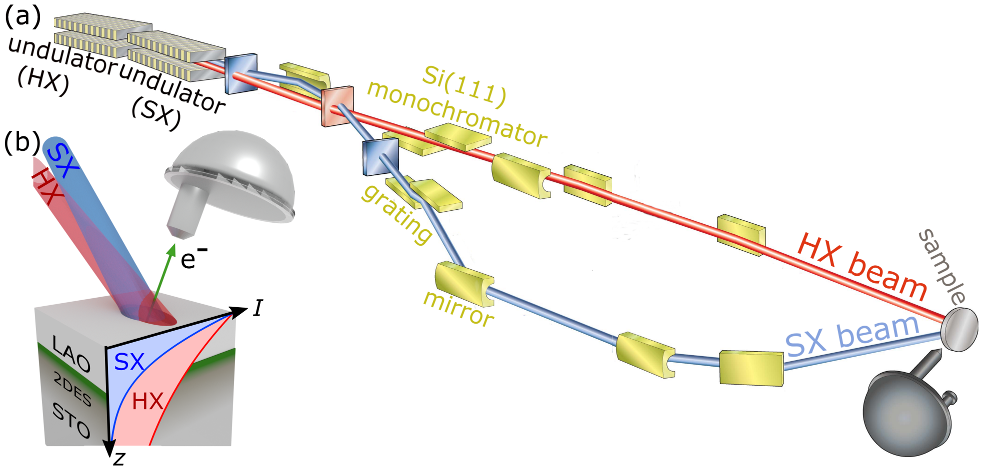

Fig. 4.2: (a) Layout of the I09 beamline at the Diamond Light Source. Two undulators in a row emit a soft and a hard x-ray beam which can be focused onto the *very same* sample spot. Figure adapted from ref. [146]. (b) Illustration of the different probing depths in SXPES and HXPES experiments. While we mainly pick up photoelectrons from the $LaAlO_3$ film in the SXPES experiments, we also acquire a sizable photoelectron signal from the $SrTiO_3$ substrate in the HXPES measurements.

4.2.1 Characterization of the wide angle acceptance lens

To investigate the depth dependence of, e.g., the band bending or the charge carrier distribution in the substrate, it does not suffice to record a *single* spectrum at an enhanced probing depth. Instead, one needs to record spectra at *several* probing depths, which can, i.a., be achieved by measuring spectra at the same photon energy but at different electron emission angles. In a conventional experimental setup, the sample is repeatedly rotated with respect to the analyzer to record spectra at different electron emission angles. At beamline I09, however, a wide angle acceptance lens in front of the analyzer allows us to measure electrons emitted over an angular range of 60° *simultaneously*. Figure 4.3 (a) shows a sketch of this measurement geometry. With this wide angle acceptance lens we can thus record the emission angle dependence of our spectra in a single shot and, in particular, in the same measurement geometry.

This approach does not only save time but is also essential for our experiments: We measure the sample in a state which is created by the x-ray beam itself and thus locally restricted to the small x-ray beam spot. Whenever the sample is rotated, the x-ray beam impinges on a fresh spot and the preparation has to start anew. Furthermore, the exact characteristics of the state as, e.g., the oxygen vacancy concentration at saturated oxygen depletion, also depend intricately on the x-ray beam. With every rotation of the sample the angle between the sample and the x-ray beam is changed, which alters the size of the beam spot and changes the state of the sample as a result. However, all these complications are bypassed by the use of the wide angle lens: For our experiments we choose the measurement geometry illustrated in the sketch in Fig. 4.3 (a). In this geometry, electrons emitted at an angle of $5° - 65°$ with respect to the sample surface normal are recorded by the analyzer. In that angular range, the effective inelastic mean free path λ_{eff} of the photoelectrons changes from $\lambda_{\mathrm{eff}} = \lambda_{\mathrm{IMPF}}$ to $\lambda_{\mathrm{eff}} = 0.42\lambda_{\mathrm{IMPF}}$.

To check the performance of the wide angle acceptance lens, we measure the Au $4f$ core level of a polycrystalline gold foil.[1] This reference sample is expected to show *no angular dependence* in the core level spectra. An electron-emission-angle-resolved Au $4f$ spectrum is shown in Fig. 4.3 (b).

---

[1] We take particular care to measure the Au $4f$ core level at a similar kinetic energy as is used in the measurements of the core levels later on.

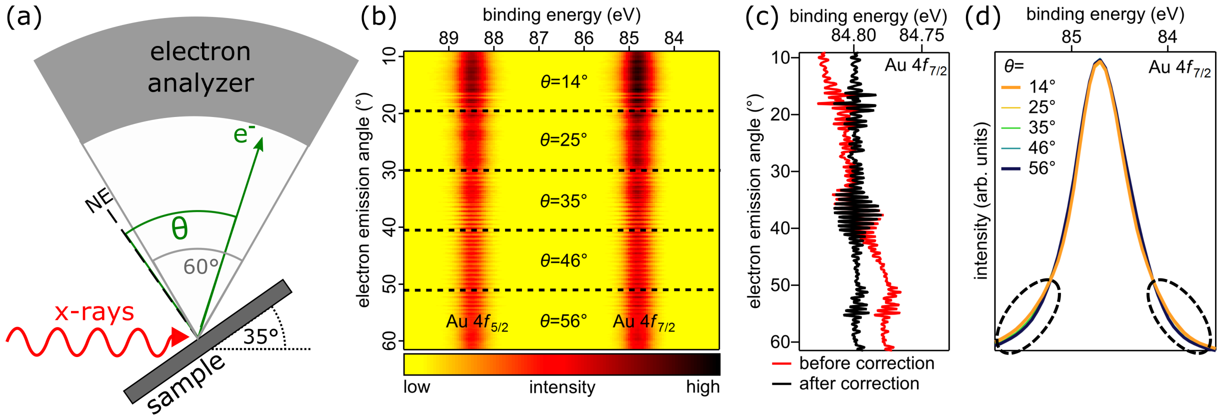

Fig. 4.3: (a) Sketch of the measurement geometry employed. (b) Electron-emission-angle-resolved Au $4f$ spectrum. (c) Binding energy of the Au $4f_{7/2}$ peak. In the raw data (red curve) the binding energy of the Au $4f_{7/2}$ peak slowly shifts with the electron emission angle. This shift is ascribed to the non-ideal calibration of the analyzer and is corrected in all following spectra (see black curve). (d) Electron-emission-angle-dependent Au $4f_{7/2}$ spectra normalized to the same area. The single curves are integrated over the angular ranges which are marked in (b). The spectra at the different electron emission angles vary slightly in width.

In Fig. 4.3 (c) we analyze the binding energy of the Au $4f_{7/2}$ peak over the whole angular range and find that its binding energy (red curve) is varying across the electron emission angle range: The fast fluctuations in the binding energy are caused by a mesh mounted in front of the wide angle lens. Since these fluctuations intricately depend on the experimental conditions and thus change for every experiment, we do not correct these fluctuations. The slow variation of the binding energy over the electron emission angle ($\Delta E \approx 50\,\mathrm{meV}$) is, however, ascribed to the non-ideal calibration of the analyzer and corrected in *all following* spectra. The black curve in Fig. 4.3 (c) exemplarily displays the binding energy of the Au $4f_{7/2}$ peak after the binding energy correction is applied.

For the subsequent analysis the 2D image is divided into five equally large angular ranges [see dashed markings in Fig. 4.3 (b)] over which the spectra are integrated. The five resulting Au $4f$ spectra are displayed in Fig. 4.3 (d). To facilitate the comparison a constant background is subtracted in the spectra, whereupon the spectra are normalized to the same integral area.[2] The spectra do not precisely lie on top of each other but slightly vary in their width [see dashed markings in Fig. 4.3 (d)]. The width of the spectra furthermore depends on the integral spectral intensity (data not shown). These variations in width are ascribed to systematic errors of the wide angle acceptance lens.

Having discussed the merits as well as the limitations of the wide angle lens, let us now turn to the experiments on the $\mathrm{LaAlO_3/SrTiO_3}$ heterostructures.

4.2.2 Comparison of hard and soft x-ray spectra

All spectra discussed in the following were recorded on a (001)-oriented 4 uc $\mathrm{LaAlO_3/SrTiO_3}$ heterostructure at a temperature of 60 K.[3] By a combination of irradiation and oxygen dosing, we first set two different states in our sample: By oxygen dosing and simultaneous HX irradiation, we establish the 'fully oxidized state'. In contrast, we prepare the state labeled 'saturated O depletion' by continuous irradiation with the HX beam: We drain oxygen from the heterostructure until the O depletion saturates and start our measurements subsequently.

Remember that this preparation affects the sample only locally in the spot where the x-ray beam impinges onto the sample. However, with careful focusing of the two x-ray beams we can investigate the *very same* spot, i.e., the *very same* sample state, with the soft as well as the hard x-rays.[4] With the soft x-ray beam we subsequently investigate the emergence of the Ti $3d$ valence band states, whereas we employ the hard x-ray beam to record core level spectra. Figure 4.4 displays these spectra for an $\mathrm{LaAlO_3/SrTiO_3}$ heterostructure in the fully oxidized state and at saturated O depletion. For a first comparison we show spectra which are integrated over the complete electron emission angle range of the wide angle lens. The spectra of a fully oxidized Nb-doped $\mathrm{SrTiO_3}$ substrate are plotted as well for comparison in Figs. 4.4 (a) and (b).

Let us first turn to the fully oxidized state of the $\mathrm{LaAlO_3/SrTiO_3}$ heterostructure: With the soft x-ray valence band spectra displayed in Figs. 4.4 (c) and (d) we confirm that we indeed prepared the fully oxidized state: We observe finite QP weight but no IG weight in the respective valence band spectra (marked in blue). The Ti $2p$ and Sr $3d$ HXPES spectra of the fully oxidized

---

[2] If not explicitly stated otherwise, all following spectra are presented in the same way.

[3] The 4 uc $\mathrm{LaAlO_3/SrTiO_3}$ heterostructure investigated here is *not* the same sample as the one studied in the previous chapter but fabricated under identical conditions. We will see that the results presented in the previous chapter are reproduced on this new sample.

[4] In principle, the different sample states form as a dynamic equilibrium is established between O depletion and reoxidation. The state of the sample is thus changing depending on whether the sample is irradiated with the HX or the SX beam. However, while we prepare the different states by irradiation with the HX beam, we only shortly record the Ti $3d$ spectra using the SX in this experiment. During the short irradiation with the SX beam, the state of the sample does not change significantly. Presumably, we thus probe the same state of the sample in the HXPES and SXPES measurements.

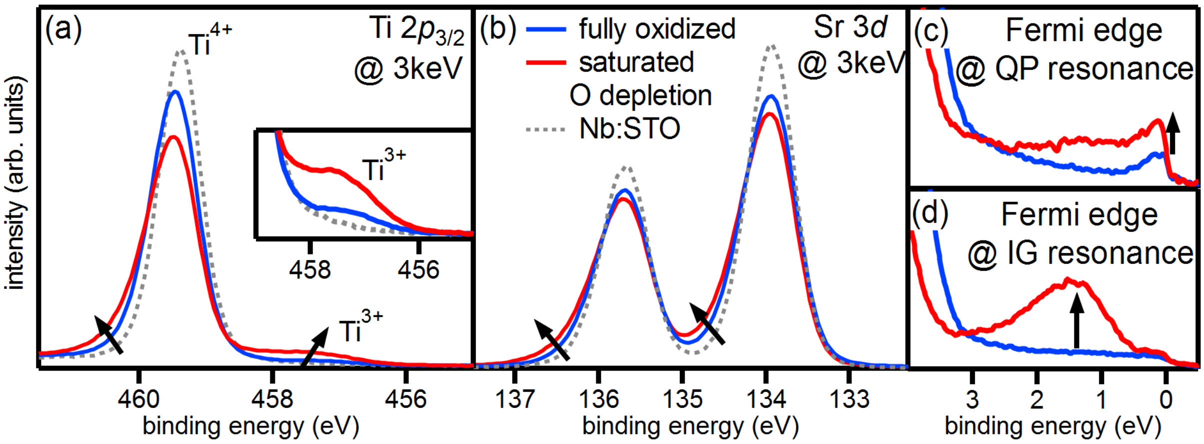

Fig. 4.4: HXPES and SXPES spectra of a $LaAlO_3/SrTiO_3$ heterostructure in the fully oxidized state and at saturated O depletion. (a) and (b) show angle-integrated Ti $2p_{3/2}$ and Sr $3d$ spectra of the sample in the two different states measured at 3 keV photon energy. The spectra of a Nb-doped $SrTiO_3$ substrate are depicted for comparison. (c) and (d) display the corresponding valence band spectra recorded with soft x-rays at the QP and the IG resonance, respectively.

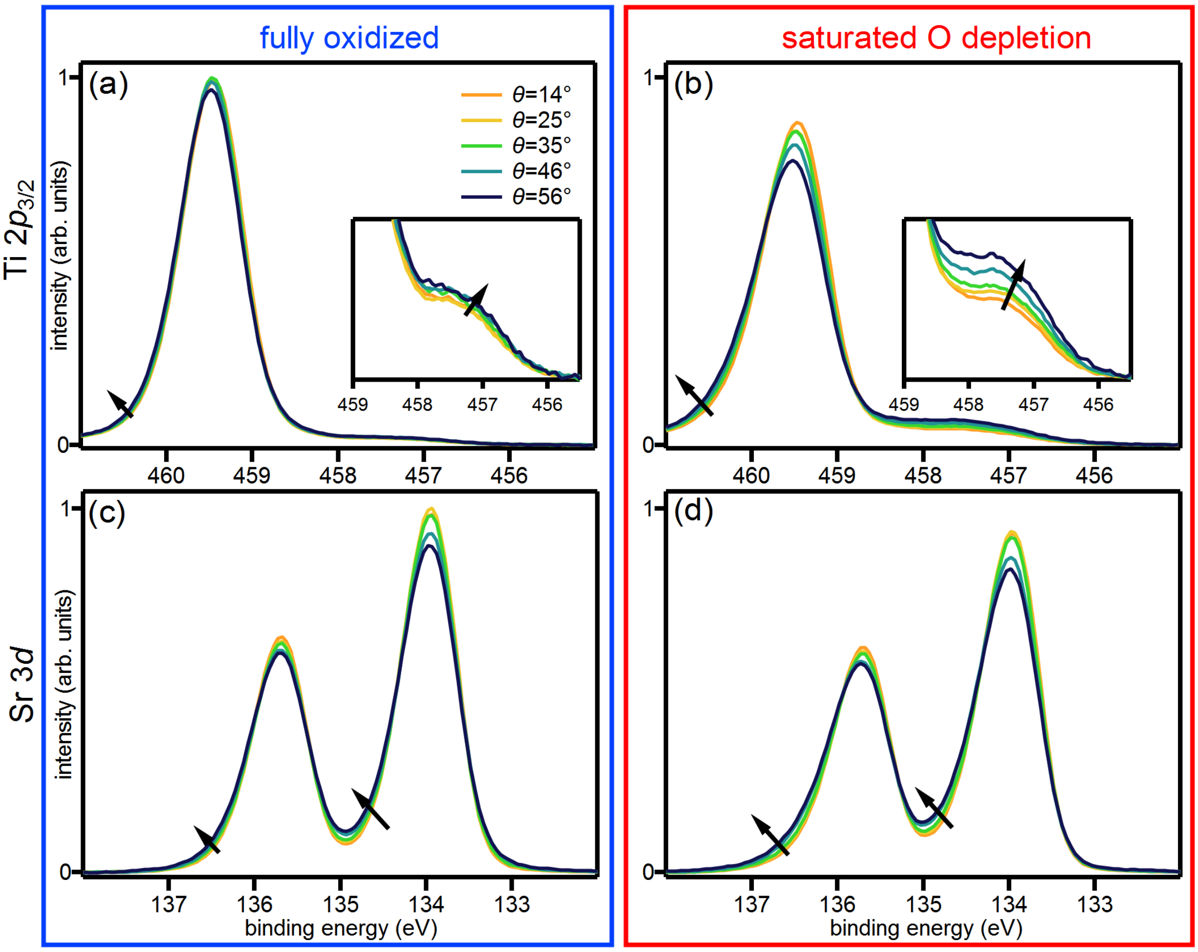

Fig. 4.5: Electron emission angle dependence of substrate core level spectra for a 4 uc $LaAlO_3/SrTiO_3$ heterostructure. Ti $2p_{3/2}$ and Sr $3d$ spectra of the sample in the fully oxidized state are depicted in (a) and (c) while the corresponding spectra at saturated O depletion are displayed in (b) and (d), respectively. See text for details.

$LaAlO_3/SrTiO_3$ heterostructure are broadened toward the high binding energy side compared to the corresponding spectra of the $SrTiO_3$ substrate [compare blue and gray spectra in Figs. 4.4 (a) and (b)]. This shows that the conduction band is bent toward higher binding energy close to the interface in the fully oxidized $LaAlO_3/SrTiO_3$ heterostructures. In the Ti 2*p* spectra of the $LaAlO_3/SrTiO_3$ heterostructure we furthermore observe non-vanishing Ti^{3+} weight which is noticeably absent in the Ti 2*p* spectra of the fully oxidized $SrTiO_3$ substrate [see inset in Fig. 4.4 (a)]. The observation of non-vanishing Ti^{3+} weight matches to the finite QP weight, i.e., the finite Ti 3*d* weight which is detected in the SX valence band spectra of the fully oxidized heterostructure [see blue spectra in Fig. 4.4 (c)].

Next, we turn to the oxygen-depleted state which is brought about by continuous irradiation with the hard x-ray beam (see red spectra in Fig. 4.4): The concomitantly increasing QP and IG weight in the spectra in Figs. 4.4 (c) and (d) evidences that oxygen vacancies are created in the $SrTiO_3$ substrate. In the HXPES core level spectra of the oxygen-depleted state, the asymmetry toward high binding energies and the Ti^{3+} weight both rise [see arrows in Fig. 4.4 (a) and (b)]. The angle-integrated HXPES spectra show that the band bending as well as the Ti 3*d* occupation are increased under oxygen depletion, confirming the conclusion from the SXPES measurement series (see Sec. 3.5).

Analyzing HXPES spectra recorded for different electron emission angles, we are now able to draw conclusions about the depth dependence of the band bending and about the charge carrier distribution.

4.2.3 Electron emission angle dependence of Sr 3*d* and Ti 2*p* spectra

Let us first comment on the qualitative trends which one observes in the electron-emission-angle-dependent Ti 2*p* and Sr 3*d* spectra displayed in Fig. 4.5 for the fully oxidized state and at saturated O depletion. Note that we adopt the same intensity scale in the Ti 2*p* graphs and Sr 3*d* graphs, respectively, to facilitate the comparison between the spectra.

We initially turn to the spectra in the fully oxidized state (see blue frame in Fig. 4.5): For high electron emission angles the Sr 3*d* as well as Ti 2*p* core level lines develop a small asymmetry toward higher binding energies (see arrows). The small Ti^{3+} spectral weight in the Ti 2*p* spectra [see inset in Fig. 4.5 (a)] also shows only a slight dependence on the electron emission angle. These observations show that the binding energy of the substrate core level lines as well as the Ti 3*d* occupation do barely change on the scale of the photoemission probing depth [see illustration in Fig. 4.6 (a)]. Tentatively, we thus conclude that the band bending in the fully oxidized state is small and that the 2DES extends far into the $SrTiO_3$ bulk.

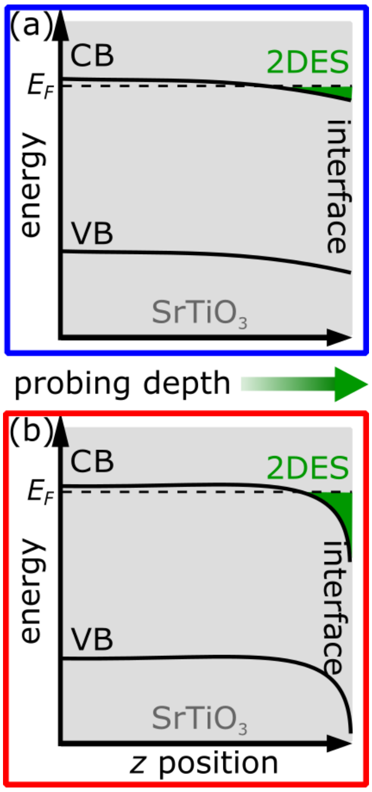

Fig. 4.6: Tentative band scheme in the $SrTiO_3$ substrate for the fully oxidized state (a) and at saturated oxygen depletion (b).

Next we focus on the spectra recorded at saturated oxygen depletion which are marked by the red frame Fig. 4.5: In contrast to before, the enhanced Ti^{3+} weight is now strongly varying with the electron emission angle [see inset in Fig. 4.5 (b)]. The asymmetry in the Sr 3*d* and Ti 2*p* core level lines at high electron emission angle is also much more pronounced [see arrows in Figs. 4.5 (b) and (d)]. These results indicate that the binding energy of the core level lines as well as the Ti 3*d* occupation considerably vary on the scale of the photoemission probing depth [see illustration in Fig. 4.6 (b)]. We infer that the band bending and the charge carrier concentration are increasing under oxygen depletion as well as that the 2DES is closely confined to the $LaAlO_3/SrTiO_3$ interface. These qualitative considerations already give an inkling of the band diagram at the interface. However, for a quantitative understanding of the band bending, we need to fit the measured data carefully which will be described in the following.

4.2.4 Background modeling

In order to analyze the delicate changes in the angle-dependent spectra, a careful subtraction of the background signal is indispensable, in particular as the background signal also changes with the electron emission angle: When a satellite peak from a film core level line is, e.g., contributing to the background signal of a substrate core level, the ratio of background to signal is varying with the electron emission angle.

For the Ti $2p$ spectra, a Shirley-like background is subtracted as exemplarily illustrated in Fig. 4.7 (a).

The background correction in the Sr $3d$ core level spectra is more intricate: Here, the background signal is composed of a La $4d$ and a Sr $3d$ satellite peak and a Shirley-like background as demonstrated in Figs. 4.7 (b) and (c). Applying appropriate constraints, the three different contributions to the Sr $3d$ background are subtracted one after the other, as described in detail in Sec. B.1 in the Appendix. Such a background modeling may seem complicated and cumbersome but renders the physically most meaningful background due to the constraints applied. Furthermore, note that the overall effect of the background subtraction onto the Sr $3d$ peak form is small and does, in particular, not change the qualitative trends described above.

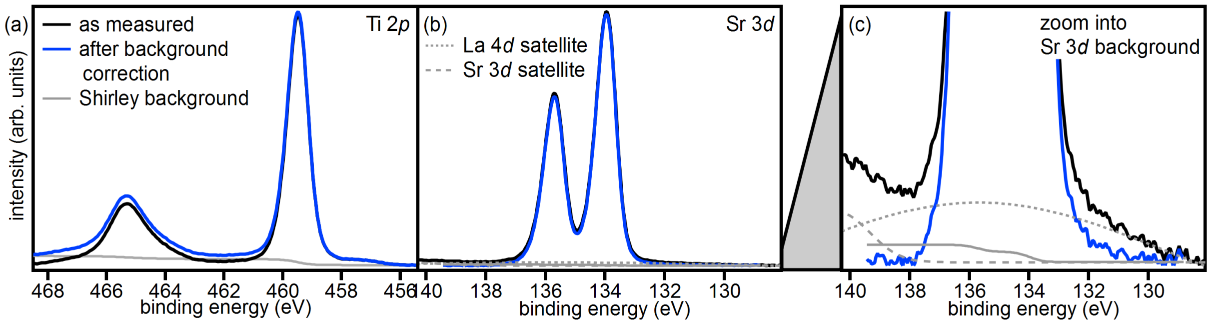

Fig. 4.7: (a) Exemplary Shirley background correction of a Ti $2p$ spectrum. (b) Exemplary background correction of a Sr $3d$ spectrum: The Sr $3d$ background is composed of a La $4d$ and a Sr $3d$ satellite peak and the Shirley background. (c) Zoom of the spectrum in (b) showing the Sr $3d$ background correction in more detail.

4.2.5 Poisson-Schrödinger ansatz

Many publications which are concerned with the electronic structure of $SrTiO_3$-based heterostructures[111,140,148] treat the charge carrier profile and the band bending which confines the 2DES with *separate* approaches. The two quantities are consequently approximated and fitted with *independent* models.

This approach is, however, problematic in specific cases: To determine the 2DES extension, the dependence of the Ti^{3+} weight on the electron emission angle is typically analyzed.[138,140,149] If the overall Ti^{3+} weight is small – as is the case for fully oxidized samples – the variations in the Ti^{3+} weight with the electron emission angle are very subtle and hard to detect in an experiment. In such cases, it is thus virtually impossible to make a statement over the charge carrier distribution in the sample, based only on the changes of the Ti^{3+} weight with the electron emission angle.

The band bending and the charge carrier profile are, however, mutually dependent and are linked by Poisson's and by Schrödinger's equation. To make the fits of both the charge carrier distribution as well as the band bending more reliable and accurate, we take advantage of the link between these two quantities and model them with functions which solve Poisson's as well as Schrödinger's equations *self-consistently*, i.e., at the same time. Within the Poisson-Schrödinger ansatz we do not have to rely solely on the electron emission angle dependence of the Ti^{3+} weight to determine the 2DES extension, but can infer information about the charge carrier profile from the band bending toward the interface as well.

Let us start with a brief review of Poisson's and Schrödinger's equation which is based on refs. [150–153]:
In the following we map the heterostructures to only *one dimension*. We assume that the charge carrier distribution as well as the band bending varies only perpendicularly to the interface as a function of z, whereas both quantities are constant parallel to the interface, i.e., in x and y direction. In one dimension, Poisson's equation reads

$$\frac{\partial}{\partial z}\left(\epsilon_r\epsilon_0\frac{\partial\Phi(z)}{\partial z}\right) = -e\left[N_D(z) - n(z)\right], \tag{4.1}$$

where $\Phi(z)$ describes the electrostatic potential and $n(z)$ denotes the concentration of mobile electrons. ϵ_0 stands for the vacuum permittivity while ϵ_r denotes the dielectric constant of the $\mathrm{SrTiO_3}$ substrate. If there are *ionized* donors present in the system, their concentration $N_D(z)$ enters Poisson's equation as well.

Next we turn to the one-dimensional time-independent Schrödinger equation, which reads

$$\left(-\frac{\hbar^2}{2m^*}\frac{\partial^2}{\partial z^2} - e\Phi(z)\right)\Psi_l(z) = E_l\Psi_l(z), \tag{4.2}$$

where m^* denotes the effective mass of the electrons. The one-dimensional Schrödinger equation is only satisfied by specific wave functions $\Psi_l(z)$ and corresponding eigenenergies E_l which are labeled by the index l. The dispersion relations perpendicular to the interface are defined by the spectrum of these discrete eigenenergies, which are also called subbands. In contrast, parallel to the interface we treat the electrons as free particles moving in a constant potential, i.e., as a free electron gas with parabolic dispersion.

In order to calculate the charge carrier profile $n(z)$, we have to add up the absolute squares $\Psi_l^*(z)\Psi_l(z)$ of the different eigenstates

$$n(z) = \sum_{l=1}^{m}\Psi_l^*(z)\Psi_l(z)n_l. \tag{4.3}$$

For every subband l we furthermore need to weight $\Psi_l^*(z)\Psi_l(z)$ with the density n_l of occupied states in this subband l

$$n_l = b\cdot\frac{m^*}{\pi\hbar^2}\int_{E_l}^{\infty}\frac{1}{1+e^{(E-E_f)/k_BT}}dE, \tag{4.4}$$

where b denotes the number of degenerate bands. n_l is computed using the density of states of a two-dimensional electron gas. By means of the Fermi-Dirac distribution $\frac{1}{1+e^{(E-E_f)/k_BT}}$ we ensure that only occupied states are included in the calculation of n_l.

We note that the electrostatic potential $\Phi(z)$ and the charge carrier distribution $n(z)$ both enter into Poisson's equation (4.1) as well as into the equations (4.2)–(4.4) which are related to the

Schrödinger equation. To find solutions for $\Phi(z)$ and $n(z)$ which simultaneously satisfy equations (4.1) to (4.4), we make use of an iteration scheme: Starting from an arbitrarily chosen trial potential $\Phi_0(z)$, one computes the charge carrier concentration $n_0(z)$ with the aid of equations (4.2) to (4.4). Inserting $n_0(z)$ into Poisson's equation (4.1), a new potential function $\Phi_1(z)$ is calculated which is once again fed into the equations (4.2)–(4.4) to compute a new charge carrier concentration $n_1(z)$ and so on and so forth. This cycle is repeated until the changes in $\Phi(z)$ (and thus also in $n(z)$) from one iteration step to the next fall below a small, predefined value δ. In this thesis the '1D Poisson' program written by Gregory Snider[152–154] is employed to find the self-consistent solutions to the Poisson-Schrödinger equations.

4.2.6 Modeling $SrTiO_3$-based heterostructures

In the following we have to relate the functions and variables defining the Poisson-Schrödinger model to physical quantities in the $SrTiO_3$-based heterostructures. First, we turn our attention to the z-dependent[5] quantities $n(z)$, $N_d(z)$ and $\Phi(z)$.

The electrostatic potential $\Phi(z)$ is linked to the conduction band profile in the $LaAlO_3/SrTiO_3$ heterostructure. While $\Phi(z)$ is defined for a positive test charge, the profile of the conduction band edge $E_c(z)$ is, in contrast, defined with an electron in mind and is thus calculated via $E_c(z) = -e\Phi(z)$. Whereas realistic values are used to model the $SrTiO_3$ band structure, the $LaAlO_3$ film is treated as an infinite potential barrier in our ansatz to prevent charge carriers from being erroneously transferred into the $LaAlO_3$ film.

But how are charge carriers doped into the $SrTiO_3$-based heterostructures in the first place? Let us briefly recall the previous chapter in which we discussed different doping mechanisms for $SrTiO_3$: In fully oxidized epitaxial $LaAlO_3/SrTiO_3$ heterostructures the *electronic reconstruction* provides mobile charge carriers and there are, in particular, no oxygen vacancies doping electrons in the $SrTiO_3$ substrate. The 2DES in disordered $LaAlO_3/SrTiO_3$ heterostructures was, in contrast, shown to be solely induced by donors in the $SrTiO_3$ substrate, i.e., by *oxygen vacancies*. In oxygen-depleted epitaxial $LaAlO_3/SrTiO_3$ heterostructures we finally observed a combination of these two doping mechanisms. Figure 4.8 illustrates how the different scenarios are modeled by a Poisson-Schrödinger ansatz. The top figures show the respective three-dimensional concentrations of mobile charge carriers $n(z)$ and of ionized donors $N_d(z)$ which are linked via the Poisson-Schrödinger equations to the conduction band profiles $E_c(z)$ plotted in the bottom figures.

In the case of electronic reconstruction (blue frame in Fig. 4.8) there are no oxygen vacancies, i.e., no ionized donor atoms in the $SrTiO_3$ substrate itself. $N_d(z)$ is consequently set to 0. The mobile charge carrier concentration is instead introduced by a finite electric displacement field D present at the interface. This electric displacement field D can be understood as an infinitesimally thin layer of positive charges, i.e., a δ-function like doping profile, right at the interface. According to charge neutrality mobile electrons in the $SrTiO_3$ substrate have to compensate these positive charges. Varying the electric displacement field we are thus able to adjust the charge carrier concentration induced by the electronic reconstruction.

When the $SrTiO_3$ is, in contrast, exclusively doped by electrons released from oxygen vacancies (gray frame in Fig. 4.8), the electric displacement field D is set to zero. According to ref. [132], we assume that one of the two electrons released by each oxygen vacancy remains localized while the other electron is mobile. Against the backdrop of the $SrTiO_3$ lattice, in which the oxygen anions are twice negatively charged, an oxygen vacancy thus effectively carries a single positive charge. The oxygen vacancies can consequently be treated as if they were *ionized* dopant atoms in the conventional semiconductor picture and enter in Poisson's equation (4.1) as the term $N_D(z)$. In the ensuing fits we assume that the oxygen vacancy concentration peaks at the interface and

---

[5] The z dependence is evaluated at discrete steps of 0.1 Å size.

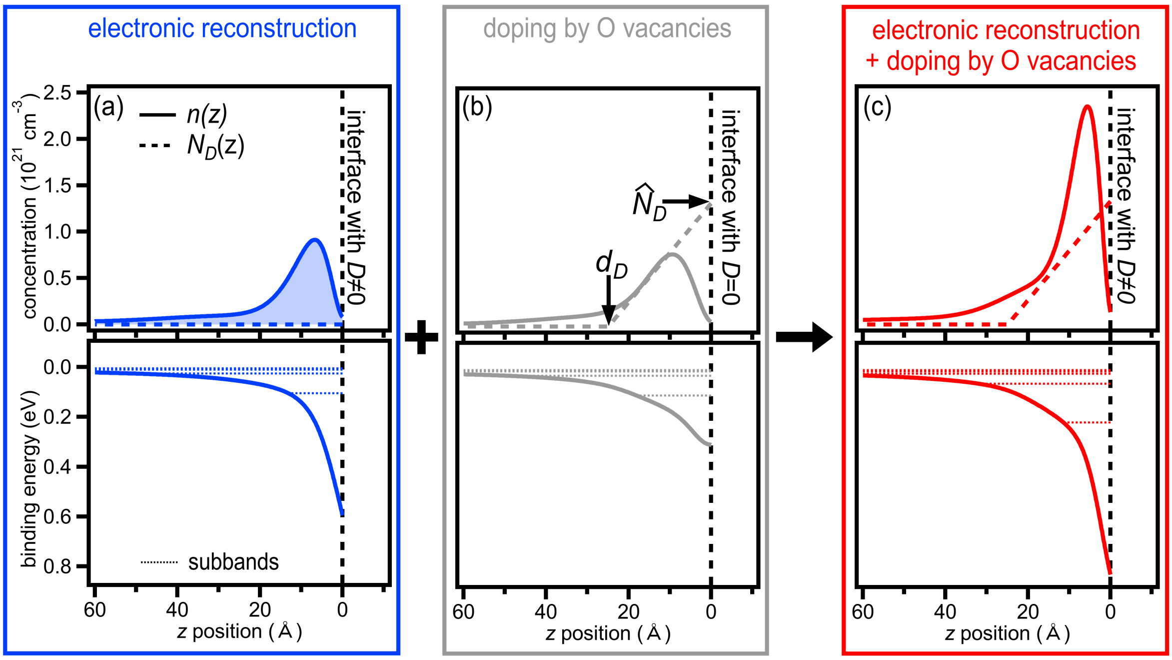

Fig. 4.8: Poisson-Schrödinger approach for different kinds of doping: Top figures: 3D concentration of mobile charge carriers (solid lines) and of ionized donors (dashed lines). Bottom figures: Conduction band profile with subband structure.
Blue: Doping by electronic reconstruction, for fully oxidized epitaxial $LaAlO_3/SrTiO_3$ samples. The free charge carriers are introduced by an electric displacement field D at the interface. No ionized donors, i.e., oxygen vacancies are present in the $SrTiO_3$ substrate.
Gray: Doping by oxygen vacancies, for, e.g., disordered $LaAlO_3/SrTiO_3$ samples. The oxygen vacancy concentration is assumed to decrease linearly into the $SrTiO_3$ bulk (dashed line). Each oxygen vacancy releases one mobile electron.
Red: Combination of doping by oxygen vacancies and electronic reconstruction, for oxygen-depleted epitaxial $LaAlO_3/SrTiO_3$ samples.

decreases linearly into the $SrTiO_3$ bulk [dashed line in Fig. 4.8 (b)]. The V_{O} profile can thus be tuned by two parameters, the V_{O} concentration $\hat{N}_D$ at the interface and the thickness d_D of the V_{O}-doped layer.

The red frame in Fig. 4.8 shows an example of a heterostructure (as, e.g., oxygen-depleted epitaxial $LaAlO_3/SrTiO_3$) which is doped by oxygen vacancies and electronic reconstruction. In this case the electric displacement field D as well as the dopant concentration $N_d(z)$, i.e., the oxygen vacancy concentration, are set to finite values.

Let us finally comment on the effective mass m^* appearing in the Poisson-Schrödinger ansatz above: In the equations (4.1)–(4.4) we assume that the conduction electrons are characterized by a single, isotropic effective mass m^*. In general, electronic transport in $SrTiO_3$-based heterostructures is more complex: In $SrTiO_3$, mobile electrons can reside in the three Ti $3d\,t_{2g}$ orbitals. Depending on the crystalline orientation of the heterostructure, the degeneracy of the three Ti $3d\,t_{2g}$ orbitals is lifted (see Sec. 3.1.2). As the d orbitals are furthermore strongly anisotropic, the in-plane and out-of-plane mass of the mobile electrons in the 2DES differs as well. However, an elaborate ansatz including anisotropic masses and non-degenerate Ti $3d\,t_{2g}$ bands would introduce many free parameters which could not be reliably fitted based on our spectroscopic measurements. To keep our model simple and the number of fit parameters manageable, we thus settle for working with an isotropic effective mass m^*. As no band is singled out in our model, we set the number b of degenerate bands universally to three, the number of the Ti $3d\,t_{2g}$ orbitals, for both the fully oxidized as well as the oxygen-deficient state.

4.2.7 Peculiarities of the $SrTiO_3$ dielectric constant

In the next section we turn our attention to the *static* dielectric constant ϵ_r of $SrTiO_3$. ϵ_r is the only external input parameter in Poisson's equation (4.1) and thus an essential parameter determining the charge carrier distribution $n(z)$ as well as the confining potential $\Phi(z)$.

For a first assessment of the impact of ϵ_r onto $n(z)$ and $\Phi(z)$, we assume that ϵ_r is constant across the substrate and model a $SrTiO_3$ substrate which is exclusively doped by electronic reconstruction. For purposes of comparison we fix the total mobile charge carrier concentration $Q_{\text{total}} = \int_{z=0}^{\infty} dz n(z)$. Figure 4.9 exemplarily sketches the conduction band profile as well as the charge carrier distribution for different values of ϵ_r:
In the limit of small ϵ_r the band bending at the interface is large and runs steep and the electrons are confined to few $SrTiO_3$ layers (see black lines in Fig. 4.9). Conversely, in the limit of large ϵ_r, the band bending runs shallow and is small at the interface and the electron density extends far into the $SrTiO_3$ bulk (see light blue lines in Fig. 4.9). We note that the charge carrier distribution and the conduction band profile at the interface are coupled as consequence of Poisson's equation.

One can also intuitively comprehend why the charge carrier and conduction band profile change with the dielectric constant ϵ_r: The dielectric constant ϵ_r mediates the screening in the semiconducting $SrTiO_3$ substrate.[155] At small ϵ_r the screening is low. The electric displacement field D, i.e., the δ-layer of positive charges at the interface, consequently gives rise to a steeply rising potential well in which the mobile electrons accumulate. These mobile electrons compensate for the layer of positive charges at the interface. The effect of the displacement field is thus no longer palpable deeper in the bulk of the $SrTiO_3$ substrate. The 2DES as well as the band bending are thus confined to the interface region.
When ϵ_r increases, the electrostatic attraction of the positive charges at the interface is screened, i.e., reduced. The $SrTiO_3$ bands are ergo not as strongly bent toward the interface as before and the mobile electrons accordingly spread further into the $SrTiO_3$ bulk. The electric displacement field is not entirely compensated for large z and continues to have an effect even far away from the interface. The spatial extension of the band bending and of the charge carrier distribution is thus comparably large in the limit of high ϵ_r.

With $SrTiO_3$ being a quantum paraelectric, ϵ_r is *strongly dependent* and *strongly varying* with the temperature as well as the electric field: Figure 4.10 (a) sketches the temperature dependence

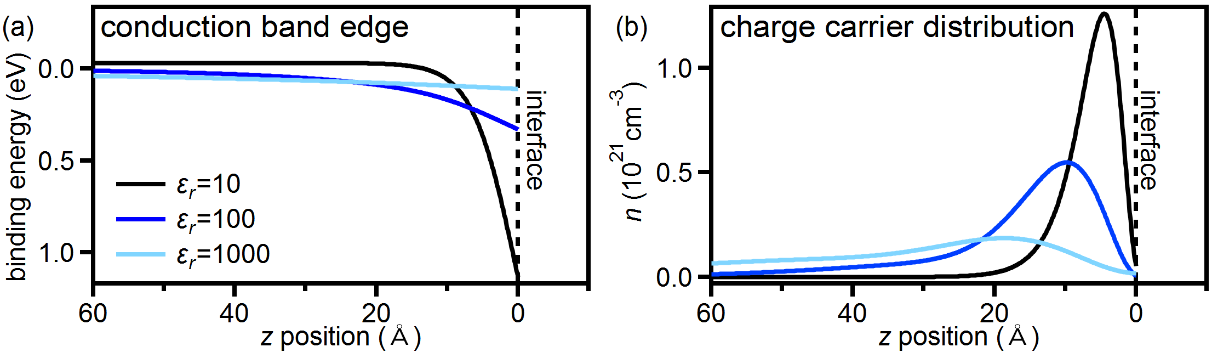

Fig. 4.9: Conduction band profile (a) and charge carrier distribution (b) in a $LaAlO_3/SrTiO_3$ heterostructure doped by electronic reconstruction calculated from a Poisson-Schrödinger model. We vary ϵ_r which is assumed to be constant across the $SrTiO_3$ substrate. The band bending at the interface and the extension of the 2DES are strongly dependent on the size of ϵ_r.

of the dielectric constant in a $SrTiO_3$ single crystal. We note that ϵ_r varies by more than two orders of magnitude between room temperature ($\epsilon_r \approx 300$) and 2 K ($\epsilon_r \approx 20\,000$). The left panel in Fig. 4.10 (b) illustrates the strong electric field dependence of ϵ_r at exemplary temperatures.

The electric field dependence of ϵ_r is of paramount importance in the model calculations:[156] We treat oxygen vacancies as *charged* impurities. A variation in the V_O concentration is thus inevitably linked to a local change in the electric field which in turn modifies the dielectric constant at that position. In our simulations we thus introduce a z-dependent ϵ_r which is changing as a function of the electric field $E(z)$. To describe the relation between the electric field E and the dielectric constant ϵ_r, we employ the following empirical formula[6] proposed by Fête *et al.*[73,158]

$$\epsilon_r(E) = 1 + \frac{B}{[1 + (E/E_0)^2]^{1/3}}. \tag{4.5}$$

The variable $B + 1$ describes the dielectric constant in the limit $E \to 0$ and E_0 indicates the electric field at which ϵ_r starts to decrease noticeably. To check the validity of equation (4.5), we use it to fit the temperature-dependent electric field dependence shown in the left panel of Fig. 4.10 (b). The fitted curves which are plotted as solid lines in Fig. 4.10 agree well with the experimental data.

The fit results for B and E_0 are given in the right panel of Fig. 4.10 (b). We see that both parameters B and E_0 are strongly varying with temperature: While B is decreasing, E_0 is increasing when the temperature is rising. At low temperatures, ϵ_r is thus high but rapidly shrinks already at moderate electric fields while at higher temperatures ϵ_r is overall smaller but more robust against variations in the electric field.

In our previous Poisson-Schrödinger ansatz, the electric field depended on the position z while ϵ_r was set to a constant value. To include the z-dependent ϵ_r in our simulations, we adapt the Poisson-Schrödinger ansatz as illustrated in Fig. 4.12: We use the electric field $E(z)$ the Poisson-Schrödinger ansatz yields to compute $\epsilon_r(z)$ via equation (4.5). Substituting the new $\epsilon_r(z)$ into Poisson's equation, we solve the Poisson-Schrödinger equations anew and subsequently calculate $\epsilon_r(z)$ again. The blue loop in Fig. 4.12 illustrates this step. The blue loop is iterated several times until the results for both the electric field $E(z)$ and the dielectric constant $\epsilon_r(z)$ converge.

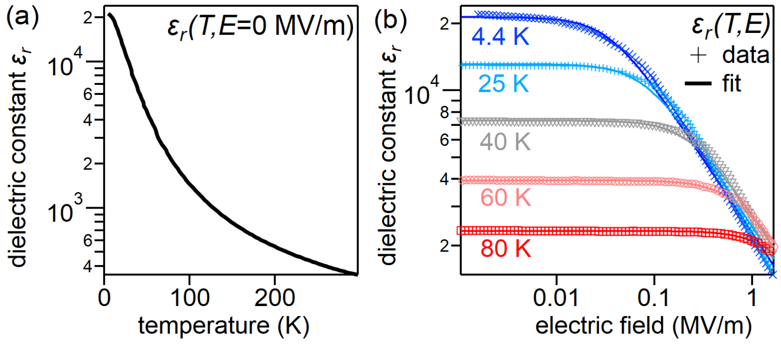

fit of $\epsilon_r(T, E)$:

T (K)	B	E_0 (MV/m)
4.4	21 390	0.035
25	13 160	0.080
40	7 330	0.233
60	3 940	0.689
80	2 340	1.642

Fig. 4.10: (a) Temperature dependence of the dielectric constant in a $SrTiO_3$ single crystal. Data adopted from ref. [73]. (b) Left panel: Electric field dependence of the dielectric constant of $SrTiO_3$ at various temperatures. Experimental data adopted from ref. [68]. Right panel: The electric field dependence of the dielectric constant of $SrTiO_3$ is fitted employing equation (4.5). The table indicates the parameters B and E_0 yielding the best fit to the data.

---

[6] This approximation has been shown to yield good approximations at *high electric fields*,[73,157] which is of particular importance as the electric fields at the $LaAlO_3/SrTiO_3$ interface turn out to be very high.

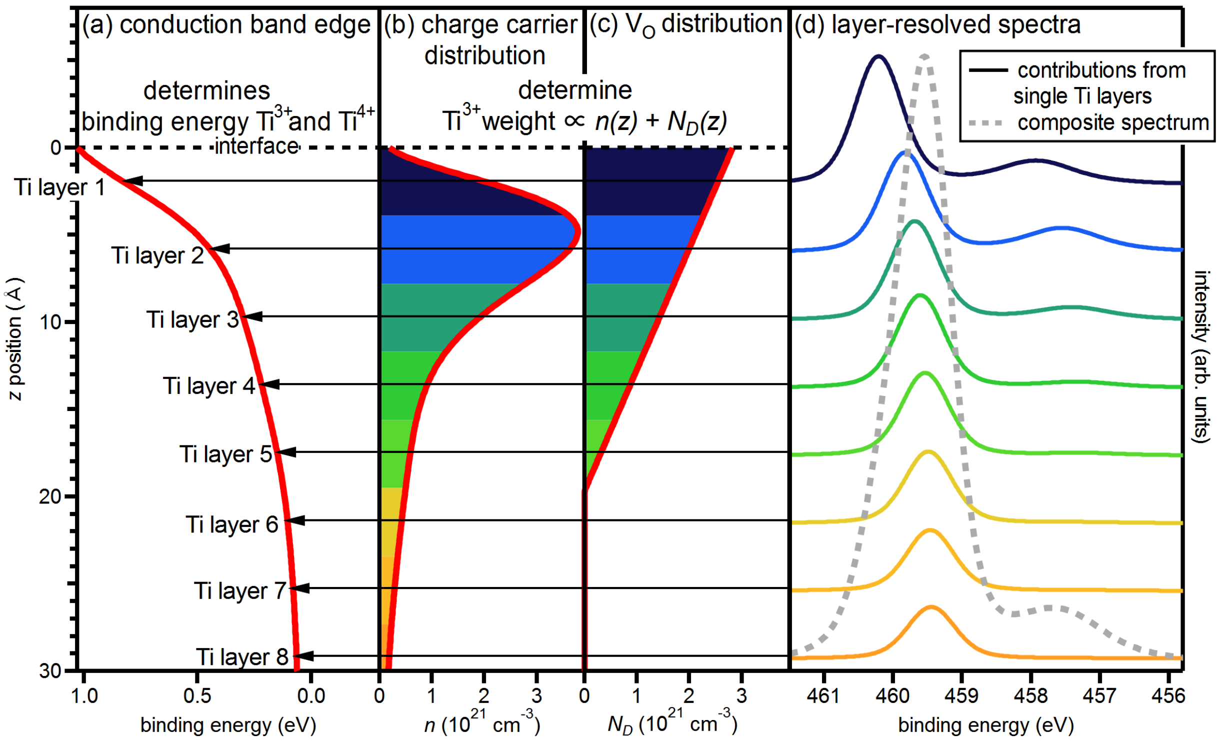

Fig. 4.11: Layer-resolved composition of an exemplary Ti 2*p* spectrum. (a) Conduction band profile near the interface. (b) Concentration of *free* charge carriers. (c) Concentration of *bound* charge carriers. (d) Ti 2*p* spectra of the uppermost TiO_2 layers. The binding energy of the single spectra in (d) is determined by the band bending at position z [see arrows in (a)]. The Ti^{3+} spectral weight in the single spectra is proportional to the sum of the free and bound charge carrier concentration which is integrated over one unit cell [see colored areas in (b) and (c)]. For clarity the layer-resolved Ti 2*p* spectra are only shown for a few layers. Yet, deeper lying layers still contribute to the composite spectrum. The composite spectrum is shown in (d) by the dashed gray line.

4.2.8 Decomposition of Sr 3*d* and Ti 2*p* spectra

In the next section, we outline how the functions $n(z)$, $N_d(z)$ and $V(z)$ which solve the Poisson-Schrödinger equations enter into the fit models of the photoemission spectra. We consider the example of a Ti 2*p* spectrum: The Ti 2*p* spectrum is made up of the contributions originating from the individual TiO_2 layers as exemplarily illustrated in Fig. 4.11 (d). For clarity the layer-resolved Ti 2*p* spectra are only shown for a few layers. Yet, layers lying deeper in the $SrTiO_3$ bulk also contribute to the composite spectrum. Note that we do not take a contribution from the $SrTiO_3$ bulk into account in our fit model. Instead, we include the contributions of layers which lie up to 200 Å deep in the $SrTiO_3$ substrate in our models. Employing such an integration boundary, we capture virtually all ($\geq$99%) Ti 2*p* photoelectrons which escape from the $SrTiO_3$ substrate.

To build up the signal originating from the single layers [see colored lines in Fig. 4.11 (d)], we model the Ti^{4+} peak with a Voigt profile. The Ti^{3+} feature is modeled by a second Voigt profile with a different spectral shape. Across all layers, we use the same spectral shape for the Ti^{4+} feature and the Ti^{3+}, respectively. We furthermore fix the binding energy difference between the Ti^{3+} and the Ti^{4+} peak in all layer-resolved spectra.

The Ti^{3+} weight $I(Ti^{3+})$ as well as the binding energy of the Ti $2p$ core level lines do, however, change across the layers with the distance z from the interface.Note that the position of the interface is chosen to coincide with the first LaO layer. To determine the binding energy of the Ti $2p$ core level lines in the layer-resolved spectra, we correct the binding energy of the core level lines in the $SrTiO_3$ bulk by the binding energy of the conduction band edge at the respective position z [see arrows in Fig. 4.11 (a)]. All mobile electrons, i.e., the electrons released by the electronic reconstruction as well as by oxygen vacancies, contribute to the Ti^{3+} weight in the layer-resolved spectra. Moreover, each oxygen vacancy does not only release one mobile electron but also one electron which remains trapped. The trapped electrons also occupy Ti $3d$ orbitals and consequently contribute to the Ti^{3+} weight. The Ti^{3+} weight $I(Ti^{3+})$ in the layer-resolved spectra is thus computed employing the following formula

$$I(\mathrm{Ti}^{3+}) \propto \int_{z-\frac{a}{2}}^{z+\frac{a}{2}} d\tilde{z} \left[n\left(\tilde{z}\right) + N_D\left(\tilde{z}\right) \right]. \tag{4.6}$$

To ensure that we capture the charge carrier concentration in its entirety, we do not read out the charge carrier concentrations at a specific position z but integrate over entire unit cells as illustrated by the colored intervals in Figs. 4.11 (b) and (c). In each of the layer-resolved Ti $2p$ spectra, the Ti^{4+} weight is diminished by the Ti^{3+} weight present in that spectrum.

Owing to the limited inelastic mean free path of the photoelectrons, the signal originating from a TiO_2 layer at depth z is exponentially damped by the factor $e^{-z/\lambda_{\mathrm{IMFP,Ti}\,2p}\cos\theta}$ where θ describes the photoelectron emission angle with respect to the surface normal and $\lambda_{\mathrm{IMFP,Ti}\,2p}$ denotes the inelastic mean free path of the Ti $2p$ photoelectrons. The value for the inelastic mean free path computed with the TPP–2M formula[27–29] is listed in Tab. B.1 in the Appendix.

We model the Sr $3d$ spectra making use of the very same approach and only briefly point out how the Sr $3d$ fits differ from the Ti $2p$ fits: The Sr $3d_{3/2}$ and the Sr $3d_{5/2}$ peak are modeled with a Voigt profile each. When modeling the spectra of the single layers, we again fix the spectral shape of the respective peaks as well as the binding energy difference between the two Voigt profiles As before, the binding energy of the layer-resolved Sr $3d$ spectra is modified according to the potential profile. This time, however, the band bending is read out at the z positions of the SrO layers. We furthermore adapt the inelastic mean free path $\lambda_{\mathrm{IMFP,Sr}\,3d}$ as the kinetic energy of the Sr $3d$ photoelectrons slightly differs from the kinetic energy of the Ti $2p$ photoelectrons (see Tab. B.1 in the Appendix).

4.2.9 Global fitting scheme

Per state (fully oxidized and at saturated O depletion) and per core level (Sr $3d$ and Ti $2p$) we extracted five spectra from our data – each at a different electron emission angle, i.e., probing depth. In total we thus have to fit twenty spectra. If we sought to fit all these Ti $2p$ or Sr $3d$ spectra *separately* in the manner outlined above, the great number of free fit parameters (i.a., the parameters of the Poisson-Schrödinger ansatz, the Gaussian and Lorentzian widths, the bulk energy position of the respective peaks) would render the fit results *meaningless*.

However, many of the parameters in the Ti $2p$ and Sr $3d$ fits are *interdependent*. We discuss this by the example of the fit parameters in the Poisson-Schrödinger ansatz: The same Poisson-Schrödinger parameters should obviously be used to fit all spectra measured in the fully oxidized state, independent of the electron emission angle or the core level spectrum which is currently investigated. Even at saturated oxygen depletion most of the parameters in the Poisson-Schrödinger ansatz should stay fixed. To describe the oxygen-deficient state, we only need to introduce a V_O profile. However, the effective mass m^* as well as the parameters B and E_0 describing the electric field dependence of ϵ_r should not change when the V_O concentration is varied. The electronic reconstruction is furthermore assumed to provide the same number of mobile charge carriers independent of the V_O concentration. The electric displacement field D at the interface is accordingly fixed to the same value in both states as well.

Instead of fitting the spectra separately, we thus model the twenty spectra *all at once* in a so-called *global fit* and set corresponding fit parameters to the same values as discussed exemplarily above. In total, 21 *independent* fit parameters appear in our global fitting scheme with which we model 20 spectra. In average we thus have only ≈1 independent fit parameter per spectrum. In the following we list the *independent* fit parameters which are relevant in our global fitting scheme:

- parameters of Poisson-Schrödinger ansatz:
    - sheet charge carrier concentration n_{er} induced by the electronic reconstruction
    - isotropic effective mass m^*
    - B and E_0 (variables which describe the electric field dependence of ϵ_r)
    - V_O concentration $\hat{N}_D$ at the interface and thickness d_D of the V_O-doped layer (variables which characterize the V_O profile in the oxygen-deficient state)
- Gaussian widths for each angular slice
  → 5 Gaussian widths in total
  (The resolution of the wide angle lens differs slightly for the 5 angular slices.)
- 1 multiplicative factor characterizing the difference in the Gaussian widths of the Ti $2p$ and Sr $3d$ core level lines
  (The resolution of the wide angle lens slightly depends on the total count rate.)
- Lorentzian width of Sr $3d_{5/2}$, Sr $3d_{3/2}$, Ti $2p^{4+}_{3/2}$ and Ti $2p^{3+}_{3/2}$ core level lines
- bulk energy position of Sr $3d_{5/2}$, Sr $3d_{3/2}$, Ti $2p^{4+}_{3/2}$ and Ti $2p^{3+}_{3/2}$ core level lines
- intensity ratio Sr $3d_{5/2}$ to Sr $3d_{3/2}$ core level lines

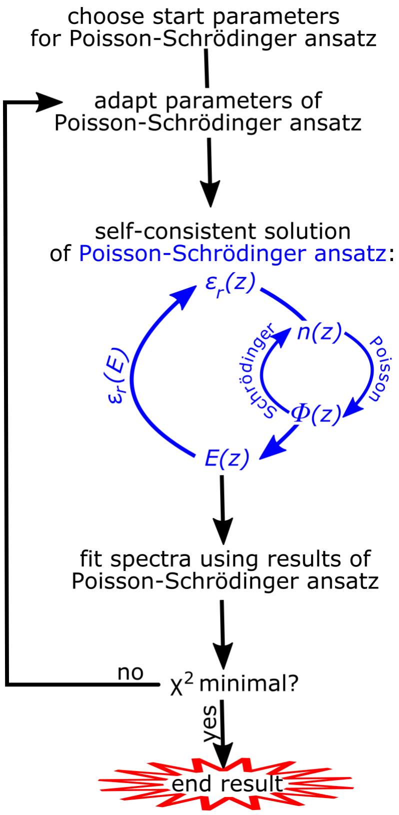

Fig. 4.12: Illustration of our global fitting scheme.

Let us finally comment on the realization of our fitting scheme: Figure 4.12 sketches how our fitting scheme works. We first choose physically meaningful start parameters for the Poisson-Schrödinger ansatz. Particular care has to be taken when selecting start values for B and E_0 as these parameters are interdependent in the high electric field regime in which we work at the $LaAlO_3/SrTiO_3$ interface. We thus let us guide by the table in Fig. 4.10 (b) when setting start values for B and E_0. We then solve the Poisson-Schrödinger equations for the fully oxidized state and at saturated O depletion. As illustrated in Fig. 4.12, we include the electric-field-dependent ϵ_r in our ansatz. Using the results of the two Poisson-Schrödinger models, we model the Ti $2p$ and Sr $3d$ spectra and determine the deviation between the fits and the measured data which is characterized by the χ^2 value. In the next step, we vary the parameters in the Poisson-Schrödinger ansatz and start all over again with solving the Poisson-Schrödinger equations. Iterating the loop over and over again, we minimize the deviation χ^2 between the measured spectra and the fits.

Having introduced our fit model, we finally address the fits and their results in the next section.

4.2.10 Discussion of fit results

Figure 4.13 compares the best fits with the measured Ti $2p_{3/2}$ and Sr $3d$ core level spectra for the fully oxidized state (blue frame) and at saturated O depletion (red frame). For the sake of clarity, only the spectra and fits recorded at the maximal and minimal electron emission angle are shown. Note that we once again use the same intensity scale in the Ti $2p$ and Sr $3d$ spectra to facilitate the comparison between the respective spectra. The fits reproduce the prominent features and trends in the spectra: The variations in the Ti^{3+} weight and in the Sr $3d$ line form with the electron emission angle are, in particular, accurately recreated.

Let us first take a close look at the fit results to check if the fits are physically meaningful.

First we turn to the fit results for the parameters describing the underlying Ti $2p_{3/2}$ and Sr $3d$ spectra. For purposes of comparison, we also fitted the Ti $2p_{3/2}$ and Sr $3d$ spectra of the fully oxidized $\mathrm{SrTiO_3}$ substrate depicted in Fig. 4.4 (a) and (b). These spectra can be adequately modeled with a single or two Voigt profiles, respectively, showing that the sample is barely affected by band bending. Thus, we view these spectra as reference spectra of $\mathrm{SrTiO_3}$ and compare them to the spectra of the single $\mathrm{SrTiO_3}$ layers in our fit model: The fit results for

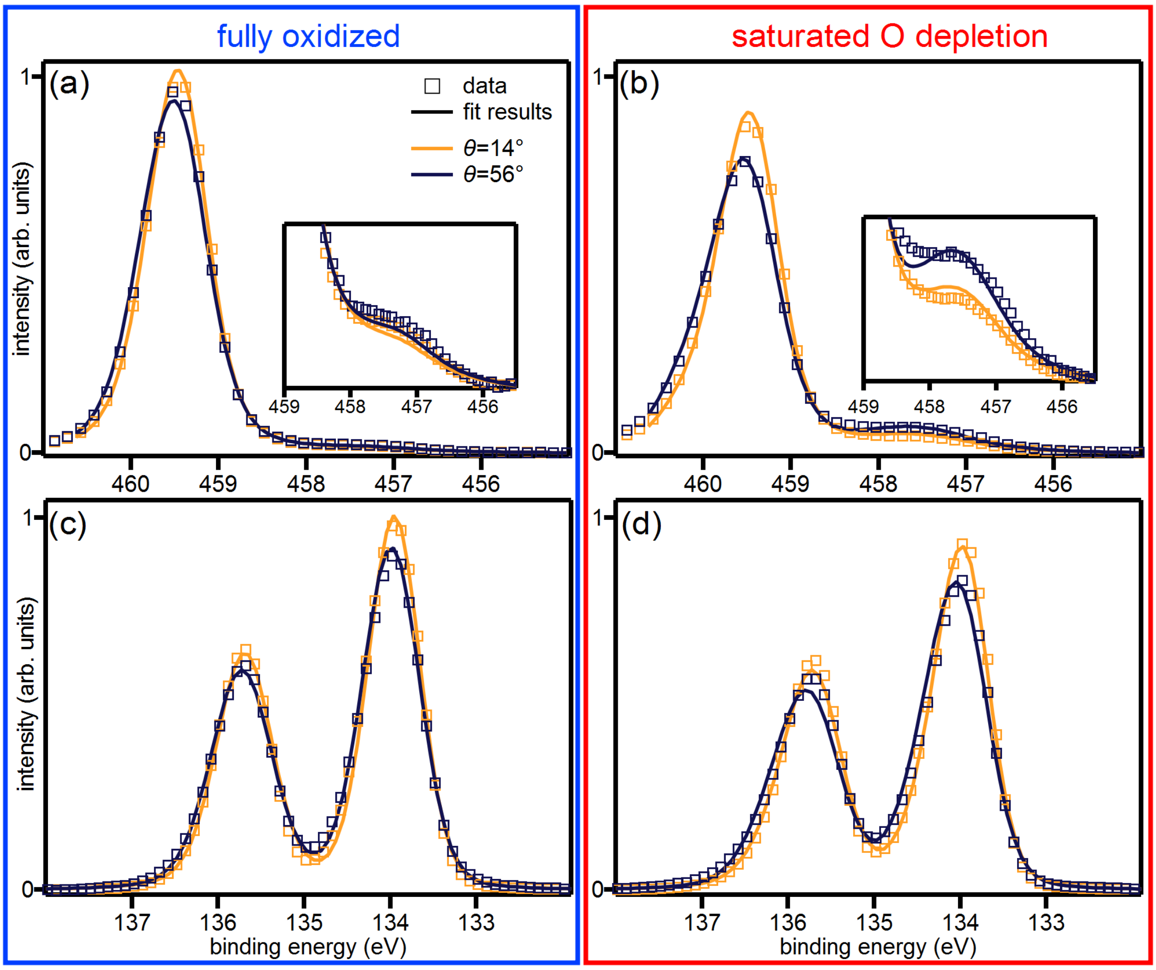

Fig. 4.13: Fits of Ti $2p$ and Sr $3d$ core level spectra with the Poisson-Schrödinger ansatz. A comparison between the Ti $2p$ spectra at the extremal electron emission angles and the corresponding fits is shown in (a) and (b) for the fully oxidized state and at saturated O depletion, respectively. Corresponding figures for the Sr $3d$ core level are shown (c) and (d). The fitted curves agree well with the measured data.

	fit parameters applicable to both states				**V_O profile at saturated O depletion**	
	n_{er} ($10^{14}\,\mathrm{cm}^{-2}$)	**m^*** (m_e)	**B**	**E_0** (MV/m)	**$\hat{N}_D$** ($10^{21}\,\mathrm{cm}^{-3}$)	**d_D** (Å)
best fit	1.66	0.84	3 400	0.95	2.83	19.8
lower limit	1.46	0.73	2 930	0.76	2.23	15.3
upper limit	1.91	1.02	3 880	1.17	3.48	23.3

Tab. 4.2: Fit results of the Poisson-Schrödinger approach for a (001)-oriented $LaAlO_3/SrTiO_3$ heterostructure. We specify the best-fit values as well as error margins.

the fully oxidized $SrTiO_3$ reference and the $LaAlO_3/SrTiO_3$ heterostructure, which are listed in the first and second column of Tab. B.2 in the Appendix, should consequently agree as well. Comparing the respective columns, we see that the fit results for the various parameters are rather similar in the case of the fully oxidized $SrTiO_3$ reference and the $LaAlO_3/SrTiO_3$ heterostructure. Furthermore, we note that the Gaussian widths used for the different electron emission angles and core levels do not change by more than 10% , which is a reasonable estimation for the varying experimental resolution considering the imperfections of the wide angle lens [cf. Fig. 4.3 (d)]. The intensity ratio between the two spin-orbit split components of the Sr 3d doublet comes close to the 3:2 ratio which is expected from the degeneracy of the respective core-hole states in a independent particle picture of photoemission.[21] The chemical shift between Ti^{4+} and Ti^{3+} the fitting routine yields also agrees with values reported in the literature for similar compounds.[135,140]

Next, we turn to the fit results for the parameters appearing in the Poisson-Schrödinger ansatz. In Tab. 4.2 we list the fit results and also indicate their error margins.[7]

The fit results for B and E_0 match to the values indicated in the table in Fig. 4.10 (b) for temperatures around 60–80 K. This estimate sounds reasonable as our measurement temperature lies in that temperature range.

The fitted value for the isotropic mass $m^* = 0.84 m_e$ has to be contrasted to calculations and experiments which also probe the effective, isotropic mass of the charge carriers: Employing fully relativistic band-structure calculations Marques *et al.*[159] estimate $m^* = 0.8 m_e$, while Okuda *et al.*[160] determine $m^* = 1.17 m_e$ based on specific-heat measurements. We conclude that the fit result for the isotropic mass is in good agreement with these values.

The oxygen vacancy concentration at saturated O depletion is compared to our assessments of the oxygen vacancy concentration in the SX measurement series in the previous chapter (cf. Sec. 3.5.2). Note that we contrast two different oxygen-depleted states in two different samples: The oxygen-depleted state in the measurement series in chapter 3 was prepared by the SX beam while the saturated O depletion was induced by the hard x-ray beam in chapter 4. We can thus only compare the order of magnitude of the effects and not the exact quantitative results. In the Poisson-Schrödinger modeling the oxygen vacancy concentration amounts to ≈16% in the $SrTiO_3$ layer right at the interface, which agrees in order of magnitude with the oxygen vacancy concentration estimated previously for the topmost $SrTiO_3$ layer (≈ 8%).

The mobile charge carrier concentrations estimated here are separately compared to the charge carrier concentrations measured in transport (see Sec. 6.2.2).

---

[7] Boundaries within which the χ^2 value deviates by less than 10% from the χ^2 value of the best fit.

4.2.11 The electrostatics at the $LaAlO_3/SrTiO_3$ interface

Let us next address the electrostatics at the $LaAlO_3/SrTiO_3$ interface our fitting routine yields. It is summarized in Fig. 4.14 for the fully oxidized state (blue lines) as well as at saturated O depletion (red lines).

The conduction band profiles are depicted in Fig. 4.14 (c). In both states the conduction bands are bent downward toward the interface creating a potential well in which the mobile electrons accumulate. At saturated O depletion the band bending at the interface is more pronounced than in the fully oxidized state: While the depth of the potential well amounts to $\approx 0.6\,\mathrm{eV}$ in the fully oxidized state, it increases to $\approx 1.0\,\mathrm{eV}$ at saturated O depletion. The increase in band bending under oxygen depletion is brought about by the oxygen vacancies which can be thought of as an interface dipole. Approaching the interface from the $SrTiO_3$ bulk, the interface dipole shifts the potential energy and therewith the binding energy. In Fig. 4.14 (c) we also sketch the ladder of subbands for the two states. In consequence of the varying characteristics of the potential well, the number and the binding energies of the subbands (as well as the corresponding eigenstates) differ considerably as a function of the V_O concentration.

Figure 4.14 (a) depicts the distribution of the mobile electrons released as a result of the electronic reconstruction as well as by oxygen vacancies. At first glance, one notices that the total mobile charge carrier concentration is considerably higher at saturated O depletion than in the fully oxidized state. The number n_er of electrons which are introduced by the electronic reconstruction is the same in both states: The disparity in the total number of mobile charge carriers is, instead, ascribed to the differing oxygen vacancy concentration in the two states. According to our assumptions, there are no oxygen vacancies in the fully oxidized state, whereas the oxygen vacancy concentration in the $SrTiO_3$ substrate is finite at saturated O depletion. In our model, each oxygen vacancy is assumed to release one mobile electron. Thus, the integral concentration of the surplus electrons [shaded red in Fig. 4.14 (a)] corresponds to the total oxygen vacancy concentration at saturated O depletion.

Scrutinizing the charge carrier profile in Fig. 4.14 (a), we note that the mobile charge carrier concentration is strongly confined and peaks close to the interface for both states. For a fair comparison of the charge carrier distributions, we normalize the charge carrier profiles by the respective total charge carrier concentration Q_total in Fig. 4.14 (b). This comparison shows that the 2DES is slightly more extended in the fully oxidized state than at saturated O depletion. The maximum of the charge carrier distribution is shifted by ≈ 2.5Å further into the $SrTiO_3$ bulk in the fully oxidized state. The charge carrier distribution in the fully oxidized state is furthermore characterized by a tail extending into the $SrTiO_3$ substrate [see arrow in Fig. 4.14 (b)] which is not present at saturated O depletion.

We conclude that the 2DES occupation and the 2DES extension react differently on changes in the V_O concentration: While the 2DES occupation is varying strongly between the two states, the 2DES extension, i.e., the charge carrier distribution in z direction, is barely depending on the V_O concentration. Thus, the question arises how this characteristic profile of the charge carrier concentration develops.

The electric field dependence of ϵ_r is at the heart of this issue. The z dependence of ϵ_r and of the electric field are depicted in Figs. 4.14 (d) and (e), respectively. Deep in the $SrTiO_3$ substrate the electric field is small and does, in particular, not differ between the two states [see dashed ellipses in Fig. 4.14 (e)]. This behavior is in line with our expectations, as in our experiment oxygen vacancies are only created in the topmost $SrTiO_3$ layers and thus should not disrupt the bands far away from the interface. The dielectric constant ϵ_r in the $SrTiO_3$ bulk accordingly also adopts high and, in particular, similar values in both states [see dashed ellipses in Fig. 4.14 (d)]. Toward the interface the electric field increases sharply in both states investigated which leads to a substantial decrease in the dielectric constant ϵ_r [see solid ellipses in Figs. 4.14 (d) and (e)].

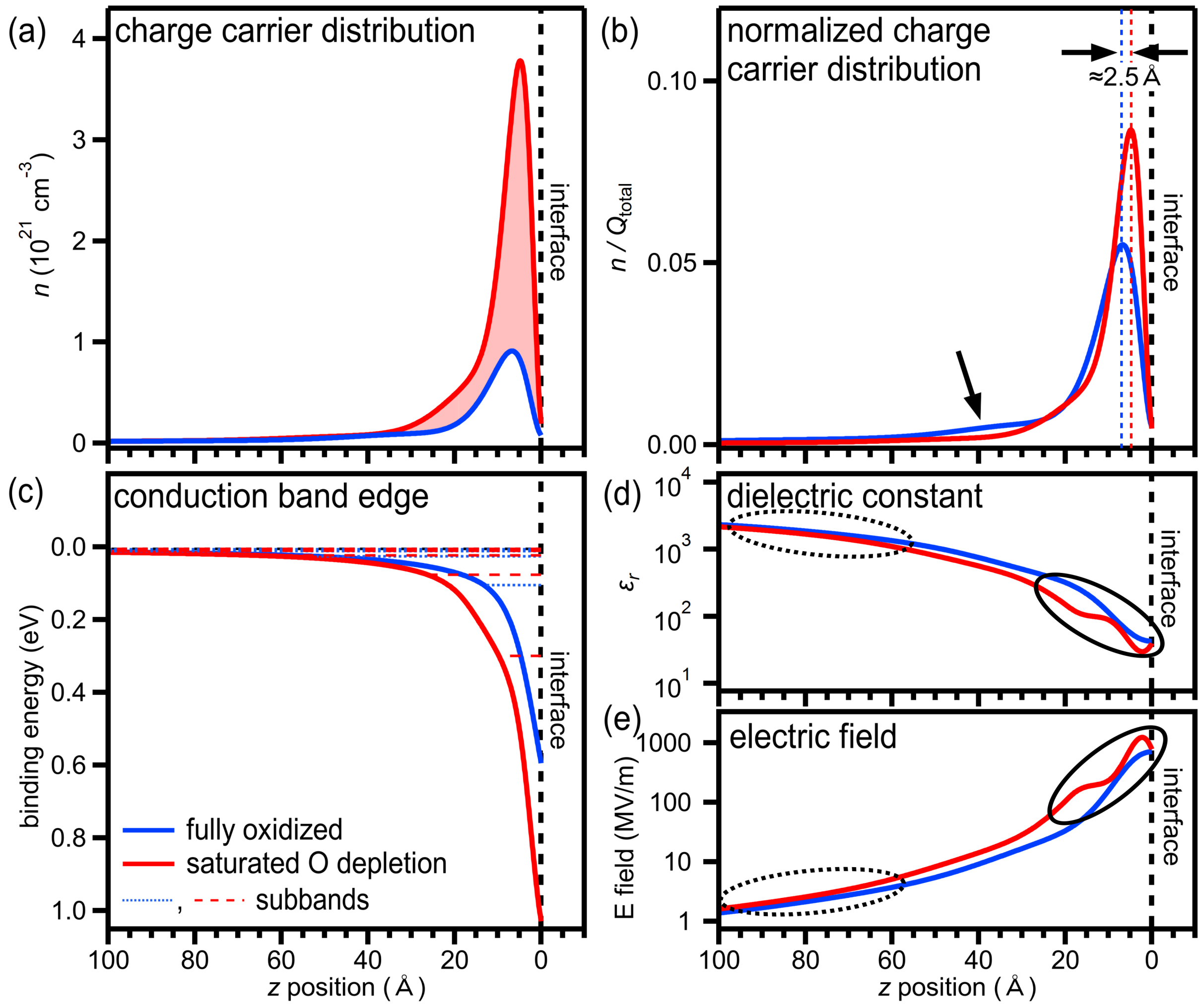

Fig. 4.14: The electrostatics at the (001)-oriented $LaAlO_3/SrTiO_3$ heterostructure in the fully oxidized state and at saturated O depletion: (a) Distribution of the mobile charge carriers. (b) Distribution of the mobile charge carriers normalized by the total mobile charge carrier concentration Q_{total}. (c) Conduction band profile with subband structure. (d) Profile of the dielectric constant. (e) Profile of the electric field. See text for discussion.

In the vicinity of the interface ϵ_r falls to only 40 – 70. The declining ϵ_r triggers the strong confinement of the electron gas at the interface. As the z dependence of ϵ_r is, on the whole, very similar in both states, the 2DES extension does barely depend on the V_{O} concentration.

However, close scrutiny of Fig. 4.14 (e) shows that overall the electric field is slightly higher at saturated O depletion (the red line lies always above the blue line). This is induced by the oxygen vacancies which release electrons. The oxygen vacancies are charged and increase the electric field toward the interface. Due to the elevated electric field, the dielectric constant is smaller near the interface at saturated O depletion. In consequence, the mobile charge carriers are more strongly confined to the interface at saturated O depletion. For the same reason, the band bending at the interface is more pronounced at saturated O depletion than in the fully oxidized state.

Having analyzed the band profile in the $SrTiO_3$ substrate, we turn to investigate the interfacial band alignment in the next section.

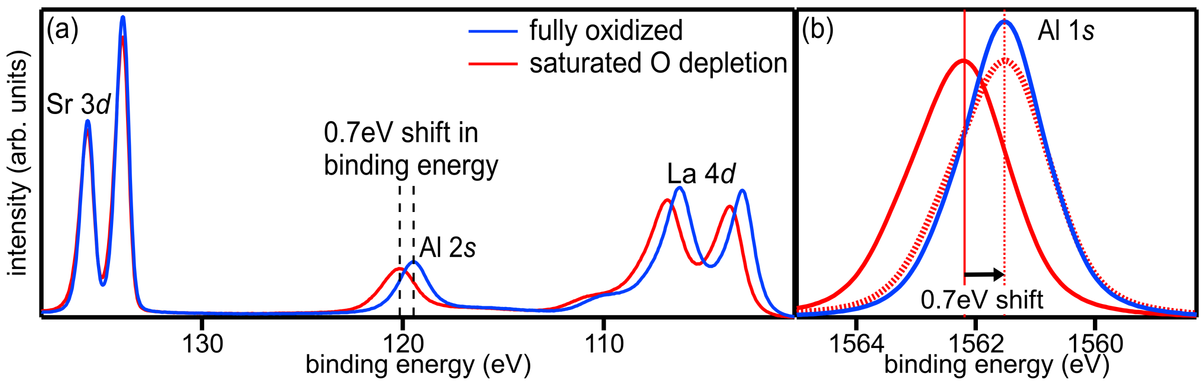

Fig. 4.15: Sr 3*d*, Al 2*s* and La 4*d* (a) and Al 1*s* (b) core level spectra of the (001) $LaAlO_3/SrTiO_3$ heterointerface in the fully oxidized state and at saturated O depletion. As a function of the V_O concentration we observe a pronounced shift in the binding energy of the *film* core levels. In (b) this shift in binding energy is exemplarily compensated for the oxygen-depleted state (see dashed line) to facilitate the comparison of the spectral shapes in the fully oxidized state and at saturated O depletion.

4.3 The interfacial band alignment

The physical properties of a heterojunction are largely determined by the alignment of the valence and conduction band between the constituent materials.[1,161] Depending on the band offsets at the interface, heterostructures can find use in diverse applications as, e.g., in electronics, photocatalysis or photovoltaics. For such device applications it is, in particular, crucial that one is not only able to track the alignment of the bands at the interface but one is able to engineer it as well. In the following we thus investigate whether the interfacial band alignment in the $LaAlO_3/SrTiO_3$ heterostructure can be tuned by the V_O concentration in the sample.

4.3.1 Analyzing the film core level shift

Angle-integrated HX La 4*d* and Al 2*s* as well as Al 1*s* spectra are depicted in Fig. 4.15 (a) and (b), respectively. Depending on the V_O concentration the absolute binding energy of the film core levels is clearly varying. In the SX measurement series discussed in Sec. 3.5 we have already made similar observations for the SXPES La 4*d* and Al 2*s* core level spectra.[8]

We note in passing that the spectral shape of the film core level lines also changes slightly as a function of the V_O concentration [compare blue solid and red dotted line in Fig. 4.15 (b)]. However, this variation in spectral shape is eclipsed by the changes in binding energy. In a first approximation we thus ignore the changes in spectral shape, assume that the bands in the $LaAlO_3$ film are flat at either V_O concentration and only analyze the variations in the binding energy of the film core levels.

Scrutinizing the core levels of the $LaAlO_3$ film in the fully oxidized state and at saturated O depletion, we can draw conclusions about the changes in the band alignment at the interface: When the binding energy of the valence band in the $LaAlO_3$ film varies, the binding energy of the Al and La core levels has to shift by the same amount. Within the flat band scenario the valence band offset can thus be determined quantitatively by analyzing the binding energy

---

[8] A more detailed quantitative comparison between the HXPES study and the SXPES measurement series is, however, precluded: The samples investigated in chapter 3 and 4 differ in their mobile charge carrier concentration in the fully oxidized state. Moreover, the oxygen-depleted states prepared in the samples vary as well because the irradiation dose as well as the incidence angle of the x-ray beam was set to different values in the two measurement series.

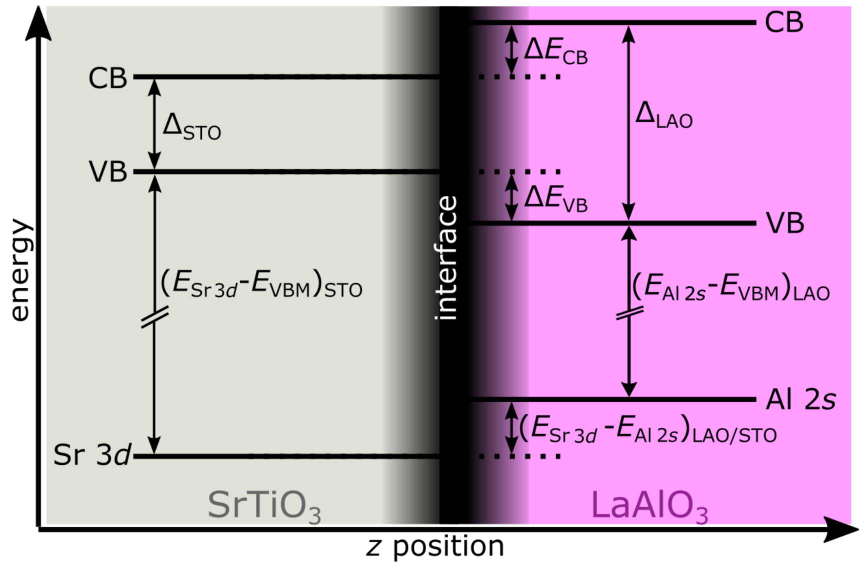

Fig. 4.16: The figure illustrates how the valence band offset is determined by analyzing the binding energy of the valence band maximum and selected core levels in $LaAlO_3/SrTiO_3$ heterostructures and in $LaAlO_3$ and $SrTiO_3$ reference samples. The binding energy differences are not drawn to scale.

difference between selected core levels and the valence band maximum (VBM) in $LaAlO_3$ and $SrTiO_3$ reference samples as well as in the $LaAlO_3/SrTiO_3$ heterostructure.[162] The $SrTiO_3$ and $LaAlO_3$ reference spectra are recorded at the same photon energy under oxygen dosing on a $SrTiO_3$ substrate and a 20 uc thick $LaAlO_3/SrTiO_3$ heterostructure, respectively. According to the scheme depicted in figure 4.16, the valence band offset ΔE_{VB} and conduction band offset ΔE_{CB} are calculated as follows

$$\Delta E_{\mathrm{VB}} = (E_{\mathrm{Sr}\,3d_{5/2}} - E_{\mathrm{VBM}})_{\mathrm{STO}} - (E_{\mathrm{Al}\,2s} - E_{\mathrm{VBM}})_{\mathrm{LAO}} - (E_{\mathrm{Sr}\,3d_{5/2}} - E_{\mathrm{Al}\,2s})_{\mathrm{LAO/STO}}, \tag{4.7}$$

$$\Delta E_{\mathrm{CB}} = \Delta_{\mathrm{LAO}} - \Delta_{\mathrm{STO}} - \Delta E_{\mathrm{VB}}, \tag{4.8}$$

where $(E_x)_y$ denotes the binding energy of feature x in the compound y and $\Delta_{\mathrm{LAO}} = 5.6\,\mathrm{eV}$[99] and $\Delta_{\mathrm{STO}} = 3.6\,\mathrm{eV}$[9] describe the band gaps of $LaAlO_3$ and $SrTiO_3$, respectively. The valence band offsets estimated by this method are specified in the topmost row of Tab. 4.3. Before we examine these results in detail, we first determine the valence band offsets by a second method.

4.3.2 Analyzing the valence band spectra

Let us turn to the HXPES valence band spectra. Due to the low photoemission cross section of the Ti 3d states in this energy regime, we do not observe any spectral weight near the Fermi level.[109] Nevertheless, it is worth analyzing the O 2p-like valence band in more detail as the spectra can yield information about the band alignment at the interface: Probing the valence band with hard x-rays, the inelastic mean free path of the photoelectrons is high ($\lambda_{\mathrm{IMFP}} \approx 45\,\text{Å}$ according to ref. [27–29]). The valence band spectra are thus composed of sizable signal originating from the $LaAlO_3$ film as well as from the $SrTiO_3$ substrate. A change in the valence band alignment thus becomes directly apparent in the valence band spectra of the $LaAlO_3/SrTiO_3$ heterostructure. Figure 4.17 (a) depicts the valence band spectra of the $LaAlO_3/SrTiO_3$ heterostructure in the two different states.

---

[9] Value estimated from valence band spectra of $SrTiO_3$ reference sample.

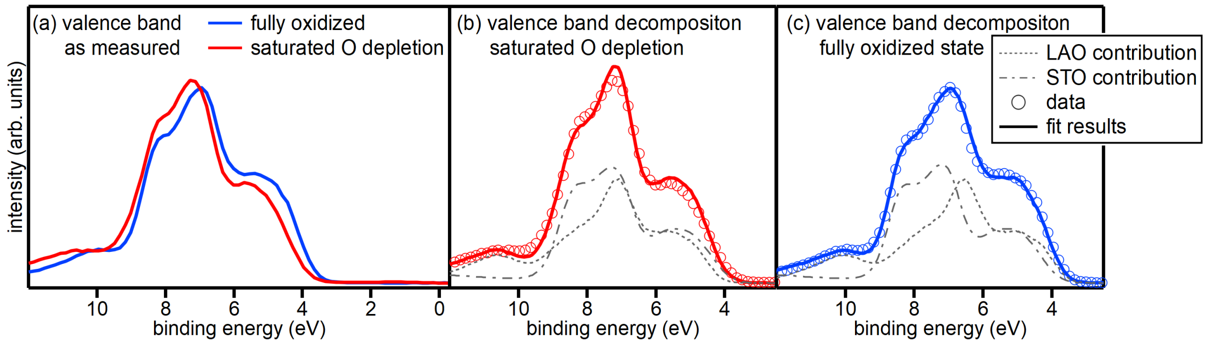

Fig. 4.17: Valence band spectra for the fully oxidized state and at saturated O depletion: (a) Comparison between the valence band spectra measured for the two different states. (b) and (c) Measured data and fit of the valence band spectrum at saturated O depletion and in the fully oxidized state, respectively. The respective decomposition of the valence band spectrum into the $LaAlO_3$ and $SrTiO_3$ contributions is shown as well in (b) and (c).

Clearly, the valence band spectra recorded at saturated O depletion and in the fully oxidized state differ which reveals that the band alignment is changing with the V_O concentration. To put a figure on the valence band alignment at the interface, we fit the valence band spectrum of the heterostructure with the bulk valence band spectra of the constituent materials:

Within the flat band picture, we assume that the spectral shape of the valence band signal originating from the $LaAlO_3$ layer does not depend on the $LaAlO_3$ film thickness. The $LaAlO_3$ contribution $VB_{LAO}(E)$ to the valence band spectra is thus modeled by the $LaAlO_3$ reference spectrum which may just be shifted in binding energy by ΔE_{LAO} to account for a possible change in band alignment at the interface of the $LaAlO_3/SrTiO_3$ heterostructure. The binding energy shift ΔE_{LAO} is corresponding to the valence band offset ΔE_{VB}.

It is a bit more intricate to work out the $SrTiO_3$ contribution $VB_{STO}(E)$ to the valence band spectra: While the spectra of the fully oxidized $SrTiO_3$ substrate are not affected by band bending, the spectra of the $LaAlO_3/SrTiO_3$ heterostructure are. As in our previous model we thus have to build up the $SrTiO_3$ contribution $VB_{STO}(E)$ layer-by-layer. We assume that each $SrTiO_3$ layer contributes with the valence band signal of the $SrTiO_3$ reference which is, however, shifted in binding energy according to the band bending profile analyzed previously (and also damped). The Fermi level in the $SrTiO_3$ band gap might furthermore be pinned at a different energy in the $LaAlO_3/SrTiO_3$ heterostructure than in the $SrTiO_3$ substrate. We thus also allow for an overall binding energy shift ΔE_{STO} of the $SrTiO_3$ valence band signal.

The valence band spectrum $VB_{LAO/STO}(E)$ of the 4 uc $LaAlO_3/SrTiO_3$ heterostructure is then described with the following relation

$$VB_{LAO/STO}(E) = A \cdot VB_{STO}(E - \Delta E_{STO}) + (1 - A) \cdot VB_{LAO}(E - \Delta E_{LAO}). \tag{4.9}$$

The parameter A specifies the relative contribution of the $SrTiO_3$ and the $LaAlO_3$ valence band spectrum. To reduce the number of fit parameters, we once again fit the valence band spectra of both states simultaneously in a global fitting scheme in which A and ΔE_{STO} are set to the same values in both states.

A comparison of fits and measured spectra is depicted in Figs. 4.17 (b) and (c) at saturated O depletion and for the fully oxidized state, respectively. In Figs. 4.17 (b) and (c) the valence band spectra are also decomposed into their $SrTiO_3$ and $LaAlO_3$ contributions. We note that in the fully oxidized state the onset of the $LaAlO_3$ valence band contribution lies at lower binding energy than the onset of the $SrTiO_3$ valence band contribution, while it is the other way round at saturated O depletion [compare onset of dashed and dotted lines in Figs. 4.17 (b) and (c)].

analysis method	**ΔE_{VB} fully oxidized state**	**ΔE_{VB} saturated O depletion**
core level analysis	(+0.14±0.2) eV	(–0.58±0.2) eV
valence band analysis	(+0.13±0.2) eV	(–0.43±0.2) eV

Tab. 4.3: Valence band offset ΔE_{VB} at the (001) $LaAlO_3/SrTiO_3$ heterointerface in the fully oxidized state and at saturated O depletion. The valence band alignment is estimated by analyzing the binding energy difference between the valence band maximum and selected core levels (labeled core level analysis) as well as by fits of the valence band (labeled valence band analysis).

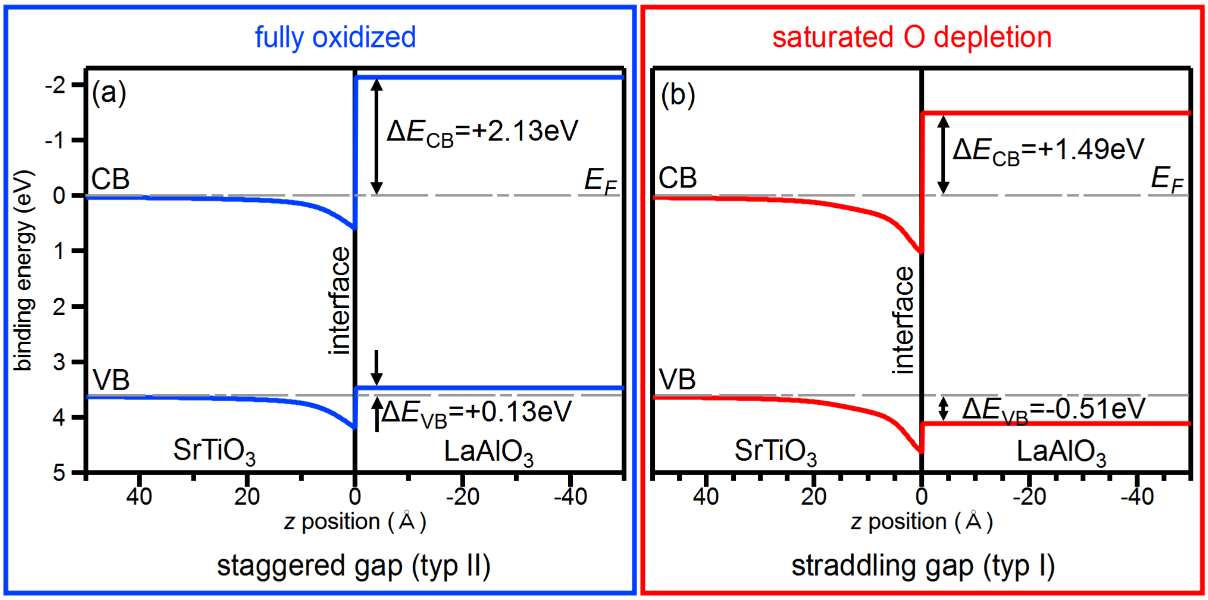

Fig. 4.18: Band diagrams of the (001)-oriented $LaAlO_3/SrTiO_3$ heterostructure in the fully oxidized state (blue) and at saturated O depletion (red). The heterojunction between $LaAlO_3$ and $SrTiO_3$ changes from a staggered gap to a straddling gap arrangement as a function of V_{O} concentration.

This observation shows that the $LaAlO_3$ valence band contribution significantly shifts in binding energy as a function of the V_{O} concentration. This is also reflected in the resulting valence band offsets ΔE_{VB} which are specified in the bottom row of Tab. 4.3.

Before moving on to discuss the interfacial band alignment, let us briefly comment on the fit result for ΔE_{STO}: The overall binding energy shift of the $SrTiO_3$ valence band signal amounts to $\Delta E_{\mathrm{STO}} = 0.06\,\mathrm{eV}$. We conclude that the Fermi level does barely shift when a $LaAlO_3$ film is deposited on the $SrTiO_3$ substrate. The Fermi edge remains pinned just below the Ti $3d$ density of states in the $SrTiO_3$ substrate confirming that the band filling in the heterostructure is small ($d^{0+\delta}$). This observation is in accordance with our previous results: When the Fermi level shifts within the $SrTiO_3$ band gap, the binding energy of the core levels has to shift by the same energy. In Figs. 4.4 (a) and (b) we saw that the binding energy of the Sr $3d$ and Ti $2p$ core levels in the $SrTiO_3$ substrate and the $LaAlO_3/SrTiO_3$ heterostructure is very similar.

4.3.3 The resulting band diagram

In the last sections we analyzed the valence band offset employing two different methods. The outcomes of the two methods are compared in Tab. 4.3 and agree within their error bars.[10] The

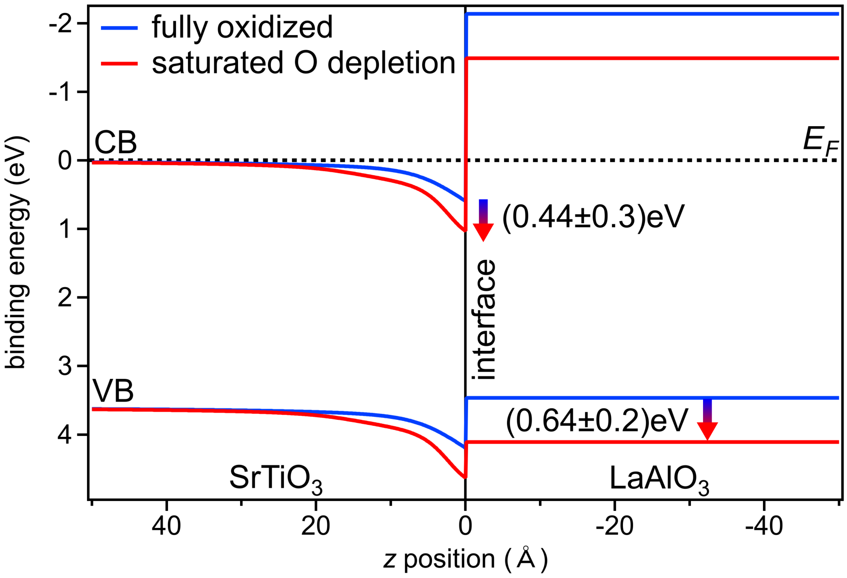

Fig. 4.19: Band diagram of the (001)-oriented $LaAlO_3/SrTiO_3$ heterostructure in the fully oxidized state and at saturated O depletion. The valence band edge in the $LaAlO_3$ film shifts concomitantly to the $SrTiO_3$ valence band edge at the interface. In other words, the offset between the valence band edge of $LaAlO_3$ and $SrTiO_3$ *right at the interface* does not vary. A change in band bending consequently triggers a change in the valence band offset as the valence band offset is defined as the alignment between the valence bands of *bulk* $SrTiO_3$ and $LaAlO_3$.

resulting band diagrams for the fully oxidized state and at saturated O depletion are sketched in Fig. 4.18. The band diagram clearly illustrates what has already become apparent in the valence band decomposition in the previous section: The valence band edge of the $LaAlO_3$ film lies above the valence band edge of the $SrTiO_3$ bulk in the fully oxidized state, while this order is reversed at saturated O depletion. Consequently, the heterojunction between $LaAlO_3$ and $SrTiO_3$ changes from a staggered gap (type II interface) to a straddling gap arrangement (type I interface) as a function of increasing V_{O} concentration. In Tab. 4.3, this change manifests itself in the sign change in the valence band offset ΔE_{VB} between the fully oxidized and oxygen-depleted state.

Figure 4.19 contrasts the variations in valence band offsets between the two states to the corresponding variations of the confining potential at the interface which was estimated previously. We note that within our accuracy[10] the values obtained agree (see arrow markings in Fig. 4.19). This suggests that the valence band edge of the $LaAlO_3$ film shifts concomitantly to the valence band edge of the $SrTiO_3$ *at the interface*. In other words, the offset between the band edges of $LaAlO_3$ and $SrTiO_3$ *right at the interface* is fixed.

In the fully oxidized state a specific valence band offset is established. When oxygen vacancies are created in the $SrTiO_3$ substrate, an interface dipole forms which alters the potential trough and, in consequence, the conduction and valence band slopes in the $SrTiO_3$ substrate. As a result of the fixed band alignment at the very $LaAlO_3/SrTiO_3$ interface, the $LaAlO_3$ band edges shift as well and the band offsets at the interface vary accordingly. As the valence band offset is, however, defined as the alignment between the valence bands of *bulk* $SrTiO_3$ and $LaAlO_3$, the change in band bending triggers the change in the valence band offset.

As oxygen atoms in the film as well as in the substrate contribute to the O 1s signal, we also put our band diagram to the test by fitting the O 1s spectra. The analysis of the O 1s spectra

---

[10] The error margins in the band bending are determined based on the error margins in the Poisson-Schrödinger fits. The error margins in the valence band offsets are estimated taking into account the accuracy of our analysis method.

is described in detail in the Appendix in Sec. B.5. Here it suffices to say that the analysis of the O 1*s* spectra corroborates the band diagram depicted in Fig. 4.19.

4.4 The potential profile in the $LaAlO_3$ film

Lastly, we scrutinize the film core level spectra to look for a possible potential gradient in the $LaAlO_3$ overlayer.

Figure 4.20 (a) shows the angle-integrated Al 1*s* and La 4*d* spectra measured in the fully oxidized state and at saturated O depletion (see blue and red solid lines). In the preceding section we have already addressed the binding energy shift in the film core levels which is observed upon O depletion. However, close scrutiny of Fig. 4.20 (a) reveals that not only is the binding energy of the core level spectra changing along with the V_O concentration but their spectral shape is varying as well. To facilitate the comparison of the spectral shape, the spectra of the oxygen-depleted state are shifted in binding energy shift and aligned to the spectra of the fully oxidized state in Fig. 4.20 (a) (see dashed lines). Note that we have to use slightly different binding energy shifts to align the Al 1*s* and La 4*d* core level spectra [see annotations in Fig. 4.20 (a)]. The Al 1*s* as well as La 4*d* spectra recorded at saturated O depletion are found to be broadened. As the spectral shape changes alike for the Al 1*s* as well as for the La 4*d* core levels under oxygen depletion, we tentatively conclude that the variations can be traced back to a common origin, i.e., a change in the potential profile in the $LaAlO_3$ film.

4.4.1 The electron emission angle dependence of the film core level spectra

To get to the bottom of the variations in spectral shape, the dependence of the film core levels on the electron emission angle is scrutinized next. For this purpose, we analyze the binding energy of the Al 1*s* and La $4d_{5/2}$ core levels across the electron emission angle of the wide angle lens. The results of this analysis are depicted in Fig. 4.20 (b). The average binding energy of the core levels in the fully oxidized state is chosen as the reference point. The analysis confirms that the binding energy of the film core levels is varying upon oxygen depletion, as already discussed in previous sections (see offset between red and blue lines).

Moreover, Fig. 4.20 (b) reveals that, in the fully oxidized state, the binding energy does not depend on the electron emission angle (see blue lines). We conclude that the bands in the $LaAlO_3$ film are flat in the fully oxidized $LaAlO_3/SrTiO_3$ heterostructure.

In contrast, at saturated O depletion the binding energy varies as a function of the electron emission angle (see red lines). This finding also clarifies why the electron-emission-angle-integrated Al 1*s* and La 4*d* core level spectra are broadened at saturated O depletion. Based on these observations, we infer that a potential is building up in the $LaAlO_3$ film under oxygen depletion. The binding energy of the film core levels is higher at large electron emission angles than at small electron emission angles which shows that the bands are bent toward higher binding energies from the interface to the surface.

Let us next discuss the potential profile in the $LaAlO_3$ film in the fully oxidized state and at saturated O depletion.

4.4.2 Modeling the potential profile in the $LaAlO_3$ film

The $LaAlO_3$ bands are found to be flat in the fully oxidized $LaAlO_3/SrTiO_3$ heterostructure, in contradiction to the simple electronic reconstruction picture.[108] This observation can be explained by a modified electronic reconstruction picture in which defect states as, e.g., oxygen vacancies at the $LaAlO_3$ surface act as the charge reservoir for the interface.[109,116,138]

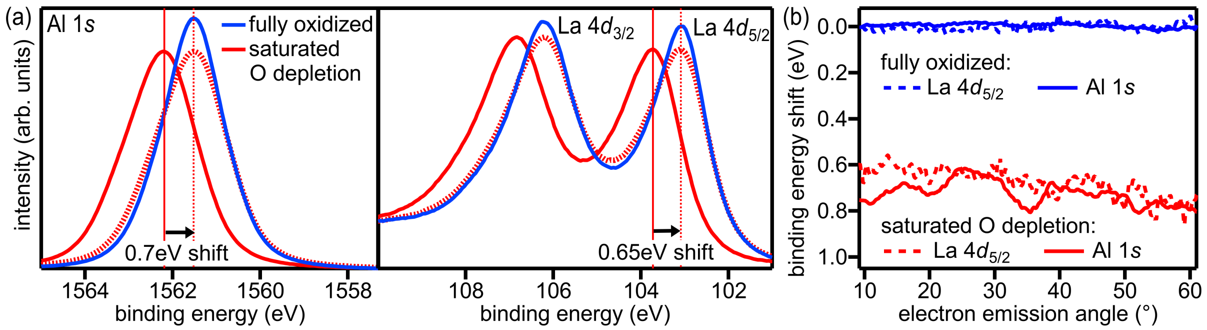

Fig. 4.20: Analyzing the core level spectra of the $LaAlO_3$ film: (a) Angle-integrated Al $1s$ and La $4d$ spectra in the fully oxidized state and at saturated O depletion. As a function of the V_O concentration not only the binding energy but also the spectral shape of the film core level changes. (b) Binding energy of the Al $1s$ and La $4d_{5/2}$ core levels as a function of the electron emission angle in the fully oxidized state and at saturated O depletion. The binding energy is compared to the average binding energy in the fully oxidized state.

We also exclude that the potential build-up in the oxygen-depleted state is due to the electronic reconstruction: The bands in the $LaAlO_3$ film are found to bend toward higher binding energies from the interface to the surface and not toward lower binding energies as expected in the electronic reconstruction scenario. The bands are only found to be bent across the $LaAlO_3$ film under oxygen depletion. It thus stands to reason that the oxygen vacancies forming in the $LaAlO_3$ film are charged and give rise to the potential across the $LaAlO_3$ film. To test this assumption, we construct a hypothetical distribution of positively charged oxygen vacancies in the $LaAlO_3$ film and analyze its effects on the binding energies of the Al $1s$ and La $4d_{5/2}$ core levels as described in the following.

In the previous chapter (cf. Sec. 3.5.3) we speculated that the oxygen depletion induces a linear gradient of oxygen vacancies in the $LaAlO_3/SrTiO_3$ heterostructure. Here, the number of oxygen vacancies is thus assumed to be maximal at the $LaAlO_3$ surface and decreases linearly toward the interface where it reaches zero [see sketch in Fig. 4.21 (a)]. According to Poisson's equation, the potential and the valence and conduction band profile is consequentially changing with z^3 in the $LaAlO_3$ film where z describes the distance from the interface. Note that this model assumes that there are no oxygen vacancies in the $SrTiO_3$ substrate. Presumably, the measured data can also be fitted by a more sophisticated model containing oxygen vacancies in the $SrTiO_3$ substrate. However, the inclusion of oxygen vacancies in the $SrTiO_3$ substrate would introduce more free parameters, viz. z^2 terms, in our model of the potential and make it ultimately less reliable. For a rough first approximation of the potential in the $LaAlO_3$ film we thus assume that the oxygen vacancy concentration decreases to zero at the $LaAlO_3/SrTiO_3$ heterointerface.

Under oxygen depletion the binding energy of the film core levels does not only shift in response to the potential building up in the $LaAlO_3$ film but may also change as the interfacial valence band offset is varying as discussed in the previous sections. To include this effect in our model, we introduce a further parameter, viz. an offset ΔE, which describes the change in the interfacial valence band offset between the fully oxidized and the oxygen-depleted state [see illustration in Fig. 4.21 (b)].

On the basis of the conjectured valence band profile in the $LaAlO_3$ film, we model the Al $1s$ and La $4d_{5/2}$ spectra building them up layer-by-layer: Since flat band behavior is observed in the fully oxidized state, we use the spectra measured under oxygen dosing [see blue spectra in Fig. 4.20 (a)] as reference spectra to simulate the Al $1s$ and La $4d$ signals originating from the single AlO_2 and LaO layers in the $LaAlO_3$ film. The spectra originating from the single layers

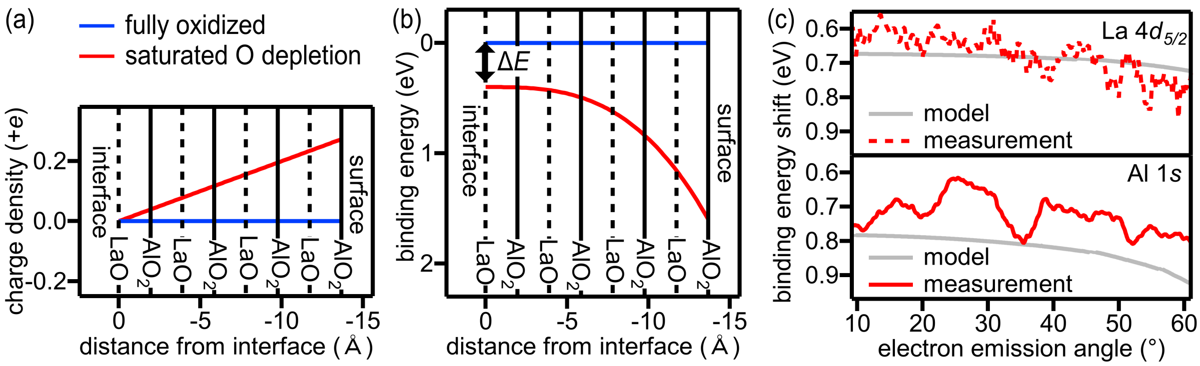

Fig. 4.21: Modeling the potential profile in the $LaAlO_3$ film: (a) Model of the charge distribution in the $LaAlO_3$ film. (b) Resulting model of the valence band profile in the $LaAlO_3$ film. (c) Measured and modeled electron emission angle dependence of the La $4d_{5/2}$ (top panel) and Al $1s$ (bottom panel) binding energy at saturated O depletion. The agreement between data and model is satisfactory for the La $4d_{5/2}$ core level but poor for the Al $1s$ core level.

are subsequently shifted in binding energy by the value of the valence band edge at these layers and attenuated according to the respective inelastic mean free path of the photoelectrons and the position of the layers.

Finally the electron emission angle dependence of the Al $1s$ and La $4d_{5/2}$ binding energy is analyzed just as in the measured spectra. The valence band profile, i.e., the oxygen vacancy distribution and the interfacial valence band offset are iteratively adapted until the electron emission angle dependence of the Al $1s$ and La $4d_{5/2}$ binding energy depicted in Fig. 4.20 (b) can be adequately reproduced. In Figs. 4.21 (a) and (b) we sketch the charge profile and the valence band profile in the $LaAlO_3$ overlayer which yields the best fit to the binding energy shifts measured. The top and bottom panel in figure 4.21 (c) compare the measured and modeled electron emission angle dependence of the La $4d_{5/2}$ and Al $1s$ binding energy at saturated O depletion, respectively. The agreement between the measured data and the model is satisfactory for the La $4d_{5/2}$ core level[11] but poor for the Al $1s$ core level which is addressed in the next section.

Our modeling uncovers why the shifts in binding energy under oxygen depletion differ for the Al $1s$ and La $4d$ core levels [see shifts labeled in Fig. 4.20 (a)]: In Fig. 4.21 (b) we mark by dotted and solid lines where the potential is read out for the LaO and AlO_2 layers, respectively. With the potential changing across the $LaAlO_3$ film, the potential read out for the AlO_2 and the LaO layers in the same unit cell differs. In consequence, different results are obtained for the absolute binding energy shift observed for the Al $1s$ and La $4d$ core levels. Note that we have also observed this effect in the SX measurement series in the previous chapter: Upon oxygen depletion the binding energy shift in the Al $2s$ core level is always slightly larger than the binding energy shift in the La $4d$ core level [see Fig. 3.15 (b)].

In our model the binding energy of the Al $1s$ and La $4d_{5/2}$ core levels differs across the entire electron emission angle range in the oxygen-depleted state [compare modeled binding energy shift in top and bottom panel of Fig. 4.21 (c)]. However, we note that in the measurements the binding energy shifts of the Al $1s$ core level are fluctuating strongly across the electron emission angle range and are, conspicuously, almost always smaller than the modeled binding energy shifts [compare measurements and model in bottom panel of Fig. 4.21 (c)]. This discrepancy is ascribed to x-ray photoelectron diffraction (in short XPD) as explained in the next section.

---

[11] Employing more sophisticated models for the oxygen vacancy distribution in the $LaAlO_3$ film the agreement between the measured data and the model could presumably be improved. We refrain from adapting our model of the oxygen vacancy distribution because it would introduce many more free parameters.

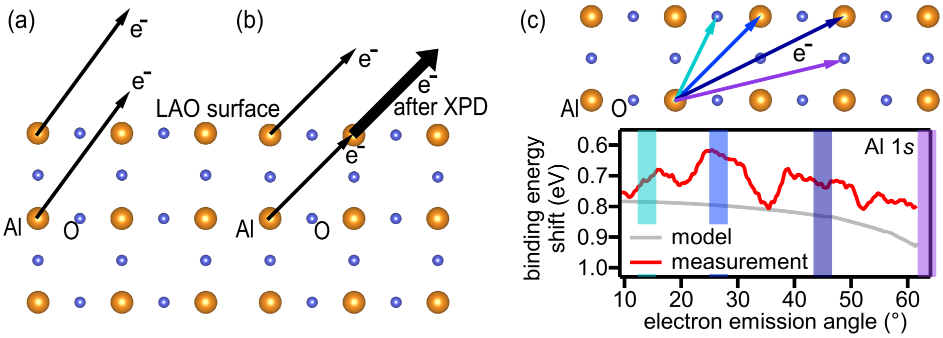

Fig. 4.22: Diffraction of Al 1*s* photoelectrons in the LaAlO$_3$ film: Depending on the electron emission angle, Al 1*s* photoelectrons from subsurface AlO$_2$ layers pass unhinderedly through the crystalline LaAlO$_3$ overlayer (a) or scatter at atoms on their way to the sample surface (b). The scattering processes enhance the photoemission signal originating from the subsurface layers. The top panel in (c) illustrates at which electron emission angles XPD may become relevant in our experimental setup. The bottom panel in (c) compares the measured and modeled variations in the Al 1*s* binding energy at saturated oxygen depletion. The deviations between the data and the model are pronounced at the electron emission angles marked in the top panel.

4.4.3 Photoelectron diffraction in the LaAlO$_3$ film

Photoelectrons traveling through the sample may encounter atoms on their way to the surface. At high kinetic energies the photoelectrons are focused forward in such encounters, which enhances the photoemission intensity at this very angle.[21] To evade the effects of XPD, we typically do not investigate how the intensity of core level lines changes with the electron emission angle but rather analyze the binding energy and spectral shape of the core level lines, which are not altered by XPD. However, probing the binding energy of the film core levels XPD effects might become relevant in an indirect manner as explained in the following.

The Al 1*s* photoemission signal originates from Al atoms in the topmost AlO$_2$ layer and from Al atoms in the three subsurface AlO$_2$ layers. Depending on the electron emission angle, we have to distinguish two cases when describing the photoemission from Al atoms. In the first case depicted in Fig. 4.22 (a) the Al 1*s* photoelectrons are emitted along an angle at which they all can unhinderedly travel through the crystalline LaAlO$_3$ overlayer without encountering any atoms. At such geometries we can assume that the signal intensity from subsurface layers is damped according to the inelastic mean free path of the photoelectrons and can apply our typical inelastic mean free path model to describe the photoemission intensity (cf. equation (2.28)). However, this model does no longer apply at other angles, such as at the geometry sketched in Fig. 4.22 (b): Al 1*s* photoelectrons which are emitted from the topmost film layer still leave the sample unhinderedly whereas Al 1*s* photoelectrons emitted from subsurface layers may scatter at atoms on their way to the surface. In consequence, the photoemission intensity from the subsurface layers is enhanced while the photoemission intensity from the topmost layer does not change [see thick and thin arrows in Fig. 4.22 (b)].

As soon as the binding energy of the Al 1*s* core level is varying across the LaAlO$_3$ film, the intensity modulation by XPD becomes relevant: At geometries such as the one depicted in Fig. 4.22 (a) the binding energy recorded varies smoothly with the electron emission angle and is adequately described by our typical inelastic mean free path model. At geometries such as the one sketched in Fig. 4.22 (b) the binding energy measured is, in contrast, deviating from our typical model and abruptly shifted toward the binding energy of the subsurface layers as the photoemission intensity from the subsurface layers is disproportionately enhanced. In our experiments this effect is of particular significance as only four AlO_2 layers contribute to the integral photoemission signal.

To test whether XPD indeed provokes the fluctuations in the Al $1s$ binding energy over the electron emission angle at saturated O depletion, we take a look at the crystal structure of our samples and compute at which angles XPD becomes relevant in our experimental setup. Taking into account the orientation of our sample with respect to the analyzer slit, we have to determine at which angles a photoelectron emitted from an Al atom might scatter at atoms in the (001) crystal plane. The top panel of Fig. 4.22 (c) shows the relevant crystal plane and illustrates at which angles XPD effects may become relevant. The bottom panel in Fig. 4.22 (c) again displays the measured and modeled shifts of the Al $1s$ binding energy at saturated O depletion. Additionally, we mark the angles at which XPD may become relevant. We note that at these angles the measured Al $1s$ binding energy is indeed deviating from the model and shifted toward lower binding energy, i.e., toward the binding energy of the subsurface layers. In between these angles the binding energy shift measured approaches the modeled binding energy shift. We note in passing that the Al $2s$ binding energy shows similar fluctuations across the electron emission angle (data not shown), confirming our interpretation.

Our reasoning about the effect of XPD is further corroborated by the fact that we only observe pronounced fluctuations in binding energy over the electron emission angle for the Al core levels, while the binding energy of the La $4d$ core levels varies more smoothly at saturated O depletion: Describing the electron emission angle dependence in La spectra we still have to distinguish between the two cases depicted in Figs. 4.22 (a) and (b). However, as all LaO layers are subsurface layers, the photoemission signal originating from all LaO layers is modulated in a similar way by XPD. In geometries as the one depicted in Fig. 4.22 (b), the photoemission intensity from *all* layers is thus enhanced. The top layer is no longer singled out and the binding energy shift measured can again be described by the inelastic mean free path model. We note in passing that such photoelectron diffraction effects are not relevant in the substrate core level measurements for the very same reason.

Owing to the photoelectron diffraction we cannot adequately model the electron emission angle dependence of the Al $1s$ binding energy. However, the fact that the binding energy of the Al $1s$ core level is strongly modulated by XPD effects in the oxygen depleted state confirms the potential build-up in the $LaAlO_3$ film. Recall that the fluctuations in the Al $1s$ binding energy only emerge when the binding energy in the $LaAlO_3$ film varies.

Let us finally refine the band diagram of the $LaAlO_3/SrTiO_3$ heterointerface based on the new results.

4.4.4 Refining the band diagram

In Sec. 4.3.3 we put forward a band diagram of the $LaAlO_3/SrTiO_3$ heterointerface in the fully oxidized state and at saturated O depletion. Estimating the valence band alignment, we assumed that the bands in the $LaAlO_3$ are flat. However, in the preceding section we saw that in the oxygen-depleted state the energy bands in the $LaAlO_3$ film are actually bent. The potential build-up in the $LaAlO_3$ film induces an overall binding energy shift in the $LaAlO_3$ valence band and core levels. Working with a flat band model, the valence band offset at saturated O depletion has thus been overestimated. Taking into account the newly established valence band profiles in the $LaAlO_3$ film [see Fig. 4.21 (b)], we refine our band diagram and depict it in Fig. 4.23.

We find that the difference in band bending between the two sample states now matches even better to the difference in the valence band offset at the interface (see arrows in Fig. 4.23). This result further solidifies our hypothesis that the band alignment right at the interface is fixed.

Let us next comment on the profile of positive charges which our modeling yields for the oxygen-depleted state [see Fig. 4.21 (a)]. The number of positive charges amounts to $+0.27 \cdot e$ at the

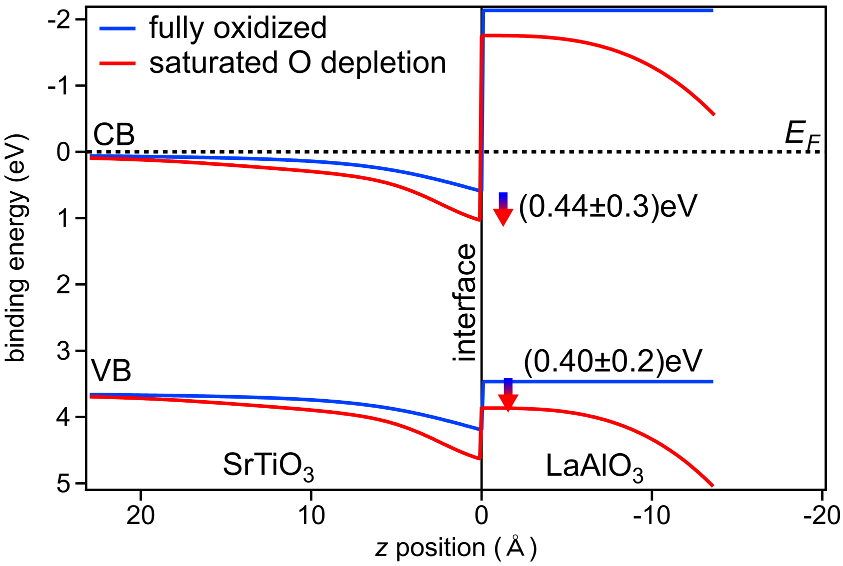

Fig. 4.23: Refined band diagram of the (001)-oriented $LaAlO_3/SrTiO_3$ heterostructure in the fully oxidized state and at saturated O depletion. The doping, as well as the band alignment and the band bending in the $SrTiO_3$ substrate and the $LaAlO_3$ film are all changing as a function of the oxygen vacancy concentration.

$LaAlO_3$ surface. To check our model for plausibility, we compare the profile of positive charges to the oxygen vacancy profile estimated in the previous chapter (see Sec. 3.5.3) where we estimated the oxygen vacancy concentration at the $LaAlO_3$ surface at 16%. We find that the two concentrations match in order of magnitude which corroborates our hypothesis that the oxygen vacancies in the $LaAlO_3$ film are positively charged and induce the potential build-up. An in-depth comparison between the models cannot be made as the two profiles were inferred for two different samples at two different V_O concentrations.

The finding that the potential build-up in the $LaAlO_3$ film at saturated O depletion is induced by positively charged oxygen vacancies prompts the question after the whereabouts of the electrons which are released by the oxygen vacancies. Just as the oxygen vacancies at the $LaAlO_3$ surface are suggested to act as a charge reservoir for the 2DES in the fully oxidized state,[116] the oxygen vacancies forming in the $LaAlO_3$ film under O depletion could dope additional mobile electrons into the interfacial 2DES.

Note that such a scenario does not contradict the results of the oxygen dosing experiments in previous chapter: In the previous chapter we identified the concomitant increase in QP and IG weight observed under oxygen depletion with oxygen vacancies being created exclusively in the $SrTiO_3$ substrate. Our observations can, however, also be reconciled with a model in which oxygen vacancies are created simultaneously in the $LaAlO_3$ film and in the $SrTiO_3$ substrate: If the number of oxygen vacancies in the $LaAlO_3$ film and in the $SrTiO_3$ substrate *continually increases in the same proportion*, the QP and IG weight would also rise concomitantly, even though electrons released by oxygen vacancies in the $SrTiO_3$ substrate as well as in the $LaAlO_3$ film contribute to the QP weight. Simulating such a scenario we would, however, have to modify our Poisson-Schrödinger ansatz as upon oxygen depletion mobile charge carriers are not only released by oxygen vacancies in the $SrTiO_3$ substrate but also by oxygen vacancies in the $LaAlO_3$ film. Since such a model would contain too many unknown parameters, we do not follow up on this ansatz. However, one can safely assume that the overall results of the simulations would largely stay the same as only the charge reservoir releasing mobile electrons would slightly change.

4.5 Discussion and comparison to previous photoemission studies

In the preceding sections we analyzed how the band diagram in epitaxial $LaAlO_3$/$SrTiO_3$ heterostructures looks like at different V_O concentrations, i.e., at different doping levels. Concomitantly with the V_O concentration and the total mobile charge carrier concentration, the band profile in the $SrTiO_3$ substrate and the $LaAlO_3$ film as well as the interfacial band alignment and the charge carrier distribution are found to alter.

Armed with this knowledge about the electronic interface properties and their dependence on the V_O concentration, we revisit the previous photoemission studies in the following and check whether their deviating results can be ascribed to differences in the oxygen stoichiometry in the samples investigated.[12] Table 4.4 lists the results of our analysis which are in the following compared to the outcomes of earlier photoemission studies which are summarized in Tab. 4.5.[13] As the oxygen vacancy concentration has proven to be an essential parameter in our measurements, we also indicate in Tab. 4.5 whether the sample is fully oxidized.[14]

4.5.1 The band profile in the $SrTiO_3$ substrate

First, we turn our focus to the band profile in the $SrTiO_3$ substrate. The findings of previous photoemission studies on the potential well in the $SrTiO_3$ substrate are listed in Tab. 4.5 (c). While previous photoemission studies only indicate individual values for the energetic width ΔE_{BB} and the spatial depth d_{BB} of the potential well our Poisson-Schrödinger model yields functions which vary with the distance z from the interface. To compare our results to the results in earlier publications, we thus have to relate these z-dependent quantities to the individual values referenced in the other publications: We determine the energetic depth of the potential trough labeled ΔE_{BB} by computing the difference in the valence band edge binding energy between the TiO_2 layer at the interface and the $SrTiO_3$ bulk. The width of the potential trough labeled d_{BB} characterizes the distance at which the band bending decreases to an insignificant value which we arbitrarily define as 10% of ΔE_{BB}.

Our experiments reveal that the energetic depth ΔE_{BB} of the potential well is small in the fully oxidized state but rises under oxygen depletion (see Fig. 4.23 as well as Tab. 4.4). The change in the potential trough under oxygen depletion is shown to be due to the oxygen vacancies releasing mobile electrons. In consequence, an interface dipole is introduced in the $LaAlO_3$/$SrTiO_3$ heterostructure which alters the spatial width as well as the energetic depth of the potential trough in the $SrTiO_3$ substrate.

Table 4.5 (c) discloses that the results of most photoemission studies fit into this scheme: Publications investigating fully oxidized samples only detect small or even no band bending in the $SrTiO_3$ substrate, while nearly all publications analyzing oxygen-depleted samples find evidence for a deep potential trough at the $LaAlO_3$/$SrTiO_3$ interface.

---

[12] The electronic interface properties depend on the exact oxygen vacancy concentration and doping in the sample which is, in turn, intricately linked to the *details* of the $LaAlO_3$ film growth process and cannot be unambiguously determined from the information provided in the publications. Thus we only check the trends in the results of the earlier photoemission studies in the following.

[13] Most of the photoemission studies have been conducted at room temperature while our data has been taken at 60 K. In the next chapter we will, however, see that the electronic interface properties do barely change between 60 K and 300 K.

[14] The samples are labeled according to the deposition conditions stated and by the Ti^{3+} weight: The samples are labeled as fully oxidized when the authors indicate that they post-oxidize the samples in a high oxygen background pressure > 10 mbar after the $LaAlO_3$ deposition. However, when samples are deposited at an oxygen partial pressure of $> 10^{-2}$ mbar, they might also be fully oxidized even without a further post-oxidation process. To estimate the oxygen vacancy concentration in such samples, we resort to the Ti^{3+} weight whenever possible and classify the samples as fully oxidized if the Ti^{3+} weight lies below $\approx$3%.

sample state	$\boldsymbol{\Delta E_{\mathrm{VB}}}$ (eV)	$\boldsymbol{\Delta E_{\mathrm{BB}}}$ (eV)	$\boldsymbol{d_{\mathrm{BB}}}$ (Å)	$\boldsymbol{d_{\mathrm{2DES}}}$ (Å)
fully oxidized	+0.13±0.20	0.46±0.10	26±5	11.3±1.6
saturated O depletion	–0.51±0.20	0.82±0.10	22±3	8.1±0.4

Tab. 4.4: Synopsis of the results of our HXPES depth profiling experiments at the (001)-oriented $LaAlO_3/SrTiO_3$ heterostructure: valence band offset ΔE_{VB}, energetic depth ΔE_{BB} and spatial width d_{BB} of the potential well in the $SrTiO_3$ substrate and 2DES extension d_{2DES} in the fully oxidized state and at saturated O depletion. All values depend strongly on the V_{O} concentration and explain why previous photoemission studies deviate strongly in their results.

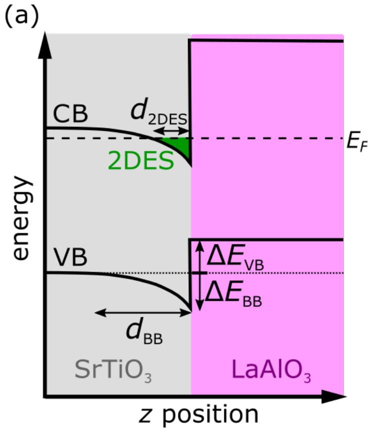

(b) **valence band offset**

publication	$\boldsymbol{\Delta E_{\mathrm{VB}}}$ (eV)	**sample fully oxidized**[14]	**trend consistent with our results**[12]
Susaki *et al.*[142]	+0.42	yes	✓
Berner *et al.*[111]	+0.36	yes	✓
Chambers *et al.*[128] (Augsburg sample)	+0.2	yes	✓
Qiao *et al.*[143,144]	+0.16	yes	✓
Yoshimatsu *et al.*[145]	0.0	yes	✓
Treske *et al.*[137]	0.0	no	✓
Chambers *et al.*[128] (Tokyo sample)	–0.06	no	✓
Drera *et al.*[136]	–0.1	no	✓
Segal *et al.*[110]	–0.35	yes	✗

(c) **potential profile in $SrTiO_3$**

publication	$\boldsymbol{\Delta E_{\mathrm{BB}}}$ (eV)	$\boldsymbol{d_{\mathrm{BB}}}$ (Å)	**sample fully oxidized**[14]	**trend consistent with our results**[12]
Berner *et al.*[111]	0±0.3	—	yes	✓
Yoshimatsu *et al.*[145]	0.25±0.07	—	yes	✓
Chambers *et al.*[128] (Augsburg sample)	0±0.06	—	yes	✓
Drera *et al.*[135]	0.8±0.2	—	no	✓
Treske *et al.*[137]	≥0.4	≥20	no	✓
Chambers *et al.*[128] (Tokyo sample)	0±0.06	—	no	✗

(d) **2DES extension in $SrTiO_3$**

publication	$\boldsymbol{d_{\mathrm{2DES}}}$ (Å)	**sample fully oxidized**[14]	**trend consistent with our results**[12]
Sing *et al.*[140] (Augsburg samples)	4–40	yes	✓
Slooten *et al.*[138] (good substrate)	≥80	yes	✗
Sing *et al.*[140] (PSI sample)	4–12	no	✓
Slooten *et al.*[138] (bad substrate)	25±15	no	✓

Tab. 4.5: Band alignment and band bending at the epitaxial (001) $LaAlO_3/SrTiO_3$ heterointerface as determined by various photoemission studies: (a) Sketch of the band profile typically obtained in photoemission spectroscopy. The figure is not drawn to scale but is defining the variables used in (b) to (d). Valence band offset at the interface (b), potential profile and 2DES extension (c) in $SrTiO_3$ as estimated by different publications. Most of the variations in the measurement results can be traced back to differences in the sample preparation which changes the doping and, in consequence, the electronic properties of the interface.

The exact results for the energetic depth ΔE_{BB} of the potential trough in the $SrTiO_3$ substrate differ in our analysis and the previous publications. In the case of the oxygen-depleted state, this discrepancy is ascribed to the differing oxygen vacancy concentration and distribution in the heterostructures under investigation which alter the potential well. In the case of the fully oxidized state, the modulation in the potential trough is attributed to the varying mobile charge carrier concentrations in the samples which directly affects the profile of the potential trough in the $SrTiO_3$ substrate.

4.5.2 The band alignment at the $LaAlO_3/SrTiO_3$ heterointerface

Next, we revisit the band alignment between the $LaAlO_3$ film and the $SrTiO_3$ substrate.

Our analysis elucidates why the valence band offset, is changing as a function of the V_{O} concentration and the doping: In the fully oxidized state a specific valence band alignment develops between the $LaAlO_3$ film and the $SrTiO_3$ substrate. Upon oxygen depletion and doping, a dipole forms in the vicinity of the interface which alters the width and depth of the potential trough in the $SrTiO_3$ substrate. As the band alignment between film and substrate *at the very interface* does not change, the $LaAlO_3$ valence band edge shifts as does the $SrTiO_3$ valence band edge at the interface. In further consequence, the valence band offset defined as the alignment between the *bulk* $SrTiO_3$ and the $LaAlO_3$ valence band varies along with the V_{O} concentration and the doping.

Our results for the valence band offset are listed in Tab. 4.4 and reveal that the band alignment changes from a staggered gap configuration in the fully oxidized state to a straddling gap configuration at saturated O depletion. Here, we refrain from correcting the valence band offsets due to the potential build-up in the $LaAlO_3$ film but indicate the valence band offsets as determined by fitting the valence band spectra and by evaluating the core level – valence band binding energy difference in Sec. 4.3.3, as the valence band offset is analyzed employing these two methods in the other photoemission studies as well.

Scrutinizing the valence band offsets obtained in earlier photoemission studies [see Tab. 4.5 (b)], we note that the variations in the valence band offset can indeed be ascribed to differences in the O stoichiometry between the samples. Samples which are fully oxidized are characterized by a staggered gap configuration while a straddling gap configuration is found in oxygen-deficient samples.

However, there is one notable exception which is the valence band offset determined by Segal *et al.*[110]. The authors analyze the valence band offset of a sample which was annealed in flowing oxygen at 350°C to quench all oxygen vacancies created during the deposition process. Yet, the valence band offset estimated by Segal *et al.* is rather reminiscent of an oxygen-depleted sample. One might speculate whether the annealing temperature chosen was not high enough and whether, in consequence, all oxygen vacancies in the $LaAlO_3/SrTiO_3$ heterostructure are indeed filled up. It should be noted that the $LaAlO_3/SrTiO_3$ heterostructures are typically post-oxidized at higher temperatures of 500°C to 600°C.[A9,140,163] The distinct band alignment in the sample Segal *et al.* investigate might, however, also be due to a pronounced variation in the cation stoichiometry of the $LaAlO_3$ film which has also been shown to affect the band alignment.[128,139] The sample investigated by Segal *et al.* is, conspicuously, the only sample in Tab. 4.5 (b) which is not fabricated by PLD but by MBE and may thus indeed differ distinctly in its cation stoichiometry.

Let us shortly return to Tab. 4.5 and scrutinize the magnitude of the valence band offset in all other samples. The valence band offset is found to vary strongly for oxygen-depleted samples as well as for fully oxidized samples. The variations in the valence band offset are attributed to the differences in the V_{O} concentration and to the differences in the integral mobile charge carrier concentration in oxygen-depleted and fully oxidized samples, respectively: Changes in the

V_O concentration as well as changes in the integral mobile charge carrier concentration alter the potential trough in the $SrTiO_3$ substrate and, in consequence, the valence band offset.

Following this line of reasoning, we also understand why some publications find the valence band offset to vary depending on the surface preparation employed.[A9,128] Contingently on the surface preparation the amount of adsorbates at the $LaAlO_3$ surface changes. Adsorbates at the $LaAlO_3$ surface are, however, known to dope charge carriers into the interfacial 2DES and alter the potential trough on the $SrTiO_3$ side of the interface and, in consequence, also the valence band offset.[A9,164]

4.5.3 The potential build-up in the $LaAlO_3$ film

Next, we discuss the potential profile in the $LaAlO_3$ film. In agreement with the earlier publications we do not find any evidence for a potential gradient in the $LaAlO_3$ film in the fully oxidized $LaAlO_3/SrTiO_3$ heterostructure.[109,110,128,135–139]

In contrast to the fully oxidized state, at saturated O depletion the energy bands in the $LaAlO_3$ film are observed to be bent downward toward the surface, which has shown to be induced by charged oxygen vacancies in the $LaAlO_3$ film. A potential gradient in the $LaAlO_3$ film of the *same sign* but with a smaller magnitude has been detected by Segal *et al.*[110] in $LaAlO_3/SrTiO_3$ heterostructures with a high oxygen vacancy concentration, corroborating our measurements. The differences in the magnitude of the potential gradient might be due to the different number and distribution of oxygen vacancies in the $LaAlO_3$ film.

4.5.4 The 2DES extension

Lastly, we touch upon the 2DES extension in the $LaAlO_3/SrTiO_3$ heterostructure.

Our measurements reveal that the mobile charge carriers are accumulating close to the interface independent of the V_O concentration and the total doping level [cf. Fig. 4.14 (a)]. We find that the dielectric constant of $SrTiO_3$ with its intricate dependence on the electric field largely induces the strong confinement of the mobile charge carriers to the interface: The decisive role of the electric field dependence of ϵ_r on the charge carrier distribution in $LaAlO_3/SrTiO_3$ heterostructures has also been established by conductive-tip atomic force microscopy in ref. [165].

To compare our quantitative results for the 2DES extension to the results of earlier publications, we have to relate the charge carrier profile $n(z)$ to the d_{2DES} values referenced in the other publications. Previous photoemission studies[138,140] estimate the 2DES extension approximating the doping at the interface by a step function: The charge carrier concentration is assumed to be finite and fixed over the distance d_{2DES} after which it drops to zero. We thus define the 2DES extension d_{2DES} in our analysis as the full width at half maximum of the charge carrier concentration $n(z)$. Table 4.4 lists our results for the 2DES extension d_{2DES} and confirms that the 2DES extension d_{2DES} is indeed only slightly larger in the fully oxidized state than at saturated O depletion.

The earlier photoemission studies listed in Tab. 4.5 (d) found that the 2DES is tightly confined to the $LaAlO_3/SrTiO_3$ interface in oxygen-depleted samples exhibiting a pronounced Ti^{3+} shoulder,[138,140] which is in agreement with our findings.

However, while we find that also in the fully oxidized state the 2DES extension only amounts to 1.1 nm, the 2DES extension in such samples is estimated to be significantly larger by Slooten *et al.*[138] Sing *et al.*[140] specify values for the 2DES extension in fully oxidized samples which are consistent with our results but are burdened by large error bars. The different results for the 2DES extension are tentatively attributed to the different approaches and fit models used by Sing *et al.* and by Slooten *et al.* and in this thesis: The fit model used by Sing *et al.* and Slooten *et al.* only analyzes the dependence of the Ti^{3+} weight on the electron emission angle which is, however, very hard to discern and to analyze when the overall Ti^{3+} weight is small as is the case in fully oxidized samples. This point is further elaborated by an illustrative example in Sec. B.3 in the Appendix. With our Poisson-Schrödinger ansatz, which fits the band bending and the charge carrier distribution simultaneously, we can, in contrast, estimate the 2DES extension more exactly.

4.6 Conclusion

Although the band bending and the band alignment at the epitaxial (001) $LaAlO_3/SrTiO_3$ heterointerface have already been investigated in numerous photoemission studies, a clear picture of the interfacial band diagram has not emerged to date. In this chapter we thus revisit the topic and investigate the electronic properties of the (001)-oriented $LaAlO_3/SrTiO_3$ heterostructure anew by hard x-ray photoemission.[15] We do not only examine a solitary sample in a specific state but also vary the doping in the sample in the photoemission experiment systematically by virtue of the V_O concentration. To be able to reliably fit the experimental spectra, an elaborate Poisson-Schrödinger ansatz is devised which yields a physically consistent model of the charge carrier and the potential profile.

Our fits provide a conclusive picture of the band diagram at the interface as a function of the V_O concentration and the mobile charge carrier concentration: Under oxygen depletion, the potential trough on the $SrTiO_3$ side of the interface varies as the oxygen vacancies introduced act as an interface dipole. A comparison of the band bending in the $SrTiO_3$ substrate and the interfacial band alignment furthermore discloses why the valence band alignment varies as a function of the V_O concentration. The band edges in the $LaAlO_3$ film are found to shift concomitantly with the $SrTiO_3$ band edges at the interface. As the $SrTiO_3$ potential well is altered, the valence band offset is thus changed as well.

The mobile charge carriers are furthermore shown to accumulate near the interface independent of the oxygen vacancy concentration. The dielectric constant of $SrTiO_3$ with its intricate dependence on the electric field proves to be the crucial parameter inducing the charge carrier confinement.

Based on these findings, we show that most of the seemingly contradicting results of earlier photoemission studies can be reconciled with each other. Our insights into the band engineering at $LaAlO_3/SrTiO_3$ heterointerfaces might furthermore prove useful for future device applications where it is essential that the electronic interface properties such as the valence band alignment can be precisely controlled and manipulated.

---

[15] Note that we conducted similar HXPES experiments also on the (111) $LaAlO_3/SrTiO_3$ heterointerface. These measurements are discussed in more detail in the Appendix in Sec. B.6. In conclusion, our findings on the (111)-oriented $LaAlO_3/SrTiO_3$ heterostructure are fully in line with our results on the (001)-oriented $LaAlO_3/SrTiO_3$ samples.

CHAPTER 5

Tuning the dielectric constant of $SrTiO_3$

The dielectric constant ϵ_r of the $SrTiO_3$ substrate plays a key role in determining the electronic interface properties of $LaAlO_3/SrTiO_3$ heterostructures, as became clear in the previous chapter. ϵ_r determines the extension of the conducting layer as well as the band alignment and band bending at the heterointerface. The analysis has hitherto been limited to samples kept at cryogenic temperatures of $\approx$60 K. Since ϵ_r is also strongly depending on the temperature, one might furthermore expect pronounced changes in the electronic interface properties as a function of the sample temperature. In the present chapter we will put this assumption to the test and scrutinize how the electronic interface properties change *as a function of the sample temperature.* Indeed, it is worthwhile examining the characteristics of the heterostructures at room temperature, since possible $SrTiO_3$-based electronic devices would ideally run in this temperature range. Detailed understanding of the electronic interface properties *at the operating temperature* could prove highly beneficial in the design and the manipulation of such devices.

In the previous chapter we analyzed how the 2DES extension and the interfacial band alignment are changing as a function of the V_O concentration, which was, in turn, *locally* varied during the course of the experiment by irradiation with the intense x-ray beam and by oxygen dosing. However, in the following experiments we do not only want to trace the changes in the electronic interface properties as a function of the V_O concentration but also as a function of the sample temperature. To separate the two effects, we endeavor to measure samples at the *same* V_O *concentration* both at low and at room temperature.

Here, we thus set out to investigate two samples in which the oxygen vacancy concentration is set by growth and ensure that the oxygen vacancy concentration does not change during the photoemission experiment: We probe a fully oxidized $LaAlO_3/SrTiO_3$ heterostructure, which is doped solely by electronic reconstruction. The second sample under investigation, an Al-capped $SrTiO_3$ substrate, is, in contrast, rendered conductive by oxygen vacancies. By core level photoemission measurements at cryogenic as well as at room temperature, we examine the temperature dependence of the 2DES extension, of the interfacial band alignment and of the band bending in both heterostructures. In the last section of the chapter, we compare the samples to each other and analyze how the dielectric constant of $SrTiO_3$ and the electronic interface properties in $SrTiO_3$-based heterostructures are manipulated by temperature and doping. The results presented here are compiled in ref. [A15].

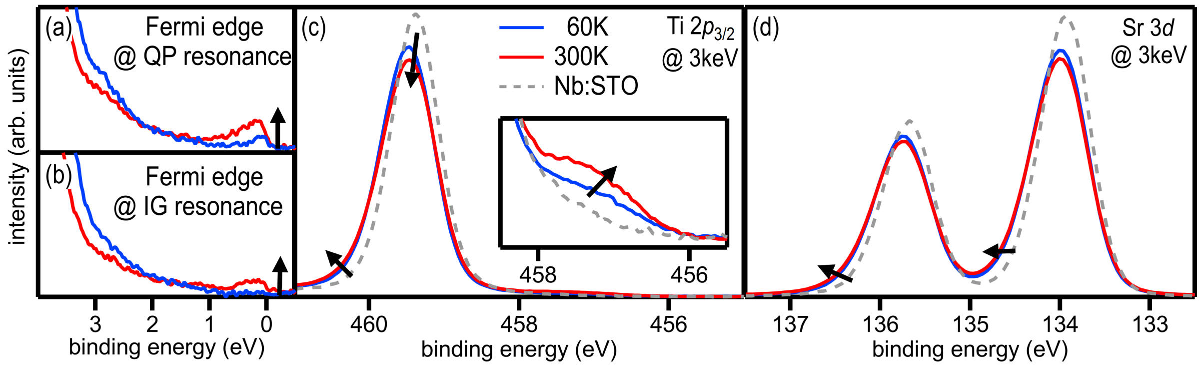

Fig. 5.1: HXPES and SXPES spectra of a $LaAlO_3/SrTiO_3$ heterointerface measured under oxygen dosing at 60 K and 300 K: Valence band spectra recorded with soft x-rays at the QP (a) and the IG resonance (b). The fully oxidized state can be stabilized at both temperatures. Angle-integrated Ti $2p_{3/2}$ (c) and Sr $3d$ (d) HXPES core level spectra of the very same states. For comparison, we also depict the spectra of a Nb-doped $SrTiO_3$ substrate.

5.1 Temperature-dependent band diagram of $LaAlO_3/SrTiO_3$ heterostructures

First we explore the temperature dependence of the band diagram for the case of a fully oxidized $LaAlO_3/SrTiO_3$ heterostructure in which the 2DES is induced by an electronic reconstruction.[1]

5.1.1 Stabilizing the fully oxidized state

First we have to ensure that we can indeed stabilize the fully oxidized state, i.e., suppress the creation of oxygen vacancies, at low as well as at room temperature. Figures 5.1 (a) and (b) reveal that this is indeed the case: While the QP weight remains finite, the IG states are completely suppressed at both measurement temperatures.

Before delving into the details of the electron emission angle dependence at low and at room temperature, we first analyze the *angle-integrated* Ti $2p$ and Sr $3d$ spectra depicted in Figs. 5.1 (c) and (d), respectively.[2] Apart from the spectra of the $LaAlO_3/SrTiO_3$ heterostructure we also show the respective spectra of a fully oxidized, Nb-doped substrate for reference. At first glance, one notes that the spectra of the heterostructure and the Nb-doped substrate vary widely In accordance with our previous measurements, we find that the spectra of the heterostructure are shifted and broadened asymmetrically toward higher binding energies in comparison to the spectra of the $SrTiO_3$ substrate. In the Ti $2p$ spectra of the $LaAlO_3/SrTiO_3$ sample we furthermore observe small, but finite Ti^{3+} weight at low as well as at room temperature.

The spectra of the $LaAlO_3/SrTiO_3$ heterostructure recorded at the different temperatures do, in contrast, hardly differ: The Sr $3d$ and Ti $2p_{3/2}$ spectra of the $LaAlO_3$ sample are marginally broadened at room temperature. The Ti^{3+} weight is furthermore slightly increased at room temperature. These observations already indicate that the band bending as well as the charge carrier distribution is very similar at low and at room temperature. To gain further insight into these quantities, the electron emission angle dependence of the Sr $3d$ and Ti $2p_{3/2}$ spectra is scrutinized in the next section as a function of the sample temperature.

---

[1] Here, we measure a (111)-oriented $LaAlO_3/SrTiO_3$ sample. In the previous chapters we saw that similar physical processes occur at (001) and (111) $LaAlO_3/SrTiO_3$ heterostructures. All subsequent findings can thus be transferred to (001)-oriented $LaAlO_3/SrTiO_3$ samples as well.

[2] For the first comparison we forgo an intricate background correction and only subtract a constant background signal. The spectra are furthermore normalized to integral area.

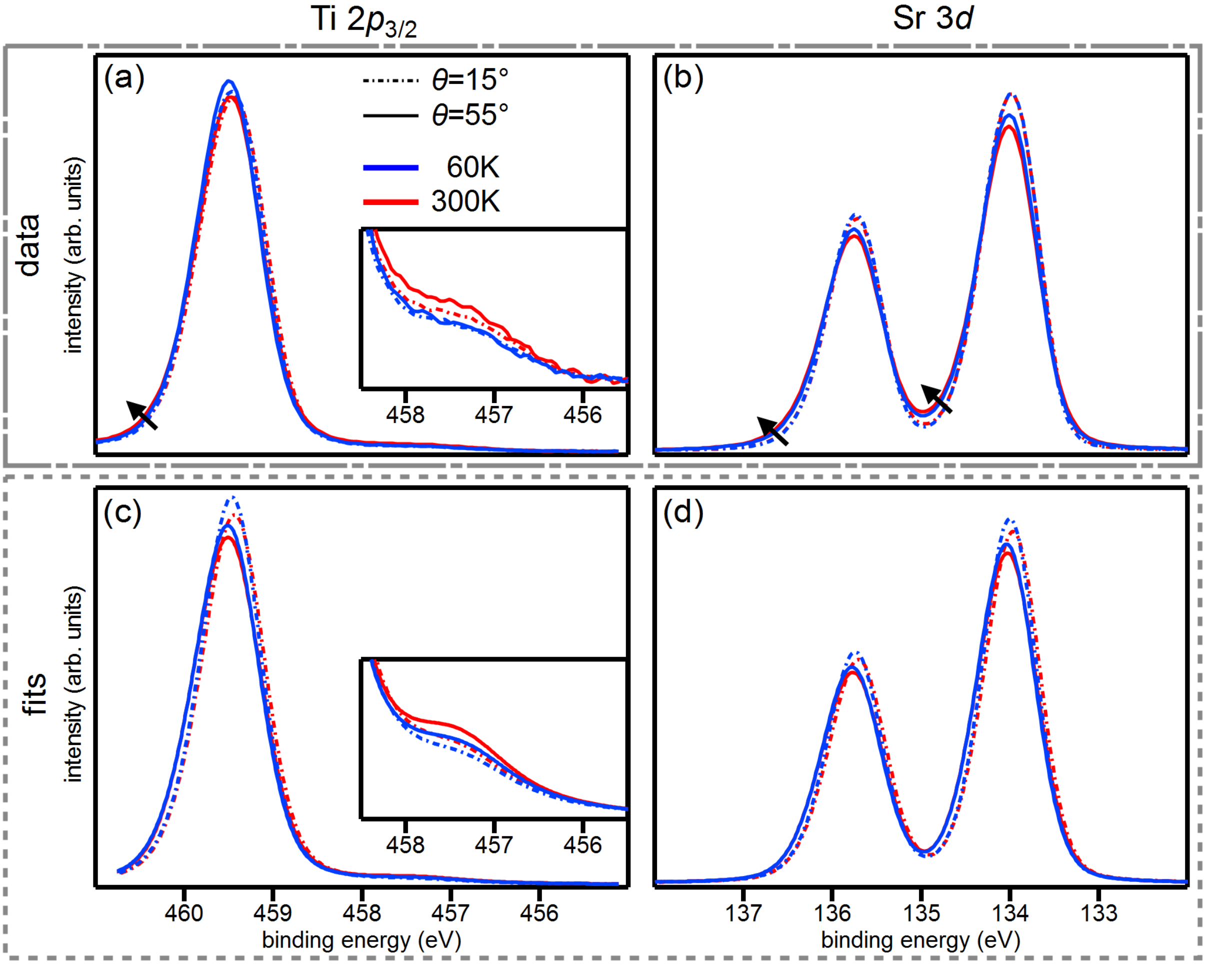

Fig. 5.2: Electron-emission-angle-dependent Ti $2p_{3/2}$ (a) and Sr $3d$ (b) core level spectra of a fully oxidized $LaAlO_3/SrTiO_3$ sample at 60 K and at 300 K. The electron emission angle dependence of the spectra is very similar at 60 K and at 300 K. Fits of the Ti $2p_{3/2}$ (c) and Sr $3d$ (d) core level spectra displayed above with the Poisson-Schrödinger ansatz. The fits reproduce the trends we observe in the measured data upon varying the electron emission angle as well as the temperature.

5.1.2 Depth profiling of the 2DES

Electron-emission-angle-resolved Ti $2p_{3/2}$ and Sr $3d$ spectra are depicted in Figs. 5.2 (a) and (b), respectively. For the sake of clarity we only display the spectra recorded at the extremal electron emission angles.[3] We compare spectra recorded at different temperatures to each other in one and the same graph, as the differences which occur upon temperature variation in the spectra are subtle.

We note that the electron emission angle dependence is very similar at both sample temperatures: At both temperatures the Sr $3d$ as well as Ti $2p_{3/2}$ spectra develop a small asymmetry toward higher binding energies at high electron emission angles [see arrows in Figs. 5.2 (a) and (b)]. The Ti^{3+} spectral weight is very small at both temperatures and its dependence on the electron emission angle only becomes apparent in the zoom-in of the Ti $2p$ spectra in the inset of Fig. 5.2 (a). These findings confirm that the band bending as well as the 2DES extension in the $SrTiO_3$ substrate are rather similar at our two measurement temperatures.

---

[3] For the subsequent quantitative analysis the background signal is carefully corrected analogously to Sec. 4.2.4.

Small differences in the electron emission angle dependence at 60 K and at 300 K can, however, be identified: The dependence of the Sr 3*d* spectra on the electron emission angle is a bit more pronounced at 300 K than at 60 K. We furthermore note that at 300 K, the Ti^{3+} spectral weight is increased for all electron emission angles. The dependence of the Ti^{3+} spectral weight on the electron emission angle differs as well between the measurements at 60 K and 300 K. At room temperature the Ti^{3+} weight is changing as a function of the electron emission angle, while it is barely varying with the electron emission angle at 60 K.

To unravel how the electronic interface properties change as a function of temperature, we once again employ a Poisson-Schrödinger ansatz and model the Sr 3*d* and Ti $2p_{3/2}$ spectra in a global fit. Such a fitting scheme which incorporates all available data is essential in this case, in order to reliably reproduce the small differences in the spectra. The Poisson-Schrödinger ansatz described in Sec. 4.2.9 is adapted to the new experiment: In the following we will not list all parameters again, but only elaborate on the parameters which change. When the measurement temperature is changed, the Gaussian width of the spectra might vary. To include this effect, we thus use different Gaussian widths to fit the data at room and at low temperature, respectively. The V_{O} concentration is set to zero at both temperatures. In the fully oxidized $\mathrm{LaAlO_3/SrTiO_3}$ sample mobile charge carriers are, instead, released by an electronic reconstruction process, a doping process which does not depend on the sample temperature. We thus assume that the total number of mobile charge carriers does not change with the temperature, as transport measurements suggest as well.[51] To reduce the number of fit parameters, we employ the effective electron mass $m^{*}{\approx}0.82m_e$ estimated in the previous chapter. At room temperature, ϵ_r does no longer show a dependence on the electric field.[95] To describe the room-temperature ϵ_r, we thus forgo the parameters B and E_0 and, instead, set ϵ_r to a constant value.

Figures 5.2 (c) and (d) depict the best fits to the Ti 2*p* and Sr 3*d* spectra which the Poisson-Schrödinger ansatz yields. Just as is the case with the measured spectra, the differences between the fitted curves are tiny. For this reason the electron emission angle dependence of the fits and the measured spectra are not compared in the same graph but shown side by side.[4] This way one can assess if the fits are able to reproduce the subtle differences in the spectra which occur when the temperature or the electron emission angle is varied.

We find that the trends which we observe in the spectra upon variation of the electron emission angle or variation of the temperature are well reproduced by our fits [compare Figs. 5.2 (a) and (b) to Figs. 5.2 (c) and (d)]. Comparing the fit curves, keep in mind that we work with different models for the dielectric constant ϵ_r at 60 K and at 300 K. Although the fit curves do barely differ for the two temperatures, our fitting routine yields meaningful results for low and for room temperature. For both temperatures, the measured as well as fitted Ti $2p_{3/2}$ and Sr 3*d* spectra are asymmetrically broadened toward high binding energies at high electron emission angles. In the Ti 2*p* spectra the differences in the Ti^{3+} weight are also replicated. In accordance with the measured spectra, the Ti^{3+} weight in the fits is higher at room temperature than at low temperature and the dependence of the Ti^{3+} weight on the electron emission angle is more pronounced at room temperature.

5.1.3 Discussion of fit results

Let us next take a closer look at the fit results of the Poisson-Schrödinger approach which are listed in Tab. 5.1. The charge carrier concentration n_{er} fitted will be compared to transport experiments in Sec. 6.2.2. The fit results for B and E_0 which model $\epsilon_r(E)$ at 60 K agree, within error bars, with the B and E_0 values expected at this temperature [cf. table in Fig. 4.10 (b)] and are also in line with the B and E_0 values obtained in the fits in the previous chapter (cf.

---

[4] A direct comparison of the measurement data and the fits in the same graph is shown in Fig. C.1 in the Appendix.

	fit parameters applicable			
	@ 60 and 300K	**@ 60K**		**@ 300K**
	n_{er} ($10^{14}\,\mathrm{cm}^{-2}$)	B	E_0 (MV/m)	ϵ_r
best fit	1.80	4030	0.75	65.5
lower limit	1.55	3600	0.63	49
upper limit	2.00	4980	1.02	112

Tab. 5.1: Fit results of the Poisson-Schrödinger approach for the fully oxidized LaAlO$_3$/SrTiO$_3$ heterostructure at 60 K and at 300 K. We specify the best-fit values as well as error margins.

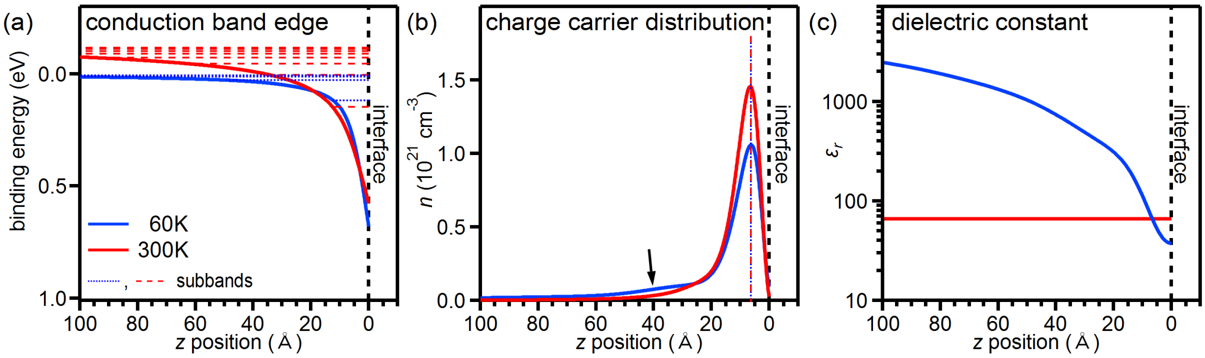

Fig. 5.3: The electrostatics of the fully oxidized LaAlO$_3$/SrTiO$_3$ heterostructure at low and at room temperature. (a) Conduction band profile with subband structure. (b) Mobile charge carrier distribution. (c) Profile of the dielectric constant. See text for a detailed discussion.

Tab. 4.2). The room temperature dielectric constant ϵ_r which the fitting routine yields is slightly smaller than the tabulated value of approximately 300.[73,94,95] The discrepancy is ascribed to a residual electric field dependence of ϵ_r at room temperature. This effect reduces the dielectric constant at very high electric field, i.e., just in the vicinity of the interface to which the fit is most sensitive. All further fit results are listed and contrasted to the fit results in chapter 4 in Tab. B.2 in the Appendix. A detailed comparison of the present and previous fit parameters shows that corresponding parameters are in accordance with one another.

The electrostatics at the fully oxidized LaAlO$_3$/SrTiO$_3$ heterointerface is summarized in Fig. 5.3. Figure 5.3 (a) shows the conduction band profile and subband structure at low and at room temperature. At room temperature, the conduction band edge in the SrTiO$_3$ bulk shifts toward higher binding energies. This shift is ascribed to the different thermal broadening of the Fermi-Dirac distribution at 60 K and at 300 K which controls the occupation of the discrete subbands: Imposing a fixed total charge carrier concentration, the conduction band edge has to shift with respect to the chemical potential when the temperature is changing. The distribution of the mobile charge carriers is depicted in Fig. 5.3 (b). The charge carrier concentration peaks closely to the interface at $z \approx 7$ Å both at low and at room temperature. However, the depth distribution of the charge carriers differs for the two temperatures: At 300 K most charge carriers are localized in the immediate vicinity of the interface, while the charge carrier concentration at 60 K is characterized by a pronounced tail which extends into the SrTiO$_3$ bulk [see arrow in Fig. 5.3 (b)].

This result is in agreement with our previous qualitative assessment of the electron emission angle dependence observed in the Ti^{3+} weight and furthermore explains why the Ti^{3+} weight is overall increased at 300 K. Due to the limited inelastic mean free path of the photoelectrons, we do not 'see' the electrons in the tail of the charge carrier profile at 60 K and the relative Ti^{3+} spectral weight is decreased. At 300 K we probe the 2DES in its entirety, on the other hand.

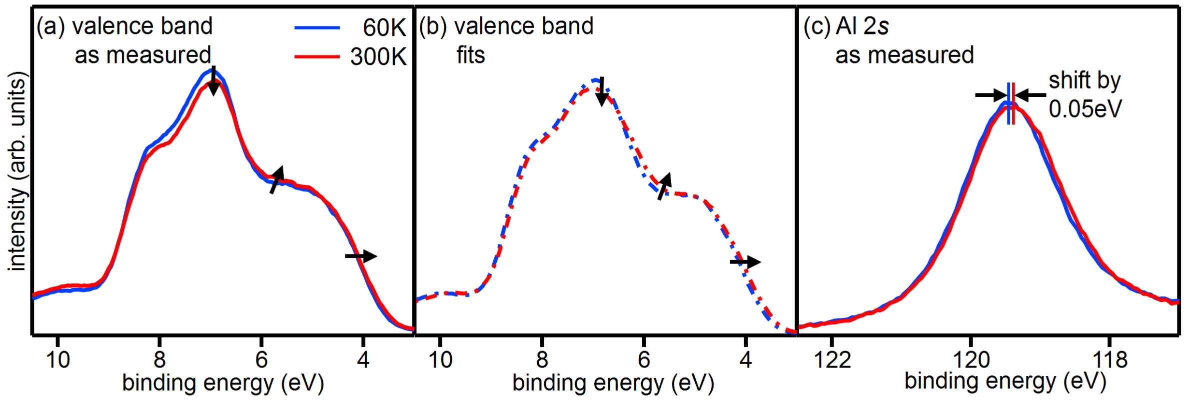

Fig. 5.4: Interfacial band alignment at low and at room temperature. (a) Angle-integrated valence band spectra recorded at 60 K and at 300 K. We only observe small shifts in binding energy and spectral weight when the temperature changes. (b) Fits of the valence band spectra at 60 K and at 300 K. (c) Al 2*s* spectra recorded at 60 K and at 300 K. At room temperature the Al 2*s* peak is shifted by 50 meV toward lower binding energies.

The differences as well as similarities in the 2DES extension at 60 K and at 300 K can once again be traced back to the profile of the dielectric constant at low and at room temperature which is depicted in Fig. 5.3 (c). The dielectric constant is small in the vicinity of the interface for both temperatures, which brings about the strong confinement to the interface at 60 K as well as at 300 K. However, for low temperatures ϵ_r rapidly increases away from the interface, while it remains small even in the bulk of the $SrTiO_3$ substrate at room temperature. Accordingly, the charge carrier profile has a pronounced tail reaching deep into the $SrTiO_3$ substrate in the former case, which is not present in the latter case.

5.1.4 Determining the interfacial band alignment

For a complete band diagram, we also recorded valence band and film core level spectra at the two temperatures: In the angle-integrated valence band spectra depicted in Fig. 5.4 (a) we only observe small shifts in binding energy and spectral weight when the sample temperature is varied. This finding already indicates that the valence band alignment does not change much between 60 K and 300 K. To verify this hypothesis, we turn to the film core level spectra since any changes in the interfacial band alignment should be reflected in a binding energy shift of the film core levels. Indeed, the Al 2*s* spectra displayed in Fig. 5.4 (c) shift only by ≈50 meV when the temperature is increased from 60 K to 300 K, confirming our hypothesis.

We furthermore estimate the valence band offsets by fitting the valence band spectra as described in the previous chapter. Due to the small differences between the spectra recorded at 60 K and at 300 K we show the fits and the measured spectra side by side in Figs. 5.4 (a) and (b). The fits reproduce the small binding energy shifts as well as the spectral weight transfer which occur upon temperature variation [see arrows in Figs. 5.4 (a) and (b)]. We additionally evaluate the valence band offset by analyzing the binding energy difference between selected film core levels and the valence band maximum.

The valence band offsets obtained by the two methods are compared in Tab. 5.2. We note that the results the two methods yield agree with each other within the error bars.

The complete band diagram is plotted in Fig. 5.5. The heterojunction is characterized by a staggered gap configuration at both temperatures. Once again, we confirm that the band alignment right at the interface does not change: The change in the band bending at the interface is of the

method	ΔE_{VB} **@ 60 K**	ΔE_{VB} **@ 300 K**
core level analysis	–0.18 eV	–0.23 eV
valence band analysis	–0.23 eV	–0.35 eV

Tab. 5.2: Valence band offset ΔE_{VB} at the fully oxidized $LaAlO_3/SrTiO_3$ heterostructure at low and at room temperature. The valence band alignment is estimated by analyzing the binding energy difference between the valence band maximum and selected core levels (labeled core level analysis) as well as by fits of the valence band spectra (labeled valence band analysis).

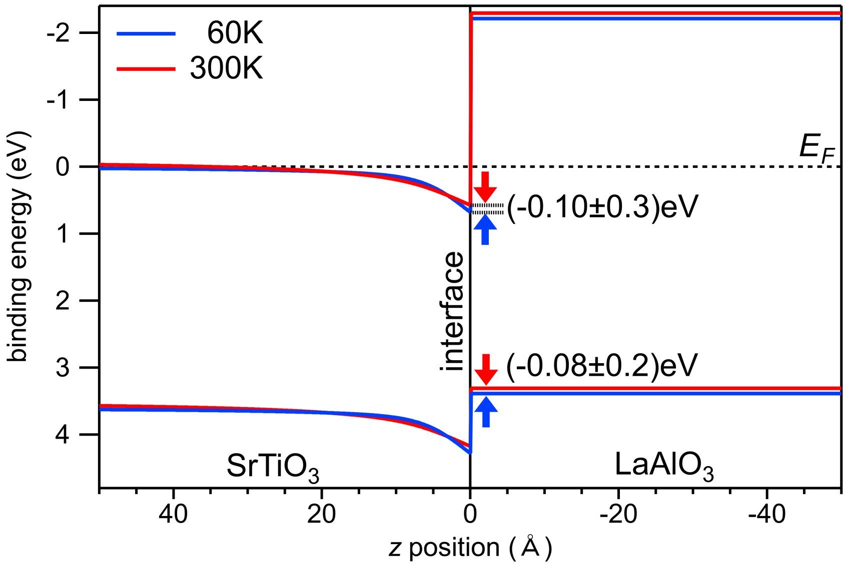

Fig. 5.5: Band diagram of the (111)-oriented fully oxidized $LaAlO_3/SrTiO_3$ heterostructure at low and at room temperature. The valence band edge in the $LaAlO_3$ film is found to shift concomitantly to the $SrTiO_3$ valence band edge at the interface.

same size as the shift in the $LaAlO_3$ conduction and valence band edges when the temperature varies (see arrow markings in Fig. 5.5).

We can furthermore check the outcome of our analysis by comparing it to the results obtained in the previous chapter in which the electronic interface properties of $LaAlO_3/SrTiO_3$ heterointerfaces are explored as a function of the V_O concentration *at low temperature*. Indeed, the low-temperature band diagram established here matches the band diagram determined in the previous chapter for a $LaAlO_3/SrTiO_3$ heterointerface in the fully oxidized state (compare blue band diagram in Fig. 5.5 and Fig. 4.19).

Since oxygen atoms in the film as well as in the substrate contribute to the O 1*s* signal, we can again put the band diagram to the test by fitting the O 1*s* spectra. These fits described in the Appendix in Sec. C.2 corroborate the band diagram established in Fig. 5.5.

In conclusion, a conclusive band diagram is derived for 60 K as well as 300 K, although the differences in the spectra recorded at low and at room temperature are very small.

5.2 Temperature-dependent electronic structure of Al/$SrTiO_3$ heterostructures

Up to now we have analyzed the temperature dependence of the electronic properties in a fully oxidized $LaAlO_3/SrTiO_3$ sample, in which the 2DES is induced by an electronic reconstruction. However, in the previous chapter we have shown that – at low temperature – also the oxygen vacancy concentration plays a crucial role in determining, e.g., the 2DES extension and the band bending at the interface. We ascribe this effect to the change in electric field and consequently in the dielectric constant which is induced by the oxygen vacancies. As the dependence of the dielectric constant on the electric field also varies strongly with temperature, one might wonder how the electronic properties evolve as a function of temperature in *oxygen-deficient* $SrTiO_3$.

To investigate a sample with a constant V_O concentration at low and at room temperature, we can, however, no longer rely on our previous approach: Up to now, we measured a single $LaAlO_3/SrTiO_3$ sample and varied its V_O concentration by irradiation in vacuum. However, we cannot set the same V_O concentration at low and at room temperature by this method: The oxygen vacancy formation is a dynamic process in which oxygen is driven out by the intense irradiation and at the same time replenished by diffusion from the $SrTiO_3$ bulk. The equilibrium between these two processes changes with the temperature.[87] The oxygen vacancy concentration induced thus also varies depending on the sample temperature. As an alternative, we measure a sample in which the oxygen vacancies in the $SrTiO_3$ substrate are already created during the growth process. With the aid of a thick capping layer, the growth-induced oxygen vacancy profile is stabilized.

To unambiguously identify the impact of the oxygen vacancies on the electronic structure of the $SrTiO_3$, we investigate a sample which is doped *exclusively* with electrons released by oxygen vacancies. Such is, e.g., the case with the disordered $LaAlO_3/SrTiO_3$ heterostructures as we have shown in chapter 3. Oxygen vacancies are created in redox reactions occurring at the substrate surface during the pulsed laser deposition: The Al atoms, the prevalent Al species in the laser plume, oxidize upon arrival at the $SrTiO_3$ substrate scavenging oxygen from the $SrTiO_3$ substrate and thereby inducing a 2DES.[117,123,166] The La species, i.e., La atoms and La oxides, in the laser plume do, in contrast, not react with the $SrTiO_3$ substrate. It is thus not surprising that one can also forgo the La component and can just as well evaporate Al by molecular beam epitaxy (in short MBE), to induce oxygen vacancies and interfacial conductivity in $SrTiO_3$ substrates.[121,122] Compared to the complex PLD process, the Al deposition by MBE is easier to operate and to control.[167] For that reason it is also a promising method of inducing a 2DES in $SrTiO_3$ which can potentially be upscaled and deployed in industrial production.

As an example of a oxygen-deficient $SrTiO_3$-based heterostructure, we thus analyze such a $SrTiO_3$ sample which is covered by a 2 nm thick Al film in the following section.

5.2.1 Stabilizing the V_O concentration

We first have to make sure that we can stabilize the V_O concentration and, consequently, the conductivity in the Al/$SrTiO_3$ heterostructure: Indeed, we observe that, when the bare Al/$SrTiO_3$ sample is exposed to air, oxygen atoms migrate through the thin Al film, fill up the oxygen vacancies in the $SrTiO_3$ substrate and suppress the metallicity of the sample.[167] To preserve the oxygen vacancy concentration in our samples, we thus deposit an additional thick disordered $LaAlO_3$ layer on top of the Al layer before taking the sample out of the vacuum. The layer structure of the sample is sketched in the top panel of Fig. 5.6 (a). To check if the $LaAlO_3$-capped sample retains its characteristics in ambient atmosphere, we measure the sheet resistance R_s of the sample – inside the vacuum vessel – once after the deposition process and once after the sample has been exposed to air.[167] The two R_s curves depicted in the bottom panel of Fig. 5.6 (a) coincide,

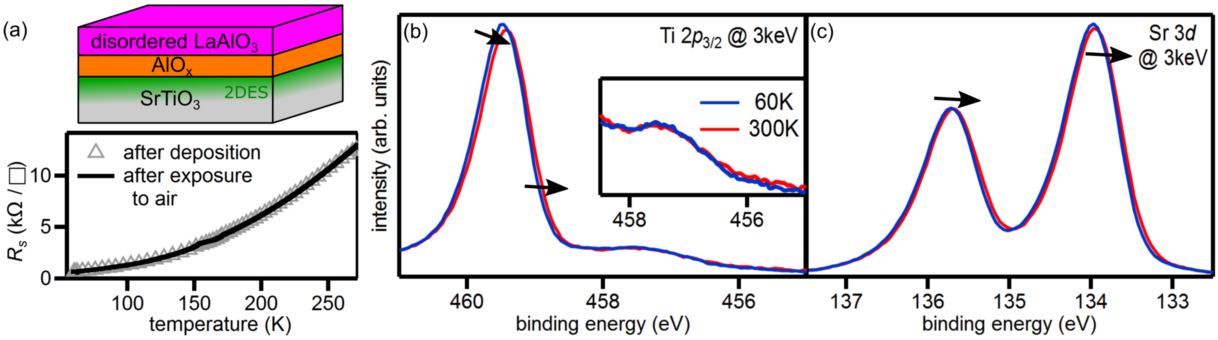

Fig. 5.6: (a) Top: Sketch of the oxygen-depleted Al/SrTiO$_3$ heterostructure. Bottom: Sheet resistance measured inside the vacuum vessel before and after the sample is exposed to air. Angle-integrated Ti 2$p_{3/2}$ (b) and Sr 3d (c) HXPES core level spectra of the oxygen-depleted Al/SrTiO$_3$ heterostructure at low and at room temperature. The thick LaAlO$_3$ capping preserves the V_O concentration in the SrTiO$_3$ substrate under irradiation and in air.

demonstrating that the thick LaAlO$_3$ capping layer preserves the oxygen vacancy concentration and the conductivity in the Al/SrTiO$_3$ heterostructure in ambient air.

We furthermore check if the oxygen vacancy concentration is stable during our photoemission experiments: In the experiments in the previous chapters we have already seen that the intense x-ray beams at the synchrotron facility can create additional oxygen vacancies in the SrTiO$_3$ substrate even when the SrTiO$_3$ is covered by a capping layer. To investigate this effect, we scrutinize successively recorded angle-integrated Ti 2p and Sr 3d spectra and find that all Ti 2p and Sr 3d spectra recorded at the same temperature lie closely on top of each other (data not shown). In this case the intense x-ray beam does not change the V_O concentration in the SrTiO$_3$ substrate, neither at low nor at room temperature.

We conclude that the V_O concentration and the metallicity in the SrTiO$_3$ substrate are successfully stabilized by the thick LaAlO$_3$ capping in ambient air as well as under x-ray irradiation. Note that we refer to the LaAlO$_3$ capped Al/SrTiO$_3$ heterostructure as Al/SrTiO$_3$ heterostructure in the following. Let us thus next analyze the temperature dependence of the electronic structure at the Al/SrTiO$_3$ interface.

5.2.2 Depth profiling of 2DES

The angle-integrated Ti 2p and Sr 3d spectra depicted in Figs. 5.6 (b) and (c) offer a first insight into the temperature dependence of the band bending and the charge carrier distribution at the Al/SrTiO$_3$ interface. Comparing the spectra recorded at 60 K and at 300 K, we only observe small changes: The spectral shape of the Ti 2p and Sr 3d core levels is similar at 60 K and at 300 K. The spectra of both core levels are marginally broadened and shifted slightly toward higher binding energies at room temperature [see arrows in Figs. 5.6 (b) and (c)]. The Ti^{3+} shoulder depicted in the inset of Fig. 5.6 (b) does also barely change. These findings already indicate that the band bending as well as the charge carrier distribution do not show a pronounced dependence on the sample temperature.

To gain a quantitative understanding of the temperature dependence of these quantities, we analyze the electron emission angle dependence of the spectra at room and at low temperature next. The electron emission angle dependence of the background-corrected[5] Ti 2p and Sr 3d

---

[5] For the subsequent analysis of the substrate core level spectra, the background signal in the spectra has once again been corrected as described in Sec. 4.2.4.

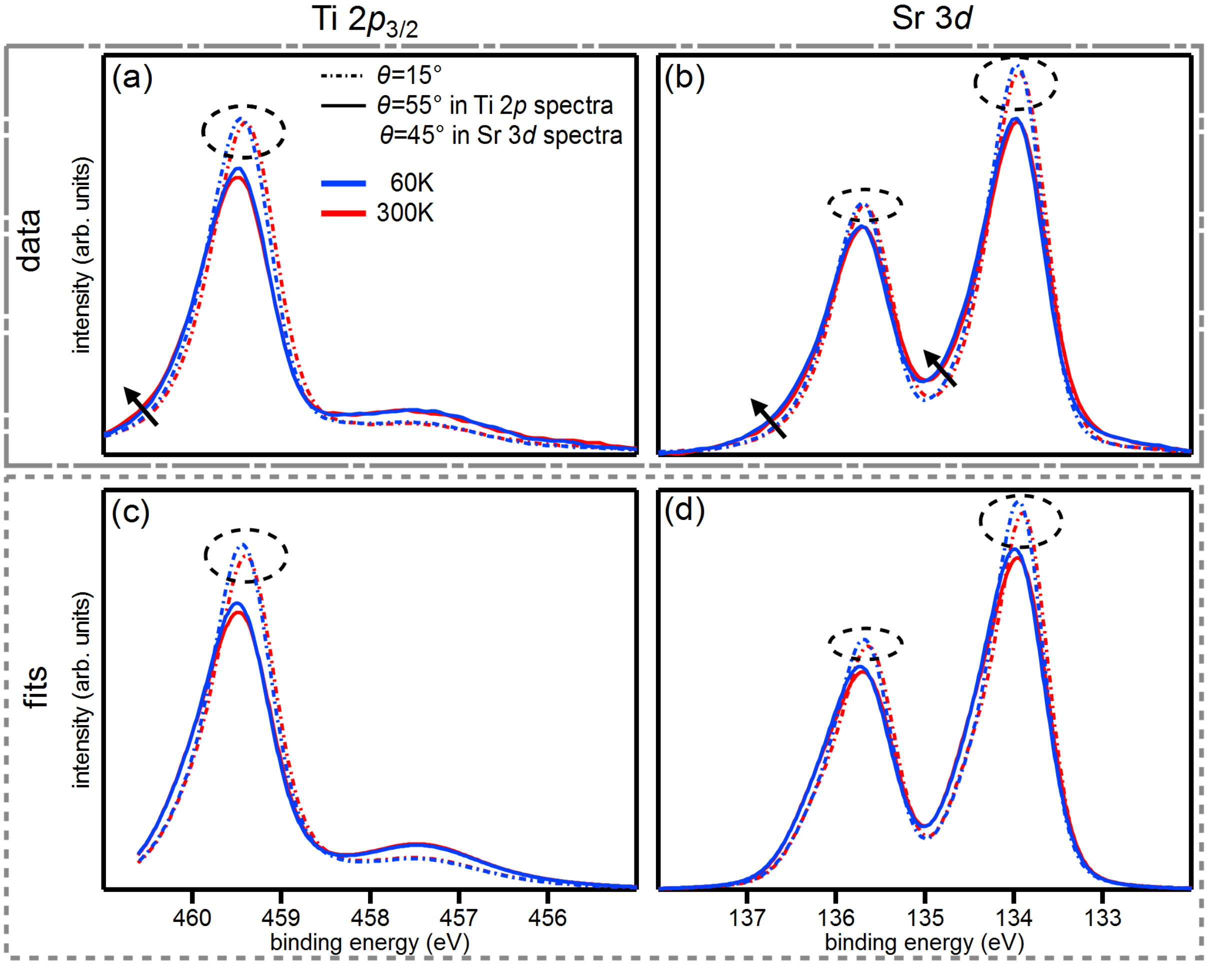

Fig. 5.7: Electron-emission-angle-dependent Ti 2$p_{3/2}$ (a) and Sr 3d (b) core level spectra of the oxygen-depleted Al/SrTiO$_3$ heterostructure at low and at room temperature. Fits of the Ti 2$p_{3/2}$ (c) and Sr 3d (d) core level spectra displayed in (a) and (b) employing the Poisson-Schrödinger ansatz. The fits reproduce the trends observed in the measured data when the electron emission angle or the sample temperature is varied. See text for details.

spectra is depicted in Figs. 5.7 (a) and (b), respectively. For the sake of clarity, just the spectra recorded at the extremal electron emission angles are shown.[6]

The dependence of the spectra on the electron emission angle is very similar at 60 K and at 300 K: Both at 60 K as well as at 300 K, we observe a pronounced asymmetry in the Sr 3d and Ti 2p spectra toward higher binding energies at high electron emission angles [see arrows in Figs. 5.7 (a) and (b)]. The Ti^{3+} weight is furthermore high and strongly dependent on the electron emission angle at both temperatures.

The most prominent difference between the respective spectra at 60 K and 300 K lies in the binding energies of the core levels, which shift toward higher values at room temperature, in particular in the bulk-sensitive measurement geometry [see circles in Figs. 5.7 (a) and (b)]. These findings indicate anew that the band bending as well as the charge carrier distribution do not change strongly as a function of temperature in the Al/SrTiO$_3$ heterostructure.

---

[6] As a result of the thick LaAlO$_3$ capping layer, the Sr 3d spectra are superimposed by an intense La satellite line. In the most surface-sensitive geometry (55° off NE) the contribution of the La satellite line is so large that it cannot be corrected reliably. In the subsequent analysis we thus exclude the Sr 3d spectra recorded at 55° off NE.

	fit parameters applicable				
	@ 60 and 300K		@ 60K		@ 300K
	$\hat{N}_D$ (10^{21} cm^{-3})	d_D (Å)	B	E_0 (MV/m)	ϵ_r
best fit	7.84	16.3	3180	1.21	63
lower limit	7.10	13.0	3120	1.18	43
upper limit	7.87	16.4	4250	1.85	78

Tab. 5.3: Fit results of the Poisson-Schrödinger approach for the oxygen-depleted Al/SrTiO$_3$ heterostructure at low and at room temperature. We specify the best-fit values as well as error margins.

To obtain a quantitative understanding of the electronic interface properties, we fit the spectra employing a Poisson-Schrödinger ansatz. The present Poisson-Schrödinger ansatz is essentially identical to the ansatz used to model the temperature dependence in the fully oxidized LaAlO$_3$/SrTiO$_3$ heterostructure in Sec. 5.1.2. It has to be amended in only one point to describe the Al/SrTiO$_3$ heterostructure: In the Al/SrTiO$_3$ heterostructure, the charge carriers are not induced by an electronic reconstruction but are exclusively released by oxygen vacancies. The mobile sheet charge carrier concentration is thus set to zero and a finite V_O profile is introduced, instead. Since the oxygen-deficient layer is formed as a result of redox reactions occurring *during the deposition process*[121] and is subsequently preserved by the thick capping layer, we furthermore assume that the V_O distribution is the same at 60 K and at 300 K.

The best fit curves the Poisson-Schrödinger ansatz yields are depicted in Figs. 5.7 (c) and (d). Comparing the fits to the data displayed directly above, we note that the fits reproduce the essential features of the spectra and, in particular, the variations occurring as a function of temperature as well as electron emission angle. The shifts in binding energy are, most notably, accurately replicated (see circles in Fig. 5.7).

5.2.3 Discussion of fit results

Table 5.3 lists the fit results for the parameters appearing in the Poisson-Schrödinger ansatz. First we look at the resulting oxygen vacancy profile: The oxygen vacancy concentration amounts to $\hat{N}_D \approx 7.84 \cdot 10^{21}$ cm^{-3} at the interface, which means that an oxygen atom is missing in almost every second SrTiO$_3$ unit cell at the interface. The oxygen vacancy concentration drops to zero after only $d_D \approx 16$ Å, showing that the oxygen vacancies are closely confined to the interface. This observation confirms the claims of Posadas *et al.*:[121] Factoring in the work function of Al and SrTiO$_3$, they claim that oxygen vacancies are only created near the interface and cannot diffuse far into the SrTiO$_3$ bulk in the Al/SrTiO$_3$ heterostructure,.

When the oxygen vacancy concentration is integrated over z, one obtains a total V_O density of $6.4 \cdot 10^{18}$ m^{-2} which is equivalent to approximately one oxygen vacancy per surface unit cell. This oxygen vacancy concentration is checked against the amount of oxidized Al found on the SrTiO$_3$ substrate: Rödel *et al.*[122] find that only the first 2 Å Al near the interface oxidize in the Al/SrTiO$_3$ heterostructure. Using the Al mass density of 2.7 g/cm^{-3} and assuming that Al$_2$O$_3$ forms under oxidation, we convert the thickness of the oxidized Al layer to a concentration of 2.8 oxygen vacancies per surface unit cell. The values estimated for the V_O concentration match within the experimental uncertainty range, taking into account that the Al thickness is calibrated using a quartz crystal microbalance which cannot yield a precise Al thickness on the Å scale.

We furthermore compare the fit results for B, E_0 and ϵ_r (300 K) to the respective values obtained in the fits of the fully oxidized LaAlO$_3$/SrTiO$_3$ heterostructure (cf. Tab. 5.1) and find that the fit results agree within their error margins.

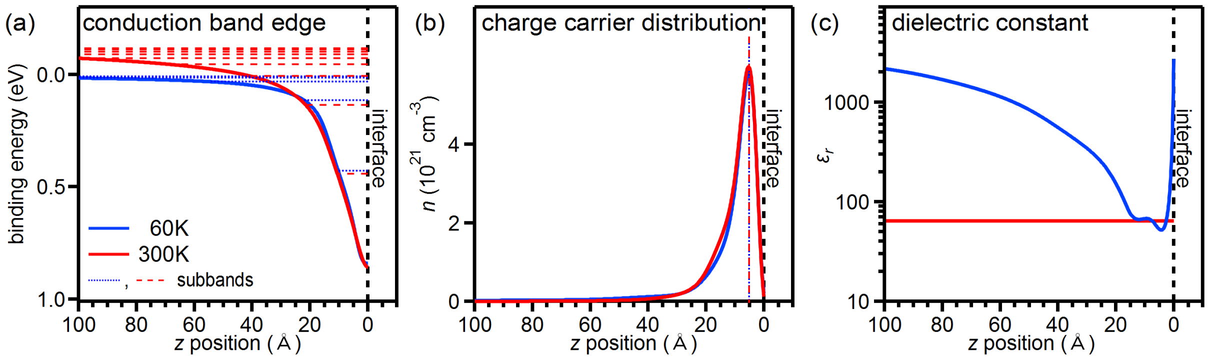

Fig. 5.8: Electrostatics of the oxygen-depleted Al/SrTiO$_3$ heterostructure at low and at room temperature. (a) Conduction band profile with subband structure. (b) Distribution of mobile charge carriers. (c) Profile of the dielectric constant. See text for discussion.

All other fit results are listed and contrasted to the preceding fits in Tab. B.2 in the Appendix. Close inspection of Tab. B.2 shows that the fit results obtained here are very similar to the fit results obtained in the fits of the LaAlO$_3$/SrTiO$_3$ heterostructures. Only the fit parameters which describe the Ti^{3+} weight do differ considerably. We ascribe this to the high V_{O} concentration at the Al/SrTiO$_3$ heterointerface which distorts the lattice as well as the electronic structure at the interface.[168] As the majority of the Ti^{3+} signal originates from interfacial layers in the Al/SrTiO$_3$ heterostructure, the Ti^{3+} peak characteristics may also change.

Let us next take a closer look at the conduction band profile at the Al/SrTiO$_3$ interface at 60 K and at 300 K depicted in Fig. 5.8 (a). It is conspicuous that the *bulk* conduction band edge shifts toward higher binding energies at room temperatures. This shift brings about the binding energy offset observed in the Ti 2*p* and Sr 3*d* core levels as a function of temperature. We observe a similar effect for the epitaxial LaAlO$_3$/SrTiO$_3$ heterostructure discussed previously and ascribe it to the temperature-dependent occupation of subband states above the Fermi level.

The distribution of the mobile charge carriers is shown in Fig. 5.8 (b). The charge carrier concentration peaks near the interface at $z \approx 5$ Å both at 60 K and at 300 K [see dashed lines in Fig. 5.8 (b)]. We note that the distribution of the mobile charge carriers is barely changing with temperature although the conduction band profile is markedly different. As the charge carrier and conduction band profile are linked via the Poisson-Schrödinger equations, this might, at first glance, seem surprising. However, the apparent discrepancy can be reconciled by taking into account the occupation probability of the various subband states in Fig. 5.8 (a): Far below the Fermi level the subbands lie at similar binding energies at low and at room temperature. These subband states are fully occupied according to Fermi-Dirac statistics and constitute the largest part of the charge carrier concentration. The subband structure near or above the Fermi edge is pronouncedly changing as a function of temperature. The population of the states near or above the Fermi level is, however, low. The charge carrier distribution is, consequently, only barely varying with temperature.

The accumulation of the charge carriers at the interface both at 60 K and at 300 K is once again traced back to the profile of the dielectric constant displayed in Fig. 5.8 (c): In the vicinity of the interface the dielectric constant is small and of similar size at low as well as at room temperature which induces the strong charge carrier confinement.

We forgo the analysis of the film core level spectra for the Al/SrTiO$_3$ heterostructure as the intricate composition of the capping layer (AlO$_x$, metallic Al, disordered LaAlO$_3$) prohibits a straightforward evaluation of these spectra.

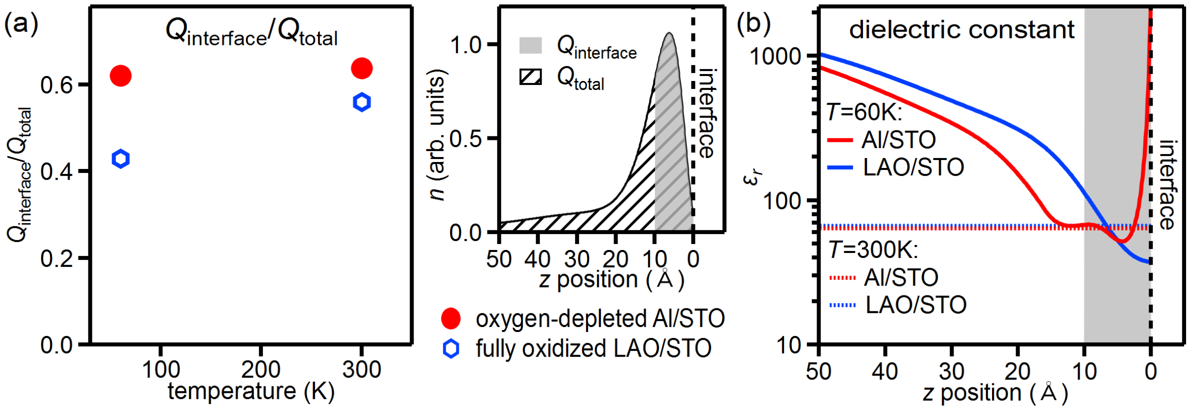

Fig. 5.9: Comparing the charge carrier distribution and the profile of the dielectric constant in the fully oxidized LaAlO$_3$/SrTiO$_3$ heterostructure and in the oxygen-depleted Al/SrTiO$_3$ sample: (a) Analysis of the charge carrier distribution. Proportion $Q_\mathrm{interface}/Q_\mathrm{total}$ of charge carriers located in the proximity of the interface (see illustration in right panel). (b) Profile of the dielectric constant at low and at room temperature in the two heterostructures.

5.3 Tuning the SrTiO$_3$ dielectric constant by temperature and doping

In the previous sections we analyzed the temperature dependence of the electronic interface properties in the oxygen-deficient Al/SrTiO$_3$ and the fully oxidized LaAlO$_3$/SrTiO$_3$ heterostructure separately. In the next section we directly compare the results obtained to identify how the band diagrams changes as a function of temperature and doping. We contrast the two heterostructures with respect to two key quantities, the distribution of the mobile charge carriers as well as the dielectric constant.

The charge carrier distributions are scrutinized first. In order to compare the charge carrier profiles, we define the quantity $Q_\mathrm{interface}/Q_\mathrm{total}$ as illustrated in the right panel of Fig. 5.9 (a). $Q_\mathrm{interface}/Q_\mathrm{total}$ describes the share of the free charge carriers which are located in direct vicinity to the interface, i.e., within 1 nm of the interface. The results of this analysis are depicted in the left panel of Fig. 5.9 (a). We note that in all cases investigated, more than 40% of the charge carriers are located in direct vicinity of the interface.

This charge carrier accumulation near the interface is ascribed to the characteristic behavior of the dielectric constant at the interface: Figure 5.9 (b) depicts the profile of the dielectric constant for the Al/SrTiO$_3$ as well as the LaAlO$_3$/SrTiO$_3$ heterostructure at low and at room temperature. Notably, ϵ_r is small near the interface in any of the cases examined [see gray bar highlighted in Fig. 5.9 (b)].[7]

On closer inspection of Fig. 5.9 (a), we see differences in the charge carrier distributions at the two heterostructures: At room temperature the mobile electrons are strongly confined to the interface for both heterostructures. In the case of the fully oxidized LaAlO$_3$/SrTiO$_3$ heterostructure, the share $Q_\mathrm{interface}/Q_\mathrm{total}$ of free charge carriers located in the vicinity of the interface decreases when the temperature is reduced [see blue hexagons in Fig. 5.9 (a)]. In contrast, the charge carrier distribution in the oxygen-depleted Al/SrTiO$_3$ heterostructure does not depend on the sample temperature [see red spheres in Fig. 5.9 (a)].

These observations can also be explained considering the ϵ_r profiles at the different temperatures

---

[7] Right at the interface ϵ_r sharply increases in the case of the Al/SrTiO$_3$ heterostructure. This increase is due to the different boundary conditions which are imposed in the two heterostructures in the Poisson-Schrödinger analysis but is negligible for the outcome of the analysis.

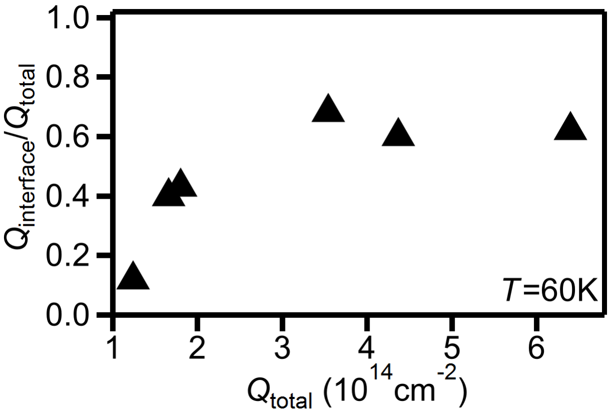

Fig. 5.10: Share of charge carriers which are located within 1 nm of the interface vs. integral charge carrier concentration at 60 K. Data gathered from all photoemission experiments in chapter 4 and 5. At low doping levels the charge carriers shift toward the $SrTiO_3$ bulk.

depicted in Fig. 5.9 (b): At room temperature ϵ_r is constant and assumes a similar value for the Al/$SrTiO_3$ and the $LaAlO_3/SrTiO_3$ heterostructure [see dotted lines in Fig. 5.9 (b)]. At 300 K the mobile electrons are thus accumulating near the interface in both heterostructures. In the case of the oxygen-depleted Al/$SrTiO_3$ heterostructure, the dielectric constant is – over long distances and even far away from the interface – of the same size at low and at room temperature [compare solid and dotted red lines in Fig. 5.9 (b)]. The charge carrier distribution in the oxygen-depleted Al/$SrTiO_3$ heterostructure is thus similar at both temperatures. In the case of the fully oxidized $LaAlO_3/SrTiO_3$ heterostructure, the ϵ_r profiles at low and at room temperature vary significantly [compare solid and dotted blue lines in Fig. 5.9 (b)]. The charge carrier distribution does thus change with the sample temperature. We conclude that the differences in the low-temperature ϵ_r profile induce the different temperature dependence of the charge carrier distribution in the two heterostructures.

We attribute these differences in the low-temperature ϵ_r profiles to the varying integral charge carrier concentration Q_{total} in the Al/$SrTiO_3$ ($Q_{\mathrm{total}} = 6.4 \cdot 10^{14}\,\mathrm{cm}^{-2}$) and the $LaAlO_3/SrTiO_3$ heterostructure ($Q_{\mathrm{total}} = 1.8 \cdot 10^{14}\,\mathrm{cm}^{-2}$): At low temperature, the profile of ϵ_r does depend on the integral charge carrier concentration, as the total charge carrier concentration is linked to the interfacial electric field which is, in turn, linked to the dielectric constant. At high total charge carrier concentrations the electric field near the interface is sizable and strongly suppresses the high low-temperature ϵ_r. At low doping levels the electric field at the interface is, in contrast, smaller. In consequence, the dielectric constant is only decreased to the low-temperature ϵ_r in the immediate vicinity of the interface but increases fast toward its high bulk value away from the interface.

This reasoning also implies that the charge carrier distribution does barely depend on the doping level at room temperature but changes with the doping level at low temperatures: At room temperature ϵ_r is always constant, while at low temperature the ϵ_r profile depends on the heterostructure and on the doping level.

The left panel in Fig. 5.9 (a) confirms that at room temperature the mobile charge carriers accumulate close to the interface in both heterostructures investigated. However, since the integral charge carrier concentration is relatively high in both samples under investigation in this chapter, we observe only moderate changes in the charge carrier distribution at low temperature.

In the previous chapter, we scrutinized the low-temperature charge carrier distribution in further samples which varied more widely in their doping level. Drawing on these measurements, we can verify whether the charge carrier distribution is connected to the doping level at low temperature.

Figure 5.10 plots the ratio $Q_{\mathrm{interface}}/Q_{\mathrm{total}}$ against the total charge carrier concentration Q_{total} at a temperature of 60 K for all samples discussed in chapter 4 and 5. The data clearly confirm that at low temperature the charge carriers shift away from the interface if the total charge carrier concentration decreases.

In conclusion, our experiments show that the mobile charge carriers always accumulate at the interface at room temperature while the charge carrier distribution changes with the doping level at low temperature. Note that this analysis does *not* contradict our findings in the previous chapter where we showed that the 2DES extension d_{2DES} does barely depend on the V_{O} concentration at 60 K. The changes in the ratio $Q_{\mathrm{interface}}/Q_{\mathrm{total}}$ are mainly induced by mobile charge carriers shifting into tail states which reach deep into the $SrTiO_3$ bulk. Due to the peculiar electric field dependence of ϵ_r the majority of the charge carriers continues to accumulate close to the interface. The effective 2DES extension does thus barely change with temperature.

Our findings disagree with the findings of Siemons *et al.*[53]. Estimating the 2DES extension at low and at room temperature, Siemons *et al.* assume dielectric constants which do not depend on the electric field and find 2DES extensions which differ in order of magnitude between low and room temperature.

Our results agree with the findings of Copie *et al.*[165] Copie *et al.* analyze the 2DES extension in $LaAlO_3/SrTiO_3$ heterostructures at 300 K and at 8 K by conducting tip atomic force microscopy. They find that the 2DES extension in their sample barely depends on temperature which they ascribe to the peculiar electric field dependence of the $SrTiO_3$ dielectric constant.

The outcome of our measurements is also in agreement with the theoretical models of Raslan *et al.*[169] Raslan *et al.* take the strongly non-linear dielectric response of $SrTiO_3$ into account and show in elaborate models that the charge carriers are accumulating close to the interface at room temperature. They predict that, depending on the total charge carrier concentration, at low temperatures some of the mobile electrons shift away from the interface into states extending far into the $SrTiO_3$ bulk.

5.4 Conclusion

In this chapter we investigated the temperature dependence of the electronic interface properties in exemplary $SrTiO_3$-based heterostructures by photoemission spectroscopy. Making use of a self-consistent Poisson-Schrödinger model, the band bending and the charge carrier distribution can be reliably determined from the measured spectra. In the oxygen-depleted Al/$SrTiO_3$ heterostructure the charge carriers are found to be confined close to the interface, independent of the sample temperature. In the fully oxidized $LaAlO_3/SrTiO_3$ heterostructure the charge carriers are also located in large part in the immediate vicinity of the interface at room temperature, while the electrons spread further into the $SrTiO_3$ bulk when the temperature is lowered. We find that the total charge carrier concentration in the heterostructure determines whether the 2DES extension changes with the sample temperature. At high charge carrier concentrations, the mobile electrons are confined to the interface independent of the temperature. At low charge carrier concentrations, the mobile electrons shift further into the $SrTiO_3$ bulk when the temperature decreases. The dielectric constant ϵ_r proves, once again, to be the pivotal parameters governing the band diagram of the $SrTiO_3$-based heterostructures: The dielectric constant is modulated by temperature but also by the electric field at the interface, which is, in turn, depending on the total charge carrier concentration.

In conclusion, our photoemission experiments enabled us to track how the dielectric constant and, in consequence, the electronic interface properties in $SrTiO_3$-based heterostructures are tuned via temperature and doping. Thinking of practical devices, the temperature is, e.g., typically a parameter which is prescribed by the application and may not easily be adapted. Thus, the question arises whether the dielectric constant ϵ_r can be manipulated by other methods as well. Figure 5.11 illustrates that the dielectric constant does, indeed, depend on many other parameters: The chemical composition and defects have been shown to affect the dielectric constant of $SrTiO_3$ thin films.[170] ϵ_r can also be tailored by imposing epitaxial strain on $SrTiO_3$ thin films.[65] Tuning ϵ_r by such means opens up new possibilities to engineer the electronic interface properties in $SrTiO_3$-based heterostructures.

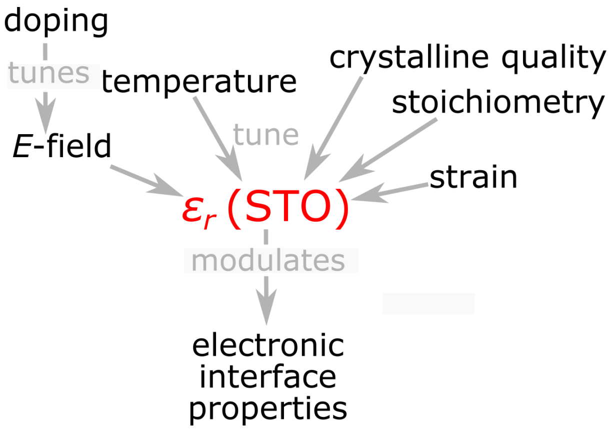

Fig. 5.11: The electronic interface properties in $SrTiO_3$-based heterostructures strongly depend on the $SrTiO_3$ dielectric constant which is, in turn, connected to temperature, doping, strain and the $SrTiO_3$ crystal quality.

Chapter 6

Interface engineering in transport experiments

So far we have investigated how the microscopic electronic structure in $SrTiO_3$-based heterostructures can be tuned by the oxygen vacancy concentration employing *spectroscopy*. In this chapter we now address the same question in *transport experiments*. Such measurements provide complementary information about the electronic structure of the materials, probing charge carrier concentrations as well as mobilities. These transport properties are interesting *per se*, as they are crucial for eventual practical device application which, e.g., rely on a high charge carrier mobility. Contrasting the results from spectroscopy and transport experiments, we furthermore gain a deeper insight into the functional properties governing transport in $SrTiO_3$-based heterostructures which might help to eventually engineer oxide materials toward practical devices.

To isolate the effect of the oxygen stoichiometry, we first analyze the transport properties of a $LaAlO_3/SrTiO_3$ heterostructure whose oxygen vacancy concentration we vary systematically. In the second part of the chapter, we focus on the comparison between transport and spectroscopy: In the photoemission experiment in the previous chapter, care has been taken that the samples do not change under the x-ray irradiation but remain in the state which is induced in the deposition process and probed in transport experiments. This allows us to directly contrast the findings from our spectroscopy and transport experiments. Lastly, we demonstrate how interface engineering via the oxygen vacancy concentration can be utilized in functional devices, using the example of a $LaAlO_3/SrTiO_3$-based memristor.

6.1 Engineering transport in $LaAlO_3/SrTiO_3$ by the oxygen vacancy concentration

Since the discovery of conductivity at the $LaAlO_3/SrTiO_3$ interface, a plethora of publications has corroborated the substantial effect of the oxygen vacancy concentration on the transport properties of the $LaAlO_3/SrTiO_3$ heterostructure.[3,4,52,53,55,163]

Varying the deposition parameters, most of these papers only differentiate between the regime where the entire $SrTiO_3$ bulk is doped with oxygen vacancies and becomes conductive and the regime in which the $SrTiO_3$ bulk retains its oxygen stoichiometry, remains insulating and only the $LaAlO_3/SrTiO_3$ interface becomes metallic.[3,4,55] However, we are not interested in the case in which oxygen vacancy doping renders the whole $SrTiO_3$ substrate metallic and do not further elaborate on this comparison. Just as in our photoemission experiments, we instead set out to investigate the transport properties in the fully oxidized state as well as in a state in which only

$SrTiO_3$ layers near the interface are doped with oxygen vacancies. The latter state is labeled as oxygen-depleted in the following.

Such a comparison has also already been addressed in literature but here the data is more sparse:[51–53,163,171] The publications consistently find that the charge carrier concentration is decreased in fully oxidized samples.[51–53,163,171] Yet, the studies do not yield clear results with respect to the dependence of the charge carrier mobility on the oxygen vacancy concentration: They find insignificant or even unsystematic changes in the charge carrier mobility as the oxygen vacancy concentration varies.[52,53,163,171]

These results might be distorted by the varying $SrTiO_3$ substrate quality. When the effect of the V_O concentration on the transport properties is analyzed in a set of samples in which the oxygen stoichiometry is varied systematically, the single samples might also differ, e.g., in the substrate quality and consequently in their transport properties. Such inhomogeneity might conceal the changes in mobility one is looking for. To avoid this complication and to isolate the effect of the V_O concentration, we probe *one and the same* sample, a 6 uc $LaAlO_3/SrTiO_3$ heterostructure, in different states instead.

Before discussing the transport properties, we shortly review the sample preparation in the next section.

6.1.1 Sample fabrication

To obtain accurate results for the charge carrier concentration and mobility, we use a sample patterned with a Hall bar geometry for the following experiment. The Hall bar was structured employing the technique proposed by Schneider *et al.*[172]: In a first step, a 2 uc thick crystalline $LaAlO_3$ film is deposited by pulsed laser deposition. Employing electron-beam lithography, the sample is patterned and SiO_2 is evaporated onto the sample. After removal of the photoresist, the disordered SiO_2 layer covers only specific predefined areas of the sample. When the $LaAlO_3$ deposition is resumed subsequently, the $LaAlO_3$ film continues to grow epitaxially atop of the 2 uc $LaAlO_3$ film, whereas it becomes disordered atop of the disordered SiO_2. In the second $LaAlO_3$ growth step, we deposit a 4 uc thick $LaAlO_3$ film. Since epitaxial $LaAlO_3/SrTiO_3$ heterostructures only become metallic when the thickness of the $LaAlO_3$ film exceeds 4 uc, a 2DES forms, wherever the $SrTiO_3$ substrate is capped with an epitaxial 6 uc thick $LaAlO_3$ film, while the sample remains insulating everywhere else.[1] This way a conducting area is written into the $SrTiO_3$ substrate which is electrically contacted by Ti/Au pads evaporated on top of the sample. The layer structure of such a sample is sketched in the top panel of Fig. 6.5 (a). Note that in Fig. 6.5 (a) a wire layout is shown, Hall bar layouts are fabricated in the same manner.

We measure the sample twice, first in the fully oxidized state, which is prepared by annealing the sample for 1 h at 600°C in a 500 mbar oxygen atmosphere. Subsequently, we create oxygen vacancies at the surface of the sample by heating it for 6 min at 300°C in a nitrogen atmosphere and measure it a second time.

6.1.2 Transport in the fully oxidized state

The comprehensive transport characterization of the fully oxidized $LaAlO_3/SrTiO_3$ heterostructure is shown in the top row of Fig. 6.1: The temperature dependence of the sheet resistance displayed in Fig. 6.1 (a) proves that the sample remains metallic down to low temperatures. The ratio of the room temperature resistance to the resistance at 2 K is called residual resistance ratio, or in short RRR, and represents a rough measure of the crystalline quality of the sample.[173]

---

[1] The disordered $LaAlO_3$ and SiO_2 layers are deposited at a high oxygen partial pressure and thus do not induce oxygen vacancies and, by association, metallicity in the $SrTiO_3$ substrate.

In the fully oxidized state, the RRR is comparably high showcasing the high crystalline quality of the $LaAlO_3/SrTiO_3$ heterointerface.

The temperature-dependent charge carrier concentration as well as the charge carrier mobility in the fully oxidized $LaAlO_3/SrTiO_3$ heterostructure are determined by Hall effect measurements: The raw data of an exemplary Hall effect measurement are depicted in the inset of Fig. 6.1 (b). The dependence of the transverse resistance R_t on the magnetic field is nicely matched by a linear fit proving that only one type of charge carrier contributes to the transport. The temperature dependence of the charge carrier concentration [mobility] is depicted in Fig. 6.1 (b) [(c)].

The charge carrier concentration is constant over the entire temperature range probed. This behavior is ascribed to the doping process in the fully oxidized samples, viz. electronic reconstruction which does not depend on the sample temperature.

Let us next take a closer look at the mobility which is strongly varying with temperature: In the Drude model, the electron mobility μ is defined as $\mu = \frac{e \cdot \tau}{m}$ where m denotes the effective mass of the electron and τ describes the integral scattering time, i.e., the average time an electron travels before it is backscattered.[173] In $SrTiO_3$-based heterostructures the mobile electrons are scattered off charged defects, other electrons and phonons:[174,175] The contributions μ_{defect}, $\mu_{\text{e-e}}$ and μ_{phonon} of the different scattering processes to the mobility are added up to the total mobility μ according to Matthiesen's rule[173]

$$\mu^{-1} = \mu_{\text{defect}}^{-1} + \mu_{\text{e-e}}^{-1} + \mu_{\text{phonon}}^{-1}. \tag{6.1}$$

μ_{defect}, $\mu_{\text{e-e}}$ and μ_{phonon} show a characteristic dependence on temperature: The mobility contribu-

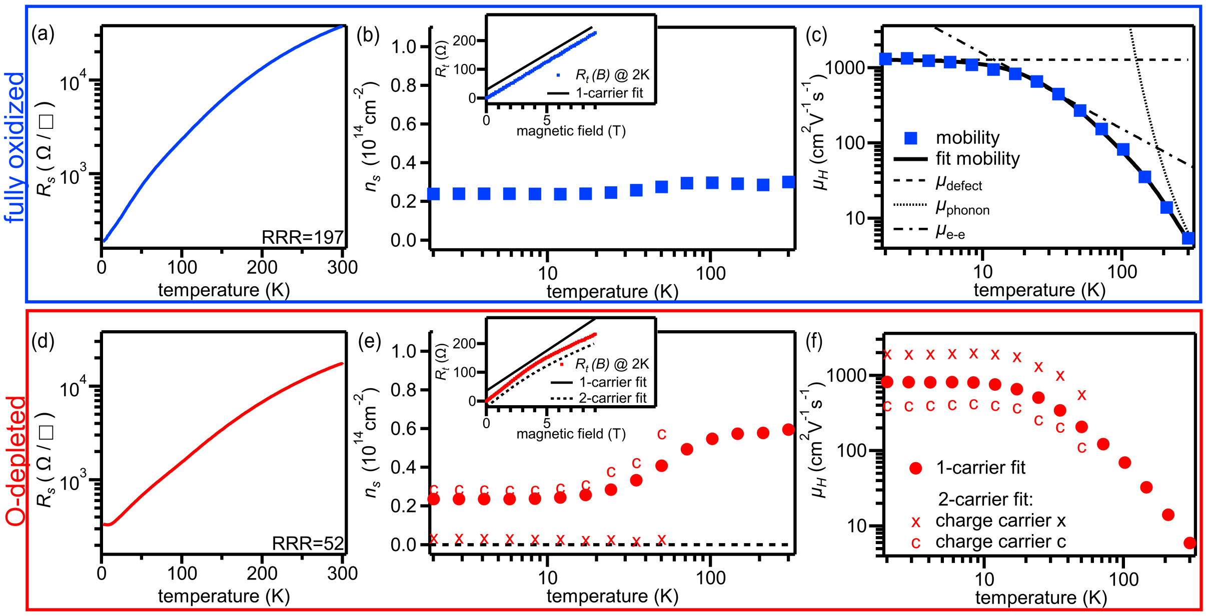

Fig. 6.1: Transport properties of a 6 uc $LaAlO_3/SrTiO_3$ heterostructure in the fully oxidized state (top row) and in an oxygen-depleted state (bottom row): Temperature-dependent sheet resistance (a), charge carrier concentration (b) and charge carrier mobility (c) in the fully oxidized state. Figures (d) to (f) depict the respective quantities for the case of the oxygen-depleted state. The insets in (b) and (e) exemplarily show the raw data of the Hall effect measurements at 2 K. The fit curves are also displayed and offset for clarity.

In the fully oxidized state we find evidence of only one charge carrier type, while at least two types of charge carriers contribute to the electronic transport in the oxygen-depleted state. The different mobilities of the charge carriers at low temperatures indicate that they originate from bands with different mass and/or from different quantum well states.

tion τ_{defect} from defect scattering is typically assumed to be independent of temperature. The mobility contribution $\mu_{\text{e-e}}$ related to electron-electron interaction scales as $\mu_{\text{e-e}} \propto T^{-2}$. The mobility contribution μ_{phonon} linked with electron-phonon interaction scales as $\mu_{\text{phonon}} \propto \exp\left(\frac{\hbar\omega_{\text{LO}}}{k_B T}\right)$ where ω_{LO} denotes the frequency of the longitudinal optical phonon modes in SrTiO_3.

A fit of the mobility using these relations is shown in Fig. 6.1 (c). The single contributions to the mobility are also separately depicted in Fig. 6.1 (c). At different temperatures different scattering processes prevail which explains the characteristic dependence of the mobility on the temperature: At low temperatures, defect scattering limits the mobility while the electron-electron interaction becomes important at intermediate temperatures. At high temperatures, the mobile charge carriers are, in contrast, mainly scattered off phonons.

6.1.3 Transport in the oxygen-depleted state

The transport properties of the oxygen-depleted $\text{LaAlO}_3/\text{SrTiO}_3$ heterointerface are depicted in the bottom row of Fig. 6.1: Also in the oxygen-depleted state, the sheet resistance decreases when the temperature is lowered from room temperature as Fig. 6.1 (d) shows. However, this trend reverses at low temperatures ($T \approx 10\,\text{K}$) and a resistance minimum is observed which Brinkman *et al.*[4] ascribe to the Kondo effect. Brinkman *et al.* claim that at low temperature the mobile charge carriers are scattered off localized magnetic moments which are introduced by the oxygen vacancies. In the oxygen-depleted state, the residual resistance ratio is decreased as well which confirms that more defects, viz. oxygen vacancies, are now present at the interface.

To determine the charge carrier concentration as well as the mobility, we once again measure the Hall effect: In the oxygen-depleted state the transverse resistance R_t does not show a linear dependence on the applied magnetic field at low temperature [cf. inset in Fig. 6.1 (e)]. A transport model which only contains one charge carrier type does thus no longer describe the experimental data satisfactorily below 50 K. To achieve a good fit to the experimental data, we have to include a second charge carrier type with a different mobility in the transport model. The inset in Fig. 6.1 (e) shows that the transverse resistance is indeed adequately modeled by a 2-carrier fit. Note that the fit curves are offset for clarity. One charge carrier type labeled c is characterized by a high concentration and a low mobility while the other charge carrier type denoted by x is characterized by a low concentration and a higher mobility. At temperatures above 50 K the Hall effect data can again adequately be fitted by a single carrier model.

The temperature-dependent mobility of the two charge carrier species is depicted in Fig. 6.1 (f). The mobility of charge carrier x and charge carrier c show a similar variation in temperature as was observed for the fully oxidized $\text{LaAlO}_3/\text{SrTiO}_3$ sample [see Fig. 6.1 (b)]. The characteristic variation of the charge carrier mobilities is ascribed to the different scattering processes which limit the electron mobility at different temperatures, as discussed above. The temperature dependence of the charge carrier mobilities also gives an indication why a single charge carrier model is applicable at temperatures above 50 K: The mobilities of the two types of charge carrier draw near each other in this temperature range. In consequence, the two kinds of charge carriers can no longer be distinguished from each other and the single charge carrier model yields the integral charge carrier concentration above 50 K.

Next, we scrutinize the charge carrier concentration in the oxygen-depleted sample which is plotted in Fig. 6.1 (e). The total charge carrier concentration is found to increase under oxygen depletion [compare Figs. 6.1 (b) and (e)]. We furthermore note that in the oxygen-depleted state the concentration of charge carrier c depends on the temperature: At a temperature below ≈60 K the charge carrier concentration decreases. Such a charge carrier freeze-out is already known from oxygen-deficient SrTiO_3 and is ascribed to charge carrier trapping at shallow donor sites, i.e., at oxygen vacancies.[176]

Finally, we compare our results to the previous studies:[52,53,163,171] The increase in the charge carrier concentration as well the carrier freeze-out observed under oxygen depletion have already been documented in the earlier publications.[52,53,163,171] We do now also observe that the low-temperature charge carrier mobilities is different in the fully oxidized and the oxygen-depleted state. The earlier papers did, in contrast, not find any significant variation in the mobility as a function of the V_{O} concentration. This discrepancy might be due to variations in the $\mathrm{SrTiO_3}$ substrate quality which distort the results of ref. [52, 53, 163, 171] as discussed above. Furthermore the discrepancy between our measurements and the earlier publications could also be traced back to the data analysis: In Figs. 6.1 (e) and (f) we also plot the charge carrier concentration and mobility one obtains if the subtle influence of the second charge carrier species is ignored and the Hall effect measurements are fitted by a single carrier model. While the integral charge carrier concentration does not change by much, one erroneously obtains a low-temperature mobility which lies close to the mobility measured in the fully oxidized state.

Having familiarized ourselves with the transport characteristics of the $\mathrm{LaAlO_3/SrTiO_3}$ heterostructure at different oxygen vacancy concentrations, we directly compare the findings of transport and photoemission experiments in the next section.

6.2 Contrasting spectroscopy and transport experiments

In the transport experiments discussed above as well as in the spectroscopy experiments in chapter 4, we sought to isolate the effect of the oxygen vacancy concentration on the electronic interface properties by measuring the *same sample once in the fully oxidized and once in an oxygen-depleted state.* Whereas in the transport experiments the oxygen-depleted state is prepared by heating the $\mathrm{LaAlO_3/SrTiO_3}$ heterostructure in a nitrogen atmosphere, in the spectroscopy experiments the oxygen vacancies are created by the intense x-ray beam. It is thus safe to assume that the oxygen-depleted states probed in the transport experiments above and the spectroscopy measurements in chapter 4 differ and cannot be directly juxtaposed.

In contrast, in chapter 5 we examined two different $\mathrm{SrTiO_3}$-based heterostructures, a fully oxidized $\mathrm{LaAlO_3/SrTiO_3}$ sample and an oxygen-depleted $\mathrm{Al/SrTiO_3}$ sample, in which the respective oxygen vacancy concentration was set at the time of growth. During the spectroscopy measurement we took special care to keep the samples in their intrinsic state, i.e., the state which is induced by the deposition process and is probed in transport experiments. In this case we can thus directly contrast the results obtained in the spectroscopic measurements to the outcome of transport experiments on these very samples.[2]

The transport characterization of the two samples investigated in the spectroscopy experiments in chapter 5 is summarized in Fig. 6.2. Although the absolute charge carrier concentrations and mobilities measured here (Fig. 6.2) and above (Fig. 6.1) differ, we immediately recognize the features which are characteristic for a fully oxidized and an oxygen-depleted $\mathrm{SrTiO_3}$-based heterostructure in the temperature-dependent charge carrier concentration [see Fig. 6.2 (a)] and mobility [see Fig. 6.2 (b)]: In the fully oxidized $\mathrm{LaAlO_3/SrTiO_3}$ sample, only one charge carrier type is found to contribute to the electronic transport. Its concentration does not depend on the temperature. In contrast, two charge carrier species which differ in their concentration and mobility are detected at low temperature in the oxygen-depleted $\mathrm{Al/SrTiO_3}$ heterostructure.

---

[2] The van der Pauw geometry is used for the following transport measurements on the samples which are investigated in photoemission. In the following measurements the whole sample area is thus probed.

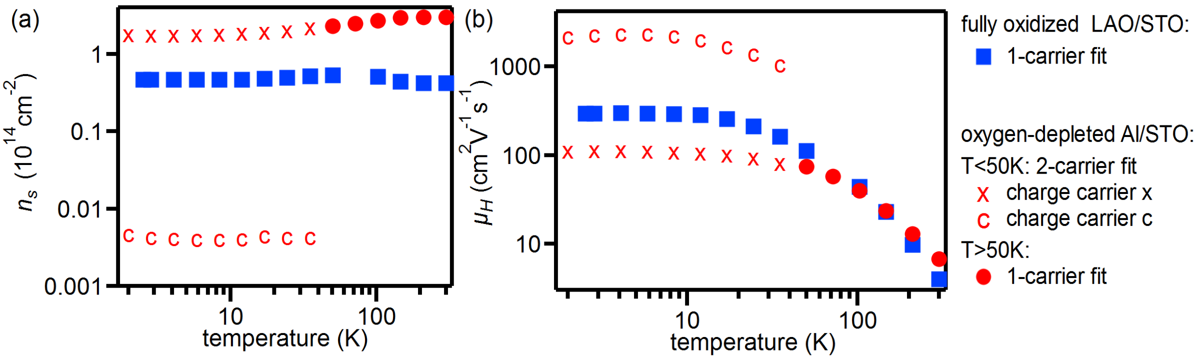

Fig. 6.2: Temperature-dependent sheet charge carrier concentration (a) and mobility (b) of the fully oxidized $LaAlO_3/SrTiO_3$ sample and the oxygen-depleted $Al/SrTiO_3$ heterostructure measured in the photoemission experiments in chapter 5.

6.2.1 Temperature dependence of charge carrier concentration

Let us first compare the temperature dependence of the charge carrier concentration in spectroscopy and transport measurements.

Analyzing the spectra in chapter 5 with the Poisson-Schrödinger ansatz we assumed that the charge carrier concentration does not depend on the measurement temperature. Figure 6.2 (a) depicts the temperature-dependence of the charge carrier concentration in the two samples which is measured in transport experiments. In the transport experiments the charge carrier concentration of the fully oxidized $LaAlO_3/SrTiO_3$ sample is indeed found to be nearly temperature-independent. In contrast, the charge carrier concentration in the oxygen-depleted $Al/SrTiO_3$ heterostructure is decreasing with temperature as some of the charge carriers freeze out at low temperatures. However, the charge carrier concentration at 60 K and at 300 K, i.e., the measurement temperatures in the photoemission experiment do not differ by much. The assumption of a constant mobile charge carrier concentration is thus justified for both samples.

In the next section, we thus exemplarily compare the charge carrier concentration estimated in transport and in spectroscopy at 60 K.

6.2.2 Quantitative comparison of charge carrier concentrations

In Tab. 6.1 we list the values of the charge carrier concentration estimated in transport and spectroscopy measurements for different samples. To improve the statistics, we do not only include the fully oxidized $LaAlO_3/SrTiO_3$ sample and the $Al/SrTiO_3$ sample discussed above but also the samples investigated in chapter 4: While the oxygen-depleted state of the samples in chapter 4 is not accessible to transport experiments, the fully oxidized state corresponds to the state of the sample after the post-oxidation and can thus be probed in transport measurements as well.[3]

Scrutinizing Tab. 6.1, we note that the charge carrier concentrations estimated by the two complementary methods differ greatly. In all heterostructures the charge carrier concentration estimated in spectroscopy is found to exceed the charge carrier concentration measured in transport experiments.

---

[3] Note that the transport measurements are conducted after the photoemission experiments. The samples in chapter 4 become inhomogeneous in the photoemission experiments as the samples are *locally* doped with oxygen vacancies during the measurement. Transport measurements of such inhomogeneous samples can, however, not be trusted (see Sec. 2.3.1). In Tab. 6.1 we thus indicate the charge carrier concentrations of nominally similar samples instead of the charge carrier concentration of the very samples probed in photoemission.

heterostructure	**discussed in**	**charge carrier concentration** ($10^{14}\,\mathrm{cm}^{-2}$)	
		in spectroscopy	**in transport**
fully oxidized $LaAlO_3/SrTiO_3$ (001)[3]	chapter 4	$1.66^{+0.25}_{-0.20}$	0.52 ± 0.15
fully oxidized $LaAlO_3/SrTiO_3$ (111)[3]	chapter 4	$0.78^{+0.12}_{-0.12}$	0.62 ± 0.23
fully oxidized $LaAlO_3/SrTiO_3$ (111)	chapter 5	$1.80^{+0.20}_{-0.25}$	0.50 ± 0.08
oxygen-depleted $Al/SrTiO_3$ (001)	chapter 5	$6.39^{+0.08}_{-1.77}$	2.3 ± 0.4

Tab. 6.1: Comparison of charge carrier concentrations estimated by spectroscopy and transport experiments. The transport measurements yield charge carrier concentrations which are smaller than the charge carrier concentrations estimated from photoemission spectroscopy.

This discrepancy in the mobile charge carrier concentrations estimated is ascribed to several factors: For the oxygen-depleted $Al/SrTiO_3$ heterostructure the number of trapped charge carriers might be underestimated in our photoemission analysis in which we assume that each oxygen vacancy releases one mobile electron while the other electron remains trapped.[132] This doping rule derived by theory might not hold true. In the experiment, more charge carriers might actually be trapped, e.g., by clustered oxygen vacancies and contribute to the Ti^{3+} weight but not to the mobile charge carrier concentration.

Yet, this scenario cannot explain why the charge carrier concentrations estimated also differ in the fully oxidized state in which all oxygen vacancies are quenched. The discrepancy in the mobile charge carrier densities is due to other effects in these samples: The resistance of $LaAlO_3/SrTiO_3$ heterostructures is known to decrease strongly and persistently when the samples are exposed to visible light as additional charge carriers are excited by the illumination.[177] To minimize the effect of the photogenerated carriers, transport is typically measured after the samples have been kept in the dark for more than 24 h. In the photoemission experiments the intense x-ray beam presumably generates additional charge carriers as well. We conclude that transport and spectroscopy experiment examine different states of the sample and thus yield different results for the charge carrier density. Recall that the charge carrier concentration estimated in spectroscopy is always higher than the charge carrier concentration measured in transport.

Furthermore the sample volume probed differs in the two measurement methods. While transport is measured across the whole sample for the heterostructures in Tab. 6.1, the spectroscopy experiments scrutinize only a small spot on the sample surface. Depending on the homogeneity of the sample, the measurement results in spectroscopy and transport experiments might thus vary. To shed light on this question, we investigated whether the charge carrier concentration is varying across the heterostructure on samples patterned with several Hall bars. Indeed, we find that the charge carrier concentration varies across the sample surface by 11% (21%) for (001) $LaAlO_3/SrTiO_3$ heterointerfaces ((111) $LaAlO_3/SrTiO_3$ heterointerfaces). Inhomogeneity in the samples might thus also contribute to the discrepancy in charge carrier concentrations observed.

While a direct comparison between spectroscopy and transport experiments is found to be inhibited, a qualitative comparison between transport and spectroscopy measurements can nevertheless be instructive and provide valuable insight into the functional properties governing transport in $SrTiO_3$-based heterostructures, as discussed in the next section.

6.2.3 Spectroscopic insight into low-temperature transport

In the previous sections we only compared the charge carrier *concentrations* estimated in transport and spectroscopy experiments. However, transport measurements also yield information about the charge carrier mobility, a property which is of particular importance in practical electronic devices.

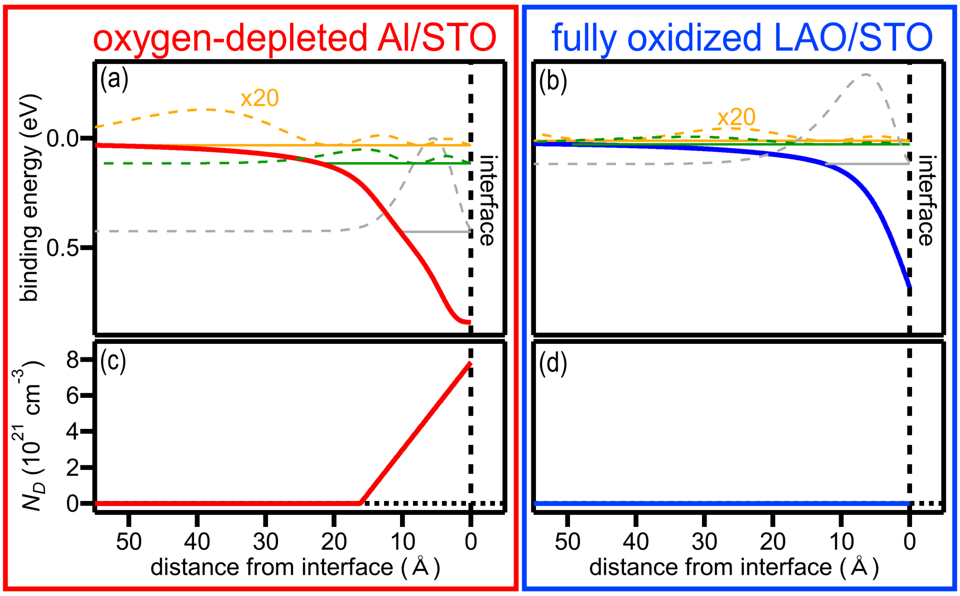

Fig. 6.3: Conduction band edge and subband structure in the oxygen-depleted Al/$SrTiO_3$ (a) and the fully oxidized $LaAlO_3$/$SrTiO_3$ sample (b). The dashed lines in (a) and (b) furthermore show the probability densities for the three subbands with the lowest eigenenergies. The oxygen vacancy distribution is shown in (c) and (d) for the oxygen-depleted Al/$SrTiO_3$ and the fully oxidized $LaAlO_3$/$SrTiO_3$ sample, respectively.

In contrast to the charge carrier concentration, the charge carrier mobility is not directly linked to a specific quantity which spectroscopy experiments probe: Our spectroscopy experiments, e.g., can only provide limited insight into the electronic transport at room temperature: At 300 K the electron mobility is mainly limited by phonon scattering processes to which our HXPES experiments are, however, not sensitive. However, below 30 K another scattering mechanism, viz. defect scattering, pushes itself to the fore [see decomposition of mobility in Fig. 6.1 (c)]. Here, our HXPES experiments probing the spatial distribution of the mobile electrons as well as of the dopant atoms may help to garner a better understanding of the microscopic mechanisms limiting the charge carrier mobility at low temperature.[4]

The oxygen-depleted Al/$SrTiO_3$ heterostructure is scrutinized first: The transport characterization depicted in Fig. 6.2 (red symbols) reveals that at low temperature two kinds of charge carriers which significantly differ in their mobility contribute to the electronic transport. While the concentration of the charge carriers with low mobility is found to be high, the concentration of the charge carriers with high mobility is found to be low.

Let us now look into the results of the photoemission experiments on the oxygen-depleted Al/$SrTiO_3$ heterostructure: As oxygen vacancies are known for their dichotomic role in $SrTiO_3$-based heterostructures in which they do not only act as dopants but also as impurity scattering centers, we compare the distribution of the oxygen vacancies to the distribution of the mobile electrons.[A5] Figure 6.3 (c) sketches the profile of the charged oxygen vacancies in the heterostructure, whereas Fig. 6.3 (a) depicts the conduction band edge and subband structure. The dashed lines in Fig. 6.3 (a) furthermore show how the mobile charge carriers distribute into the three

---

[4] Note that our HXPES measurements which yield the distribution of the mobile electrons and dopants are conducted at a temperature of 60 K. However, in the previous chapter we found that the charge carrier distribution does not change strongly as the temperature is varied due to the peculiar electric field dependence of the dielectric constant. We can thus safely compare our HXPES results to the electron mobility measured below 30 K.

subband states with the lowest eigenenergies.[5] We see that the charge carriers in the gray and green subband states accumulate in the immediate vicinity of the interface, viz. in the region doped with oxygen vacancies. The electrons in the yellow quantum well state spread, in contrast, further into the $SrTiO_3$ substrate and only barely overlap with the V_O-doped zone. Notably, the former quantum well states are highly occupied while the latter quantum well states accommodate far less electrons. Thus we tentatively attribute the charge carriers with the high density to the quantum well states localized at the interface, while the charge carriers with the low density are ascribed to the quantum well states extending into the $SrTiO_3$ bulk. This assignment also matches to the mobilities measured for the different charge carrier types: The charge carriers with the high density accumulate in the vicinity of the interface and encounter many defects, in particular oxygen vacancies, and thus scatter often. Their mobility is thus decreased. In contrast, the charge carriers with the low density extend far into the $SrTiO_3$ bulk where they move rather undisturbed. Their mobility is thus high. Any more quantitative comparison is impeded as the charge carrier concentration estimated in transport and spectroscopy measurements widely differ.

The comparison between spectroscopy and transport measurements on the $Al/SrTiO_3$ heterostructure showcases that it is crucial to separate the oxygen vacancies from the mobile charge carriers to increase the charge carrier mobility.

Next, we have a look at the other heterostructure we investigated in transport and spectroscopy measurements, the fully oxidized $LaAlO_3/SrTiO_3$ heterostructure in which all oxygen vacancies in the $SrTiO_3$ substrate are quenched. According to the reasoning above, this sample should behave distinctly different in transport experiments: Although the charge carriers also distribute into different quantum well states in this sample [see dashed lines in Fig. 6.3 (b)], in absence of an oxygen vacancy gradient [cf. Fig. 6.3 (d)] the charge carriers in the different quantum well states are expected to scatter equally often moving through the crystal. Indeed, in the transport characterization depicted in Fig. 6.2 (blue symbols) we only find evidence of a single charge carrier species.

The low-temperature mobility of these charge carriers is, however, quite low considering that the dopants and the mobile charge carriers are separated in the fully oxidized $LaAlO_3/SrTiO_3$ heterostructure. The low mobility is in part due to the specific sample investigated. The mobility measured for (111) heterointerfaces is typically lower than for (001) heterointerfaces.[6] We furthermore speculate that the mobility is low as the majority of the charge carriers are accumulating in the vicinity of the interface, viz. in defect-rich layers, as Fig. 6.3 (b) shows. The strong confinement of the charge carriers is, in turn, ascribed to the high integral charge carrier concentration in the sample ($Q_{\text{total}} = 1.8 \cdot 10^{14}\,\text{cm}^{-2}$, estimated in photoemission experiments).

Juxtaposing transport and spectroscopy experiments, we follow up on this hypothesis: Our spectroscopy measurements in the last chapters revealed that the charge carriers shift away from the interface into the $SrTiO_3$ bulk when the total charge carrier concentration is decreasing (see Fig. 6.4 (b) which is replicated from the previous chapter). Note that this effect is expected to be even more pronounced if the charge carrier concentration is lowered even further than in Fig. 6.4 (b), owing to the electric field dependence of ϵ_r. Following the line of reasoning above, we expect that the low-temperature mobility is increasing when the charge carrier concentration is decreasing as the mobile charge carriers shift away from the interface. To check this hypothesis, we compile the transport properties of our assorted (001)-oriented post-oxidized $LaAlO_3/SrTiO_3$ samples in Fig. 6.4 (a). Depending on the deposition conditions in use, the charge carrier concentration and mobility are found to be strongly varying. It is, however, evident that the charge carrier mobility is increasing as the charge carrier concentration is decreasing.

---

[5] The occupation of the subbands lying even closer to the Fermi edge is small and is ignored.

[6] The lower mobility is ascribed to the worse quality of the highly polar $SrTiO_3$ (111) substrates.

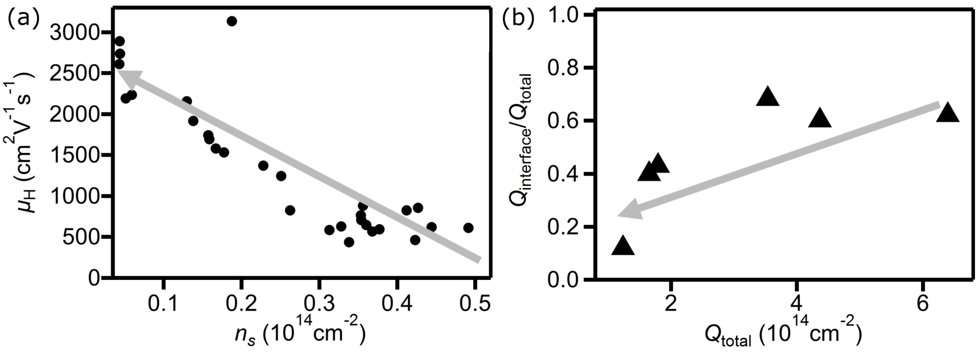

Fig. 6.4: (a) Low-temperature charge carrier mobility μ_H vs. charge carrier concentration n_s of fully oxidized $LaAlO_3/SrTiO_3$ samples. (b) Share $Q_{\text{interface}}/Q_{\text{total}}$ of charge carriers which are located within 1 nm of the interface vs. the integral charge carrier concentration Q_{total} at low temperature. Values estimated in photoemission experiments in chapter 4 and 5. Note that Q_{total} (used in the photoemission analysis) and n_s (used in transport analysis) describe the same quantity. When the total charge carrier concentration is increasing, the electrons accumulate in the defect-rich interfacial layers where they scatter more often. This finding may explain why the low-temperature electron mobility decreases when the charge carrier concentration rises.

The anti-correlation between the charge carrier concentration and the charge carrier mobility in $SrTiO_3$-based heterostructures has also been established in many other publications.[103,104,178] These observations corroborate the hypothesis that the low-temperature mobility in the fully oxidized $LaAlO_3/SrTiO_3$ sample is limited as the majority of the charge carriers are confined in the defect-rich layers near the interface.

This finding also shows the way to increased low-temperature charge carrier mobilities in fully oxidized $LaAlO_3/SrTiO_3$ heterostructures: The charge carrier mobility is enhanced when the interface quality is improved[102] as well as when the charge carrier concentration is decreased.[103,104,178] Furthermore, one could try to tune the electric field dependence of the relative permittivity to change the charge carrier distribution and, in consequence, the charge carrier mobility.

6.3 Tailoring a $LaAlO_3/SrTiO_3$-based memristor device

Previously, we have investigated in transport as well as in spectroscopy experiments how the electronic properties of the heteroepitaxial $LaAlO_3/SrTiO_3$ interface can be adjusted by varying the V_O concentration. The controllability of these electronic interface properties is not only interesting from the point of view of fundamental physics but is also a key requirement for applications of the $LaAlO_3/SrTiO_3$ heterostructure in future electronic devices. By the example of a memristor, we will demonstrate how a $LaAlO_3/SrTiO_3$-based device can be customized by means of the V_O concentration.

6.3.1 The memristor device

A memristor is a circuit element whose resistance is depending on the prior charge flow through the element. This behavior becomes apparent in its current-voltage characteristics in which the current I shows a memory behavior, i.e., a hysteresis, depending on the previously applied bias voltage V_b. The hysteresis loop of a memristor is pinched, i.e., it passes through the coordinate origin as there is no charge flow at zero bias voltage.

The memory behavior is at the heart of the memristor functionality: Memristors are, e.g., utilized to emulate synapses in artificial neural networks:[96] In such an application, the conductance of the memristor encodes the synaptic strength.[179] Bias voltage pulses mimicking nerve impulses excite the memristor device and change the conductance of the memristor. Depending on the exact characteristics of the memory effect in the device, one can build artificial synapses which store their conductance and thus information reliably or other synapses which respond fast to new stimuli, i.e., adapt their conductance quickly to changing voltage pulses.

In the following, we demonstrate the functionality of a $LaAlO_3/SrTiO_3$-based memristor. The results presented here are published in ref. [A7]. The memristor device was built in collaboration with Patrick Maier and Fabian Hartmann, Technische Physik Würzburg. To this end, a thin conducting wire was patterned in the $LaAlO_3/SrTiO_3$ sample as sketched in the top panel of Fig. 6.5 (a). The sample was structured using the method by Schneider*et al.*[172] described in Sec. 6.1.1. Prior to the transport measurements, the sample was post-oxidized to prepare the fully oxidized state. Subsequently, the oxygen vacancy concentration is controlled by annealing the sample in a nitrogen atmosphere at 300°C.

6.3.2 Tuning the memristor by the back gate voltage

Figure 6.5 (b) displays exemplary current-voltage curves measured at cryogenic temperatures on the $LaAlO_3/SrTiO_3$ sample after the fully oxidized sample was annealed in a nitrogen atmosphere for 6 min. We observe pinched hysteresis loops, which are indicative of memristive behavior. By analyzing the equivalent circuit of the device [see bottom panel of Fig. 6.5 (a)], we can comprehend how the memory effect emerges: Using the current I and the bias voltage V_b, the total resistance $R_{\mathrm{tot}} = V_b/I$ of the device is computed according to Ohm's law. R_{tot} is comprised of the resistance R_{wire} of the conducting wire and the contact resistances $R_{\mathrm{LAO},1}$ and $R_{\mathrm{LAO},2}$

$$R_{\mathrm{tot}} = R_{\mathrm{wire}} + R_{\mathrm{LAO},1} + R_{\mathrm{LAO},2}. \tag{6.2}$$

First we focus on the regime of negative bias voltage and consider that the bias voltage is slowly increased from 0 V toward negative values [see dotted arrow in Fig. 6.5 (b)]. The resistance R_{wire} is always ohmic and thus constant independent of the bias voltage. The contact resistances $R_{\mathrm{LAO},1}$ and $R_{\mathrm{LAO},2}$ can, in contrast, be viewed as Schottky barriers. With rising bias voltage, tunneling electrons might gradually charge trap states in the Schottky barriers, which increases the Schottky barrier height and thereby the resistances $R_{\mathrm{LAO},1}$, $R_{\mathrm{LAO},2}$ as well as the total resistance R_{tot} according to equation (6.2). Due to the increasing resistance R_{tot} at higher bias voltage, the current I is not increasing linearly with the bias voltage but more slowly.

When the bias voltage is now decreased again [see dashed arrow in Fig. 6.5 (b)], the trap states temporarily remain charged. At the same bias voltage, the total resistance in the downward sweep is thus higher than in the upward sweep and the current I passing through the memristor is consequently smaller. Only when the sign of the bias voltage is finally reversed, the trap states are bit by bit discharged and the total resistance R_{tot} is reduced again. With this effect in mind, the hysteresis at positive bias voltages can then be explained following a similar line of thought as above.

The memory effect, which is also termed memristance, is quantified by determining the area which is enclosed by the hysteresis loop [see colored areas in Fig. 6.5 (b)]. Figure 6.5 (b) shows that the current-voltage characteristics and the memory effect can be tuned by the application of a back gate voltage V_g: The area enclosed by the pinched hysteresis loop is largest for a back gate voltage of –3 V, while it decreases for both, larger and smaller back gate voltages.

Thinking back to equation (6.2), we can explain this behavior. Applying a negative back gate voltage V_g, mobile charge carriers are depleted from the interface and R_{wire} is increased accordingly.[9] At a constant bias voltage, the voltage drop across the contact resistances $R_{\mathrm{LAO},1}$ and $R_{\mathrm{LAO},2}$ is thus smaller at a negative back gate voltage than at zero back gate voltage. The charging of the trap states is less effective and the memory effect is consequently smaller. In

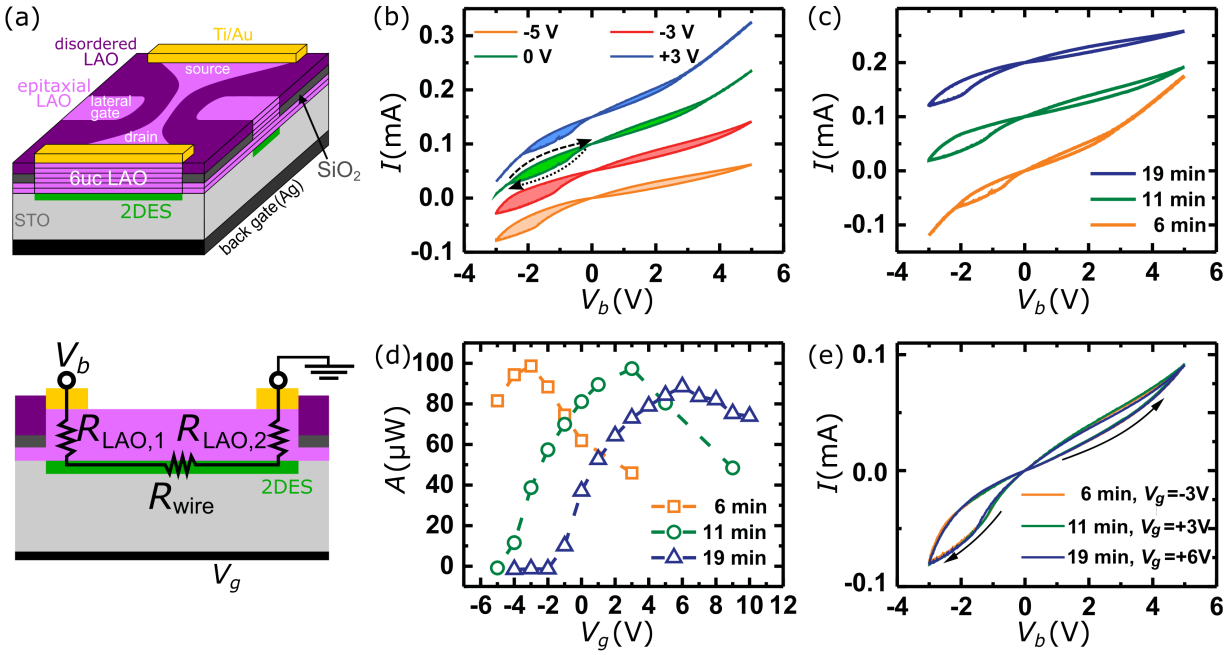

Fig. 6.5: (a) Sketch (top figure) and equivalent circuit (bottom figure) of the memristor device. A 2DES only forms in regions where the $SrTiO_3$ substrate is capped with an epitaxial 6 uc $LaAlO_3$ film. (b) Current-voltage characteristics at different back gate voltages. The sample was annealed in a nitrogen atmosphere for 6 min at 300°C. (c) Current-voltage characteristics depending on annealing time. In this experiment the back gate voltage was set to $V_g = +3$ V. The curves in (b) and (c) are artificially offset. In the current-voltage plots the characteristic feature of a memristor, a pinched hysteresis loop, is observed. (d) Area enclosed by the pinched hysteresis loops depending on back gate voltage and annealing time. (e) Current-voltage characteristics for different combinations of annealing time and back gate voltage. The area enclosed by the pinched hysteresis loop can be tuned by varying the back gate voltage as well as the annealing time. Figure adapted from ref. [A7].

contrast, at a positive back gate voltage electrons accumulate in the conducting channel as well as at the contacts.[9] Thus, the contact resistances $R_{\mathrm{LAO},1}$ and $R_{\mathrm{LAO},2}$ become more ohmic and the memory effect vanishes altogether. At a specific intermediate back gate voltage, the memristance is therefore maximal.

6.3.3 Tuning the memristor by the oxygen vacancy concentration

The memristance cannot only be tuned by the back gate voltage but also by the oxygen vacancy concentration which is varied by annealing. Figure 6.5 (c) depicts the current-voltage characteristics of the memristor device at a back gate voltage of $V_g = +3$ V after different annealing periods.[7] The area of the hysteresis loop is noticeably changing with the annealing time.

Figure 6.5 (d) shows a comprehensive analysis of the area enclosed by the hysteresis loop as a function of the back gate voltage V_g and annealing time. At each annealing time, we observe a characteristic variation of the memory effect depending on the back gate voltage. However, the memory effect peaks at higher back gate voltages, the longer the sample is annealed and the more oxygen vacancies are created. By adjusting the annealing time, one can even switch between normally-on and normally-off memristors which do or do not show a memory effect at zero gate

---

[7] In the original publication[A7] we mistakenly indicated that zero back gate voltage was applied in this particular measurement run.

voltage. The shift in Fig. 6.5 (d) is attributed to the additional mobile electrons released by the oxygen vacancies, which screen the back gate voltage. This reasoning is confirmed in Fig. 6.5 (e): The hysteresis loops shown in the figure are measured at different combinations of annealing times and back gate voltages but lie almost on top of each other.

6.3.4 Engineering the $LaAlO_3/SrTiO_3$-based memristor

We demonstrated that the memory effect in the $LaAlO_3/SrTiO_3$ based memristor can be tuned in two ways, reversibly by applying a back gate voltage and irreversibly by varying the oxygen vacancy concentration.[8]

The tuning via the gate voltage can, in particular, be exploited to adjust the memristor to the experimental tasks *in operando*: When memristors are embedded in artificial neural networks, one could, e.g., control the speed of learning processes by the back gate voltage.[A7] Furthermore the back gate voltage could compensate variability in the fabrication process: The oxygen vacancy concentration is known to depend strongly on the deposition parameters and also on the post-deposition sample treatment. As the memristance in turn reacts very sensitively to the oxygen vacancy concentration, it might be necessary to adjust the memory effect after the deposition process which can be achieved by applying a back gate voltage. In this manner one could realize fault-tolerant memristor networks, which is of paramount importance for an eventual upscaling of the device fabrication.

While the back gate voltage can be employed to fine-tune the memristance in a straightforward way, it is more cumbersome to modulate the memristance by the oxygen vacancy concentration in the experiments discussed here as we have to anneal the samples for that purpose: On the one hand, the effect of the annealing cannot easily be reversed. On the other hand, the annealing cannot be limited to a specific area and affects the sample as a whole. This is a big caveat as eventually one would like to build several memristor devices on one sample which could then not be tuned individually by annealing.

However, as demonstrated in chapter 3 and 4 one can also use a *focused* x-ray beam to control the oxygen vacancy concentration in $LaAlO_3/SrTiO_3$ heterostructures. Further on, this effect could be exploited as a lithography method to pattern $LaAlO_3/SrTiO_3$ samples. One might, e.g., raster an x-ray beam across a $LaAlO_3/SrTiO_3$ heterostructure to tune the conductivity locally and to structure the sample. This method has the advantage that it only increases the oxygen vacancy concentration locally right at the spot on which the x-ray beam impinges. When one combines the irradiation with the x-ray beam with oxygen dosing one can even change the oxygen vacancy concentration reversibly.[9]

The whole sample could potentially even be structured with the x-ray beam instead of using the elaborate patterning method described above. For this purpose one must be able to create insulating regions by the irradiation with the x-ray beam and/or oxygen dosing. This can not be achieved for epitaxial $LaAlO_3/SrTiO_3$ heterostructures as the metallic carriers which are induced by the electronic reconstruction cannot be suppressed. With disordered $LaAlO_3/SrTiO_3$ samples this might be, however, feasible as the conductivity in these samples can be completely quenched. (The capping is needed to preserve the oxygen vacancy concentration in the $SrTiO_3$ substrate in air.) Employing such a patterning process one could thus not only achieve a precise spatially

---

[8] The experiments discussed have all been conducted at cryogenic temperatures. However, with slight modifications (e.g., by replacing the back gate with a top gate) one might be able to observe similar effects at room temperature.

[9] The reoxidation by oxygen dosing is not as locally limited as the oxygen depletion by the x-ray beam. However, in our experiments we found that the reoxidation is still only affecting the immediate vicinity of the x-ray beam spot. The reoxidation is probably brought about by O radicals excited by the x-ray beam which can diffuse a bit away from the x-ray spot.

resolved and reversible control over the oxygen vacancy concentration but could also greatly reduce the number of processing steps.

6.4 Conclusion

In this chapter we again investigate how the electronic properties of the $LaAlO_3/SrTiO_3$ heterostructure depend on the oxygen vacancy concentration but use a different probe than before, viz. transport measurements.

The transport experiments confirm that the charge carrier concentration is increasing along with the oxygen vacancy concentration. The low-temperature charge carrier mobility is also found to vary with the oxygen vacancy concentration.

To gain a deeper understanding of the functional properties governing the charge carrier transport, we compare the findings of transport and spectroscopy measurements. We discover that the charge carrier concentrations estimated by the two measurement methods cannot be directly related to each other as transport and spectroscopy probe different states.

A qualitative comparison between transport and spectroscopy nevertheless yields valuable insight into the principles governing low-temperature transport in $SrTiO_3$-based heterostructures: The low-temperature mobility of fully oxidized $LaAlO_3/SrTiO_3$ is shown to be limited due to the charge carriers accumulating in the defect-rich layers near the interface, where they often scatter. In oxygen-depleted states, one charge carrier species with a high density and a low mobility and one charge carrier species with a low density and high mobility are found to contribute to transport. The charge carriers with a high density but a low mobility are found to be localized at the interface where they frequently collide at defects as well as at oxygen vacancies. The second charge carrier type with a higher mobility is, in contrast, ascribed to electrons in quantum well states which penetrate deeply into the substrate. Far away from the interface these electrons move rather undisturbedly which explains their enhanced mobility.

Additionally, we demonstrate how the interface engineering via the oxygen vacancy concentration can be exploited in an electronic device and show that a $LaAlO_3/SrTiO_3$-based memristor can effectively be engineered by gating as well as by the oxygen vacancy concentration.

Chapter 7

The two-dimensional electron system at the (111) $LaAlO_3/SrTiO_3$ interface

Starting with the discovery of the two-dimensional electron system, rich electronic behavior has been found to emerge at the (001) $LaAlO_3/SrTiO_3$ heterointerface. Recently interest has also arisen in $LaAlO_3/SrTiO_3$ heterostructures oriented in other crystal directions: Akin to the well-established (001)-oriented $LaAlO_3/SrTiO_3$ samples, a 2DES, e.g., also forms at the (111) interface between $LaAlO_3$ and $SrTiO_3$.[180] The (111) heterointerfaces are, in particular, of special interest as their peculiar geometry is predicted to support topologically non-trivial states.[77,181] In a density functional theory study (111)-oriented $LaAlO_3/SrTiO_3$ heterostructures have, e.g., been called 'a three-orbital strongly correlated generalization of graphene'.[77]

In this chapter, we thus take a closer look at the (111) $LaAlO_3/SrTiO_3$ heterointerface: The peculiar topology of $SrTiO_3$ in the (111) orientation and its effects on the electronic structure are discussed first. We demonstrate the high-quality of the fabricated $LaAlO_3/SrTiO_3$ heterostructures and investigate their electronic properties in transport measurements. Employing soft x-ray angle-resolved photoemission, the microscopic low-energy electronic structure of the (111) $LaAlO_3/SrTiO_3$ interface is scrutinized. The Fermi surface and band maps measured reveal information on the dimensionality of the electron system as well as on the character of the interfacial charge carriers. The results presented here are compiled in ref. [A13].

7.1 $SrTiO_3$ in (111) orientation

In (111) orientation the $SrTiO_3$ crystal can be thought of as alternating SrO_3 and Ti planes as Fig. 7.1 (a) illustrates. One film monolayer (in short ML) which is comprised of one SrO_3 and Ti plane is 2.3 Å thick.

The low-energy electronic structure in $SrTiO_3$ is governed by the Ti $3d_{t_{2g}}$ orbitals. We thus take a closer look at the arrangement of the Ti atoms at the (111) interface. In the single layers the Ti atoms form a triangular lattice [see largest atoms in Fig. 7.1 (b)]. The single Ti layers are not positioned directly on top of each other but are periodically shifted as depicted in Fig. 7.1 (b). Two triangular lattices of Ti atoms constitute a buckled honeycomb lattice, while three triangular Ti layers form a dice lattice together.

As the result of the change in interface topology, completely new physics may emerge at the (111)-oriented interface. Thin (111)-oriented $SrTiO_3$ films can be regarded as topologically equivalent to graphene which is known to host topologically non-trivial phases.[182,183] However, while p_z orbitals near the Fermi level determine the physics in graphene,[184] the three Ti $3d$ t_{2g} orbitals

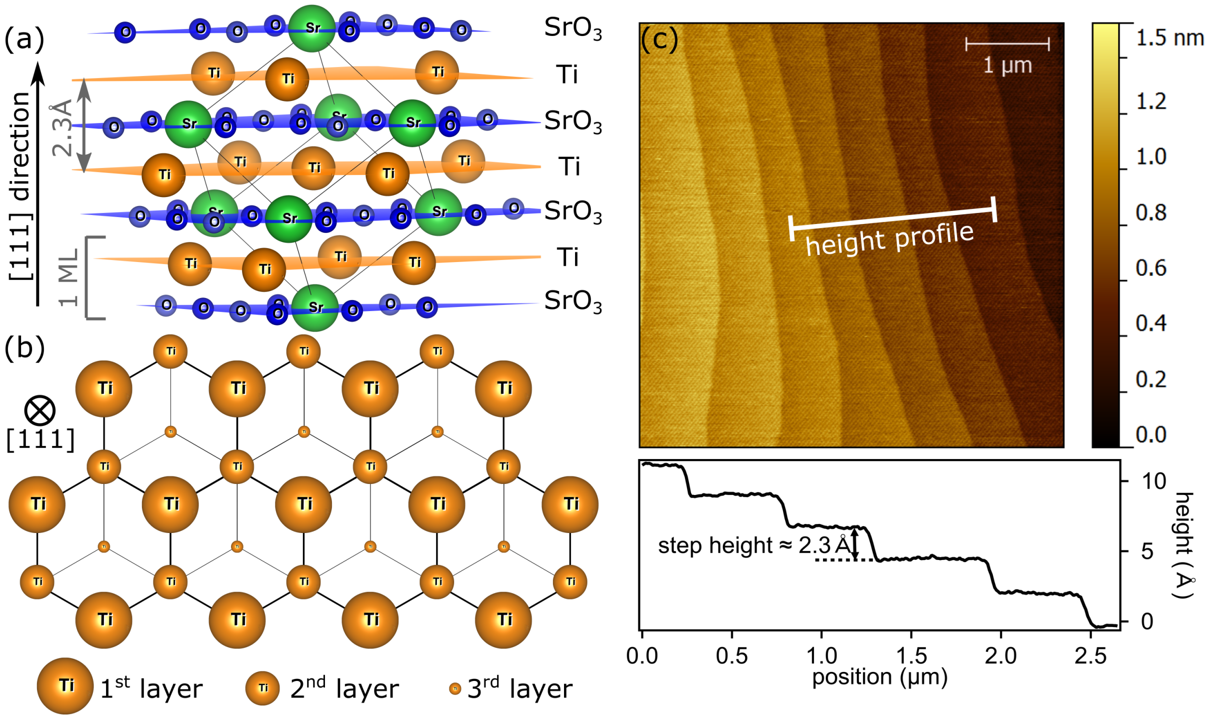

Fig. 7.1: (a) Crystal structure of $SrTiO_3$: Oriented in [111] direction the $SrTiO_3$ crystal can be thought of as a sequence of SrO_3 and Ti planes. We define a monolayer (ML) as comprised of one SrO_3 and one Ti plane. (b) Arrangement of Ti atoms at the (111) $SrTiO_3$ surface: The two topmost planes of Ti atoms (a Ti bilayer) form the characteristic honeycomb lattice. (c) AFM topography image of (111)-oriented $SrTiO_3$ crystal after HF treatment and annealing. From the AFM image a height profile is extracted which is depicted in the bottom figure. The crystal surface is single terminated and atomically flat after the termination procedure.

take on this role in $SrTiO_3$. Since the Ti $3d$ t_{2g} orbitals are more localized, correlations are furthermore expected to be enhanced, which makes such (111)-oriented heterostructures a promising candidate to realize strongly correlated topological phases. Employing density-functional calculations, Doennig *et al.*[77], e.g., investigated $(LaAlO_3)_N(SrTiO_3)_M$ superlattices and found an unexpected richness of phases. Depending on the $SrTiO_3$ quantum well thickness as well as on the strain and symmetry imposed in the heterostructure, different ground states are predicted to develop, ranging from topological phases with Dirac point Fermi surfaces to charge ordered multiferroic flat band phases. However, the experimental realization and investigation of such highly polar (111)-oriented $LaAlO_3/SrTiO_3$ heterostructures is still widely lacking and their potential remains largely untapped.

Here, we report on the growth and the characterization of (111)-oriented $LaAlO_3/SrTiO_3$ heterostructures.

7.2 Characterization of the (111) $LaAlO_3/SrTiO_3$ heterointerface

A defined surface termination is a prerequisite for controlled thin film growth. Similar to the (001)-oriented substrates a defined surface termination can also be achieved for (111)-oriented $SrTiO_3$ substrates:[185] The customary termination procedure for (001)-oriented $SrTiO_3$ substrates relies on the fact that, immersed in water and subsequently in a hydrofluoric acid solution, the SrO layers are preferably etched while the TiO_2 layers are more stable.[88,89] Due to the similar chemical composition of the single layers in [111] and [001] direction,[1] one can employ an alike process to attain a Ti-terminated $SrTiO_3$ (111) surface. The termination procedure for the (111)-oriented $SrTiO_3$ has been implemented during the course of this thesis. Detailed preparation parameters are given in Sec. D.1 in the Appendix. After the termination procedure the surface morphology is characterized employing atomic force microscopy (AFM). An exemplary AFM image of a $SrTiO_3$ (111) surface is depicted in Fig. 7.1 (c) and proves that the surface is single terminated and atomically flat.

The $LaAlO_3$ films are subsequently deposited by PLD on the Ti-terminated substrates: The $LaAlO_3$ is ablated from a single-crystal $LaAlO_3$ target using a KrF excimer laser at a laser fluence of $0.9\,\mathrm{J/cm^2}$ and a pulse repetition rate of 1 Hz. For the deposition, the substrate is maintained at a temperature of 780 °C. To forestall the formation of oxygen vacancies, the oxygen background pressure is set to $1 \cdot 10^{-3}$ mbar during heating as well as during the film growth. To ensure full oxidation, the samples are furthermore cooled down after the deposition in 500 mbar O_2 with the temperature being held constant for 1 h at 600 °C.

The growth of the $LaAlO_3$ films is monitored by RHEED. Following the intensity of the specularly reflected electron beam, we track the relative surface coverage of the $LaAlO_3$ film in real time during the deposition. Exemplary RHEED oscillations recorded during the deposition of a 7-ML-thick $LaAlO_3$ film are shown in Fig. 7.2 (a). The regular oscillations show that the $LaAlO_3$ film builds up layer-by-layer. We note in passing that – at the same deposition conditions – one needs a factor $\frac{1}{\sqrt{3}}$ less laser pulses to grow a monolayer $LaAlO_3$ on a (111)-oriented sample than on a (001)-oriented sample. The disparate growth speed can be traced back to the different thickness of the $LaAlO_3$ monolayers in the [001] ($1\,\mathrm{ML} \mathrel{\widehat{=}} 3.905\,\text{Å}$) and the [111] direction ($1\,\mathrm{ML} \mathrel{\widehat{=}} 2.3\,\text{Å}$). The inset of Fig. 7.2 (a) furthermore shows the RHEED pattern of the $LaAlO_3/SrTiO_3$ heterostructure right after the deposition. The clear diffraction spots as well as the Kikuchi lines in the RHEED pattern prove the high crystalline quality of the $LaAlO_3$ film deposited.

With low energy electron diffraction (LEED) one can probe the symmetry of the $LaAlO_3$ film surface. A typical LEED pattern of our samples is depicted in Fig. 7.2 (b). We observe clear diffraction spots, which is indicative of an ordered surface. In the LEED pattern the sixfold symmetry of the (111) surface is clearly discernible: The diffraction pattern marked by red circles matches in its periodicity to the surface lattice constants. We furthermore detect additional diffraction spots (blue circles) attributed to a (2x2) surface reconstruction, which might be brought about by the polarity inherent in the (111)-oriented $LaAlO_3/SrTiO_3$ sample as discussed in the next section.[2]

While we can draw conclusions about the $LaAlO_3$ film surface based on the LEED and RHEED diffraction patterns, we can analyze the interface quality by scanning transmission electron microscopy (STEM). Figure 7.2 (c) depicts a STEM image of a 9-ML-thick $LaAlO_3/SrTiO_3$ sample and a line profile which is extracted across the interface (see red line in the STEM image). The STEM measurements reveal that the crystal structure of the $LaAlO_3/SrTiO_3$ sample is uniform and coherent. The interface between the $LaAlO_3$ film and the $SrTiO_3$ substrate is atomically sharp and comparable in width and quality to the (001)$LaAlO_3/SrTiO_3$ interfaces.[A9] Furthermore we note that the $LaAlO_3$ film thickness deduced from the STEM image corresponds to the thickness which is inferred from RHEED oscillations. The crystal properties of the $LaAlO_3/SrTiO_3$ heterostructures are moreover characterized by x-ray diffraction (XRD): A θ–2θ scan of a thick $LaAlO_3/SrTiO_3$ heterostructure is shown in Fig. 7.2 (d). The peaks in the spectrum can be assigned to reflections at the (111) lattice planes in the $SrTiO_3$ substrate and

---

[1] While the $SrTiO_3$ substrate is built up from a sequence of SrO and TiO_2 layers in [001] direction, SrO_3 layers alternate with Ti layers in [111] direction.

[2] The (2x2) surface reconstruction cannot be explained by tilted oxygen octahedra, i.e., by the rhombohedral symmetry of the $LaAlO_3$ film in (111)-oriented samples. This is in contrast to the (001)-oriented surface.[A9]

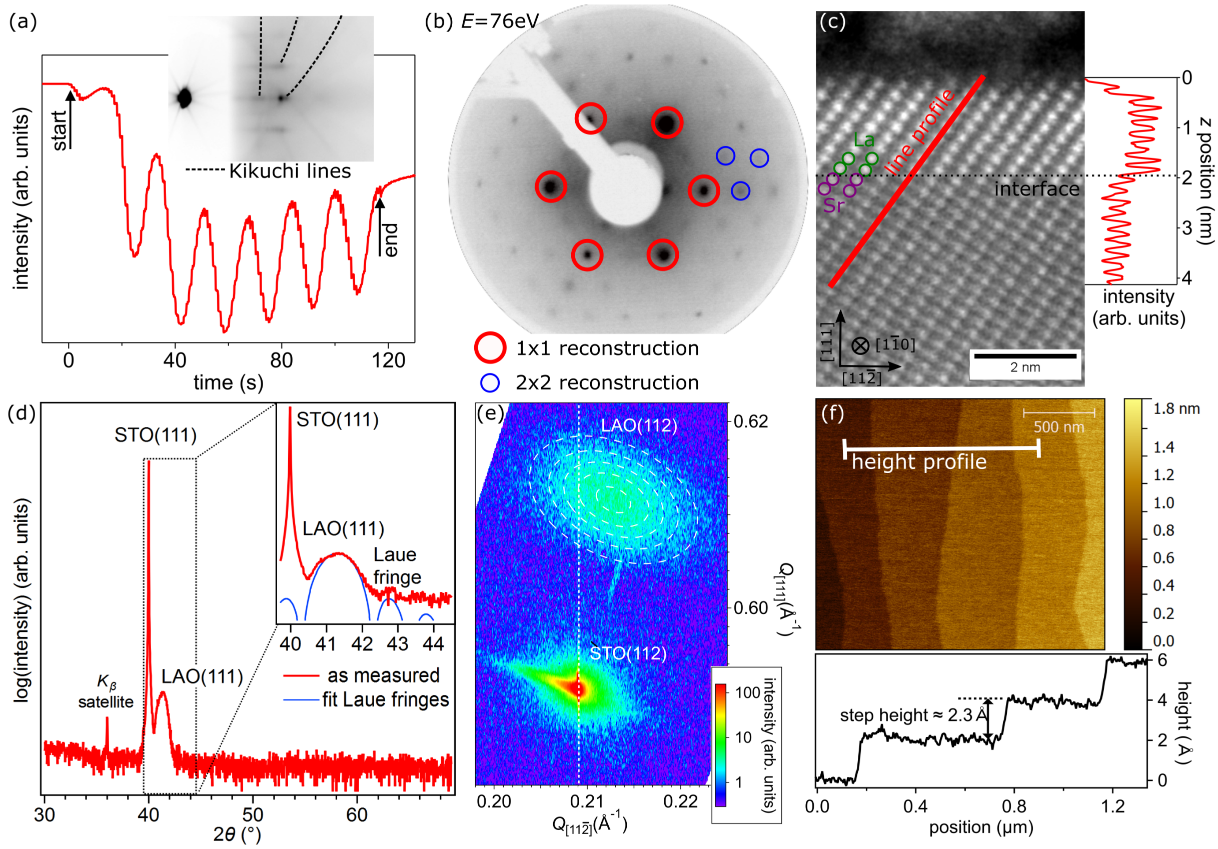

Fig. 7.2: Characterization of the (111)-oriented $LaAlO_3/SrTiO_3$ heterostructure: (a) RHEED intensity oscillations recorded during the deposition of a 7-ML-thick $LaAlO_3$ film. The inset shows the RHEED image right after the deposition. (b) LEED pattern of 8-ML-thick $LaAlO_3/SrTiO_3$ sample. The sharp RHEED and LEED diffraction patterns after the film deposition attest to the good crystalline order of the $LaAlO_3$ surface. (c) STEM image of a 9-ML-thick $LaAlO_3/SrTiO_3$ heterostructure. The STEM image as well as the line profile depicted alongside confirm that the interface is atomically sharp. (d) XRD θ–2θ scan of a 43-ML-thick $LaAlO_3/SrTiO_3$ sample. The appearance of Laue interference fringes confirms that the $LaAlO_3$ film is of high crystalline quality. (e) Reciprocal space map of a 50-ML-thick $LaAlO_3/SrTiO_3$ sample. The $LaAlO_3$ film is no longer coherently strained to the $SrTiO_3$ substrate but not yet fully relaxed. (f) AFM topography image of a non post-oxidized 9-ML-thick $LaAlO_3/SrTiO_3$ heterostructure showing an atomically flat film surface.

the $LaAlO_3$ film, confirming the single phase character of the $LaAlO_3$ thin film. Zooming in on the $LaAlO_3$ (111) peak, one takes notice of Laue interference fringes beside the main peak. Such fringe patterns are due to interference effects and emerge if the x-ray photons scatter at a finite number of equally-spaced planes.[186] From the spacing of the Laue fringes we estimate the number of crystalline $LaAlO_3$ monolayers which amounts to 43 ML. This value coincides with the film thickness of 43–46 ML $LaAlO_3$ which is determined on the basis of the RHEED oscillation analysis. The agreement between the analysis methods indicates that the entire $LaAlO_3$ film is highly crystalline, homogeneous in thickness and confined between well-defined interfaces.

We also recorded a complete map of the reciprocal space for a 50-ML-thick $LaAlO_3/SrTiO_3$ sample around the (112) reciprocal lattice peak, which is shown in Fig. 7.2 (e). We note that, compared to the $SrTiO_3$-related diffraction peak, the $LaAlO_3$-related diffraction peak is shifted vertically in $Q_{[111]}$ direction as well as horizontally in $Q_{[11\bar{2}]}$ direction. This reveals that the $LaAlO_3$ film and the $SrTiO_3$ substrate differ in their out-of-plane as well as in their in-plane lattice constant, respectively. We can thus conclude that the 50-ML-thick $LaAlO_3$ film is no longer epitaxially strained to the $SrTiO_3$ substrate but relaxed.

Figure 7.2 (f) depicts an AFM topography image of a non-post-oxidized $LaAlO_3/SrTiO_3$ heterostructure. After the $LaAlO_3$ deposition, the sample surface is still smooth and atomically flat. The surface roughness is comparable to the one of the underlying $SrTiO_3$ substrate. The step height of the terraces corresponds to the step height found for the $SrTiO_3$ substrate [cf. Fig. 7.1 (c)]. The AFM experiments thus confirm that the $LaAlO_3$ film grows in a layer-by-layer mode as inferred from the RHEED measurements.

Having confirmed the good structural quality of our (111)-oriented $LaAlO_3/SrTiO_3$ samples, we turn to their transport characterization in the next section.

7.3 The polar discontinuity in (111)-oriented $LaAlO_3/SrTiO_3$ heterostructures

We first look at the transport properties of $LaAlO_3/SrTiO_3$ heterostructures as a function of the film thickness. In *fully oxidized* (111)-oriented $LaAlO_3/SrTiO_3$ heterostructures a film-thickness-dependent metal-insulator transition is observed at a $LaAlO_3$ overlayer thickness of 6 ML, as Fig. 7.3 (c) shows. The appearance of such a critical thickness points to an electronic reconstruction which is triggered by a polar discontinuity at the heterointerface, as is the case for the (001)-oriented samples.[A6]

Let us thus take a closer look at the sequence of layer charges across the (111) $LaAlO_3/SrTiO_3$ interface to check for such a polar discontinuity: The $SrTiO_3$ substrate as well as the $LaAlO_3$ film are highly polar in the [111] direction: The $SrTiO_3$ substrate ($LaAlO_3$ film) in (111) orientation is built up of lattice planes with charge ∓ 4 (∓ 3) [see layer charges depicted in gray in the left panel of Fig. 7.3 (b)]. Subtracting the substrate polarity, the sequence of layer charges changes [see effective layer charges depicted in black in the left panel of Fig. 7.3 (b)]. Compared to the SrO_3 planes (charge –4) the LaO_3 planes (charge –3) carry a single positive charge. Contrasted to the Ti^{4+} planes, the Al^{3+} planes are effectively single negative charged. Notably, the change in polarity across the (111) $LaAlO_3/SrTiO_3$ interface is of the same size as the change in polarity at the (001)-$LaAlO_3/SrTiO_3$ heterointerface [compare left panels in Figs. 7.3 (a) and (b)].

The resulting potential build-up is thus also similar for both crystalline orientations [see middle panels in Figs. 7.3 (a) and (b)]. As the layers with charge ±1 are closer together, the potential rises in more steps in the (111)-oriented heterostructures. The increase in potential per step is, however, smaller which, in turn, compensates the larger number of potential steps. In the simple electronic reconstruction scenario electrons are transferred from the $LaAlO_3$ surface to the interface as soon as the potential build-up exceeds the $LaAlO_3$ band gap.[107] Following this reasoning, the critical thickness expressed in nanometers is expected to be similar for the (001)- and (111)-oriented samples which is indeed the case as Fig. 7.3 (d) illustrates (compare blue and red symbols).

In Figs. 7.3 (c) and (d) a theory estimate of the critical thickness in (001)-oriented $LaAlO_3/SrTiO_3$ heterostructures by Reinle-Schmitt *et al.*[107] is also shown (gray dashed line). Based upon a simple electrostatic model, the authors calculate the critical thickness and arrive at a value of 13.75Å which is in very good agreement with the critical thickness observed for the (111)-oriented heterostructure.

This raises the question why the approach based on the effective layer charges works: Instead of considering effective layer charges, one might argue that the polarity in the (111)-oriented $SrTiO_3$ substrate already has to be compensated prior to growth. LEED patterns of the bare (111) substrate surface indeed show evidence for a surface reconstruction. In this case one would have to consider a polar discontinuity between a neutral substrate and a film with layer charge

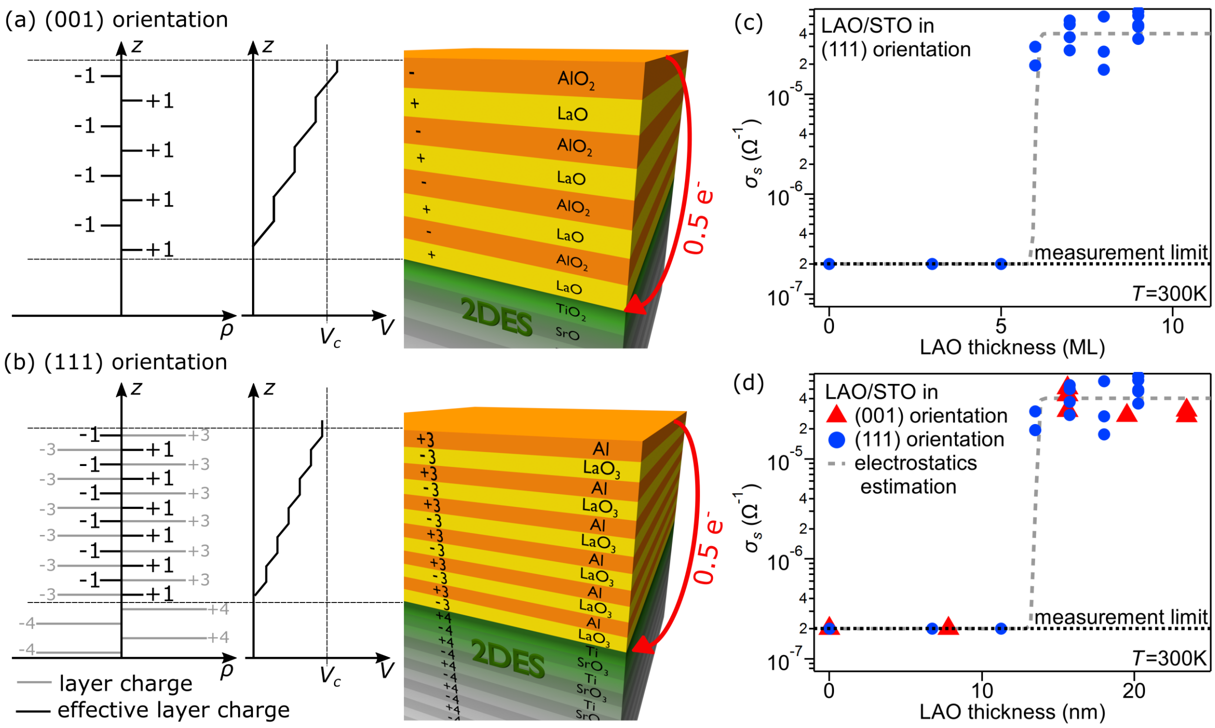

Fig. 7.3: Polar discontinuity in (001)- and (111)-oriented $LaAlO_3/SrTiO_3$ heterostructures: Ionic charge of the atomic layers and potential profile across the (001)- (a) and (111)-oriented (b) $LaAlO_3/SrTiO_3$ heterointerface. While the layer charges differ in the (001) and (111) orientation, the change in polarity at the interface is of the same size for both orientations (compare effective layer charges). The slope of the potential in the $LaAlO_3$ film is consequently also alike. (c) Room-temperature sheet conductance of (111)-oriented $LaAlO_3/SrTiO_3$ heterostructures as a function of the $LaAlO_3$ film thickness in ML. (d) Room-temperature sheet conductance of (001)- and (111)-oriented $LaAlO_3/SrTiO_3$ heterostructures as a function of the $LaAlO_3$ film thickness in nm. The critical thickness observed for the (001) and (111) interfaces is very similar when expressed in nm.

±3. Such a model would yield an entirely different potential build-up and critical thickness and would, in particular, call for an interface which is doped with hole charge carriers. However, this scenario is clearly not observed in the experiments.

Here, one has to bear in mind that the $LaAlO_3$ film is deposited on a $SrTiO_3$ substrate which is heated to high temperatures under a low oxygen partial pressure: While the $SrTiO_3$ (111) substrate is insulating at room temperature, $SrTiO_3$ as well as $LaAlO_3$ shows a measurable conductance at growth temperature.[187,188] Whereas the $SrTiO_3$ surface reconstructs at room temperature to compensate for the finite polarity of the crystal, metallic charge carriers can presumably screen the polarity of the $SrTiO_3$ crystal at the growth temperature, prevent a surface reconstruction and restore the surface to the bulk structure. Such a process has already been shown to occur on (111)-oriented $LaAlO_3$ substrates[188] but might apply to $SrTiO_3$ substrates as well. On an unreconstructed $SrTiO_3$ surface the $LaAlO_3$ film can grow coherently which matches to the structural characterization presented in the previous section [see, e.g., RHEED oscillations in Fig. 7.2 (a) and TEM image in Fig. 7.2 (c)].

In such a picture, the polarity of the $LaAlO_3/SrTiO_3$ heterostructure as a whole is compensated by metallic charge carriers at the deposition. When the sample is subsequently cooled down to room temperature after the deposition process and $LaAlO_3$ as well as the $SrTiO_3$ bulk become insulating again, only the change in polarity from substrate to film layers is compensated at the

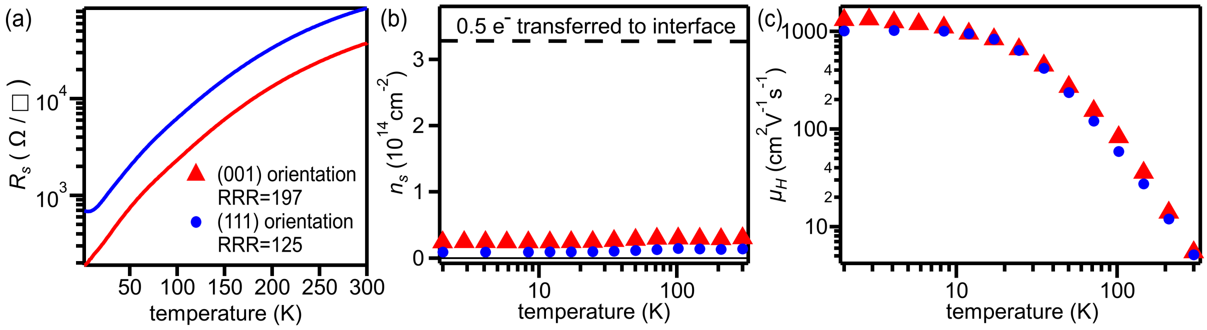

Fig. 7.4: Transport characterization of (111)-oriented 9 ML $LaAlO_3/SrTiO_3$ heterostructure. Temperature-dependent sheet resistance (a), charge carrier concentration (b) and charge carrier mobility (c). The transport characterization of a typical (001)-oriented $LaAlO_3/SrTiO_3$ heterostructure is also displayed for comparison.

$LaAlO_3/SrTiO_3$ heterointerface, while the surface of the $LaAlO_3$ film reconstructs to alleviate the finite polarity of the whole heterostructure. Indeed, we observe a surface reconstruction in the room-temperature LEED pattern of the (111)-oriented $LaAlO_3/SrTiO_3$ samples [see Fig. 7.2 (b)].

The appearance of a polar discontinuity and an ensuing electronic reconstruction also goes well with our photoemission experiments in chapter 3 in which we investigated doping mechanisms not only in (001)-oriented but also in (111)-oriented $LaAlO_3/SrTiO_3$ heterostructures: Just as for the (001)-oriented $LaAlO_3/SrTiO_3$, the quasiparticle weight is not completely suppressed for the (111)-oriented $LaAlO_3/SrTiO_3$ samples under oxygen dosing. We ascribed the remaining quasiparticle weight to an electronic reconstruction which is triggered by a polar discontinuity.[A6]

A comprehensive characterization of the electronic transport in a (111)-oriented heterostructure is displayed in Fig. 7.4. For comparison, Fig. 7.4 also depicts the results of transport measurements on a fully oxidized (001) $LaAlO_3/SrTiO_3$ heterointerface which shows very similar characteristics. This observation supports our hypothesis that the (001)- and (111)-oriented $LaAlO_3/SrTiO_3$ heterointerfaces are doped by the same mechanism, i.e., an electronic reconstruction which is triggered by a polar discontinuity at the heterointerfaces. The low-temperature mobility exceeding $1000\,\mathrm{cm}^2\mathrm{V}^{-1}\mathrm{s}^{-1}$ attests to the high crystalline quality of the (111) $LaAlO_3/SrTiO_3$ heterointerface [see Fig. 7.4 (c)].[3] Just as for the (001)-oriented sample, the charge carrier concentration in the (111)-oriented samples also falls short of the 0.5 electrons/interfacial unit cell which are expected to be transferred to the interface in the most simple electronic reconstruction scenario [see Fig. 7.4 (b)]. This discrepancy is tentatively ascribed to the fact that the polar discontinuity at the (111) $LaAlO_3/SrTiO_3$ heterointerface is partially alleviated by other processes and that charges may also be trapped at defects, as is discussed for the (001) heterointerfaces.[116]

7.4 Tuning the charge carrier concentration by an electric field

For any future technological application it is crucial that one can tune the electronic interface properties of the (111)-oriented $LaAlO_3/SrTiO_3$ heterostructure. For the case of the (001)-oriented $LaAlO_3/SrTiO_3$ interface, numerous studies[9,100,189] have already demonstrated that immediate control over the interface properties is achieved by the electric field effect. This way one can even switch the (001)-oriented interface from an insulating to a metallic state[9] or toggle

---

[3] Typically, the low-temperature mobilities of our (111)-oriented $LaAlO_3/SrTiO_3$ are smaller ($\mu_H \approx (300–500)\,\mathrm{cm}^2(\mathrm{Vs})^{-1}$) and vary, in particular, considerably across the sample area, which is attributed to the worse crystalline quality of the (111)-oriented substrates.

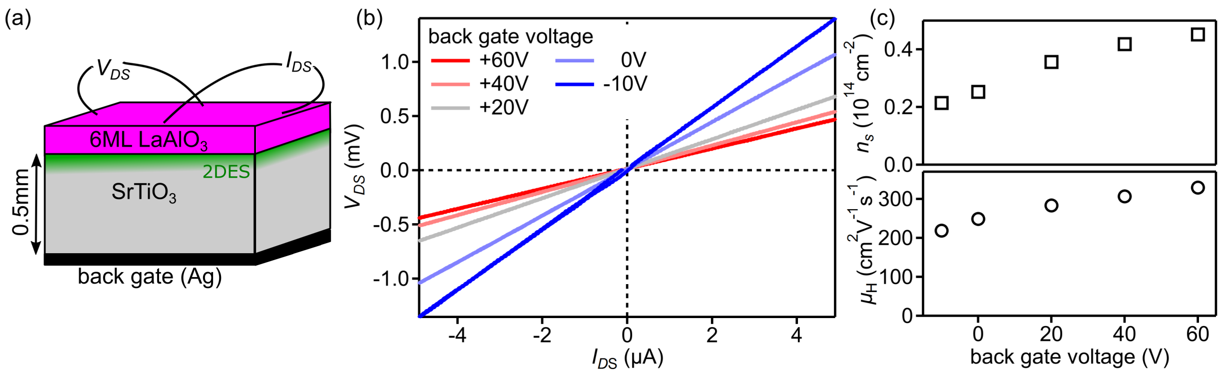

Fig. 7.5: Tuning the 2DES at the (111) $LaAlO_3/SrTiO_3$ heterointerface by the electric field effect: (a) Sketch of the sample geometry. (b) Current-voltage characteristics depending on the back gate voltage at 10 K. (c) Sheet charge carrier concentration (top panel) and mobility (bottom panel) as a function of the back gate voltage at 10 K.

superconductivity[100] by the electric field effect. In the next section we investigate if the electronic properties of the (111) heterointerface can also be adjusted by the electric field effect.

A sketch of the sample geometry employed is shown in Fig. 7.5 (a). The electric field is applied via a back gate at a temperature of 10 K.[4] Figure 7.5 (b) depicts current-voltage curves which are recorded at different back gate voltages. At all back gate voltages >-10 V, the voltage drop V_{DS} measured scales linearly with the current I_{DS} which is passed through the sample. The slope of the current-voltage curves is, however, changing. This shows that we can effectively tune the resistance of the (111)-oriented $LaAlO_3/SrTiO_3$ heterointerface by the electric field effect: At positive back gate voltages the resistance is decreasing, while it is increasing at negative back gate voltages. When the back gate voltage is set to -20 V or even higher values, the sample even becomes insulating (resistance $>1\,\mathrm{M}\Omega$).

To comprehend why the resistance changes with the gate voltage, we furthermore performed Hall effect measurements and determined how the sheet charge carrier concentration as well as the mobility change as a function of the back gate voltage. The results of this analysis are depicted in Fig. 7.5 (c). The charge carrier concentration is found to increase concomitant to the back gate voltage [see upper panel in Fig. 7.5 (c)]. One can understand the changes in the charge carrier concentration by thinking of the $LaAlO_3/SrTiO_3$ heterostructure in Fig. 7.5 (a) as a capacitor. When a positive back gate voltage is applied, the other plate of the capacitor, i.e. the 2DES at the interface, is negatively charged and electrons accumulate at the interface. At negative back gate voltage the interface is, in contrast, positively charged and electrons drain from the conducting channel. We note that the charge carrier mobility is varying as well with the back gate voltage [see lower panel in Fig. 7.5 (c)]. This might be due a concomitant change in the 2DES extension which might alter the number of scattering centers encountered by the mobile electrons and in turn modulate the mobility.[190]

Our experiments show that the electronic properties of the (111) $LaAlO_3/SrTiO_3$ interface can be effectively controlled by the electric field effect. For the 6 ML $LaAlO_3/SrTiO_3$ sample we can even toggle between the metallic and the insulating state modulating the resistance of the sample by orders of magnitude, a feature which is crucial for potential device applications.

---

[4] The back gate is 0.5 mm away from the $LaAlO_3/SrTiO_3$ interface. Gating only works efficiently at low temperatures where the dielectric constant of $SrTiO_3$ is high and the electric field generated by the back gate extends far into the $SrTiO_3$ substrate.

7.5 The electronic structure of the (111) $LaAlO_3/SrTiO_3$ heterointerface

In the next section the microscopic electronic structure of the 2DES at the (111) $LaAlO_3/SrTiO_3$ heterointerface is investigated in detail. By soft x-ray angle-resolved photoemission spectroscopy (SX-ARPES), we are able to directly probe the band structure and map the Fermi surface, even though the conducting layer in question is buried below a $LaAlO_3$ film.

7.5.1 Tight binding description of the (111) $LaAlO_3/SrTiO_3$ heterointerface

Before turning to the ARPES measurements, we construct a tight binding (TB) model to compare our data to. Such an approach has been shown to describe the electronic structure in $SrTiO_3$-based heterostructures accurately in various publications.[80,191,192] In Sec. 3.1.2 we have already introduced the basic ingredients for a tight binding approach which models the k-dependent electronic structure of the conduction band in the $SrTiO_3$ bulk. However, in the (111)-oriented $LaAlO_3/SrTiO_3$ heterostructures the 2DES is confined to the interface and the $SrTiO_3$ conduction band is consequently only doped with electrons in the uppermost atomic planes of the substrate. To describe the electronic structure of such a thin conducting $SrTiO_3$ slab, the tight binding approach has to be adapted accordingly.[181]

For simplicity we consider the case of a (111)-oriented $SrTiO_3$ slab which consists of only two triangular Ti layers as depicted in Fig. 7.6 (a). In our tight binding approach we disregard the potential difference between the two layers and neglect all hopping occurring between orbitals of different character. It thus suffices to discuss the hopping processes for one of the three $d_{t_{2g}}$ orbitals.

We take the example of the d_{xy} orbital and illustrate in Fig. 7.6 (a) which hopping processes occur in the Ti bilayer: Electrons might hop from the central Ti atom in Fig. 7.6 (a) to the nearest-neighbor Ti atoms in x, y and z direction which lie in the Ti layer below. In x and y direction, the electrons move parallel to the lobes of the d_{xy} orbital. The large resulting hopping integral is labeled t_π after the character of the chemical bond between the adjacent orbitals. In z direction the electrons, in contrast, hop perpendicular to the orbital lobes. The hopping amplitude is accordingly denoted as $t_{\delta'}$ and smaller. Electrons might also hop to the second-nearest-neighbor atom. We only take into account second nearest neighbor hopping parallel to the orbital lobes, i.e., in direction $\pm(x-y)$ for the case of the d_{xy} orbital as depicted in Fig. 7.6 (a). $t_{\sigma''}$ is the integral describing the second nearest neighbor hopping.

Repeating these considerations for the other $d_{t_{2g}}$ orbitals, one arrives at the following expression for the tight binding Hamiltonian H

$$H = \begin{pmatrix} d_{a1}^\dagger \\ d_{a2}^\dagger \\ d_{b1}^\dagger \\ d_{b2}^\dagger \\ d_{c1}^\dagger \\ d_{c2}^\dagger \end{pmatrix}^T \begin{pmatrix} \epsilon_a & \tilde{\epsilon}_a & & & & \\ \tilde{\epsilon}_a^* & \epsilon_a & & & & \\ & & \epsilon_b & \tilde{\epsilon}_b & & \\ & & \tilde{\epsilon}_b^* & \epsilon_b & & \\ & & & & \epsilon_c & \tilde{\epsilon}_c \\ & & & & \tilde{\epsilon}_c^* & \epsilon_c \end{pmatrix} \begin{pmatrix} d_{a1} \\ d_{a2} \\ d_{b1} \\ d_{b2} \\ d_{c1} \\ d_{c2} \end{pmatrix}, \tag{7.1}$$

where the indices a, b and c denote the orbital character xy, xz, yz and the indices 1 and 2 label the atomic layer.

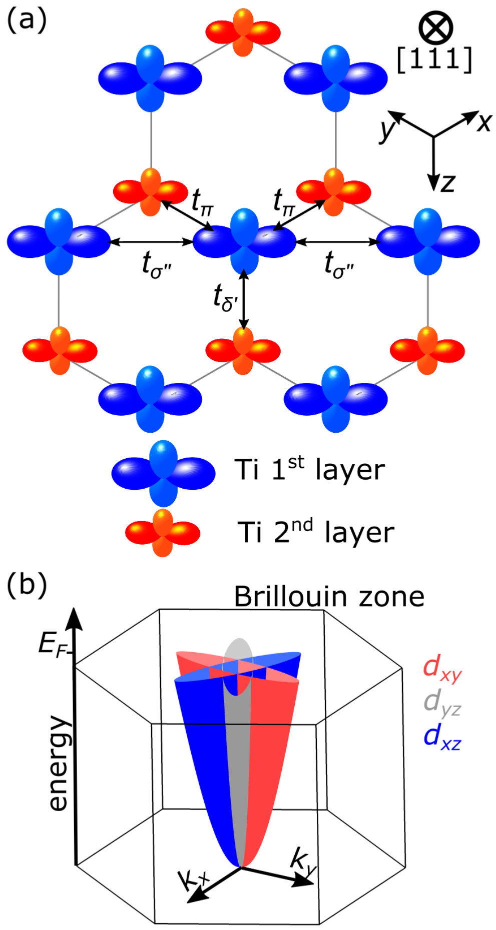

Fig. 7.6: (a) Setting up the tight binding model for a Ti honeycomb lattice.[181] We only allow hopping between orbitals of the same symmetry and exemplarily depict the hopping matrix elements for the d_{xy} orbitals. (b) Band structure obtained from tight binding model of a Ti honeycomb lattice.

The single entries of the Hamiltonian matrix read

$$\epsilon_a = -2t_{\sigma''}\cos\left(-\frac{\sqrt{3}}{2}\tilde{a}k_x + \frac{3}{2}\tilde{a}k_y\right),$$

$$\epsilon_b = -2t_{\sigma''}\cos\left(\frac{\sqrt{3}}{2}\tilde{a}k_x + \frac{3}{2}\tilde{a}k_y\right),$$

$$\epsilon_c = -2t_{\sigma''}\cos\left(-\sqrt{3}\tilde{a}k_x\right),$$

$$\tilde{\epsilon}_a = -t_\pi\left[1 + e^{i\left(\frac{\sqrt{3}}{2}\tilde{a}k_x - \frac{3}{2}\tilde{a}k_y\right)}\right] - t_{\delta'}e^{-i\left(\frac{\sqrt{3}}{2}\tilde{a}k_x + \frac{3}{2}\tilde{a}k_y\right)},$$

$$\tilde{\epsilon}_b = -t_\pi\left[1 + e^{-i\left(\frac{\sqrt{3}}{2}\tilde{a}k_x + \frac{3}{2}\tilde{a}k_y\right)}\right] - t_{\delta'}e^{i\left(\frac{\sqrt{3}}{2}\tilde{a}k_x - \frac{3}{2}\tilde{a}k_y\right)},$$

$$\tilde{\epsilon}_c = -2t_\pi\cos\left(\frac{\sqrt{3}}{2}\tilde{a}k_x\right)e^{-i\frac{3}{2}\tilde{a}k_y} - t_{\delta'}$$

with $\tilde{a} = a\sqrt{2/3}$ where a denotes the lattice constant of the cubic perovskite. The tight binding Hamiltonian is now a function of the two momenta $k_x = k_{\langle 1\bar{1}0\rangle}$ and $k_y = k_{\langle 11\bar{2}\rangle}$. Note that there is no k_z-dependence due to the two-dimensional nature of our slab.

In the last step we have to diagonalize the Hamiltonian H. As a result of our stipulation that electrons can only hop between identical orbitals, the d orbitals of different character do not mix in the Hamiltonian. The tight binding Hamiltonian H can consequently be decomposed into three (2x2) matrices which are not coupled to each other and which can thus be diagonalized separately. We exemplarily solve the tight binding model for the d_{yz} orbital

$$H_c = \begin{pmatrix} d_{c1}^\dagger & d_{c2}^\dagger \end{pmatrix} \begin{pmatrix} \epsilon_c & \tilde{\epsilon}_c \\ \tilde{\epsilon}_c^* & \epsilon_c \end{pmatrix} \begin{pmatrix} d_{c1} \\ d_{c2} \end{pmatrix}. \tag{7.2}$$

The eigenvalues E_1 and E_2 of the Hamiltonian H_c are

$$E_1 = \epsilon_c + |\tilde{\epsilon}_c|,\ E_2 = \epsilon_c - |\tilde{\epsilon}_c|. \tag{7.3}$$

At low band filling, only the smaller eigenvalue E_2 is relevant to describe the electronic band structure. The eigenvector corresponding to the eigenvalue E_2 reads

$$\begin{pmatrix} d_{c1} \\ d_{c2} \end{pmatrix} = \frac{1}{\sqrt{2}}\begin{pmatrix} 1 \\ -e^{-i\alpha} \end{pmatrix}, \tag{7.4}$$

where α denotes the argument of the complex number $\tilde{\epsilon}_c = |\tilde{\epsilon}_c| \cdot e^{i\alpha}$. The eigenvalues and eigenvectors for the d_{xz} and d_{xy} orbitals can be computed in similar fashion. As the entries in the Hamiltonian H are a function of k_x and k_y, the resulting energy eigenvalues and eigenvectors depend on k_x and k_y as well. The energy eigenvalues describe the electronic band structure in reciprocal space, while the eigenvectors show which orbitals contribute to this band structure.

Adopting the hopping parameters which Rödel *et al.*[193] find for the bare $SrTiO_3$ surface,[5] we plot the resulting band structure in Fig. 7.6 (b). It consists of three bands which can be directly

---

[5] $t_{\sigma''} = 0.05\,\text{eV}$, $t_\pi = 1.6\,\text{eV}$, $t_{\delta'.} = 0.07\,\text{eV}$

matched to the three $d_{t_{2g}}$ orbitals. Please note that one obtains a very similar band structure, if more than two Ti layers are included in the tight binding approach (see calculation in Sec. D.2 in the Appendix). The tight binding approach is thus also applicable if the electrons are confined to several Ti layers.

Let us next take a look at the experimental data.

7.5.2 Experimental details

To be able to probe the Fermi surface of the buried interface, we have to boost the weak Ti $3d$ signal at the Fermi edge.[109] To this end, we measure again at the photon energy at the Ti L edge for which the QP weight is resonantly enhanced. The SX-ARPES measurements were performed at the ADRESS beamline[194] at the Swiss Light Source at a sample temperature of 10 K. We are interested in the electronic structure of the fully oxidized $LaAlO_3/SrTiO_3$ heterointerface. We thus recorded all of the following data under oxygen dosing and made sure that the IG weight in the valence band spectra which is indicative of oxygen vacancies is fully suppressed. To be sensitive to all Ti $3d$ orbitals independent of their symmetry, the data discussed in the following were recorded with circularly polarized x-rays.

7.5.3 Fermi surface mapping

The measured Fermi surface map is depicted in Fig. 7.7 (a). We detect spectral weight at the Γ points, which vanishes when the photon energy is moved off-resonance (data not shown). Thus, we conclude that the entire spectral weight at the Fermi edge originates from Ti $3d$ orbitals at the $LaAlO_3/SrTiO_3$ interface.

In the most simple electronic reconstruction scenario, electrons from the O $2p$ valence band at the $LaAlO_3$ surface are expected to dope the Ti $3d$ orbitals at the interface.[108] Following this line of reasoning, we expect to observe additional metallic surfaces states, viz. hole pockets of O $2p$ character, which appear in the Fermi surface map, independent of the photon energy. Notably, we do not find any evidence of such O $2p$-related bands in the experiment. Similar observations have been reported for (001)-oriented samples and have been interpreted by a modified electronic reconstruction picture in which adsorbates or defect states at the $LaAlO_3$ surface act as a charge reservoir for the interfacial 2DES.[109]

In the Fermi surface map we can already recognize the distinctive symmetry of the (111) orientation. However, the pronounced asymmetry of the Fermi surface map in Fig. 7.7 (a) makes the data interpretation and analysis challenging. To facilitate the data interpretation, we sum up the data of all Brillouin zones and symmetrize it. In the resulting Fermi surface map [see Fig. 7.7 (b)] the three ellipses corresponding to the three degenerate Ti $3d_{t_{2g}}$ orbitals can now be clearly identified.

Based on the Fermi surface volume, one can also estimate the charge carrier concentration in the interfacial 2DES.[A8] For that purpose we have to determine the Fermi vectors in Fig. 7.7 (b). However, no clear contours of the three ellipses can be detected in the diffuse Fermi surface maps. Straub *et al.*[195] show that, in such cases, the Fermi vectors can be more precisely identified in the two-dimensional gradient $|\nabla_{\mathbf{k}} I(\mathbf{k})|$ of the original intensity map $I(\mathbf{k})$. The gradient $|\nabla_{\mathbf{k}} I(\mathbf{k})|$ computed around Γ_{11} is displayed in Fig. 7.7 (c). The Fermi surface contour is now discerned and fitted by a tight binding model.[181,193] In Fig. 7.7 (c) we indicate the best fit of the Fermi surface contours as well as the upper and lower boundary we estimate.[6] We arrive at a charge carrier concentration of $n_{2D} = \left(1.3^{+0.7}_{-0.4}\right) \cdot 10^{14}\,\mathrm{cm}^{-2}$.

---

[6] Due to the low signal intensity in our measurements we do not adjust the parameters of the tight binding model but use the parameters for the hopping matrix element Rödel *et al.*[193] indicate and only adapt the band filling.

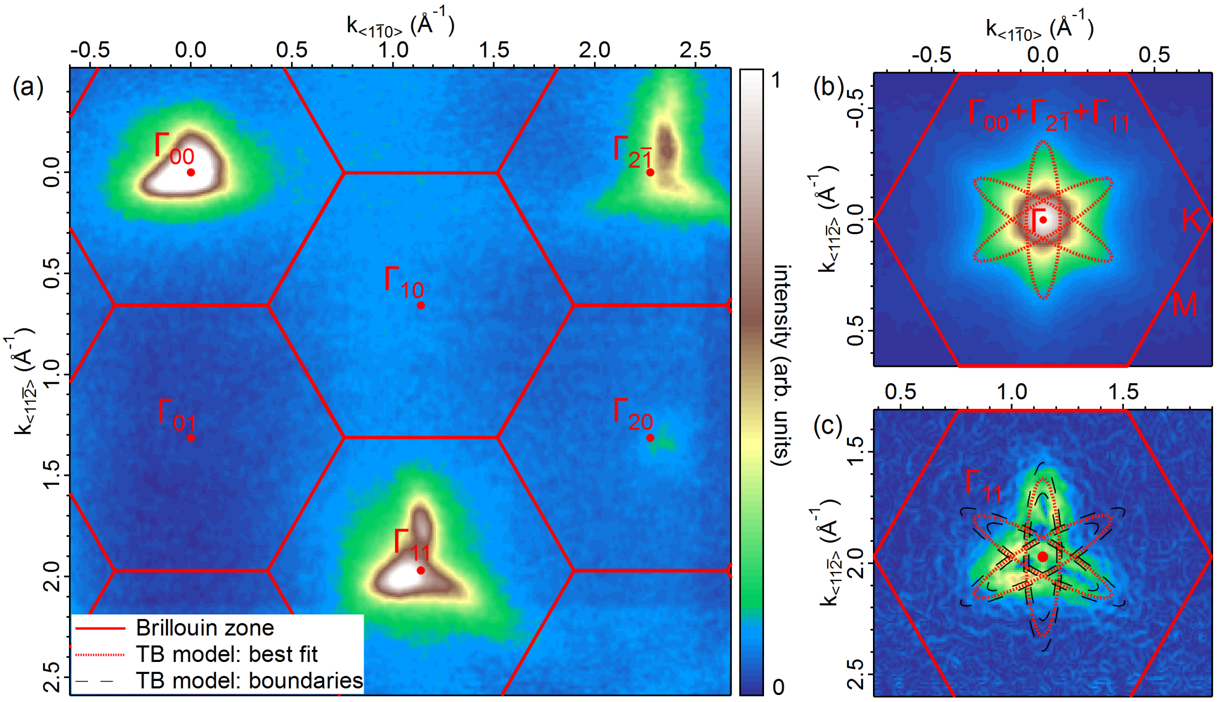

Fig. 7.7: Fermi surface map of the (111) $LaAlO_3/SrTiO_3$ heterointerface measured under oxygen dosing: (a) Fermi surface map as measured. At the Γ points, Ti 3*d*-related signal is detected. (b) Fermi surface data summed over Γ points and symmetrized. The Fermi surface modeled with a tight binding approach is overlaid on the data. (c) Two-dimensional gradient of the Fermi surface map around Γ_{11}. In this map the contours of the Fermi surface become apparent and the Fermi surface area can be determined. To this end, we fit the data with the tight binding model from ref. [193].

In transport experiments the charge carrier concentration of the sample is estimated at $n_{2D} = (0.65 \pm 0.23) \cdot 10^{14}\,\mathrm{cm}^{-2}$. Here, we, once again, find that the charge carrier concentration measured in transport measurements is lower than the charge carrier concentrations estimated from spectroscopy. In contrast, the charge carrier concentration estimated from HXPES experiments on similar samples (sample in chapter 4: $n_{2D} = (0.78 \pm 0.12) \cdot 10^{14}\,\mathrm{cm}^{-2}$, sample in chapter 5: $n_{2D} = \left(1.80^{+0.20}_{-0.25}\right) \cdot 10^{14}\,\mathrm{cm}^{-2}$) agree within error bars with the charge carrier concentration the Fermi volume analysis yields here. This agreement validates the spectroscopic estimates of the charge carrier concentration. The reconfirmed discrepancy between the spectroscopy and transport results indicates that the measurement methods indeed probe different states as discussed in detail in chapter 6.

7.5.4 High-resolution band mapping

Beside the Fermi surface maps, band maps along high-symmetry directions[7] can provide further information on the electronic structure of the $LaAlO_3/SrTiO_3$ interface.

Figure 7.8 (a) depicts a band map along the $\Gamma - M$ line measured with a high energy resolution of 45 meV.[196] The expected band dispersion which is inferred from the tight binding approach is overlaid in the image as well. Comparing the modeled dispersion with the experimental data, one notes that the bands with differing dispersion cannot be resolved in the band map. Furthermore, the binding energy of the bands distinctly differs in the measurement and in the tight binding model. Moreover, in the measured band map a pronounced peak-dip-hump structure is

---

[7] The high-symmetry points of the Brillouin zones are labeled in Fig. 7.7 (b).

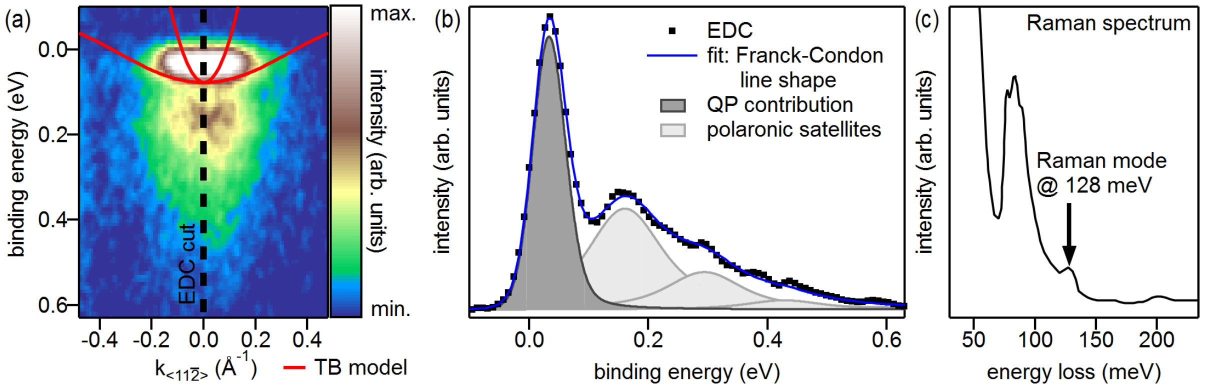

Fig. 7.8: (a) Band map along the Γ–M direction. The band structure the tight binding approach yields is superimposed but does not match to the band map measured. (b) Energy distribution curve extracted from the band map as indicated in (a). The peak-dip-hump structure can be modeled by a Franck-Condon line shape. (c) Raman spectrum of a (111)-oriented $LaAlO_3/SrTiO_3$ heterostructure. The energy difference between the satellite peaks in the Franck-Condon model matches to a Raman mode.

observed which is not present in the tight binding model. The peak-dip-hump structure becomes particularly apparent in Fig. 7.8 (b) which shows an energy distribution curve (EDC) extracted from the band map in Fig. 7.8 (a).

In ARPES measurements on (001)-oriented $LaAlO_3/SrTiO_3$ heterostructures similar effects were detected and ascribed to the formation of polarons.[196] A polaron is a quasiparticle which describes an electron whose movement through the crystal is accompanied by lattice distortions, i.e., by phonons.

The polarons are identified in the photoemission spectra by two features:
The composite charge carrier is characterized by an enhanced effective mass. Although the band mass cannot reliably be fitted in our band maps due to the limited resolution, one clearly sees that the dispersion and the effective mass in the tight binding approach have to be renormalized to match the experiment.

Moreover, the polaronic character of the interfacial charge carriers becomes apparent in the peak-dip-hump line shape in the band maps: Photoemission spectroscopy probes the one-electron removal spectral function and is thus also sensitive to interactions, including electron-phonon coupling. Indeed, we have already seen that the measured band map can no longer be described adequately by a tight binding model which assumes non-interacting electrons. In the measured spectra, the main line at the Fermi level is instead attributed to the quasiparticle, while the hump feature is ascribed to a series of satellite peaks arising as phonons are excited.

In such a scenario the spectral function can be adequately modeled by a Franck-Condon line shape[197] as is illustrated in Fig. 7.8 (b): The quasiparticle peak and the satellite peaks are separated in binding energy by $\hbar\omega$, i.e., the energy of the phonon mode, while the intensity of the satellite peaks follows a Poisson distribution.[198] The main peak as well as the satellite peaks are modeled by Voigt peaks. The Gaussian width of the quasiparticle and the satellite peaks are set to the same value. However, to achieve a good fit of the experimental data, we have to allow the Lorentzian widths of the quasiparticle peak and the satellite peaks to differ. This shows that the lifetimes of the various states differ.

The energy of the phonon mode estimated by the Franck-Condon fit amounts to $\hbar\omega \approx 134\,\text{meV}$. We check our interpretation by looking for phonon modes with a complementary technique, i.e., Raman spectroscopy.[8] The Raman spectrum of a (111)-oriented $LaAlO_3/SrTiO_3$ heterostructure depicted in Fig. 7.8 (c) indeed reveals a phonon mode at an energy of $\hbar\omega \approx 128.1$ meV, which matches to the photoemission experiments. The phonon mode is attributed to the longitudinal optical phonon branch in $SrTiO_3$ which typically has energies around $\approx$ 100 meV[199] but which shifts toward higher energy in $LaAlO_3/SrTiO_3$ heterostructures.[196]

From the Franck-Condon fit we also determine the quasiparticle residue $Z_0 \approx 0.4$ in the integral spectral weight. For the case of short-range electron-phonon interaction relevant in $SrTiO_3$, the quasiparticle residue is directly linked to the dimensionless electron-phonon coupling constant $\lambda \approx 1 - Z_0 = 0.6$,[196] which places the electron-phonon interaction at the (111) $LaAlO_3/SrTiO_3$ interface in the regime of weak coupling.[200] The value of the coupling constant furthermore reveals that large polarons form at the $LaAlO_3/SrTiO_3$ heterointerface in which the lattice distortion extends over several unit cells.[196,201] Very similar characteristics were reported for the polarons forming at the (001) $LaAlO_3/SrTiO_3$ heterointerfaces.[196]

Let us finally compare our measurements to other experiments which are sensitive to the electronic structure: Based on transport experiments, Davis *et al.*[202] speculate that the band bottoms of the d bands in (111)-oriented $LaAlO_3/SrTiO_3$ heterostructures are non-degenerate at low temperatures. Employing x-ray absorption spectroscopy, De Luca *et al.*[81] also find that the degeneracy of the $d_{t_{2g}}$ bands is lifted due to the peculiar crystal field at the (111) $LaAlO_3/SrTiO_3$ heterointerface. We do not observe that the degeneracy of the $d_{t_{2g}}$ bands is lifted. However, the changes in energy of the $d_{t_{2g}}$ bands De Luca *et al.* find are very small ($\approx$8 meV) and lie below the experimental resolution of our experiments.

We also do not find any evidence of the phases predicted by density functional theory for few monolayer thick $SrTiO_3$ quantum wells.[77] This discrepancy is tentatively ascribed to the fact that the electrons at the (111) $LaAlO_3/SrTiO_3$ heterointerface are not strictly confined to a thin $SrTiO_3$ slab but also spread into the $SrTiO_3$ substrate.

7.5.5 Elucidating the orbital character of the band structure

The band structure data discussed so far have been measured with circularly polarized light. To investigate the orbital character of the electronic structure, we now turn to Fermi surface maps which are recorded with linearly polarized photons. In such experiments one is able to disentangle the contributions of the different orbitals if these orbitals have a defined parity with respect to the mirror plane of the experiment.[75]

Let us thus first have a look at the symmetry of the $3d$ orbitals in our experimental setup. The mirror plane of our experiment is chosen to coincide with the $(1\bar{1}0)$ plane of the $LaAlO_3/SrTiO_3$ heterostructure. Figure 7.9 (a) depicts how the three $d_{t_{2g}}$ orbitals are oriented with respect to the $(1\bar{1}0)$ crystal plane. One notes at first glance that only the d_{xy} orbital is symmetric to the mirror plane. When the d_{xz} orbital is reflected at the mirror plane, it turns into an d_{yz} orbitals and vice versa. One can thus easily construct linear combinations of the d_{xz} and d_{yz} orbitals which have a defined symmetry with respect to the experimental mirror plane

$$d_+ = \frac{1}{\sqrt{2}}(d_{xz} + d_{yz}), \; d_- = \frac{1}{\sqrt{2}}(d_{xz} - d_{yz}). \tag{7.5}$$

Figure 7.9 (b) sketches the new orbital basis and illustrates that the d_+ orbital has parity +1, while the d_- orbital has parity −1 with respect to the experimental mirror plane.

To reveal how the d_+ and d_- orbitals contribute to the electronic structure, we have to solve the tight binding approach anew based on this set of orbitals: The change from the conventional orbital basis $\{d_{xy}, d_{xz}, d_{yz}\}$ to the new orbital basis $\{d_{xy}, d_+, d_-\}$ can be represented as a unitary

---

[8] Raman measurements provided by S. Elsässer and J. Geurts.

transformation. For the tight binding model of the Ti bilayer introduced in Sec. 7.5.1 the relevant unitary operator U reads

$$U = U^{-1} = U^{\dagger} = \frac{1}{\sqrt{2}} \begin{pmatrix} \sqrt{2} & 0 & 0 & 0 & 0 & 0 \\ 0 & \sqrt{2} & 0 & 0 & 0 & 0 \\ 0 & 0 & 1 & 0 & 1 & 0 \\ 0 & 0 & 1 & 0 & -1 & 0 \\ 0 & 0 & 0 & 1 & 0 & 1 \\ 0 & 0 & 0 & 1 & 0 & -1 \end{pmatrix}. \tag{7.6}$$

The tight binding Hamiltonian in equation (7.1) then transforms as

$$H = \boldsymbol{d}^{\dagger} M \boldsymbol{d} = \boldsymbol{d}^{\dagger}(U^{-1}U)M(U^{-1}U)\boldsymbol{d} = (U\boldsymbol{d})^{\dagger}(UMU^{-1})(U\boldsymbol{d}) = \hat{\boldsymbol{d}}^{\dagger}\hat{M}\hat{\boldsymbol{d}}, \tag{7.7}$$

where $\boldsymbol{d}$ and M refer to the vector of d orbitals and the matrix of hopping elements in the $\{d_{xy}, d_{xz}, d_{yz}\}$ basis, while $\hat{\boldsymbol{d}}$ and $\hat{M}$ describe the same quantities in the $\{d_{xy}, d_+, d_-\}$ basis.

While the unitary transformation does not change the eigenvalues of the tight binding model, i.e., the resulting electronic structure, it does affect the single entries of the hopping matrix: The original hopping matrix M can be decomposed into three decoupled matrices. Diagonalization of these matrices yields the three bands which can be matched to the d_{xy}, d_{xz} and d_{yz} orbital, respectively. In the hopping matrix $\hat{M}$ only the contribution of the d_{xy} orbitals can be decoupled and solved separately, which generates one of the ellipses in the Fermi surface map. In contrast, the contributions of the d_+ and the d_- orbitals cannot be disentangled in the matrix $\hat{M}$. Thus the two other ellipses in the Fermi surface map contain contributions from both the d_+ and the d_- orbitals. To estimate the orbital character of these two ellipses, we look at the eigenvectors to the corresponding eigenenergies and find that the d_+ as well as the d_- orbitals contribute to both ellipses equally with 50% intensity.

Based upon these considerations we can now predict which orbitals emerge in the Fermi surface maps as a function of the light polarization (see Sec. 2.2.1). Measuring with p-polarized light (parity +1) one can only excite orbitals which have parity +1 with respect to the mirror plane of the experiment, i.e., the d_{xy} and the d_+ orbital. In the corresponding Fermi surface map we thus expect to observe the ellipse corresponding to the d_{xy} orbital. The two other ellipses should

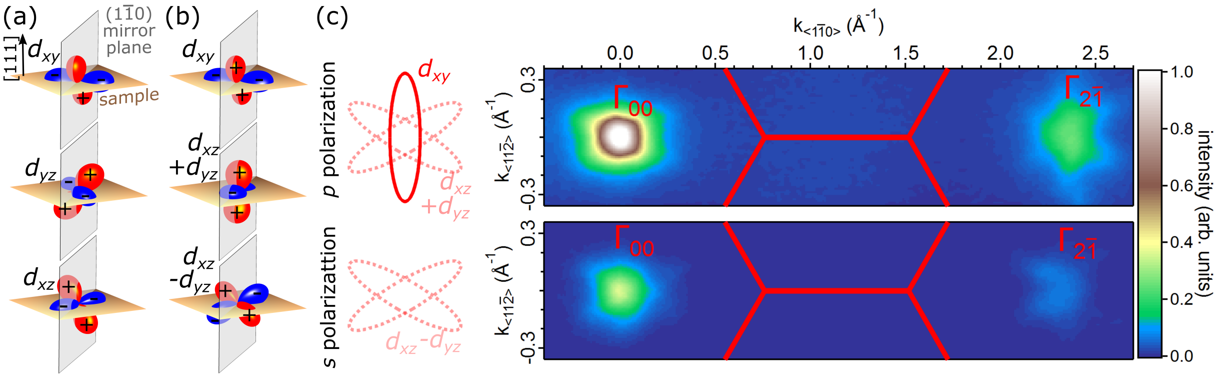

Fig. 7.9: Dependence of the Fermi surface maps on the light polarization: (a) Orientation of the $d_{t_{2g}}$ orbitals with respect to the experimental mirror plane. While the d_{xy} orbital is symmetric with respect to the mirror plane, the d_{xz} and d_{yz} orbitals do not have a defined symmetry. (b) Linear combinations of the $d_{t_{2g}}$ orbitals which have a defined parity with respect to the mirror plane. (c) Left: Model of the Fermi surface maps depending on the light polarization computed with a tight binding approach. Right: Fermi surface maps recorded using p- and s-polarized light. Modeled and measured data compare favorably.

also be visible but only with half of the intensity of the d_{xy} related ellipse. Conversely, with s-polarized light (parity –1) only orbitals with parity –1, i.e., the d_- orbitals, are excited. In the Fermi surface map one should thus only observe two ellipses with half intensity. Figure 7.9 (c) summarizes how we expect the Fermi surface maps to look as a function of the light polarization (left panels) and contrasts the models to the respective measured Fermi surface maps (right panels).[9]

In the measured Fermi surface maps we note that the overall intensity is lower for the s-polarized light than for the p-polarized light which is in agreement with our Fermi surface models. In particular around $\Gamma_{2\bar{1}}$, we can furthermore clearly recognize the symmetries which the tight binding approach predicts. The photoemission intensity in the measured Fermi surface maps is modulated beyond the polarization dependence which is presumably owed to further matrix element effects.

Summing up, we are able to match the electronic structure to the single d orbitals using polarization-dependent ARPES measurements, although the assignment is more complex than for the (001)-oriented heterostructures.

7.6 The dimensionality of the electron system

We observe pronounced asymmetries not only in the Fermi surface maps measured with linearly polarized light but also in the Fermi surface map in Fig. 7.7 (a) measured with circularly polarized light: Whereas – following the tight binding description – one expects to observe a sixfold symmetric Fermi surface in every Brillouin zone [cf. Fig. 7.10 (a)], the Fermi surfaces measured are threefold symmetric and vary strongly in intensity and shape among different Brillouin zones.

7.6.1 Assessing the 2DES extension by the photoemission structure factor

The discrepancy between the tight binding model and the experiment can be traced back to the peculiar topology of the (111) interface: To derive the tight binding model, the interface has been represented by two Ti layers, i.e., by a buckled honeycomb lattice. To build such a honeycomb lattice one needs to include *two* Ti atoms in each unit cell. With the atoms being identical but sitting at different positions, the wave functions of their atomic orbitals may superimpose and interfere constructively or destructively. As a result, the photoemission intensity in the reciprocal space is modulated and the Fermi surface is no longer sixfold symmetric. A similar effect is well known from x-ray diffraction experiments and captured in the so-called structure factor.[186]

In the one-electron matrix element characterizing the photoemission process, a similar term can be identified which is called photoemission structure factor[203,204]

$$F(\mathbf{k}) = \sum_m \exp(-i\mathbf{G}\boldsymbol{\tau}_m)c_m(\mathbf{q}). \tag{7.8}$$

where $|F(\mathbf{k})|^2$ modulates the photoemission intensity pattern inferred from the tight binding approach. The sum in equation (7.8) runs over all inequivalent atoms m in the unit cell where $\boldsymbol{\tau}_m$ describe the positions of the atoms. $\mathbf{k} = \mathbf{q} + \mathbf{G}$ denotes an arbitrary vector in reciprocal space which is expressed as the sum of a vector $\mathbf{q}$ in the first Brillouin zone and a reciprocal lattice vector $\mathbf{G}$. The prefactor $c_m(\mathbf{q})$ can be compared to the atomic form factors appearing in the x-ray diffraction scattering factor. Here, the coefficients $c_m(\mathbf{q})$ describe how the orbitals of

---

[9] The Fermi surface maps are furthermore normalized to the photon flux of the s- and the p-polarized light.[194] To facilitate the comparison between our model and the experiment, Fermi surface maps recorded at two equivalent angles are summed up. This minimizes the asymmetry of the Fermi surface maps without altering the symmetries we are looking for.

the different atoms in the unit cell contribute to the wave function of the photoemission initial state. In the tight binding approach these quantities are captured in the eigenvectors.

In the following, we compute the photoemission structure factor for a two-dimensional honeycomb lattice. The photoemission structure factor has to be calculated separately for each orbital. Here, we exemplarily determine the photoemission structure factor for the d_{yz} orbitals. The unit cells chosen are shown in Fig. 7.10 (d). The vectors describing the real space unit cell are denoted by $\mathbf{a}_1$ and $\mathbf{a}_2$ while $\mathbf{b}_1$ and $\mathbf{b}_2$ denote the corresponding lattice vectors in reciprocal space. An arbitrary lattice vector $\mathbf{G} = h\mathbf{b}_1 + k\mathbf{b}_2$ in reciprocal space can then be expressed as a linear combination of the vectors $\mathbf{b}_1$ and $\mathbf{b}_2$ where h and k are integers. Each unit cell of the hexagonal lattice contains two inequivalent atoms sitting at the positions $\boldsymbol{\tau_1} = \mathbf{0}$ and $\boldsymbol{\tau_2} = \frac{2}{3}\mathbf{a}_1 + \frac{1}{3}\mathbf{a}_2$.

To compute the photoemission structure factor, we have to insert the coefficients $c_m(\mathbf{q})$ which are read out from the eigenvector in equation (7.4). Using these expressions, we rewrite $|F(\mathbf{k})|^2$

$$|F(\mathbf{k})|^2 = \frac{1}{2}|1 - e^{-i\mathbf{G}\boldsymbol{\tau}_2} e^{-i\alpha(\mathbf{q})}|^2. \tag{7.9}$$

To facilitate the analysis, we only examine the intensity modulation at the Γ points, i.e., $\mathbf{q}=\mathbf{0}$, in the following. At the Γ points, $\alpha(\mathbf{0})=\pi$ holds (see equation (7.3)). Exploiting the relation between reciprocal and real space lattice vectors $\mathbf{a}_x \cdot \mathbf{b}_y = 2\pi\delta_{xy}$, we can further simplify $|F(\mathbf{k})|^2$

$$|F(\mathbf{k})|^2 = \frac{1}{2}|1 + e^{-i\mathbf{G}\boldsymbol{\tau}_2}|^2 = \frac{1}{2}\left\{\left[1 + \cos\left(\frac{\pi}{3}(2h+k)\right)\right]^2 + \sin^2\left(\frac{\pi}{3}(2h+k)\right)\right\}. \tag{7.10}$$

The result of this equation depends on the value of $2h + k$, i.e., on the reciprocal lattice vector $\mathbf{G}$ or, in other words, on the Brillouin zone we are looking at. Due to the 2π periodicity inherent in the $\cos(x)$ and $\sin(x)$ terms, we only have to differentiate between two cases and arrive at the following result for $|F(\mathbf{k})|^2$ for the d_{xy} orbital

$$|F(\mathbf{k})|^2 = \begin{cases} 2 & \text{if } 2h + k = 3m \text{ with } m \in \mathbb{Z} \\ 0.5 & \text{otherwise.} \end{cases} \tag{7.11}$$

The same $|F(\mathbf{k})|^2$ values are obtained for the d_{xz} and d_{xy} orbitals. In the last step, we modulate the Fermi surface inferred from the tight binding model [Fig. 7.10 (a)] by $|F(\mathbf{k})|^2$ and plot the resulting Fermi surface in Fig. 7.10 (c): We note that the photoemission structure factor correctly predicts the pattern of dark and bright Brillouin zones. However, the intensity ratio between the dark and the bright Γ points does differ between model and experiment. It amounts to $\frac{0.5}{2} = 0.25$ in our model while it maximally approaches 0.04 in the experiment [see line profile in the lower panel of Fig. 7.10 (b)]. This might indicate that even more than two Ti layers contribute to the photoemission signal.

To check this hypothesis, we compute the photoemission structure factor anew but extend our model to include N Ti layers. For this purpose, we consider a slab consisting of N triangular lattices as sketched in Fig. 7.10 (e). The calculation runs along the same lines as before and is described in detail in Sec. D.3 in the Appendix. We find that, independent of the thickness of the slab, the pattern of dark and bright Brillouin zones is always identical to the pattern derived above for the honeycomb lattice. The intensity ratio between the dark and the bright Γ points does, in contrast, depend on the number N of Ti layers in the slab model. Table 7.1 lists the intensity ratio for several values of N. For $N=2$ the intensity ratio calculated based upon the slab model coincides with the intensity ratio calculated for the hexagonal lattice. When the number N of Ti layers increases, the intensity ratio drops sharply.

Comparing the values in Tab. 7.1 with the intensity ratio measured in the experiment, we roughly estimate the 2DES extension at 3–5 Ti layers or 6.8-11.3 Å. This value agrees with the 2DES

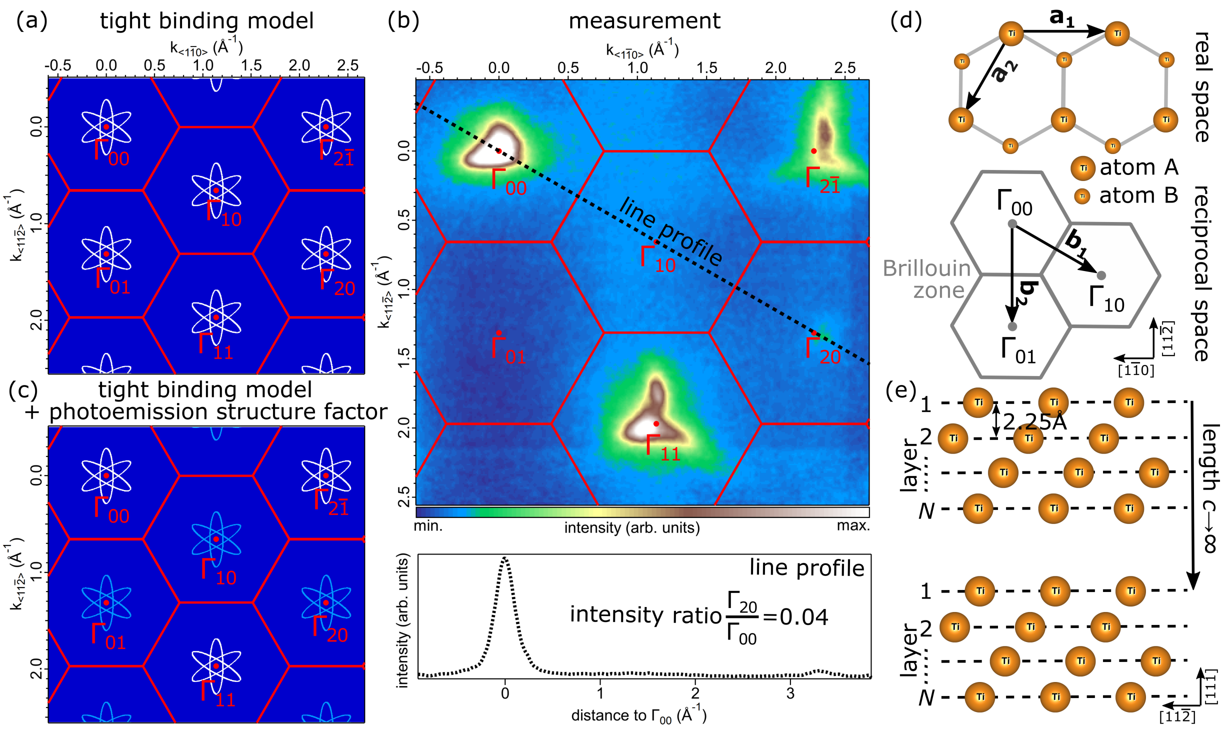

Fig. 7.10: (a) Fermi surface map as predicted by the two-dimensional tight-binding model. (b) Upper panel: measured Fermi surface map. lower panel: line profile through several Γ (see dashed line in upper panel). In the measured Fermi surface map the intensity varies strongly between the different Brillouin zones which is not observed in the modeled Fermi surface map in (a). The discrepancy is ascribed to the photoemission structure factor which quenches the intensity in some Brillouin zones: (c) Fermi surface map modeled by the two-dimensional tight-binding model. Intensity additionally modulated according to the photoemission structure factor of a honeycomb lattice. (d) Real space unit cell and atomic basis of a honeycomb lattice, and corresponding reciprocal lattice vectors. (e) Slab model used to compute the photoemission structure factor.

extension of 9 Å estimated by our HAXPES depth profiling experiments for a fully oxidized (111)-oriented $LaAlO_3/SrTiO_3$ sample (see Tab. B.5 in the Appendix).

According to our model we expect finite –albeit potentially weak– intensity at every Γ point. However, in the measured Fermi surface map the photoemission signal is completely quenched in the Brillouin zones surrounding Γ_{00}. This suppression of the photoemission signal is tentatively ascribed to photoelectron diffraction: Photoelectrons appearing at, e.g., Γ_{10} (and by symmetry at all other Γ points directly adjacent to Γ_{00}) take off along the [11$\bar{2}$] crystal direction traveling at an angle of ≈6.8° with respect to the [111] crystal direction. Figure 7.11 (a) depicts a cut through the crystalline plane in which the photoelectrons move. Indeed, we find O atoms sitting in the line of movement of the photoelectrons showing up at Γ_{10} [see sketch in Fig. 7.11 (a)]. These

	N=2	N=3	N=4	N=5	N=6	N=7	N=8
intensity ratio $\frac{\textbf{dark } \Gamma \textbf{ points}}{\textbf{bright } \Gamma \textbf{ points}}$	0.25	0.015	0.005	0.010	0.001	0.001	0.002

Tab. 7.1: Photoemission intensity ratio between the Γ points of bright and dark Brillouin zones estimated employing a slab model. The intensity ratio depends strongly on the number N of Ti layers included in the slab.

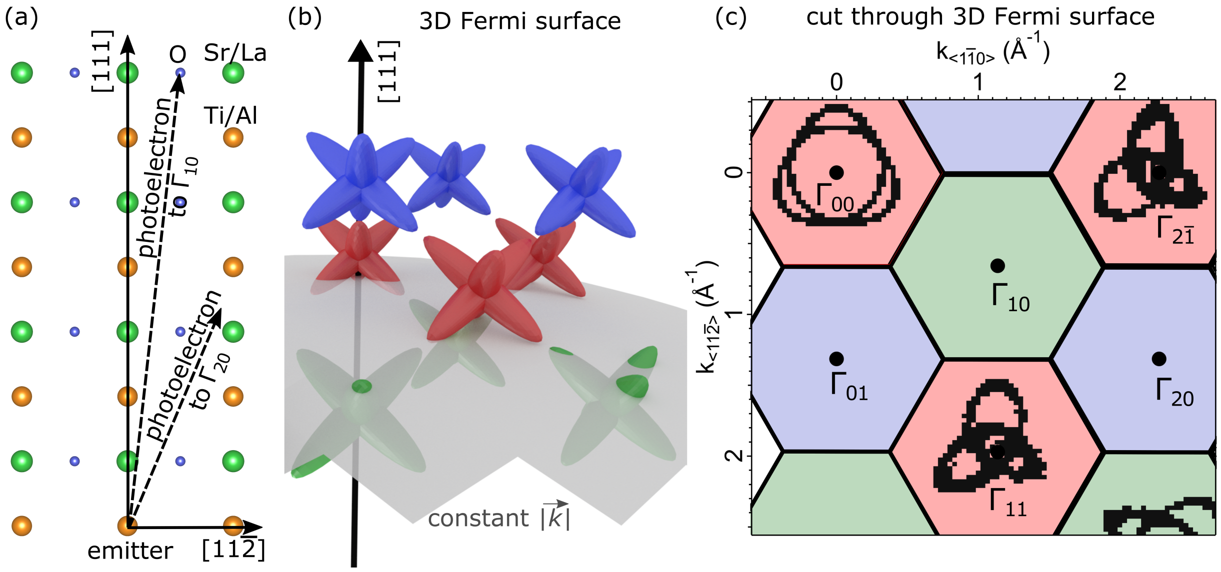

Fig. 7.11: (a) Cut through the crystal structure of the (111)-oriented samples. At specific angles the photoemission signal might get modulated due to the photoelectrons diffracting at other atoms. (b) Fermi surface inferred from a three-dimensional tight binding model. The figure also shows how our experiments cut the 3D Fermi surface (gray surface). (c) Projection of the three-dimensional Fermi surface to two dimensions as measured in our experiment. The colors in (b) and (c) illustrate the mapping between the Brillouin zones in 3D and 2D, respectively.

very photoelectrons diffract at the O atoms. In the Brillouin zones surrounding Γ_{00}, the already small signal presumably gets diffuse such that it can no longer be detected. In contrast, no atom lies in the line of movement of photoelectrons appearing at Γ_{20} [see sketch in Fig. 7.11 (a)].

7.6.2 Investigating the three-dimensional character of the Fermi surface

One can also approach the question of the dimensionality of the Fermi surface from another angle and assume that we are measuring a cut trough an intrinsically three-dimensional Fermi surface.

Figure 7.11 (b) depicts the three-dimensional Fermi surface which is inferred from a three-dimensional tight binding description of the $SrTiO_3$ band structure (see Sec. 3.1.2). In addition, we illustrate how the k space is cut in our measurement setup.[10] The resulting two-dimensional projection of the three-dimensional Fermi surface is sketched in Fig. 7.11 (c). To illustrate the correspondence between the projected Fermi surface and the three-dimensional Fermi surface, we color the Fermi surface lobes and the Brillouin zones in Figs. 7.11 (b) and (c), respectively.

The three-dimensional Fermi surface model provides an explanation for the threefold symmetry observed in the photoemission signal in the single Brillouin zones: Figure 7.11 (b) clearly illustrates that a cut through an intrinsically three-dimensional Fermi surface yields a pattern which is threefold symmetric.[11] In contrast, a purely two-dimensional tight binding model always yields a sixfold symmetric Fermi surface. The threefold symmetry of the photoemission signal thus confirms that the 2DES is not strictly confined to the interface.

However, not all asymmetries in the measured Fermi surface can be traced back to the fact that an intrinsically three-dimensional Fermi surface is projected onto two dimensions: Our three-dimensional Fermi surface model is chosen such that it captures the symmetry of the signal

---

[10] As the kinetic energy of the photoelectrons in the Fermi surface map is set and constant, the magnitude of the photoelectron momentum $|\mathbf{k}|$ is constant as well.

[11] Except when the cut runs right through the center of the Fermi surface lobes.

observed in the bright Brillouin zones in the experiment [compare Fig. 7.10 (b) to Fig. 7.11 (c)]. However, it cannot reproduce the finite signal appearing at Γ_{20} *at the same time*: In the three-dimensional Fermi surface model in Fig. 7.11 (b), the Fermi surface cut measured is marked in gray. It only cuts red and green Fermi surface lobes and does not come close to the blue Fermi surface lobes. In the two-dimensional projection in Fig. 7.11 (c) finite signal is, in consequence, only observed in red and green Brillouin zones and not at Γ_{20} which lies in a blue Brillouin zone.

The three-dimensional Fermi surface model can only be reconciled with the experiment, if one assumes that the three dimensional Fermi surface is broadened in k_z direction. This broadening can, in principle, be brought about by the experiment itself: As the inelastic mean free path of the photoelectrons is finite, k_z cannot be precisely determined in our experiments according to Heisenberg's uncertainty principle. At the high kinetic energies we work at, the k_z broadening is, however, comparatively small ($\Delta k_z \approx 0.1$ Å). Thus the k_z broadening is, instead, attributed to the mobile electrons accumulating at the interface: Due to the confinement of the mobile electrons in z direction, their k_z momentum is not precisely defined. Assessing the broadening of the three-dimensional Fermi surface one can also estimate the extension of the interfacial electron system.[205]

In conclusion, we find that the electron system at the (111) heterointerface is neither purely two-dimensional nor is it purely three-dimensional but extends over several monolayers.

7.7 Conclusion

In this chapter the two-dimensional electron system at the (111) $LaAlO_3/SrTiO_3$ heterointerface is investigated: We demonstrate the high-quality of our $LaAlO_3/SrTiO_3$ heterointerfaces and show that the fully oxidized (111) $LaAlO_3/SrTiO_3$ heterointerfaces are doped by an electronic reconstruction brought about by the polar discontinuity between the $LaAlO_3$ film and the $SrTiO_3$ substrate. We find that also in the (111)-oriented samples, the charge carrier concentration in the 2DES can be effectively tuned by the electric field effect.

The electronic structure of the (111)-oriented heterointerface is investigated by soft x-ray angle-resolved resonant photoelectron spectroscopy: The Fermi surface maps measured showcase the distinctive symmetry of the (111) orientation. Changing the light polarization, we identify the orbital symmetries in the Fermi surface map. High-resolution band maps identify the interfacial charge carriers as polarons but do not provide any evidence of the new electronic phases density functional theory predicts for the (111)-oriented heterostructures.[77] The asymmetry in the Fermi surface map reveals that the electron system is not strictly two-dimensional but extends over several $SrTiO_3$ layers which may also explain the discrepancy between the experimental results and the predictions from density functional theory as these are made for $LaAlO_3/SrTiO_3$ heterostructures containing $SrTiO_3$ bilayers and trilayers.

Our careful characterization and analysis of the (111) $LaAlO_3/SrTiO_3$ heterointerfaces and the peculiar effects therein lay the foundation for further experiments: To put the predictions of density functional theory for highly confined $SrTiO_3$ quantum wells to the test, one could investigate the momentum-resolved electronic structure of $LaAlO_3/SrTiO_3$ superlattices in which the $SrTiO_3$ layer thickness is artificially confined to a small number of bilayers. To comb for new phases, one could furthermore systematically vary the electron doping and the $SrTiO_3$ quantum well shape in these heterostructures by engineering the oxygen vacancy concentration. One could also deposit the $LaAlO_3/SrTiO_3$ superlattices on different substrates, which changes the strain imposed on the $SrTiO_3$ thin film and also affects the electronic phase according to density functional theory predictions.[77]

Chapter 8

Conclusion and Outlook

The present thesis investigates how the interfaces of functional oxides can be engineered. Employing photoemission spectroscopy and transport experiments, we probe the electronic structure of the textbook example for an interface in the oxide electronics community, i.e., the conductive interface forming between the band insulators $SrTiO_3$ and $LaAlO_3$. We demonstrate how the electronic interface properties can be systematically manipulated, on the one hand, by the oxygen vacancy concentration and, on the other hand, by the crystalline orientation of the heterointerface. Such control over oxide interfaces is not only interesting for fundamental research but is also essential with regard to applications of oxide materials in future electronic devices.

The doping mechanism at work in the $LaAlO_3/SrTiO_3$ heterointerface are scrutinized first by photoelectron spectroscopy: Varying the key parameters defining the $LaAlO_3/SrTiO_3$ heterostructure, we resolve the long-standing controversy surrounding the doping mechanism in epitaxial $LaAlO_3/SrTiO_3$ heterostructures. Fully oxidized $LaAlO_3/SrTiO_3$ heterostructures are shown to be doped by an electronic reconstruction which is triggered by the polar discontinuity at the interface. The doping level of the heterostructure can furthermore be precisely adjusted by virtue of the oxygen vacancy concentration, which can, in turn, be varied during the photoemission experiment itself combining the intense x-ray irradiation with an oxygen treatment.

Exploiting this technique, we investigate by hard x-ray photoemission how the electronic interface properties, i.e., the charge carrier distribution, the band bending as well as the band alignment at the buried interface, change as a function of the oxygen vacancy concentration and of the doping at low temperature. For a reliable analysis of the charge carrier distribution and the band bending a fit model based on the Poisson-Schrödinger equations is introduced. We find that the band bending systematically varies with the doping which brings along a change in the band alignment at the interface as the $LaAlO_3$ bands are found to shift concurrently with the $SrTiO_3$ band edges at the interface. Based on these findings, we can reconcile the seemingly contradicting experimental results for the valence band offset that are reported in literature.

The dielectric constant of the $SrTiO_3$ substrate and, in particular, its strong non-linear dependence on the electric field proves to be the essential parameter governing the band diagram of the $LaAlO_3/SrTiO_3$ heterostructures. It leads to a strong confinement of the charge carriers to the interface which is only reduced at low doping levels.

The dependence of the dielectric constant of $SrTiO_3$ on temperature and its impact on the electronic interface properties are investigated as well. We find that the electronic interface properties and, in particular, the charge carrier distribution do only depend on temperature when the mobile charge carrier concentration is small. This observation is traced back to the combined effect of temperature and electric field on the dielectric constant of $SrTiO_3$.

The effect of the oxygen vacancy concentration on the electronic properties in the $LaAlO_3/SrTiO_3$ heterostructure is also studied by a complementary method, viz. by transport experiments. These measurements confirm that the concentration of mobile electrons is increasing along with the oxygen vacancy concentration. The charge carrier mobilities are varying concomitantly with the charge carrier concentration. A comparison between spectroscopy and transport experiments yields information about the functional properties governing transport. We also demonstrate how the interface engineering can be exploited in an electronic device using the example of a $LaAlO_3/SrTiO_3$-based memristor: The memristor is shown to be effectively tuned in its properties by gating but also by the oxygen vacancy concentration.

The electronic structure is also affected by the crystalline orientation of the heterostructures. Switching from the common (001)- to (111)-oriented $LaAlO_3/SrTiO_3$ heterostructures, the real space lattice at the interface adopts the peculiar honeycomb-type geometry, which is predicted to host topologically non-trivial states.[77] To scrutinize the effect of the interface topology on the electronic structure, high-quality (111)-oriented $LaAlO_3/SrTiO_3$ heterostructures are fabricated and characterized. The (111) heterointerfaces are also found to be doped by an electronic reconstruction brought about by the polar discontinuity between the $SrTiO_3$ substrate and the $LaAlO_3$ film. The distinctive symmetry of the (111) interface becomes apparent in the Fermi surface map probed by angle-resolved photoemission spectroscopy. Based on the asymmetry in the Fermi surface, the dimensionality of the metallic layer is assessed. By measurements with different light polarizations, the contributions of the single orbitals are furthermore extracted. The spectral function measured identifies the charge carriers at the interface as large polarons but does not yield any evidence of the new phases predicted by density functional theory.

In conclusion, we established methods to manipulate the properties of the $LaAlO_3/SrTiO_3$ heterointerfaces at will, be it by the oxygen vacancy concentration or by the interface topology. The various findings about the interface engineering open up opportunities for applications but may also kick off further research as pointed out in the following:
The manipulation of the oxygen vacancy concentration by the x-ray beam and by oxygen dosing has proven to be an effective way to control the electronic interface properties precisely in a spatially confined area. In the future, this may turn out useful as a lithography method to pattern samples.
Having demonstrated that the $LaAlO_3/SrTiO_3$ interface can effectively be engineered by the oxygen vacancy concentration, this technique can also be transferred to other oxide heterointerfaces which are prone to oxygen vacancies, such as the high-mobility 2DES at the interface between disordered $LaAlO_3$ and $KTaO_3$.[206]
The relative permittivity of $SrTiO_3$ is found to be the crucial parameter determining the interfacial band alignment as well as the 2DES extension and, in consequence, the mobility in $SrTiO_3$-based heterostructures. To tune these electronic interface properties even further, one may tailor the relative permittivity by other parameters beside the doping and, e.g., exploit that the relative permittivity is also changed in strained $SrTiO_3$ thin films.[65]
Another yet unexplored way to engineer the electronic properties in $SrTiO_3$-based heterointerfaces is to manipulate the thickness of the conducting $SrTiO_3$ layer directly. By building heterostructures with very thin $SrTiO_3$ layers, charge carriers can artificially be confined to a specific geometry, as, e.g., the honeycomb lattice in (111)-oriented heterostructures, which might give rise to new electronic phases.[77]

Bibliography

[1] H. Kroemer, Reviews of Modern Physics **73**, 783 (2001).

[2] J. Heber, Nature **459**, 28 (2009).

[3] A. Ohtomo and H. Y. Hwang, Nature **427**, 5 (2004).

[4] A. Brinkman, M. Huijben, M. van Zalk, J. Huijben, U. Zeitler, J. C. Maan, W. G. van der Wiel, G. Rijnders, D. H. A. Blank, and H. Hilgenkamp, Nature Materials **6**, 493 (2007).

[5] A. D. Caviglia, M. Gabay, S. Gariglio, N. Reyren, C. Cancellieri, and J.-M. Triscone, Physical Review Letters **104**, 126803 (2010).

[6] N. Reyren, S. Thiel, A. D. Caviglia, L. F. Kourkoutis, G. Hammerl, C. Richter, C. W. Schneider, T. Kopp, A.-S. Rüetschi, D. Jaccard, M. Gabay, D. A. Muller, J.-M. Triscone, and J. Mannhart, Science **317**, 1196 (2007).

[7] J. A. Bert, B. Kalisky, C. Bell, M. Kim, Y. Hikita, H. Y. Hwang, and K. A. Moler, Nature Physics **7**, 767 (2011).

[8] L. Li, C. Richter, J. Mannhart, and R. C. Ashoori, Nature Physics **7**, 762 (2011).

[9] S. Thiel, G. Hammerl, A. Schmehl, C. W. Schneider, and J. Mannhart, Science **313**, 1942 (2006).

[10] B. Förg, C. Richter, and J. Mannhart, Applied Physics Letters **100**, 053506 (2012).

[11] E. Lesne, Y. Fu, S. Oyarzun, J. C. Rojas-Sánchez, D. C. Vaz, H. Naganuma, G. Sicoli, J.-P. Attané, M. Jamet, E. Jacquet, J.-M. George, A. Barthélémy, H. Jaffrès, A. Fert, M. Bibes, and L. Vila, Nature Materials **15**, 1261 (2016).

[12] Q. Song, H. Zhang, T. Su, W. Yuan, Y. Chen, W. Xing, J. Shi, J. Sun, and W. Han, Science Advances **3**, e1602312 (2017).

[13] R. Eason, *Pulsed Laser Deposition of Thin Films: Applications-Led Growth of Functional Materials* (Wiley, 2007).

[14] P. R. Willmott and J. R. Huber, Reviews of Modern Physics **72**, 315 (2000).

[15] A. A. Læssøe, commons.wikimedia.org/wiki/File:Pulsed_Laser_Deposition_in_Action.jpg under license creativecommons.org/licenses/by-sa/4.0/legalcode, retrieved 09/06/2018.

[16] H. Hertz, Annalen der Physik und Chemie **267**, 983 (1887).

[17] W. Hallwachs, Annalen der Physik und Chemie **269**, 301 (1888).

[18] P. Lenard, Annalen der Physik **307**, 359 (1900).

[19] A. Einstein, Annalen der Physik **322**, 132 (1905).

[20] C. Nordling, E. Sokolowski, and K. Siegbahn, Physical Review **105**, 1676 (1957).

[21] S. Hüfner, *Photoelectron Spectroscopy: Principles and Applications* (Springer, 2003).

[22] S. Suga and A. Sekiyama, *Photoelectron Spectroscopy: Bulk and Surface Electronic Structures* (Springer, 2013).

[23] C. N. Berglund and W. E. Spicer, Physical Review **136**, A1030 (1964).

[24] A. Damascelli, Physica Scripta **T109**, 61 (2004).

[25] M. P. Seah and W. A. Dench, Surface and Interface Analysis **1**, 2 (1979).

[26] J. J. Yeh and I. Lindau, Atomic Data and Nuclear Data Tables **32**, 1 (1985).

[27] S. Tanuma, C. J. Powell, and D. R. Penn, Surface and Interface Analysis **21**, 165 (1994).

[28] S. Tanuma, C. J. Powell, and D. R. Penn, Surface and Interface Analysis **35**, 268 (2003).

[29] C. J. Powell and A. Jablonski, *NIST Electron Inelastic-Mean-Free-Path Database 71, Version 1.1*, National Standard Reference Data Series, 2000.

[30] J. W. Cooper, Physical Review A **47**, 1841 (1993).

[31] M. B. Trzhaskovskaya, V. K. Nikulin, V. I. Nefedov, and V. G. Yarzhemsky, Optics and Spectroscopy **96**, 765 (2004).

[32] D. Briggs and M. P. Seah, *Practical Surface Analysis, Auger and X-ray Photoelectron Spectroscopy* (Wiley, 1990).

[33] C. Fadley, Physica Scripta **T17**, 39 (1987).

[34] D. A. Shirley, Physical Review B **5**, 4709 (1972).

[35] S. Hüfner, *Very High Resolution Photoelectron Spectroscopy* (Springer, 2007).

[36] U. Fano, Physical Review **124**, 1866 (1961).

[37] M. Huijben, G. Rijnders, D. H. A. Blank, S. Bals, S. V. Aert, J. Verbeeck, G. V. Tendeloo, A. Brinkman, and H. Hilgenkamp, Nature Materials **5**, 556 (2006).

[38] L. J. van der Pauw, Philips Technical Review **20**, 220 (1958).

[39] A. Ramadan, R. Gould, and A. Ashour, Thin Solid Films **239**, 272 (1994).

[40] P. Drude, Annalen der Physik **306**, 566 (1900).

[41] D. C. Look, *Electrical Characterization of GaAs Materials and devices* (Wiley, 1989).

[42] F. Gunkel, C. Bell, H. Inoue, B. Kim, A. G. Swartz, T. A. Merz, Y. Hikita, S. Harashima, H. K. Sato, M. Minohara, S. Hoffmann-Eifert, R. Dittmann, and H. Y. Hwang, Physical Review X **6** (2016).

[43] D. W. Koon, Review of Scientific Instruments **60**, 271 (1989).

[44] D. W. Koon, A. A. Bahl, and E. O. Duncan, Review of Scientific Instruments **60**, 275 (1989).

[45] T. Matsumura and Y. Sato, Journal of Modern Physics **01**, 340 (2010).

[46] O. Bierwagen, T. Ive, C. G. Van de Walle, and J. S. Speck, Applied Physics Letters **93**, 242108 (2008).

[47] S. Jandl, K. D. Usadel, and G. Fischer, Review of Scientific Instruments **45**, 1479 (1974).

[48] J. Volger, Physical Review **79**, 1023 (1950).

[49] M. Z. Minhas, H. H. Blaschek, F. Heyroth, and G. Schmidt, AIP Advances **6**, 035002 (2016).

[50] N. Banerjee, M. Huijben, G. Koster, and G. Rijnders, Applied Physics Letters **100**, 041601 (2012).

[51] Z. Q. Liu, C. J. Li, W. M. Lü, X. H. Huang, Z. Huang, S. W. Zeng, X. P. Qiu, L. S. Huang, A. Annadi, J. S. Chen, J. M. D. Coey, T. Venkatesan, and Ariando, Physical Review X **3**, 021010 (2013).

[52] A. Kalabukhov, R. Gunnarsson, J. Börjesson, E. Olsson, T. Claeson, and D. Winkler, Physical Review B **75**, 121404 (2007).

[53] W. Siemons, G. Koster, H. Yamamoto, W. A. Harrison, G. Lucovsky, T. H. Geballe, D. H. A. Blank, and M. R. Beasley, Physical Review Letters **98**, 196802 (2007).

[54] F. Trier, K. V. Reich, D. V. Christensen, Y. Zhang, H. L. Tuller, Y. Chen, B. I. Shklovskii, and N. Pryds, Applied Physics Letters **111**, 092106 (2017).

[55] G. Herranz, M. Basletić, M. Bibes, C. Carrétéro, E. Tafra, E. Jacquet, K. Bouzehouane, C. Deranlot, A. Hamzić, J.-M. Broto, A. Barthélémy, and A. Fert, Physical Review Letters **98**, 216803 (2007).

[56] P. R. Willmott, S. A. Pauli, R. Herger, C. M. Schlepütz, D. Martoccia, B. D. Patterson, B. Delley, R. Clarke, D. Kumah, C. Cionca, and Y. Yacoby, Physical Review Letters **99**, 155502 (2007).

[57] J. A. Sulpizio, S. Ilani, P. Irvin, and J. Levy, Annual Review of Materials Research **44**, 117 (2014).

[58] A. Okazaki and M. Kawaminami, Materials Research Bulletin **8**, 545 (1973).

[59] V. Goldschmidt, Naturwissenschaften **14**, 477 (1926).

[60] K. A. Müller, W. Berlinger, and F. Waldner, Physical Review Letters **21**, 814 (1968).

[61] P. A. Fleury, J. F. Scott, and J. M. Worlock, Physical Review Letters **21**, 16 (1968).

[62] L. F. Mattheiss, Physical Review B **6**, 4740 (1972).

[63] Y. Frenkel, N. Haham, Y. Shperber, C. Bell, Y. Xie, Z. Chen, Y. Hikita, H. Y. Hwang, E. K. H. Salje, and B. Kalisky, Nature Materials **16**, 1203 (2017).

[64] M. Itoh, R. Wang, Y. Inaguma, T. Yamaguchi, Y. J. Shan, and T. Nakamura, Physical Review Letters **82**, 3540 (1999).

[65] J. H. Haeni, P. Irvin, W. Chang, R. Uecker, P. Reiche, Y. L. Li, S. Choudhury, W. Tian, M. E. Hawley, B. Craigo, A. K. Tagantsev, X. Q. Pan, S. K. Streiffer, L. Q. Chen, S. W. Kirchoefer, J. Levy, and D. G. Schlom, Nature **430**, 4 (2004).

[66] K. A. Müller and H. Burkard, Physical Review B **19**, 3593 (1979).

[67] T. Sakudo and H. Unoki, Physical Review Letters **26**, 851 (1971).

[68] H.-M. Christen, J. Mannhart, E. J. Williams, and C. Gerber, Physical Review B **49**, 12095 (1994).

[69] C. S. Koonce, M. L. Cohen, J. F. Schooley, W. R. Hosler, and E. R. Pfeiffer, Physical Review **163**, 380 (1967).

[70] Z. Salman, O. Ofer, M. Radovic, H. Hao, M. Ben Shalom, K. H. Chow, Y. Dagan, M. D. Hossain, C. D. P. Levy, W. A. MacFarlane, G. M. Morris, L. Patthey, M. R. Pearson, H. Saadaoui, T. Schmitt, D. Wang, and R. F. Kiefl, Physical Review Letters **109**, 257207 (2012).

[71] P. Moetakef, J. R. Williams, D. G. Ouellette, A. P. Kajdos, D. Goldhaber-Gordon, S. J. Allen, and S. Stemmer, Physical Review X **2**, 021014 (2012).

[72] D. A. Dikin, M. Mehta, C. W. Bark, C. M. Folkman, C. B. Eom, and V. Chandrasekhar, Physical Review Letters **107**, 056802 (2011).

[73] A. Fête, "Magnetotransport Experiments at the $LaAlO_3/SrTiO_3$ Interface", PhD thesis (Université de Genève 2014).

[74] M. Salluzzo, J. C. Cezar, N. B. Brookes, V. Bisogni, G. M. De Luca, C. Richter, S. Thiel, J. Mannhart, M. Huijben, A. Brinkman, G. Rijnders, and G. Ghiringhelli, Physical Review Letters **102**, 166804 (2009).

[75] C. Cancellieri, M. L. Reinle-Schmitt, M. Kobayashi, V. N. Strocov, P. R. Willmott, D. Fontaine, P. Ghosez, A. Filippetti, P. Delugas, and V. Fiorentini, Physical Review B **89**, 121412 (2014).

[76] A. F. Santander-Syro, O. Copie, T. Kondo, F. Fortuna, S. Pailhès, R. Weht, X. G. Qiu, F. Bertran, A. Nicolaou, A. Taleb-Ibrahimi, P. Le Fèvre, G. Herranz, M. Bibes, N. Reyren, Y. Apertet, P. Lecoeur, A. Barthélémy, and M. J. Rozenberg, Nature **469**, 189 (2011).

[77] D. Doennig, W. E. Pickett, and R. Pentcheva, Physical Review Letters **111**, 126804 (2013).

[78] K. Song, S. Ryu, H. Lee, T. R. Paudel, C. T. Koch, B. Park, J. K. Lee, S.-Y. Choi, Y.-M. Kim, J. C. Kim, H. Y. Jeong, M. S. Rzchowski, E. Y. Tsymbal, C.-B. Eom, and S. H. Oh, Nature Nanotechnology **13**, 198 (2018).

[79] S. McKeown Walker, A. de la Torre, F. Y. Bruno, A. Tamai, T. K. Kim, M. Hoesch, M. Shi, M. S. Bahramy, P. D. C. King, and F. Baumberger, Physical Review Letters **113**, 177601 (2014).

[80] T. C. Rödel, C. Bareille, F. Fortuna, C. Baumier, F. Bertran, P. Le Fèvre, M. Gabay, O. Hijano Cubelos, M. J. Rozenberg, T. Maroutian, P. Lecoeur, and A. F. Santander-Syro, Physical Review Applied **1**, 051002 (2014).

[81] G. M. De Luca, R. Di Capua, E. Di Gennaro, A. Sambri, F. M. Granozio, G. Ghiringhelli, D. Betto, C. Piamonteze, N. B. Brookes, and M. Salluzzo, Physical Review B **98**, 115143 (2018).

[82] K. van Benthem, C. Elsässer, and R. H. French, Journal of Applied Physics **90**, 6156 (2001).

[83] M. I. Cohen and R. F. Blunt, Physical Review **168**, 929 (1968).

[84] M. Cardona, Physical Review **140**, A651 (1965).

[85] K.-J. Zhou, M. Radovic, J. Schlappa, V. Strocov, R. Frison, J. Mesot, L. Patthey, and T. Schmitt, Physical Review B **83**, 201402(R) (2011).

[86] G. Khalsa and A. H. MacDonald, Physical Review B **86** (2012).

[87] T. C. Rödel, "Two-Dimensional Electron Systems in Functional Oxides Studied by Photoemission Spectroscopy", PhD thesis (Université Paris-Saclay 2016).

[88] G. Koster, G. Rijnders, D. H. A. Blank, and H. Rogalla, Physica C: Superconductivity **339**, 215 (2000).

[89] M. M. Kawasaki, K. K. Takahashi, T. T. Maeda, R. R. Tsuchiya, M. M. Shinohara, O. O. Ishiyama, T. T. Yonezawa, M. M. Yoshimoto, and H. H. Koinuma, Science **266**, 1540 (1994).

[90] R. A. McKee, F. J. Walker, and M. F. Chisholm, Physical Review Letters **81**, 3014 (1998).

[91] L. Kornblum, E. N. Jin, D. P. Kumah, A. T. Ernst, C. C. Broadbridge, C. H. Ahn, and F. J. Walker, Applied Physics Letters **106**, 201602 (2015).

[92] E. N. Jin, L. Kornblum, D. P. Kumah, K. Zou, C. C. Broadbridge, J. H. Ngai, C. H. Ahn, and F. J. Walker, APL Materials **2**, 116109 (2014).

[93] pixabay.com/de/prozessor-cpu-computer-chip-2217771/ under license creativecommons.org/publicdomain/zero/1.0/deed.de, retrieved 10/20/2018.

[94] H. R. Huff and D. C. Gilmer, eds., *High dielectric constant materials: VLSI MOSFET applications* (Springer, 2005).

[95] R. C. Neville, B. Hoeneisen, and C. A. Mead, Journal of Applied Physics **43**, 2124 (1972).

[96] D. B. Strukov, G. S. Snider, D. R. Stewart, and R. S. Williams, Nature **453**, 80 (2008).

[97] C. Baeumer, C. Schmitz, A. H. H. Ramadan, H. Du, K. Skaja, V. Feyer, P. Müller, B. Arndt, C.-L. Jia, J. Mayer, R. A. De Souza, C. Michael Schneider, R. Waser, and R. Dittmann, Nature Communications **6**, 9610 (2015).

[98] P. Kanhere, Z. Chen, P. Kanhere, and Z. Chen, Molecules **19**, 19995 (2014).

[99] M. Huijben, A. Brinkman, G. Koster, G. Rijnders, H. Hilgenkamp, and D. H. A. Blank, Advanced Materials **21**, 1665 (2009).

[100] A. D. Caviglia, S. Gariglio, N. Reyren, D. Jaccard, T. Schneider, M. Gabay, S. Thiel, G. Hammerl, J. Mannhart, and J.-M. Triscone, Nature **456**, 624 (2008).

[101] A. D. Caviglia, S. Gariglio, C. Cancellieri, B. Sacépé, A. Fête, N. Reyren, M. Gabay, A. F. Morpurgo, and J.-M. Triscone, Physical Review Letters **105**, 236802 (2010).

[102] M. Huijben, G. Koster, M. K. Kruize, S. Wenderich, J. Verbeeck, S. Bals, E. Slooten, B. Shi, H. J. A. Molegraaf, J. E. Kleibeuker, S. van Aert, J. B. Goedkoop, A. Brinkman, D. H. A. Blank, M. S. Golden, G. van Tendeloo, H. Hilgenkamp, and G. Rijnders, Advanced Functional Materials **23**, 5240 (2013).

[103] A. Fête, C. Cancellieri, D. Li, D. Stornaiuolo, A. D. Caviglia, S. Gariglio, and J.-M. Triscone, Applied Physics Letters **106**, 051604 (2015).

[104] S. Zeng, W. Lü, Z. Huang, Z. Liu, K. Han, K. Gopinadhan, C. Li, R. Guo, W. Zhou, H. H. Ma, L. Jian, T. Venkatesan, and Ariando, ACS Nano **10**, 4532 (2016).

[105] A. Ron and Y. Dagan, Physical Review Letters **112**, 136801 (2014).

[106] A. Annadi, G. Cheng, H. Lee, J.-W. Lee, S. Lu, A. Tylan-Tyler, M. Briggeman, M. Tomczyk, M. Huang, D. Pekker, C.-B. Eom, P. Irvin, and J. Levy, Nano Letters **18**, 4473 (2018).

[107] M. Reinle-Schmitt, C. Cancellieri, D. Li, D. Fontaine, M. Medarde, E. Pomjakushina, C. Schneider, S. Gariglio, P. Ghosez, J.-M. Triscone, and P. Willmott, Nature Communications **3**, 932 (2012).

[108] R. Pentcheva and W. E. Pickett, Phys. Rev. Lett. **102**, 107602 (2009).

[109] G. Berner, M. Sing, H. Fujiwara, A. Yasui, Y. Saitoh, A. Yamasaki, Y. Nishitani, A. Sekiyama, N. Pavlenko, T. Kopp, C. Richter, J. Mannhart, S. Suga, and R. Claessen, Physical Review Letters **110**, 247601 (2013).

[110] Y. Segal, J. H. Ngai, J. W. Reiner, F. J. Walker, and C. H. Ahn, Physical Review B **80**, 241107(R) (2009).

[111] G. Berner, A. Müller, F. Pfaff, J. Walde, C. Richter, J. Mannhart, S. Thiess, A. Gloskovskii, W. Drube, M. Sing, and R. Claessen, Physical Review B **88**, 115111 (2013).

[112] Z. Zhong, P. X. Xu, and P. J. Kelly, Physical Review B **82**, 165127 (2010).

[113] N. C. Bristowe, P. B. Littlewood, and E. Artacho, Physical Review B **83**, 205405 (2011).

[114] Y. Li, S. N. Phattalung, S. Limpijumnong, J. Kim, and J. Yu, Physical Review B **84**, 245307 (2011).

[115] N. Pavlenko, T. Kopp, E. Y. Tsymbal, J. Mannhart, and G. A. Sawatzky, Physical Review B **86**, 064431 (2012).

[116] L. Yu and A. Zunger, Nature Communications **5**, 5118 (2014).

[117] Y. Chen, N. Pryds, J. E. Kleibeuker, G. Koster, J. Sun, E. Stamate, B. Shen, G. Rijnders, and S. Linderoth, Nano Letters **11**, 3774 (2011).

[118] Y. Aiura, I. Hase, H. Bando, T. Yasue, T. Saitoh, and D. S. Dessau, Surface Science **515**, 61 (2002).

[119] W. Meevasana, P. D. C. King, R. H. He, S.-K. Mo, M. Hashimoto, A. Tamai, P. Songsiririt-thigul, F. Baumberger, and Z.-X. Shen, Nature Materials **10**, 114 (2011).

[120] S. M. Walker, F. Y. Bruno, Z. Wang, A. de la Torre, S. Riccó, A. Tamai, T. K. Kim, M. Hoesch, M. Shi, M. S. Bahramy, P. D. C. King, and F. Baumberger, Advanced Materials **27**, 3894 (2015).

[121] A. B. Posadas, K. J. Kormondy, W. Guo, P. Ponath, J. Geler-Kremer, T. Hadamek, and A. A. Demkov, Journal of Applied Physics **121**, 105302 (2017).

[122] T. C. Rödel, F. Fortuna, S. Sengupta, E. Frantzeskakis, P. L. Fèvre, F. Bertran, B. Mercey, S. Matzen, G. Agnus, T. Maroutian, P. Lecoeur, and A. F. Santander-Syro, Advanced Materials **28**, 1976 (2016).

[123] A. Sambri, D. V. Christensen, F. Trier, Y. Z. Chen, S. Amoruso, N. Pryds, R. Bruzzese, and X. Wang, Applied Physics Letters **100**, 231605 (2012).

[124] S. A. Chambers, Surface Science **605**, 1133 (2011).

[125] T. Higuchi, D. Baba, T. Takeuchi, T. Tsukamoto, Y. Taguchi, Y. Tokura, A. Chainani, and S. Shin, Physical Review B **68**, 104420 (2003).

[126] N. Nakagawa, H. Y. Hwang, and D. A. Muller, Nature Materials **5**, 204 (2006).

[127] C. L. Jia, S. B. Mi, M. Faley, U. Poppe, J. Schubert, and K. Urban, Physical Review B **79**, 081405(R) (2009).

[128] S. A. Chambers, M. H. Engelhard, V. Shutthanandan, Z. Zhu, T. C. Droubay, L. Qiao, P. V. Sushko, T. Feng, H. Lee, T. Gustafsson, E. Garfunkel, A. B. Shah, J.-M. Zuo, and Q. M. Ramasse, Surface Science Reports **65**, 317 (2010).

[129] G. Salvinelli, G. Drera, A. Giampietri, and L. Sangaletti, ACS Applied Materials & Interfaces **7**, 25648 (2015).

[130] Z. Wang, Z. Zhong, X. Hao, S. Gerhold, B. Stöger, M. Schmid, J. Sánchez-Barriga, A. Varykhalov, C. Franchini, K. Held, and U. Diebold, Proceedings of the National Academy of Sciences **111**, 3933 (2014).

[131] G. Drera, F. Banfi, F. F. Canova, P. Borghetti, L. Sangaletti, F. Bondino, E. Magnano, J. Huijben, M. Huijben, G. Rijnders, D. H. A. Blank, H. Hilgenkamp, and A. Brinkman, Applied Physics Letters **98**, 052907 (2011).

[132] C. Lin and A. A. Demkov, Physical Review Letters **111**, 217601 (2013).

[133] H. O. Jeschke, J. Shen, and R. Valentí, New Journal of Physics **17**, 023034 (2015).

[134] F. Lechermann, L. Boehnke, D. Grieger, and C. Piefke, Physical Review B **90**, 085125 (2014).

[135] G. Drera, G. Salvinelli, A. Brinkman, M. Huijben, G. Koster, H. Hilgenkamp, G. Rijnders, D. Visentin, and L. Sangaletti, Physical Review B **87**, 075435 (2013).

[136] G. Drera, G. Salvinelli, F. Bondino, E. Magnano, M. Huijben, A. Brinkman, and L. Sangaletti, Physical Review B **90**, 035124 (2014).

[137] U. Treske, N. Heming, M. Knupfer, B. Büchner, E. D. Gennaro, A. Khare, U. S. Di Uccio, F. M. Granozio, S. Krause, and A. Koitzsch, Scientific Reports **5**, 14506 (2015).

[138] E. Slooten, Z. Zhong, H. J. A. Molegraaf, P. D. Eerkes, S. de Jong, F. Massee, E. van Heumen, M. K. Kruize, S. Wenderich, J. E. Kleibeuker, M. Gorgoi, H. Hilgenkamp, A. Brinkman, M. Huijben, G. Rijnders, D. H. A. Blank, G. Koster, P. J. Kelly, and M. S. Golden, Physical Review B **87**, 085128 (2013).

[139] C. Weiland, G. E. Sterbinsky, A. K. Rumaiz, C. S. Hellberg, J. C. Woicik, S. Zhu, and D. G. Schlom, Physical Review B **91**, 165103 (2015).

[140] M. Sing, G. Berner, K. Goß, A. Müller, A. Ruff, A. Wetscherek, S. Thiel, J. Mannhart, S. A. Pauli, C. W. Schneider, P. R. Willmott, M. Gorgoi, F. Schäfers, and R. Claessen, Physical Review Letters **102**, 176805 (2009).

[141] M. Sunding, K. Hadidi, S. Diplas, O. Løvvik, T. Norby, and A. Gunnæs, Journal of Electron Spectroscopy and Related Phenomena **184**, 399 (2011).

[142] T. Susaki, S. Ueda, K. Matsuzaki, T. Kobayashi, Y. Toda, and H. Hosono, Physical Review B **94**, 075311 (2016).

[143] L. Qiao, T. Droubay, V. Shutthanandan, Z. Zhu, P. Sushko, and S. Chambers, Journal of Physics: Condensed Matter **22**, 312201 (2010).

[144] L. Qiao, T. C. Droubay, T. C. Kaspar, P. V. Sushko, and S. A. Chambers, Surface Science **605**, 1381 (2011).

[145] K. Yoshimatsu, R. Yasuhara, H. Kumigashira, and M. Oshima, Physical Review Letters **101**, 026802 (2008).

[146] www.diamond.ac.uk/Instruments/Structures-and-Surfaces/I09/Beamline-layout.html, retrieved 05/17/2018.

[147] T.-L. Lee and D. A. Duncan, Synchrotron Radiation News **31**, 16 (2018).

[148] P. Schütz, F. Pfaff, P. Scheiderer, Y. Z. Chen, N. Pryds, M. Gorgoi, M. Sing, and R. Claessen, Physical Review B **91**, 165118 (2015).

[149] Y. Z. Chen, N. Bovet, T. Kasama, W. W. Gao, S. Yazdi, C. Ma, N. Pryds, and S. Linderoth, Advanced Materials **26**, 1462 (2014).

[150] F. Stern, Physical Review B **5**, 4891 (1972).

[151] F. Stern and W. E. Howard, Physical Review **163**, 816 (1967).

[152] G. L. Snider, I. Tan, and E. L. Hu, Journal of Applied Physics **68**, 2849 (1990).

[153] I. Tan, G. L. Snider, L. D. Chang, and E. L. Hu, Journal of Applied Physics **68**, 4071 (1990).

[154] www3.nd.edu/~gsnider, retrieved 06/05/2018.

[155] W. Demtröder, *Elektrostatik* (Springer, 2017).

[156] H. Peelaers, K. Krishnaswamy, L. Gordon, D. Steiauf, A. Sarwe, A. Janotti, and C. G. Van de Walle, Applied Physics Letters **107**, 183505 (2015).

[157] M. Stengel, Physical Review Letters **106**, 136803 (2011).

[158] S. Gariglio, M. Gabay, and J.-M. Triscone, APL Materials **4**, 060701 (2016).

[159] M. Marques, L. K. Teles, V. Anjos, L. M. R. Scolfaro, J. R. Leite, V. N. Freire, G. A. Farias, and E. F. da Silva, Applied Physics Letters **82**, 3074 (2003).

[160] T. Okuda, K. Nakanishi, S. Miyasaka, and Y. Tokura, Physical Review B **63**, 113104 (2001).

[161] A. Giampietri, G. Drera, and L. Sangaletti, Advanced Materials Interfaces **4**, 1700144 (2017).

[162] E. A. Kraut, R. W. Grant, J. R. Waldrop, and S. P. Kowalczyk, Physical Review Letters **44**, 1620 (1980).

[163] C. Cancellieri, N. Reyren, S. Gariglio, A. D. Caviglia, A. Fête, and J.-M. Triscone, Europhysics Letters **91**, 17004 (2010).

[164] Y. Xie, Y. Hikita, C. Bell, and H. Y. Hwang, Nature Communications **2**, 494 (2011).

[165] O. Copie, V. Garcia, C. Bödefeld, C. Carrétéro, M. Bibes, G. Herranz, E. Jacquet, J.-L. Maurice, B. Vinter, S. Fusil, K. Bouzehouane, H. Jaffrès, and A. Barthélémy, Physical Review Letters **102**, 216804 (2009).

[166] F. Trier, S. Amoruso, D. V. Christensen, A. Sambri, Y. Z. Chen, X. Wang, E. Stamate, R. Bruzzese, and N. Pryds, Applied Physics Letters **103**, 031607 (2013).

[167] B. Leikert, "Kontrollierte Variation der elektronischen Eigenschaften der Heterostruktur von Al/$SrTiO_3$", Masterarbeit (Universität Würzburg 2017).

[168] A. Chikina, F. Lechermann, M.-A. Husanu, M. Caputo, C. Cancellieri, X. Wang, T. Schmitt, M. Radovic, and V. N. Strocov, ACS Nano **12**, 7927 (2018).

[169] A. Raslan, P. Lafleur, and W. A. Atkinson, Physical Review B **95**, 054106 (2017).

[170] O. Okhay, A. Tkach, A. Wu, and P. M. Vilarinho, Journal of Physics D: Applied Physics **46**, 505315 (2013).

[171] C. Li, Z. Liu, W. Lü, X. R. Wang, A. Annadi, Z. Huang, S. Zeng, Ariando, and T. Venkatesan, Scientific Reports **5**, 13314 (2015).

[172] C. W. Schneider, S. Thiel, G. Hammerl, C. Richter, and J. Mannhart, Applied Physics Letters **89**, 122101 (2006).

[173] N. W. Ashcroft and N. D. Mermin, *Solid State Physics* (Holt, Rinehart and Winston, 1976).

[174] S. Raghavan, J. Y. Zhang, and S. Stemmer, Applied Physics Letters **106**, 132104 (2015).

[175] D. V. Christensen, Y. Frenkel, P. Schütz, F. Trier, S. Wissberg, R. Claessen, B. Kalisky, A. Smith, Y. Z. Chen, and N. Pryds, Physical Review Applied **9**, 054004 (2018).

[176] Z. Q. Liu, D. P. Leusink, X. Wang, W. M. Lü, K. Gopinadhan, A. Annadi, Y. L. Zhao, X. H. Huang, S. W. Zeng, Z. Huang, A. Srivastava, S. Dhar, T. Venkatesan, and Ariando, Physical Review Letters **107**, 146802 (2011).

[177] A. Tebano, E. Fabbri, D. Pergolesi, G. Balestrino, and E. Traversa, ACS Nano **6**, 1278 (2012).

[178] T. D. Sanders, M. T. Gray, F. J. Wong, and Y. Suzuki, Physical Review B **91**, 205112 (2015).

[179] S. H. Jo, T. Chang, I. Ebong, B. B. Bhadviya, P. Mazumder, and W. Lu, Nano Letters **10**, 1297 (2010).

[180] G. Herranz, F. Sánchez, N. Dix, M. Scigaj, and J. Fontcuberta, Sci. Rep. **2**, 758 (2012).

[181] D. Xiao, W. Zhu, Y. Ran, N. Nagaosa, and S. Okamoto, Nature Communications **2**, 596 (2011).

[182] C. L. Kane and E. J. Mele, Physical Review Letters **95**, 146802 (2005).

[183] C. L. Kane and E. J. Mele, Physical Review Letters **95**, 226801 (2005).

[184] A. H. Castro Neto, F. Guinea, N. M. R. Peres, K. S. Novoselov, and A. K. Geim, Reviews of Modern Physics **81**, 109 (2009).

[185] A. Biswas, P. B. Rossen, C.-H. Yang, W. Siemons, M.-H. Jung, I. K. Yang, R. Ramesh, and Y. H. Jeong, Applied Physics Letters **98**, 051904 (2011).

[186] B. E. Warren, *X-Ray Diffraction* (Courier Corporation, 2012).

[187] C. Xu, C. Bäumer, R. A. Heinen, S. Hoffmann-Eifert, F. Gunkel, and R. Dittmann, Scientific Reports **6**, 22410 (2016).

[188] J. L. Blok, X. Wan, G. Koster, D. H. A. Blank, and G. Rijnders, Applied Physics Letters **99**, 151917 (2011).

[189] A. E. M. Smink, J. C. de Boer, M. P. Stehno, A. Brinkman, W. G. van der Wiel, and H. Hilgenkamp, Physical Review Letters **118**, 106401 (2017).

[190] C. Bell, S. Harashima, Y. Kozuka, M. Kim, B. G. Kim, Y. Hikita, and H. Y. Hwang, Physical Review Letters **103**, 226802 (2009).

[191] Z. Zhong, A. Tóth, and K. Held, Physical Review B **87**, 161102(R) (2013).

[192] Z. Wang, S. McKeown Walker, A. Tamai, Y. Wang, Z. Ristic, F. Y. Bruno, A. de la Torre, S. Riccò, N. C. Plumb, M. Shi, P. Hlawenka, J. Sánchez-Barriga, A. Varykhalov, T. K. Kim, M. Hoesch, P. D. C. King, W. Meevasana, U. Diebold, J. Mesot, B. Moritz, T. P. Devereaux, M. Radovic, and F. Baumberger, Nature Materials **15**, 835 (2016).

[193] T. C. Rödel, F. Fortuna, F. Bertran, M. Gabay, M. J. Rozenberg, A. F. Santander-Syro, and P. Le Fèvre, Physical Review B **92**, 041106 (2015).

[194] V. N. Strocov, T. Schmitt, U. Flechsig, T. Schmidt, A. Imhof, Q. Chen, J. Raabe, R. Betemps, D. Zimoch, J. Krempasky, X. Wang, M. Grioni, A. Piazzalunga, and L. Patthey, Journal of Synchrotron Radiation **17**, 631 (2010).

[195] T. Straub, R. Claessen, P. Steiner, S. Hüfner, V. Eyert, K. Friemelt, and E. Bucher, Physical Review B **55**, 13473 (1997).

[196] C. Cancellieri, A. S. Mishchenko, U. Aschauer, A. Filippetti, C. Faber, O. S. Barišić, V. A. Rogalev, T. Schmitt, N. Nagaosa, and V. N. Strocov, Nature Communications **7**, 10386 (2016).

[197] G. A. Sawatzky, Nature **342**, 480 (1989).

[198] G. D. Mahan, *Many-Particle Physics* (Springer, 2013).

[199] F. Gervais, J.-L. Servoin, A. Baratoff, J. G. Bednorz, and G. Binnig, Physical Review B **47**, 8187 (1993).

[200] A. S. Mishchenko, N. Nagaosa, G. De Filippis, A. de Candia, and V. Cataudella, Physical Review Letters **114**, 146401 (2015).

[201] T. Holstein, Annals of Physics **8**, 325 (1959).

[202] S. Davis, V. Chandrasekhar, Z. Huang, K. Han, Ariando, and T. Venkatesan, Physical Review B **95**, 035127 (2017).

[203] H. Daimon, S. Imada, H. Nishimoto, and S. Suga, Journal of Electron Spectroscopy and Related Phenomena **76**, 487 (1995).

[204] F. Matsui, T. Matsushita, and H. Daimon, Journal of Electron Spectroscopy and Related Phenomena **195**, 347 (2014).

[205] V. N. Strocov, Journal of Electron Spectroscopy and Related Phenomena **229**, 100 (2018).

[206] M. Zapf, "High-Z Perovskite Oxides: Thin Film Deposition and Spectroscopic Investigations", PhD thesis (Universität Würzburg 2019).

[207] U. Treske, N. Heming, M. Knupfer, B. Büchner, A. Koitzsch, E. Di Gennaro, U. Scotti di Uccio, F. Miletto Granozio, and S. Krause, APL Materials **2**, 012108 (2014).

[208] S. Mukherjee, B. Pal, D. Choudhury, I. Sarkar, W. Drube, M. Gorgoi, O. Karis, H. Takagi, J. Matsuno, and D. D. Sarma, Physical Review B **93**, 245124 (2016).

[209] S. Noschese, L. Pasquini, and L. Reichel, Numerical Linear Algebra with Applications **20**, 302 (2013).

List of own publications

[A1] Y. Motoyui, T. Taniuchi, P. Scheiderer, J. N. Lee, J. Gabel, F. Pfaff, M. Sing, M. Lippmaa, R. Claessen, and S. Shin, Journal of the Physical Society of Japan **88**, 034717 (2019).

[A2] P. Scheiderer, M. Schmitt, J. Gabel, M. Zapf, M. Stübinger, P. Schütz, L. Dudy, C. Schlueter, T.-L. Lee, M. Sing, and R. Claessen, Advanced Materials **30**, 1706708 (2018).

[A3] F. Pfaff, H. Fujiwara, G. Berner, A. Yamasaki, H. Niwa, H. Kiuchi, A. Gloskovskii, W. Drube, J. Gabel, O. Kirilmaz, A. Sekiyama, J. Miyawaki, Y. Harada, S. Suga, M. Sing, and R. Claessen, Physical Review B **97**, 035110 (2018).

[A4] P. Schütz, D. Di Sante, L. Dudy, J. Gabel, M. Stübinger, M. Kamp, Y. Huang, M. Capone, M.-A. Husanu, V. N. Strocov, G. Sangiovanni, M. Sing, and R. Claessen, Physical Review Letters **119**, 256404 (2017).

[A5] P. Schütz, D. V. Christensen, V. Borisov, F. Pfaff, P. Scheiderer, L. Dudy, M. Zapf, J. Gabel, Y. Z. Chen, N. Pryds, V. A. Rogalev, V. N. Strocov, C. Schlueter, T.-L. Lee, H. O. Jeschke, R. Valentí, M. Sing, and R. Claessen, Physical Review B **96**, 161409(R) (2017).

[A6] J. Gabel, M. Zapf, P. Scheiderer, P. Schütz, L. Dudy, M. Stübinger, C. Schlueter, T.-L. Lee, M. Sing, and R. Claessen, Physical Review B **95**, 195109 (2017).

[A7] P. Maier, F. Hartmann, J. Gabel, M. Frank, S. Kuhn, P. Scheiderer, B. Leikert, M. Sing, L. Worschech, R. Claessen, and S. Höfling, Applied Physics Letters **110**, 093506 (2017).

[A8] L. Dudy, M. Sing, P. Scheiderer, J. D. Denlinger, P. Schütz, J. Gabel, M. Buchwald, C. Schlueter, T.-L. Lee, and R. Claessen, Advanced Materials **28**, 7443 (2016).

[A9] P. Scheiderer, F. Pfaff, J. Gabel, M. Kamp, M. Sing, and R. Claessen, Physical Review B **92**, 195422 (2015).

[A10] J. E. Kleibeuker, Z. Zhong, H. Nishikawa, J. Gabel, A. Müller, F. Pfaff, M. Sing, K. Held, R. Claessen, G. Koster, and G. Rijnders, Physical Review Letters **113**, 237402 (2014).

[A11] A. Yamasaki, S. Tachibana, H. Fujiwara, A. Higashiya, A. Irizawa, O. Kirilmaz, F. Pfaff, P. Scheiderer, J. Gabel, M. Sing, T. Muro, M. Yabashi, K. Tamasaku, H. Sato, H. Namatame, M. Taniguchi, A. Hloskovskyy, H. Yoshida, H. Okabe, M. Isobe, J. Akimitsu, W. Drube, R. Claessen, T. Ishikawa, S. Imada, A. Sekiyama, and S. Suga, Physical Review B **89**, 121111 (2014).

[A12] S. J. Callori, J. Gabel, D. Su, J. Sinsheimer, M. V. Fernandez-Serra, and M. Dawber, Physical Review Letters **109**, 067601 (2012).

[A13] J. Gabel, M. Zapf, P. Scheiderer, O. Kirilmaz, S. Elsässer, J. Geurts, C. Cancellieri, V. Rogalev, V. Strocov, M. Sing, and R. Claessen, "Elucidating the electronic structure and the dimensionality of the electron system at the (111) $LaAlO_3/SrTiO_3$ interface", Manuscript.

[A14] J. Gabel, P. Scheiderer, M. Zapf, M. Stübinger, C. Schlueter, T.-L. Lee, M. Sing, and R. Claessen, "Interface band engineering in $LaAlO_3/SrTiO_3$ heterostructures", Manuscript.

[A15] J. Gabel, B. Leikert, M. Stübinger, P. Scheiderer, M. Zapf, C. Schlueter, T.-L. Lee, M. Sing, and R. Claessen, "Tailoring two-dimensional electron systems in $SrTiO_3$-based heterostructures: the impact of the dielectric constant", Manuscript.

Appendix

A Disentangling generic and specific doping mechanisms in oxide heterostructures

In chapter 3 we analyze how the valence band spectra of (001)-oriented $SrTiO_3$-based heterostructures change as a function of the V_O concentration. Similar experiments were performed on (111)-oriented heterostructures. These measurements are presented and discussed in the following.

A.1 Experimental details

8-ML-thick $LaAlO_3$ films were deposited by pulsed laser deposition on (111)-oriented, Ti-terminated $SrTiO_3$ substrates in $1{\cdot}10^{-3}$ mbar oxygen partial pressure at a substrate temperature of 780 °C, a laser fluence of $0.9\,\mathrm{J/cm^2}$ and a pulse repetition rate of 1 Hz. To ensure full oxidation, the samples were cooled down to room temperature in 500 mbar O_2 with the temperature being held constant for 1 h at 600 °C.

The (111)-oriented Nb-doped $SrTiO_3$ substrates investigated had a defined Ti termination.

All samples were transported to the synchrotron in air and were measured without a further surface preparation.

The (111)-oriented samples were all oriented with the analyzer slit aligned parallel to the Γ–K crystal direction.

A.2 Doping mechanisms in (111)-oriented heterostructures

The results of the oxygen dosing experiments are depicted in Fig. A.1 and in Fig. A.2 for the (111) $SrTiO_3$ surface and the epitaxial (111) $LaAlO_3/SrTiO_3$ heterointerface, respectively.

Just as for the corresponding (001) $SrTiO_3$ surface, the metallicity in the (111) $SrTiO_3$ surface is found to be induced by photon-induced oxygen depletion. Under irradiation, the QP and IG features rise concomitantly. In the fully oxidized state both the QP and the IG weight are, however, completely suppressed.

The doping in the (111)-oriented $LaAlO_3/SrTiO_3$ heterostructures can also be effectively adjusted via the oxygen vacancy concentration: Upon oxygen depletion, both the QP as well as the IG weight rise. Yet, the (111)-oriented $LaAlO_3/SrTiO_3$ heterostructure is metallic also in the absence of oxygen vacancies: Residual QP weight is observed for the fully oxidized epitaxial (111)-

oriented $LaAlO_3/SrTiO_3$ heterostructure [see blue shading in Fig. A.2 (a)] which we ascribe to an electronic reconstruction driven by the polar discontinuity at the (111) heterointerface.

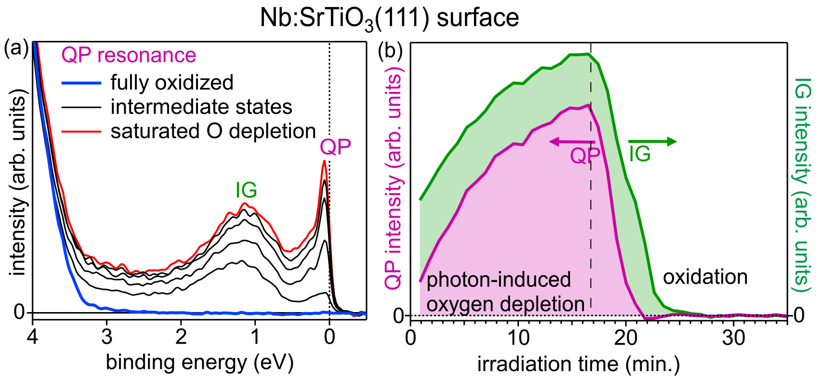

Fig. A.1: (a) Valence band spectra of the bare $SrTiO_3$ (111) surface at different V_O concentrations. All spectra are recorded on the QP resonance. (b) QP and IG weight as a function of irradiation/oxidation.
In the case of the bare $SrTiO_3$ (111) surface, both the QP and the IG weight are completely suppressed in the fully oxidized state. Figure adapted from ref. [A6].

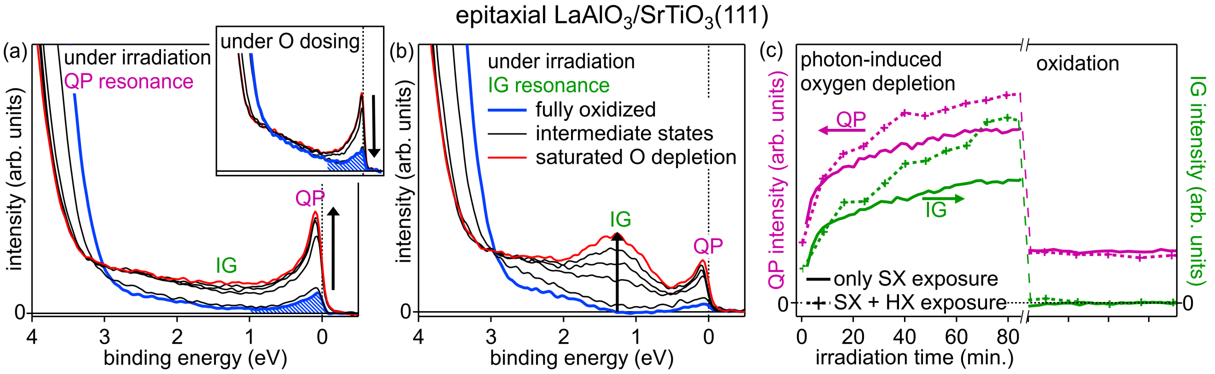

Fig. A.2: Valence band spectra of the epitaxial (111) $LaAlO_3/SrTiO_3$ heterointerface as a function of the oxygen vacancy concentration. The spectra recorded on the QP (a) and IG (b) resonance change under oxygen depletion/oxidation. The arrows show in which sequence the measurements were recorded. (c) Quantitative analysis of QP and IG weight as a function of oxygen depletion/oxidation.
Just as for the (001)-oriented heterostructures, residual QP weight is observed for the fully oxidized epitaxial (111)-oriented $LaAlO_3/SrTiO_3$ heterostructure [see blue shading in figure (a)]. Figure adapted from ref. [A6].

B Interface band engineering in $LaAlO_3/SrTiO_3$ heterostructures

This section gives additional information on the data manipulation and analysis presented in chapter 4.

B.1 Sr 3*d* background subtraction

The background signal underlying the Sr 3*d* spectra is composed of a La 4*d* and a Sr 3*d* satellite peak and a Shirley-like background. To reduce the number of free parameters entering into the background subtraction, the three contributions are subtracted one after the other, exploiting physical constraints whenever possible.

The La 4*d* satellite line is subtracted first. The La 4*d* satellite lies directly beneath the Sr 3*d* peaks,[111] becomes most apparent in the slope at the low binding energy side of the Sr 3*d* spectrum and is approximated with a Gaussian profile. The position and width of the Gaussian profile is determined from a corresponding reference spectrum obtained from a thick $LaAlO_3$ film in which the satellite line can be unambiguously assigned and analyzed. The intensity of the satellite signal is furthermore required to be proportional to the intensity of the La 4*d* main peak.

The Sr 3*d* satellite on the high binding energy side of the Sr 3*d* peaks is also approximated by a Gaussian profile and is subtracted next. The width and position of the Gaussian peak has to be fitted in this case. However, width and position are not fitted separately for each spectrum at the different electron emission angles. Instead, we assume that width and position of the satellite line do not change with the electron emission angle and determine one value for the width and one value for the position which applies to all spectra of a particular state. As before, the intensity of the satellite line is furthermore chosen to be proportional to the intensity of the Sr 3*d* main peak.

In the last step a Shirley-like background is subtracted.

B.2 Modeling the effect of Sr segregations

By photoemission spectroscopy in the soft x-ray regime, Treske *et al.*[207] find evidence of Sr segregations on the surface of $SrTiO_3$-based heterostructures: Beside the Sr 3*d* doublet ascribed to the $SrTiO_3$ substrate they observe a second doublet which is shifted toward higher binding energies and which becomes particularly pronounced in surface-sensitive measurements. They reason that the oxidation state of the segregated Sr differs from the oxidation state of Sr in the $SrTiO_3$ bulk which triggers the shift in binding energy. Treske *et al.* speculate that the submonolayer thick Sr segregations on the surface are composed of SrO, $SrCO_3$ or $Sr(OH)_2$ compounds. The Sr segregations are floating on the film surface[207] and might possibly be left over after the substrate termination or might be induced by the high-temperature growth process. Such Sr segregations at the $LaAlO_3$ surface could potentially induce an asymmetry in our Sr 3*d* HXPES photoemission spectra as well. What's more, this asymmetry would also depend on the surface-sensitivity of the measurement, i.e., the electron emission angle, and could thus be mistaken for band bending.

To find out if such a scenario is indeed realistic, we exemplarily model spectra for a 4 uc $LaAlO_3/SrTiO_3$ sample with a hypothetical Sr contamination which is depicted in Fig. B.1 (a). The Sr segregations are assumed to cluster as depicted in Fig. B.1 (a). The coverage of the sample surface with Sr segregations is adapted to the values Treske *et al.* estimate. The binding energy difference between the two Sr 3*d* doublets is also adopted from Treske *et al.*The same spectral shape is used to model the spectra originating from the $SrTiO_3$ substrate and the Sr segregations. For the sake of the argument, we furthermore assume that the electron emission

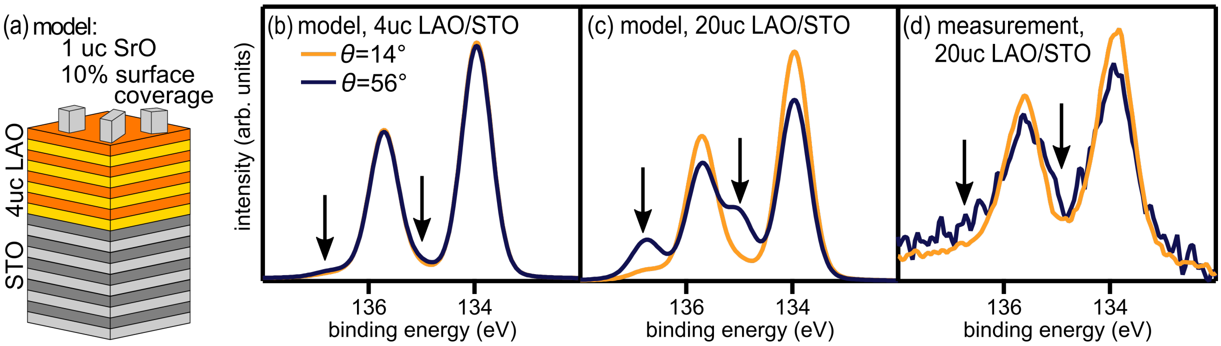

Fig. B.1: Modeling the effect of Sr segregations: (a) Hypothetical Sr segregations on a 4 uc $LaAlO_3/SrTiO_3$ heterostructure. (b) Modeled HXPES ($h\nu$=3 keV) Sr 3d spectra of the sample depicted in (a). (c) Modeled HXPES ($h\nu$=3 keV) Sr 3d spectra of a 20 uc $LaAlO_3/SrTiO_3$ heterostructure with Sr segregations on the $LaAlO_3$ film surface. (d) Measured HXPES spectra of a 20 uc $LaAlO_3/SrTiO_3$ heterostructure.
The Sr 3d doublet related to Sr segregations is shifted toward higher binding energies [see arrow markings in figures (b) – (d)]. Notably, there is no sizable feature which may be ascribed to Sr segregations in the measured spectra in figure (d).

angle dependence in the Sr 3d spectra is indeed solely induced by such Sr segregations on the $LaAlO_3$ surface.

The Sr 3d spectra modeled for the 4 uc $LaAlO_3/SrTiO_3$ sample depicted in Fig. B.1 (a) are displayed in Fig. B.1 (b). The modeled Sr 3d spectra only show a minor dependence on the electron emission angle. We can thus conclude that, even if present, Sr segregations on the $LaAlO_3$ surface hardly have any influence on the electron emission angle dependence measured at $h\nu$=3 keV.

To check for the existence of Sr segregations on the sample surface, we additionally turn to a 20 uc $LaAlO_3/SrTiO_3$ heterostructure: When the $LaAlO_3$ thickness is increased, the Sr 3d signal originating from the $SrTiO_3$ substrate is further damped and the Sr 3d signal originating from the Sr segregation on the $LaAlO_3$ surface is more pronounced, in particular in surface-sensitive measurements. The modeled spectra of a 20 uc $LaAlO_3/SrTiO_3$ heterostructure with Sr segregations which are depicted in Fig. B.1 (c) illustrate this: The Sr 3d doublet which is related to the Sr segregations is clearly discernible in the modeled spectra at an electron emission angle of 56° (see arrow markings). However, our measurements of a 20 uc $LaAlO_3/SrTiO_3$ heterostructure do not match the modeled spectra of a 20 uc $LaAlO_3/SrTiO_3$ sample with a severe SrO contamination [compare Fig. B.1 (d) to Fig. B.1 (c)]. In contrast to the simulations, there is no sizable feature in the measured spectra which may be ascribed to Sr segregations [see arrow markings in Fig. B.1 (d)].

In summary, our samples thus do not seem to be affected by Sr segregations. This observation is at variance with the findings of Treske *et al.*[207] but may be explained by the slightly different substrate and sample treatment in both instances. With reasonable certainty we can, in particular, exclude that Sr segregations distort the electron emission angle dependence in our samples.

B.3 The difficulties in interpreting angle-dependent Ti 2p spectra

To determine the 2DES extension, the dependence of the Ti^{3+} weight on the electron emission angle is typically analyzed.[138,140,149] If the overall Ti^{3+} weight is small – as is the case for fully oxidized samples – this is not easily accomplished. Figure B.2 illustrates the complications arising during such an analysis: We simulate Ti 2p spectra for heterostructures which are characterized

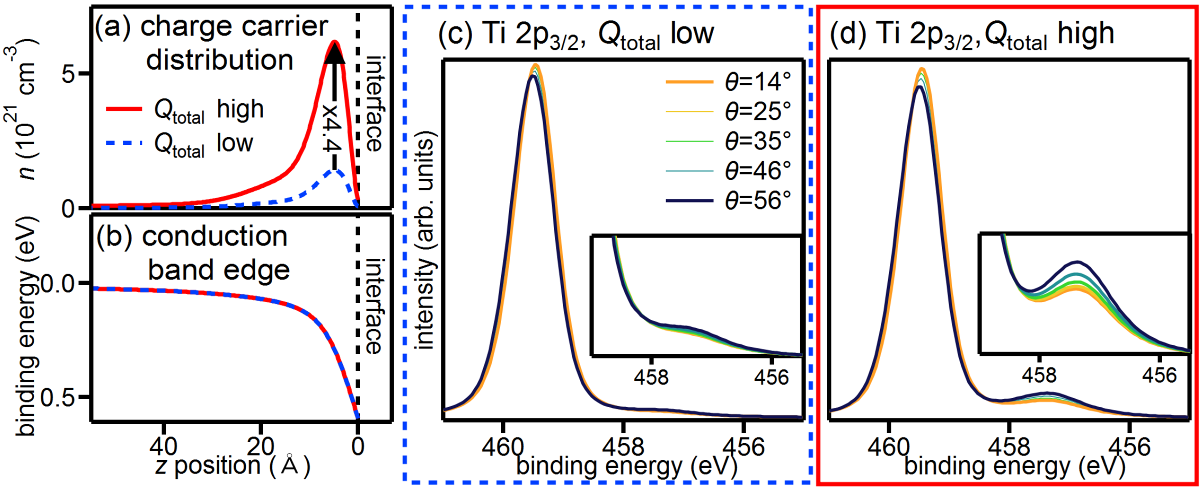

Fig. B.2: Electron emission angle dependence of the Ti 2$p_{3/2}$ spectra in a sample with a low and high total charge carrier concentration Q_{total}.
Model of the charge carrier distribution (a) and conduction band profile (b). We adopt the same charge carrier and conduction band profile for both simulations but multiply the charge carrier profile once by a factor 1 and once by a factor 4.4 to emulate the case of a high total charge carrier concentration. Simulated Ti 2$p_{3/2}$ spectra of the sample with the low (c) and high (d) charge carrier concentration. We only observe a pronounced variation in the Ti^{3+} weight for the heterostructure with the high charge carrier concentration.

by the same 2DES extension but differ in their *total* charge carrier concentration Q_{total}. To emulate these characteristics, we use a predefined charge carrier profile which is multiplied by the coefficient 1 and by the coefficient 4.4 to set different total charge carrier concentrations Q_{total} [cf. Fig. B.2 (a)]. To isolate the effects of the varying total charge carrier concentration on the Ti 2p spectra, we furthermore adopt the same conduction band profile for both heterostructures which is shown in Fig. B.2 (b). Note that the conduction band and charge carrier profiles are set by hand here and do not fulfill the Poisson-Schrödinger equations. The simulated Ti 2p spectra for the sample with the low and high total charge carrier concentration are depicted in Figs. B.2 (c) and (d), respectively. To facilitate the comparison between the spectra, the same scaling is used in Figs. B.2 (c) and (d) as well as in the two insets which zoom into the Ti^{3+} shoulder.

At first glance, we note that the absolute Ti^{3+} weight changes strongly with the electron emission angle for the heterostructure with the high total charge carrier concentration, while the variation in the Ti^{3+} weight is hardly noticeable for the heterostructure with the low total charge carrier concentration – even though the 2DES extension is similar in both models. This example points out the difficulties in interpreting the electron emission angle dependence of the Ti^{3+} weight in samples with a low charge carrier concentration: It is hard to detect any variations in the small Ti^{3+} weight, in particular in experiments which are always limited in their accuracy. In conclusion, for samples characterized by small Ti^{3+} weight it is thus virtually impossible to make a statement over the charge carrier distribution based only on the changes of the Ti^{3+} weight with the electron emission angle.

B.4 Modeling photoemission spectra

This section gives additional information which is relevant to the fits discussed in this thesis: Table B.1 lists the inelastic mean free path of the photoelectrons which is used in modeling the various spectra. Furthermore, Tab. B.2 compares the fit results for the parameters which are employed to model the Sr 3*d* and Ti 2*p* spectra of the various heterostructures in this thesis.

spectrum	**kinetic energy** (eV)	λ_{IMFP} **in** $\mathbf{SrTiO_3}$ (Å)	λ_{IMFP} **in** $\mathbf{LaAlO_3}$ (Å)
HX Ti 2*p*	2540	40.8	38.1
HX Sr 3*d*	2865	45.0	42.0
HX O 1*s*	2865	39.9	37.2
HX valence band	2990	46.5	43.5
SX Ti 2*p*, Sr 3*d*, valence band	455	11.1	10.5
SX O 1*s*	382	9.9	9.3

Tab. B.1: Inelastic mean free path of the photoelectrons in $SrTiO_3$ and $LaAlO_3$ estimated by the TPP–2M formula[27–29] for the kinetic energies used in our SXPES and HXPES measurements.

parameter	$\mathbf{Nb{:}SrTiO_3}$ **(001) reference sample**	$\mathbf{LaAlO_3/SrTiO_3}$ **(001)** V_O **dependence**	$\mathbf{LaAlO_3/SrTiO_3}$ **(111)** V_O **dependence**	$\mathbf{LaAlO_3/SrTiO_3}$ **(111) T dependence**	$\mathbf{Al/SrTiO_3}$ **T dependence**
Gaussian width slice 15° (eV)	0.60	0.62	0.61	0.60	0.54
Gaussian width slice 25° (eV)	n/a	0.62	0.61	0.59	0.55
Gaussian width slice 35° (eV)	n/a	0.63	0.63	0.60	0.59
Gaussian width slice 45° (eV)	n/a	0.66	0.64	0.61	0.62
Gaussian width slice 55° (eV)	n/a	0.68	0.65	0.64	0.59
relative Gaussian width Sr 3*d* @ 60 K	1	1	1	1	1
relative Gaussian width Ti 2*p* @ 60 K	1.02	0.98	1.01	1.00	0.94
relative Gaussian width Sr 3*d* @ 300 K	n/a	n/a	n/a	0.98	0.94
relative Gaussian width Ti 2*p* @ 30 0K	n/a	n/a	n/a	1.01	0.9
Lorentzian width Sr $3d_{5/2}$ (eV)	0.11	0.11	0.11	0.12	0.14
Lorentzian width Sr $3d_{3/2}$ (eV)	0.14	0.21	0.16	0.16	0.22
Lorentzian width Ti $2p^{4+}_{3/2}$ (eV)	0.23	0.27	0.23	0.24	0.38
Lorentzian width Ti $2p^{3+}_{3/2}$ (eV)	n/a	1.04	1.03	1.03	1.49
energy position Sr $3d_{5/2}$ (eV)	133.95	133.89	133.90	133.93	133.85
energy position Sr $3d_{3/2}$ (eV)	135.70	135.62	135.64	135.67	135.59
energy position Ti $2p^{4+}_{3/2}$ (eV)	459.39	459.39	459.39	459.38	459.35
chemical shift Ti^{3+} and Ti^{4+} (eV)	n/a	2.23	2.23	2.23	2.57
intensity ratio Sr $3d_{5/2}$/Sr $3d_{3/2}$	0.65	0.71	0.69	0.67	0.71

Tab. B.2: Synopsis over the fit results for the parameters which are employed to model the HXPES Ti 2*p* and Sr 3*d* spectra of the various $SrTiO_3$-based heterostructures. The good agreement between the fit results for the different heterostructures confirms the validity of our fits.

B.5 Analysis of O 1s spectra

As oxygen atoms in the film as well as in the substrate contribute to the O 1s signal, we also put our band diagram to the test by fitting the O 1s spectra. Electron-emission-angle-dependent O 1s spectra are depicted in Figs. B.4 (a) and (b) for the fully oxidized state and at saturated O depletion, respectively. Note that we adopt the same intensity scale in all panels of Fig. B.4 to facilitate the comparison between the spectra. Comparing the overall spectral shapes in the two states, we find that the spectra recorded at saturated O depletion are broadened, while the spectra recorded at full oxidation are considerably sharper. The electron emission angle dependence changes as well as a function of the V_{O} concentration: Whereas it is strongly pronounced at saturated O depletion, it is barely noticeable in the fully oxidized state.

To comprehend how these differences arise, we fit the O 1s spectra: Once again we adopt a global fitting scheme and fit the spectra in the different states at once. In the HX regime oxygen atoms in the substrate as well as in film layers contribute to the O 1s signal. As in the models before we build up the O 1s signal layer-by-layer. We model the O 1s signal originating from the single substrate layers by a Voigt profile. We assume that the binding energy of the O 1s core level shifts concomitantly to the binding energy of the valence band as Fig. B.3 illustrates. The binding energy of the O 1s signals originating from the single substrate layers is thus shifted according to the band diagram established previously (see Fig. 4.19).

Within the flat band scenario, we set the O 1s binding energy to a constant value in the $LaAlO_3$ film and model the O 1s signal originating from the $LaAlO_3$ film by another Voigt profile. The O 1s binding energy in the $LaAlO_3$ film is assumed to differ by ΔE between the fully oxidized and the oxygen-depleted state (see Fig. B.3). To test our band diagram, we do not fix this value ΔE but fit it and compare it subsequently to the binding energy shift in the $LaAlO_3$ film estimated previously.

For the electron emission angle of 56°, a comparison between the fits and the measured spectra is exemplarily displayed in Figs. B.4 (c) and (d) in the fully oxidized state and at saturated O depletion, respectively. Our model provides a reasonably good fit to the measured spectra. Figures B.4 (c) and (d) additionally illustrate how the respective O 1s spectra at an electron emission angle of 56° split up into the $LaAlO_3$- and $SrTiO_3$-related signals. With these fits one grasps why the spectral shapes as well as the electron emission angle dependence differs between the two states: The signals originating from the $LaAlO_3$ and the $SrTiO_3$ layer have a similar binding energy in the fully oxidized state. Accordingly, the resulting composite spectrum of the $LaAlO_3/SrTiO_3$ heterostructure is sharp and does not show a pronounced dependence on the electron emission angle. In contrast, at saturated O depletion the $LaAlO_3$- and the $SrTiO_3$-related signals are pushed apart in binding energy which induces the broadening as well as the electron emission angle dependence of the O 1s spectra.

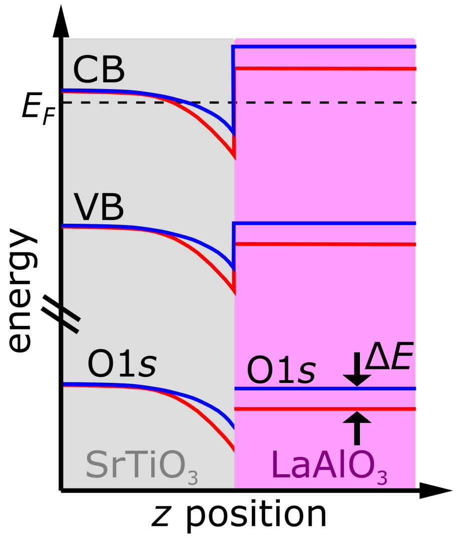

Fig. B.3: Band diagram underlying the fit of the O 1s spectra.

The binding energy of the $LaAlO_3$ contribution to the O 1s signal differs by $\Delta E = (0.7 \pm 0.2)$ eV between the fully oxidized state and at saturated O depletion. This estimate agrees with the binding energy shift of the $LaAlO_3$ core levels derived before (cf. Fig. 4.19, $\Delta E = (0.64 \pm 0.2)$ eV). We conclude that the analysis of the O 1s spectra corroborates our band diagram.

We note in passing that the fit and the data deviate slightly at high binding energies. This might be due to the fact that one picks up appreciable O 1s spectral weight originating from surface adsorbates which lies at higher binding energies.[A9] Keep in mind that we compare the fits and the spectra for the electron emission angle of 56°, i.e., a surface-sensitive measurement geometry. Mukherjee *et al.*[208] furthermore propose that the O 1s spectra of oxygen atoms in the $LaAlO_3$ layer with a V_O neighbor are shifted toward higher binding energies. Oxygen vacancies at the $LaAlO_3$ surface might thus *indirectly* induce the increased spectral weight at higher binding energies which is not reproduced by the fits.

The deviations between the data and the fits are, indeed, more pronounced at saturated O depletion which might confirm these hypotheses. We refrain from introducing such scenarios in our fits as such models would be too elaborate and entail too many free parameters to yield reliable results.

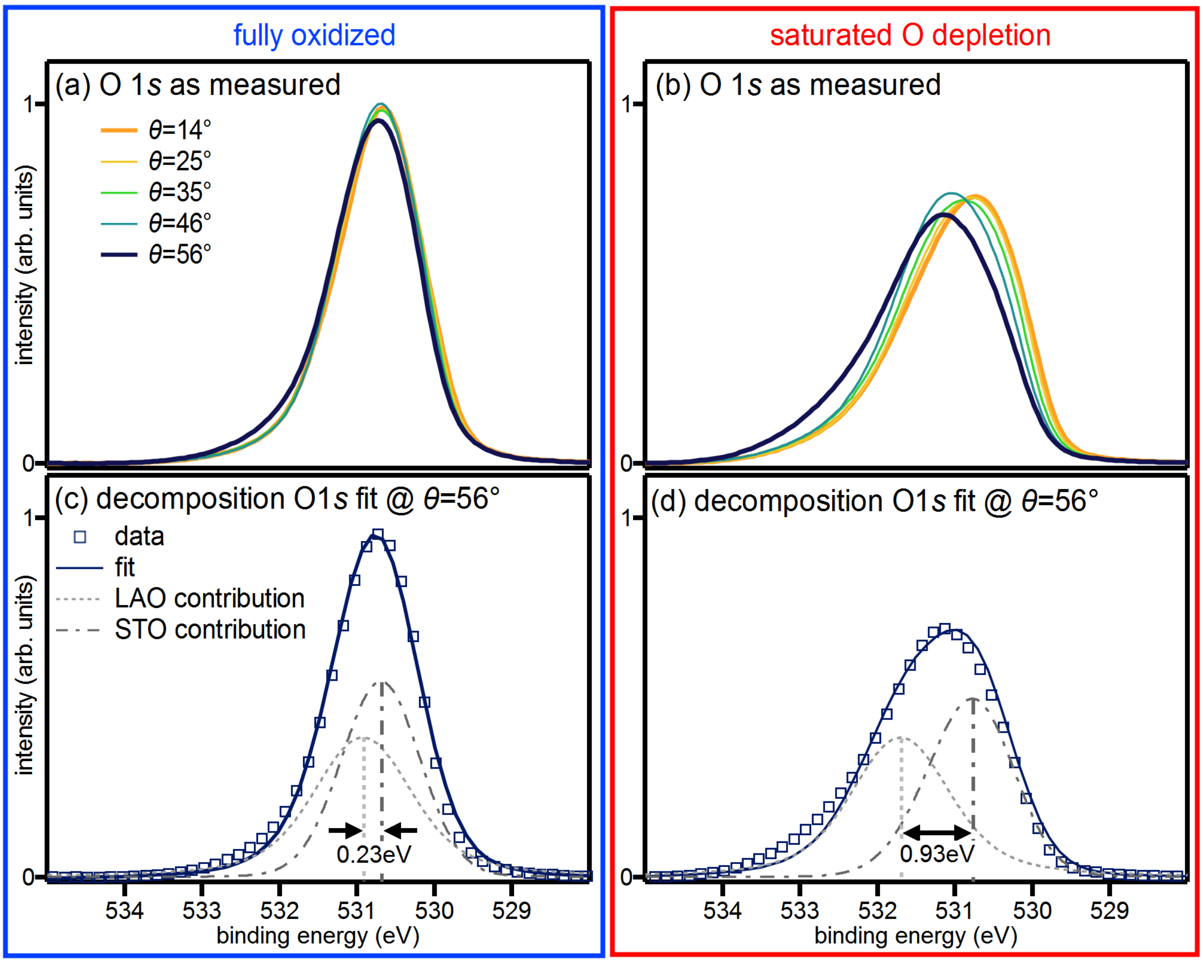

Fig. B.4: Electron emission angle dependence of O 1s spectra of (001)-oriented $LaAlO_3/SrTiO_3$ in the fully oxidized state (a) and at saturated O depletion (b). A comparison between the spectra and the fits at the electron emission angle $\theta = 56°$ is shown in (c) for the fully oxidized state and in (d) for saturated O depletion. Figures (c) and (d) also show the decomposition of the fits into the $LaAlO_3$ and $SrTiO_3$ contribution. See text for details.

B.6 Interface band engineering at the (111) $LaAlO_3/SrTiO_3$ heterointerface

In chapter 4 we analyze how the band bending and band alignment changes as a function of the V_O concentration at the (001)-oriented $LaAlO_3/SrTiO_3$ heterostructure. Similar experiments were performed on (111)-oriented heterostructures. The results of these measurements are presented and discussed in the following.

Depth profiling of the two-dimensional electron system

In the (111)-oriented $LaAlO_3/SrTiO_3$ heterostructure, we also prepare and measure two different states which differ in their oxygen vacancy concentration: By oxygen dosing and simultaneous HX irradiation, we establish the 'fully oxidized state' while we prepare the state labeled 'saturated O depletion' by continuous irradiation with the HX beam. The two states are characterized by valence band spectra measured on the QP and IG resonance which are depicted in Figs. B.5 (c) and (d). Figures B.5 (a) and (b) show the angle-integrated HXPES Ti $2p_{3/2}$ and Sr $3d$ spectra corresponding to the two different states. In the fully oxidized state, the Ti $2p$ and Sr $3d$ core level lines are marginally broadened toward the high binding energy side compared to the corresponding spectra of the $SrTiO_3$ substrate. We furthermore detect small, but non-vanishing Ti^{3+} weight. At saturated O depletion, the asymmetry in the core level line increases, just as the Ti^{3+} weight. The angle-integrated HXPES spectra already indicate that the band bending as well as the Ti $3d$ occupation are increased under oxygen depletion.

To gain a better understanding of the charge carrier distribution as well as the band bending, we analyze the electron emission angle dependence of the Ti $2p$ and Sr $3d$ spectra which is depicted in Fig. B.6: In the fully oxidized state (blue frame), the small Ti^{3+} spectral weight does not show a dependence on the electron emission angle [see inset in Fig. B.6 (a)]. Furthermore, the Sr $3d$ as well as Ti $2p_{3/2}$ spectra furthermore only develop a small asymmetry toward higher binding energies at high electron emission angles [see arrows in Figs. B.6 (a) and (c)]. In contrast, at saturated oxygen depletion (red frame), the enhanced Ti^{3+} weight is strongly dependent on the electron emission angle [see inset in Fig. B.6 (b)]. Moreover, the asymmetry in the Sr $3d$ and Ti $2p_{3/2}$ spectra toward higher binding energies at high electron emission angle is more pronounced [see arrows in Figs. B.6 (b) and (d)].

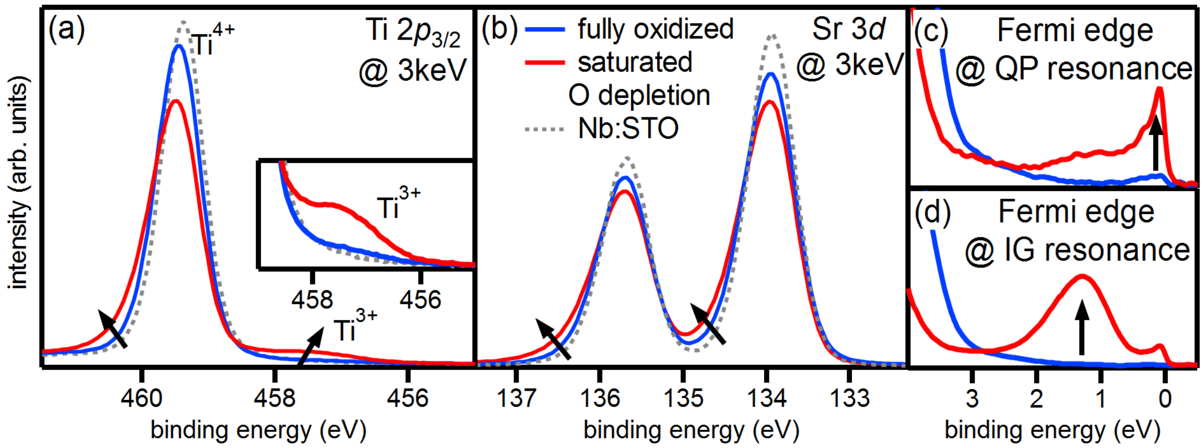

Fig. B.5: HXPES and SXPES spectra of a (111)-oriented $LaAlO_3/SrTiO_3$ heterostructure in the fully oxidized state and at saturated O depletion: Angle-integrated Ti $2p_{3/2}$ (a) and Sr $3d$ (b) spectra of the two different states measured at 3 keV photon energy. The spectra of a Nb-doped $SrTiO_3$ substrate are depicted for comparison as well. Valence band spectra of the very same states recorded with soft x-rays at the QP (c) and the IG (d) resonance.

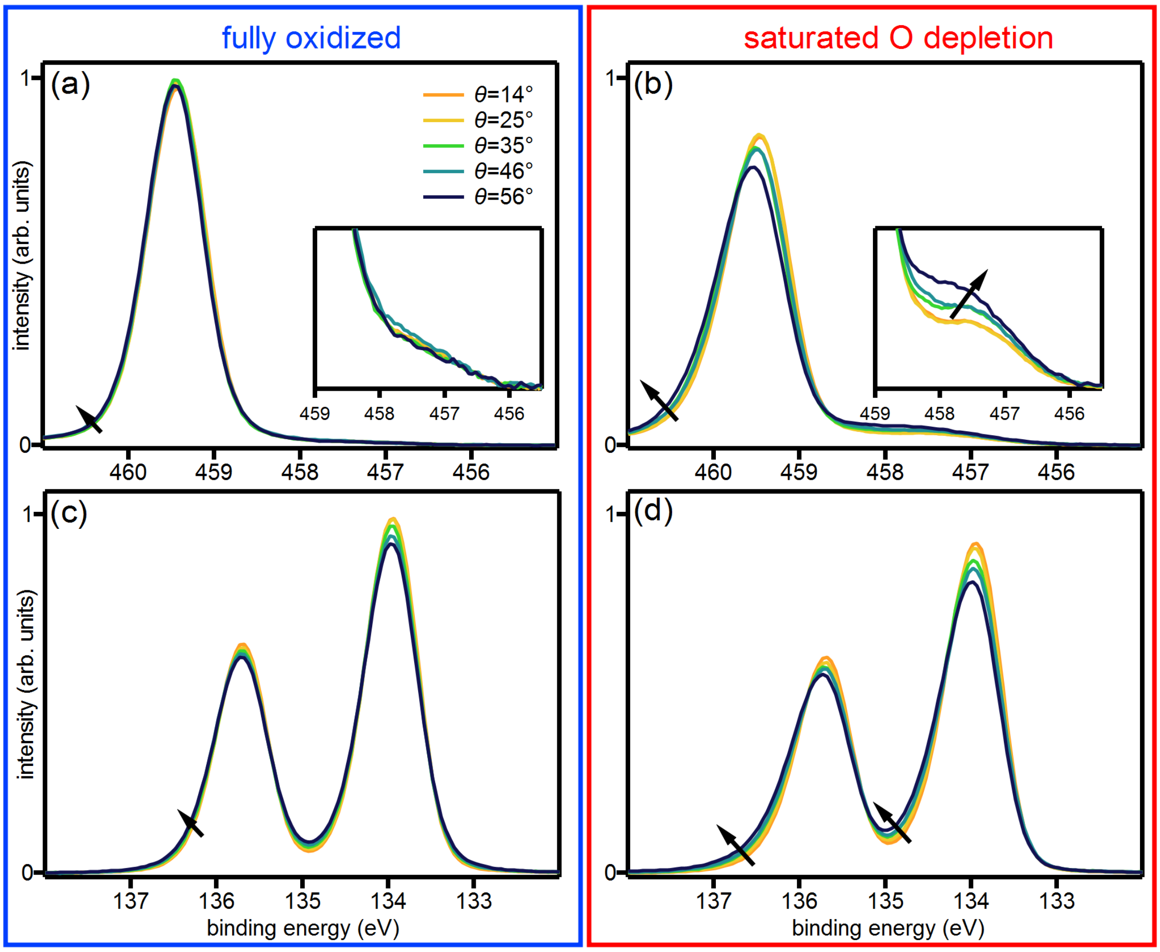

Fig. B.6: Electron emission angle dependence of substrate core level spectra for a (111)-oriented $LaAlO_3/SrTiO_3$ heterostructure. Ti $2p$ [Sr $3d$] spectra of the sample in the fully oxidized state (a) [(c)] and at saturated oxygen depletion (b) [(d)].

To estimate the depth dependence of the band bending and the charge carrier distribution, we again employ a Poisson-Schrödinger ansatz to fit the electron-emission-angle-dependent Sr $3d$ as well as Ti $2p_{3/2}$ spectra. Just as the (001)-oriented heterostructures, the fully oxidized (111)-oriented heterostructures are doped by electronic reconstruction (cf. Sec. A and Sec. 7.3) while oxygen vacancies release additional electrons at saturated O depletion. Since the underlying physics in both heterostructure is similar, the spectra of the (111)-oriented heterostructure are modeled with the same assumptions which were used for the (001)-oriented heterostructures in chapter 4. Figure B.7 shows that the fitted curves agree well with the measured data.

Let us next take a closer look at the fit results. The fit results relevant to the Poisson-Schrödinger ansatz are specified in Tab. B.3 and contrasted to the corresponding values of the (001)-oriented heterostructure. The fitting routine yields comparable values for the electron effective masses for (001)- and (111)-oriented samples. This observation is in line with our modeling as we assume an isotropic effective mass, which should thus not depend on the crystalline orientation of the samples. The oxygen vacancy profiles characterizing the oxygen-depleted state are also alike for the two samples with different orientations. The fit results for B and E_0 which describe the electric field dependence of the dielectric constant do also not differ significantly between the (001)- and (111)-oriented sample and correspond to values which one would expect at our measurement temperatures. For the comparison between the charge carrier concentration estimated

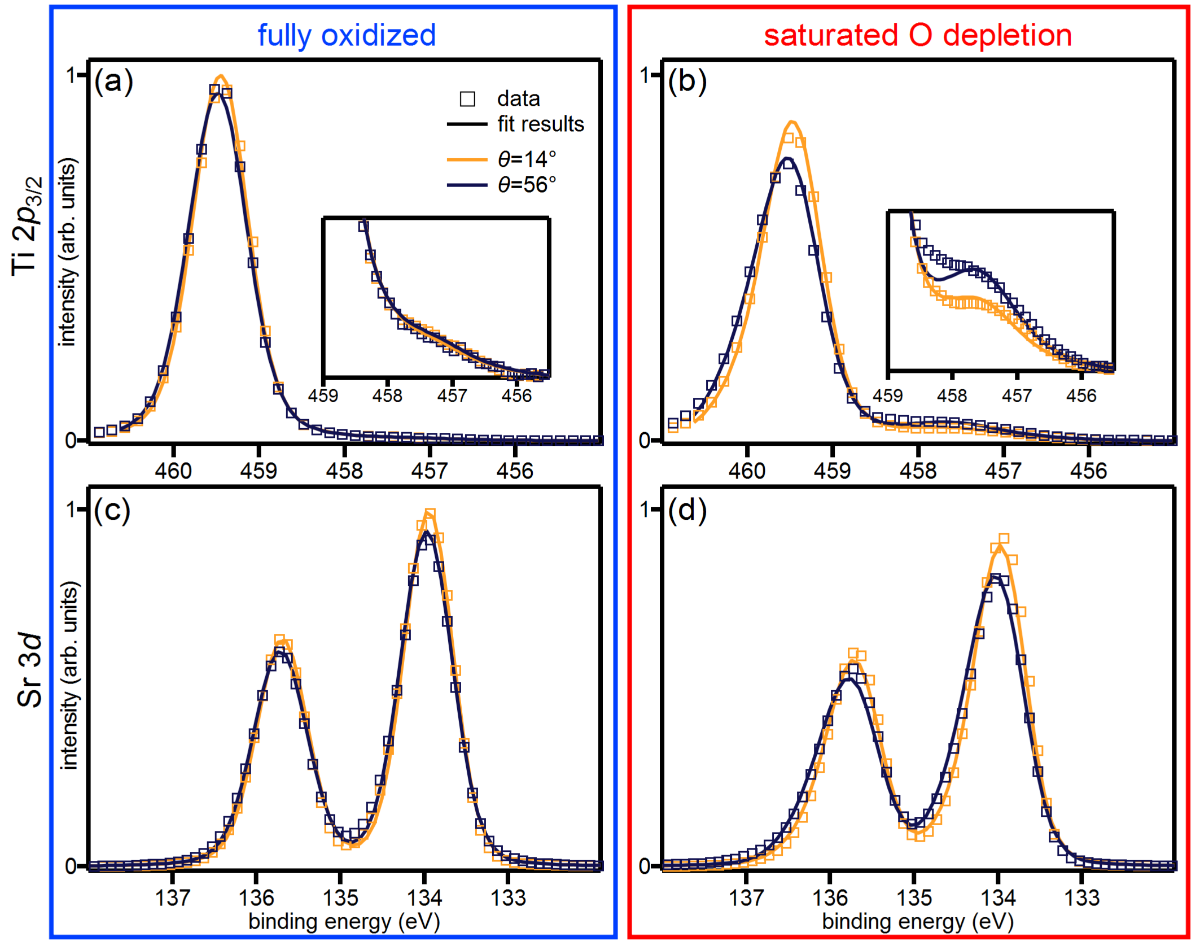

Fig. B.7: Fits of the Ti $2p$ and the Sr $3d$ core levels of a (111)-oriented LaAlO$_3$/SrTiO$_3$ heterostructure employing the Poisson-Schrödinger ansatz: A comparison between the Ti $2p$ spectra and the fits for the extremal electron emission angles is shown in (a) for the fully oxidized state and in (b) for saturated O depletion. Corresponding figures for the Sr $3d$ core level are presented in (c) and (d). The fitted curves agree well with the measured data.

	fit parameters applicable to both states				**V_O profile at saturated O depletion**	
	n_{er} ($10^{14}\,\mathrm{cm}^{-2}$)	m^* (m_e)	B	E_0 (MV/m)	$\hat{N}_D$ ($10^{21}\,\mathrm{cm}^{-3}$)	d_D (Å)
best fit	0.78	0.82	2 980	0.68	2.66	17.2
lower limit	0.66	0.72	2 520	0.57	2.23	14.4
upper limit	0.90	0.94	3 250	0.83	3.18	20.6
(001)-oriented heterointerface	1.66	0.84	3 400	0.95	2.83	19.8

Tab. B.3: Fit results of the Poisson-Schrödinger ansatz for (111) LaAlO$_3$/SrTiO$_3$ heterointerface. The corresponding fit results for a (001) heterointerface are also shown for comparison.

in transport and spectroscopy the reader is referred to Sec. 6.2.2. In Tab. B.2 we furthermore list the fit results for the parameters describing the underlying Ti $2p$ and Sr $3d$ spectra and compare them with our previous fits. Scrutinizing the table, we find that the fit results for the (001)- and

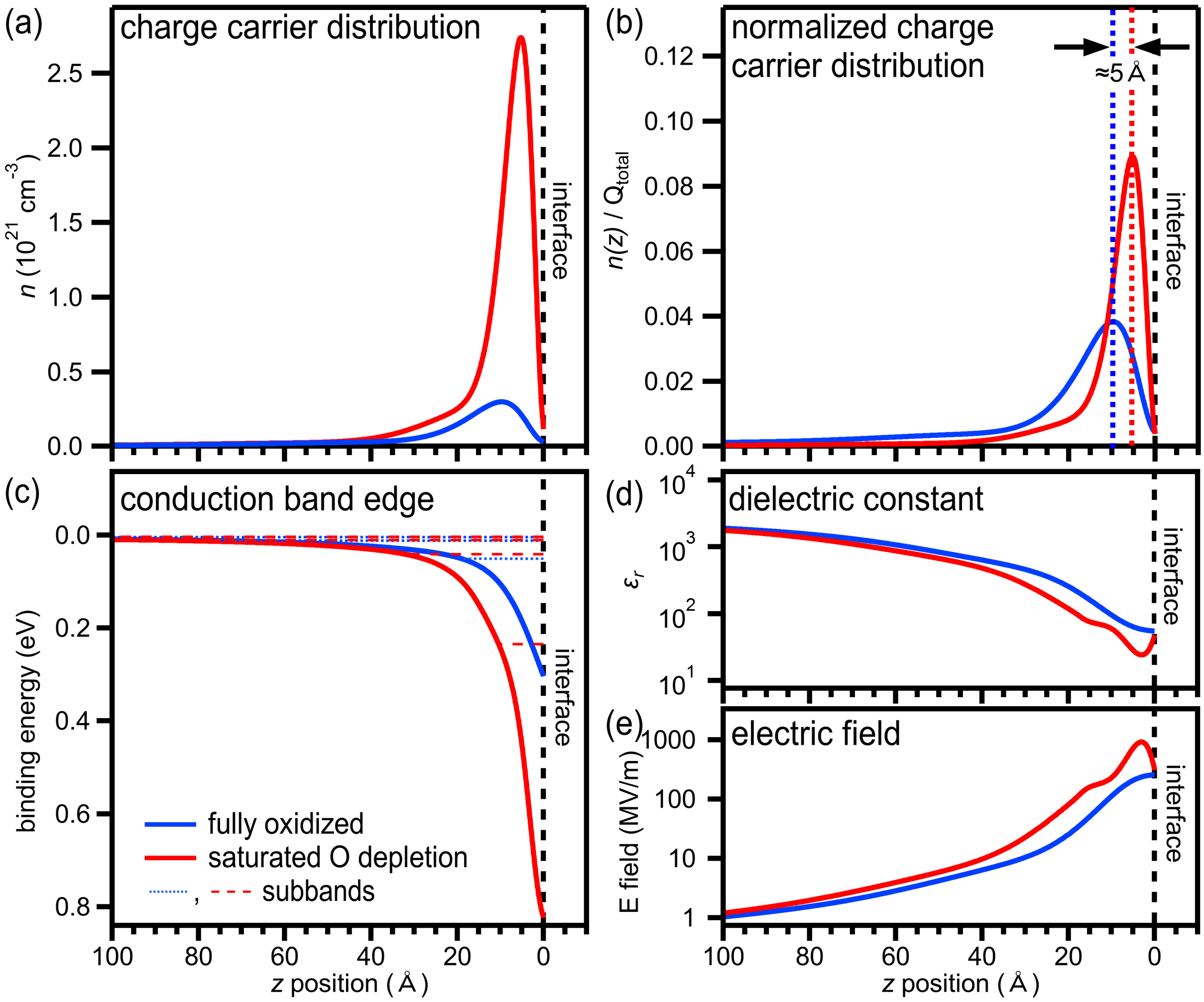

Fig. B.8: The electrostatics at the (111)-oriented $LaAlO_3/SrTiO_3$ heterostructure in the fully oxidized state and at saturated O depletion: (a) Distribution of the mobile charge carriers (b) Distribution of the mobile charge carriers normalized by the total mobile charge carrier concentration Q_{total}. (c) Conduction band profile with subband structure. (d) Profile of the dielectric constant. (e) Profile of the electric field.

(111)-oriented samples closely match. In other words, the spectral shape of the underlying Ti $2p$ and Sr $3d$ spectra does *not* depend on the crystalline orientation of the sample which confirms the validity of our fitting routine.

The electronic properties of the (111)-oriented $LaAlO_3/SrTiO_3$ interface are summarized in Fig. B.8. Figure B.8 (a) depicts the distribution of the mobile electrons. While the charge carrier concentration is strongly depending on the V_O concentration, the mobile charge carriers are confined closely to the interface for the fully oxidized state as well as at saturated O depletion, at first glance. For a detailed comparison of the charge carrier profile, we again normalize the charge carrier profiles by the respective total charge carrier concentration Q_{total} in Fig. B.8 (b). Now we see that the charge carriers spread a bit further out into the $SrTiO_3$ bulk in the fully oxidized state of the (111)-oriented heterostructure. While the charge carrier concentration peaks at ≈10 Å in the fully oxidized state, it peaks at ≈5 Å at saturated O depletion. The characteristic charge carrier distribution $n(z)$ is, once again, induced by the profile of the $SrTiO_3$ dielectric constant which declines sharply toward the interface [see Fig. B.8 (d)]. The decline in ϵ_r is, in turn, caused by the high electric fields at the interface [see Fig. B.8 (e)]. Figure B.8 (c) further-

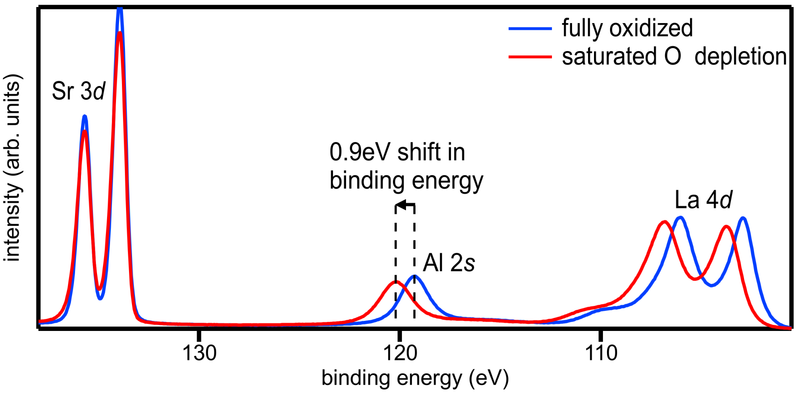

Fig. B.9: Angle-integrated Sr 3*d*, Al 2*s* and La 4*d* spectra of the (111)-oriented $LaAlO_3/SrTiO_3$ heterostructure in the fully oxidized state and at saturated O depletion. Upon oxygen depletion we observe a pronounced shift in the binding energy of the *film* core levels.

more shows that, just as in the (001)-oriented sample, the band bending at the interface is more pronounced at saturated O depletion than in the fully oxidized state. The change in the band bending is ascribed to the interface dipole the oxygen vacancies introduce.

The interfacial valence band alignment

We also investigate the valence band alignment for the (111)-oriented sample by analyzing the valence band as well as the film core level spectra of the heterointerface.

Figure B.9 depicts the angle-integrated Sr 3*d*, Al 2*s* and La 4*d* spectra in the fully oxidized state and at saturated O depletion. In both states the film core level lines are rather sharp and, in particular, not asymmetrically broadened which points to flat bands in the $LaAlO_3$ film. Upon oxygen depletion we observe a pronounced shift in the binding energy of the *film* core levels which is attributed to a variation in the interfacial band alignment. The spectral shape of the film core level lines also changes slightly as a function of the V_O concentration. As this variation in spectral shape is eclipsed by the change in binding energy, we ignore the change in spectral shape in first approximation. Instead, we assume that the bands in the $LaAlO_3$ film are flat at either V_O concentration and only analyze the variations in the binding energy of the film core levels in the following.

Within the flat band scenario the valence band offset ΔE_{VB} is determined by analyzing the binding energy difference between the core level peaks and the valence band onset. The results of this analysis are listed in the top row of Tab. B.4.

The change in the valence band offset ΔE_{VB} also becomes apparent in the hard x-ray valence band spectra depicted in Fig. B.10: Depending on the V_O concentration in the heterostructure, the valence band onset in Fig. B.10 (a) is found to shift considerably. Fitting the hard x-ray valence band spectra, we also indicate values for the valence band offsets which are listed in the bottom row of Tab. B.4.

Scrutinizing Tab. B.4, we note that the results obtained in the film core level and the valence band analysis match within their error bars. The resulting band diagram for the fully oxidized state and at saturated oxygen depletion is depicted in Fig. B.11. Just as for the (001)-oriented sample, the valence band alignment between the two materials also changes in the (111)-oriented sample as a function of the V_O concentration: Whereas a staggered gap configuration forms in the fully oxidized state, the valence band alignment changes to a straddling gap configuration under oxygen depletion.

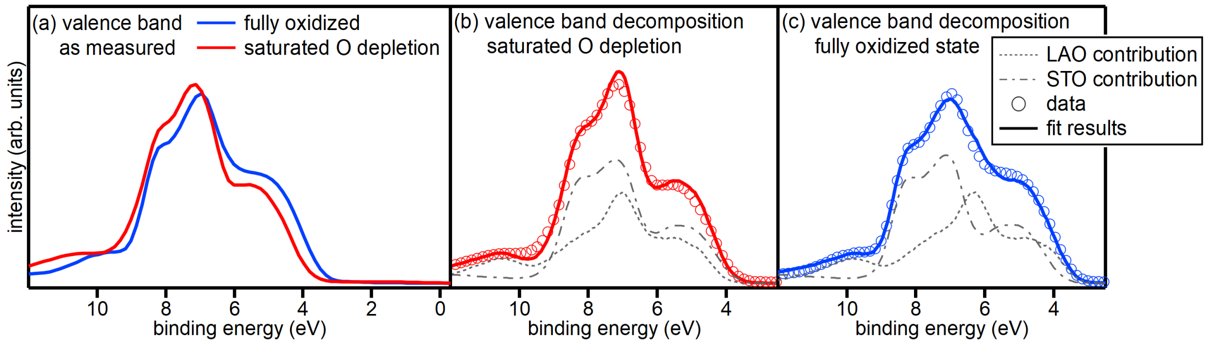

Fig. B.10: (a) Valence band spectra of the (111)-oriented $LaAlO_3/SrTiO_3$ heterostructure in the fully oxidized state and at saturated O depletion. (b)/(c) Fit and decomposition of the valence band spectrum into the $LaAlO_3$ and $SrTiO_3$ contributions at saturated O depletion/in the fully oxidized state. The $LaAlO_3$ valence band contribution shifts significantly in binding energy as a function of the V_O concentration.

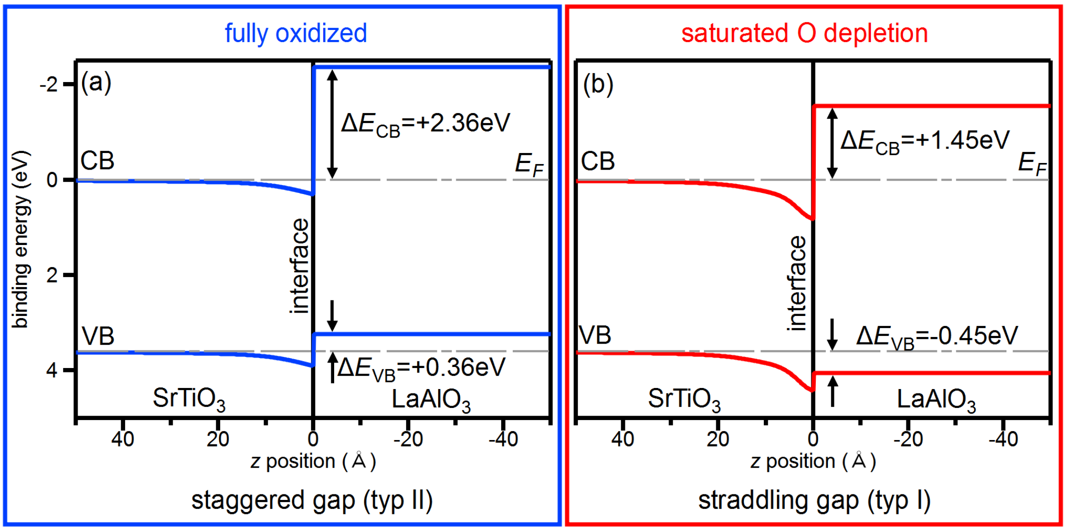

Fig. B.11: Band diagram of the (111)-oriented $LaAlO_3/SrTiO_3$ heterostructure in the fully oxidized state (blue) and at saturated O depletion (red). The band alignment at the interface changes from a staggered gap to a straddling gap arrangement as a function of the V_O concentration.

In Fig. B.12 we furthermore compare the change in valence band alignment to the variation in band bending observed upon oxygen depletion and oxidation: While the alignment between the valence bands of *bulk* $SrTiO_3$ and $LaAlO_3$ changes in the aforementioned way, we note that the band alignment *right at the interface* does not seem to vary as a function of the V_O concentration (within the error margins). The arrows in Fig. B.12 highlight that the $LaAlO_3$ valence band edge shifts concomitantly to the $SrTiO_3$ valence band edge at the interface. We conclude that the change in band bending in the $SrTiO_3$ substrate triggers the change in the binding energy of the $LaAlO_3$ valence band.

We also put our band diagram to the test by analyzing and fitting the electron-emission-angle-dependent O 1*s* spectra depicted in Figs. B.13 (a) and (b) for the fully oxidized state and at saturated O depletion, respectively: As for the (001)-oriented heterostructures, we find that the overall spectral shape as well as the electron emission angle dependence strongly varies as a function of the V_O concentration. To model the O 1*s* spectra, we proceed as described in Sec. B.5.

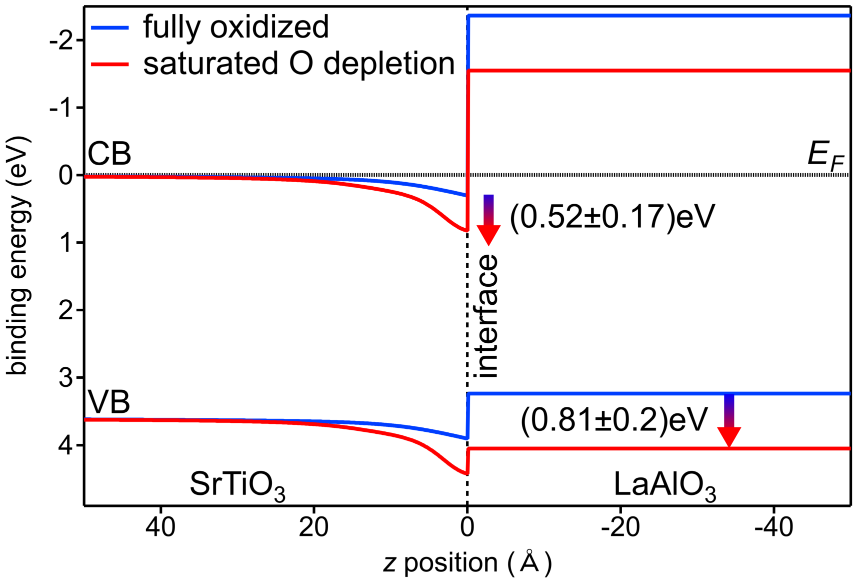

Fig. B.12: Band diagram summarizing the results of the band bending and band alignment analysis. The valence band edge in the $LaAlO_3$ film shifts concomitantly to the $SrTiO_3$ valence band edge at the interface, i.e., the offset between the valence band edge of $LaAlO_3$ and $SrTiO_3$ *right at the interface* is fixed. The change in band bending consequently triggers the change in the valence band offset.

analysis method	**ΔE_{VB} fully oxidized state**	**ΔE_{VB} saturated O depletion**
core level analysis	(+0.34±0.20) eV	(−0.56±0.20) eV
valence band analysis	(+0.37±0.20) eV	(−0.34±0.20) eV

Tab. B.4: Valence band offset ΔE_{VB} at a (111) $LaAlO_3/SrTiO_3$ heterointerface in the fully oxidized and at saturated O depletion. The valence band alignment is estimated by analyzing the binding energy difference between the valence band maximum and selected core levels (labeled core level analysis) as well as by fits of the valence band (labeled valence band analysis).

An exemplary comparison between the fits and the measured data, as well as an decomposition of the fit is shown in Figs. B.13 (c) and (d) for the fully oxidized state and at saturated O depletion, respectively. The figures reveal why the spectral shape as well as the electron emission angle dependence of the O 1*s* core level lines changes: The signals originating from the $LaAlO_3$ and the $SrTiO_3$ layer have a similar binding energy in the fully oxidized state. Accordingly, the resulting composite spectrum of the $LaAlO_3/SrTiO_3$ heterostructure is sharp and does not show a pronounced dependence on the electron emission angle. In contrast, at saturated O depletion the $LaAlO_3$- and the $SrTiO_3$-related signal are pushed apart in binding energy which induces the broadening as well as the electron emission angle dependence of the O 1*s* spectra. The binding energy of the $LaAlO_3$ contribution to the O 1*s* signal differs by (0.99 ± 0.2) eV between the fully oxidized state and at saturated O depletion. This estimate agrees, within the error margins, with the binding energy shift of the $LaAlO_3$ core levels of (0.81 ± 0.2) eV derived previously (cf. Fig. B.12). We conclude that the analysis of the O 1s spectra corroborates our band diagram.

A synopsis of the results of the HXPES depth profiling experiments at the (111)-oriented $LaAlO_3/SrTiO_3$ heterostructure is given in Tab. B.5. In conclusion, our findings on the (111)-oriented $LaAlO_3/SrTiO_3$ heterostructure are fully in line with our results on the (001)-oriented $LaAlO_3/SrTiO_3$ samples.

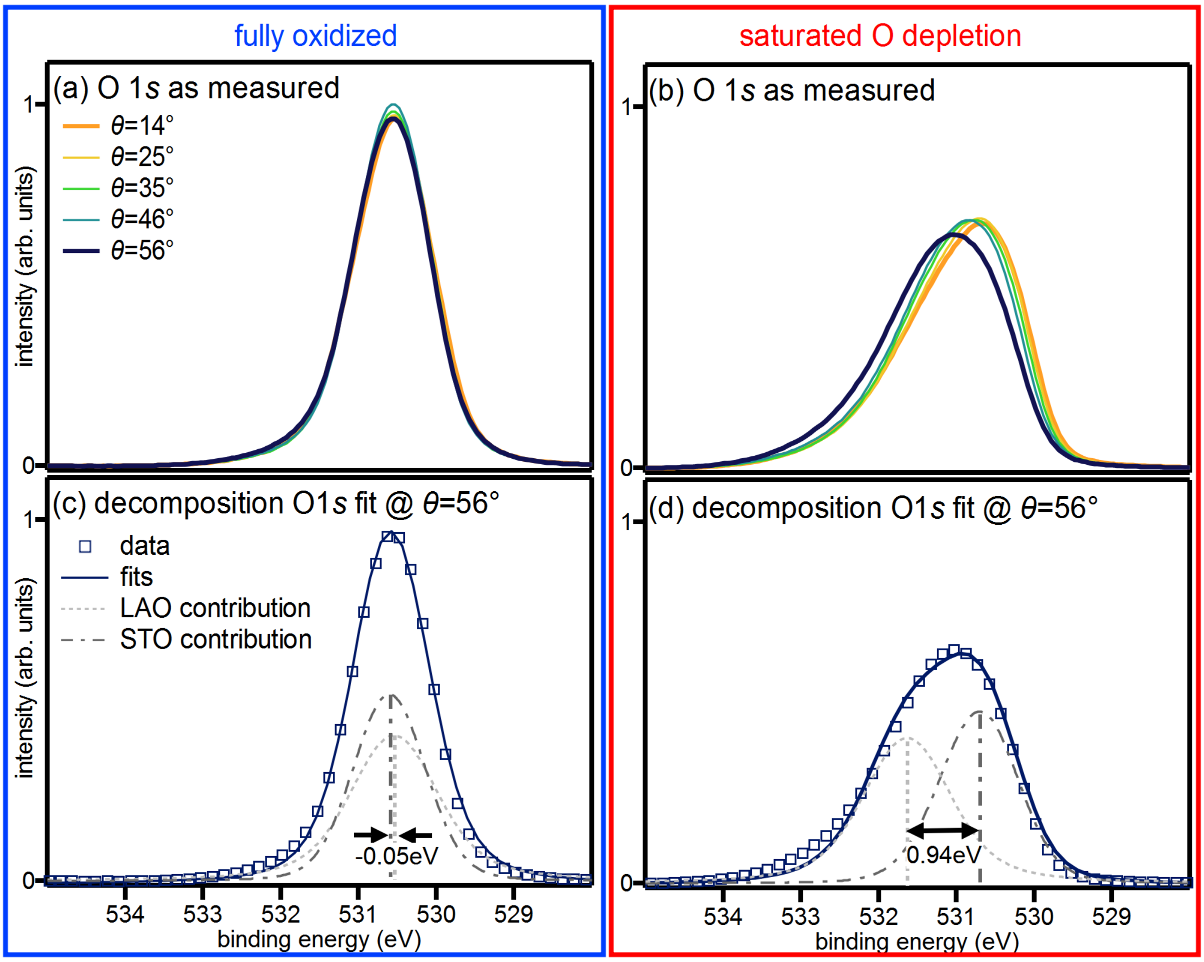

Fig. B.13: Electron emission angle dependence of O 1*s* spectra of the (111)-oriented $LaAlO_3/SrTiO_3$ heterostructure in the fully oxidized state (a) and at saturated O depletion (b). To elucidate the different evolution of the spectra with electron emission angle, the spectra are fitted. A comparison between the spectra and the fits at the electron emission angle $\theta = 56°$ is shown in (c) for the fully oxidized state and in (d) for saturated O depletion. Figures (c) and (d) also show the decomposition of the fits into the $LaAlO_3$ and $SrTiO_3$ contribution. The analysis of the O 1*s* spectra corroborates the band diagram shown in Fig. B.4.

sample state	ΔE_{VB} (eV)	ΔE_{BB} (eV)	d_{BB} (Å)	d_{2DES} (Å)
fully oxidized	+0.36±0.2	0.27±0.07	32±10	16.6±2.4
saturated O depletion	–0.45±0.2	0.77±0.08	22±3	8.2±0.5

Tab. B.5: Synopsis of the results of the HXPES depth profiling experiments at the (111)-oriented $LaAlO_3/SrTiO_3$ heterostructure: valence band offset ΔE_{VB}, spatial width d_{BB} and energetic depth ΔE_{BB} of the potential well in the $SrTiO_3$ substrate and 2DES extension d_{2DES} in the fully oxidized state and at saturated O depletion. All values depend strongly on the V_O concentration.

C Tuning the dielectric constant of $SrTiO_3$

This section gives additional information on the data analysis presented in chapter 5.

C.1 Analyzing the electronic interface properties by the Poisson-Schrödinger ansatz

In chapter 5 we only show a side-by-side comparison between the measured spectra and the fits employing the Poisson-Schrödinger ansatz. For the sake of completeness a direct comparison between the data and the fits is shown in the following in Fig. C.1 for the fully oxidized $LaAlO_3/SrTiO_3$ heterostructure and in Fig. C.2 for the oxygen-depleted $Al/SrTiO_3$ heterostructure.

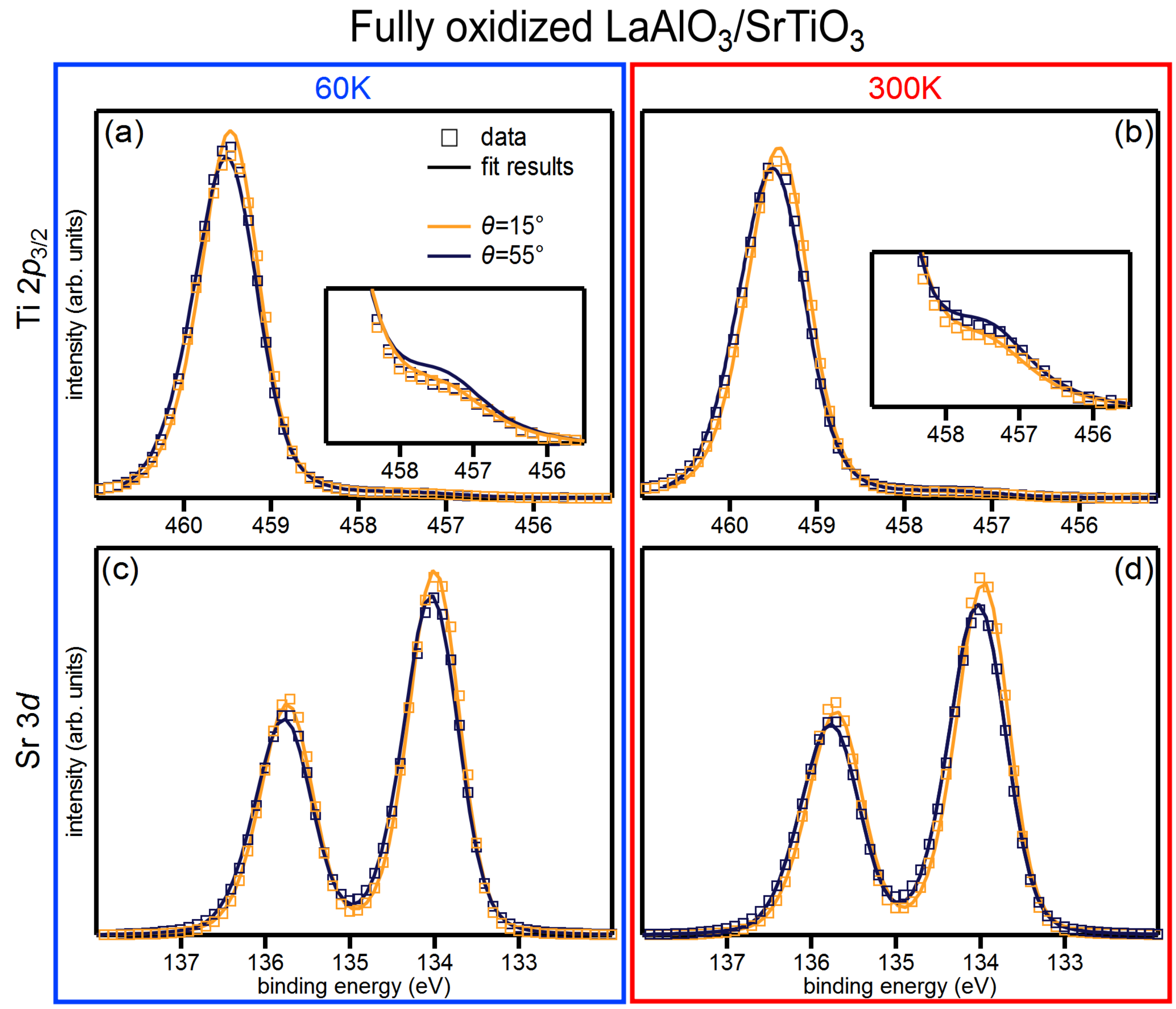

Fig. C.1: Fitting the Ti 2p and Sr 3d core level spectra of the fully oxidized (111)-oriented $LaAlO_3/SrTiO_3$ heterostructure at different temperatures with the Poisson-Schrödinger ansatz: The Ti 2p spectra and the fits are compared at the extremal electron emission angles in (a) and (b) for $T = 60$ K and $T = 300$ K, respectively. Corresponding figures for the Sr 3d core level are displayed in (c) and (d). The fitted curves agree well with the measured data.

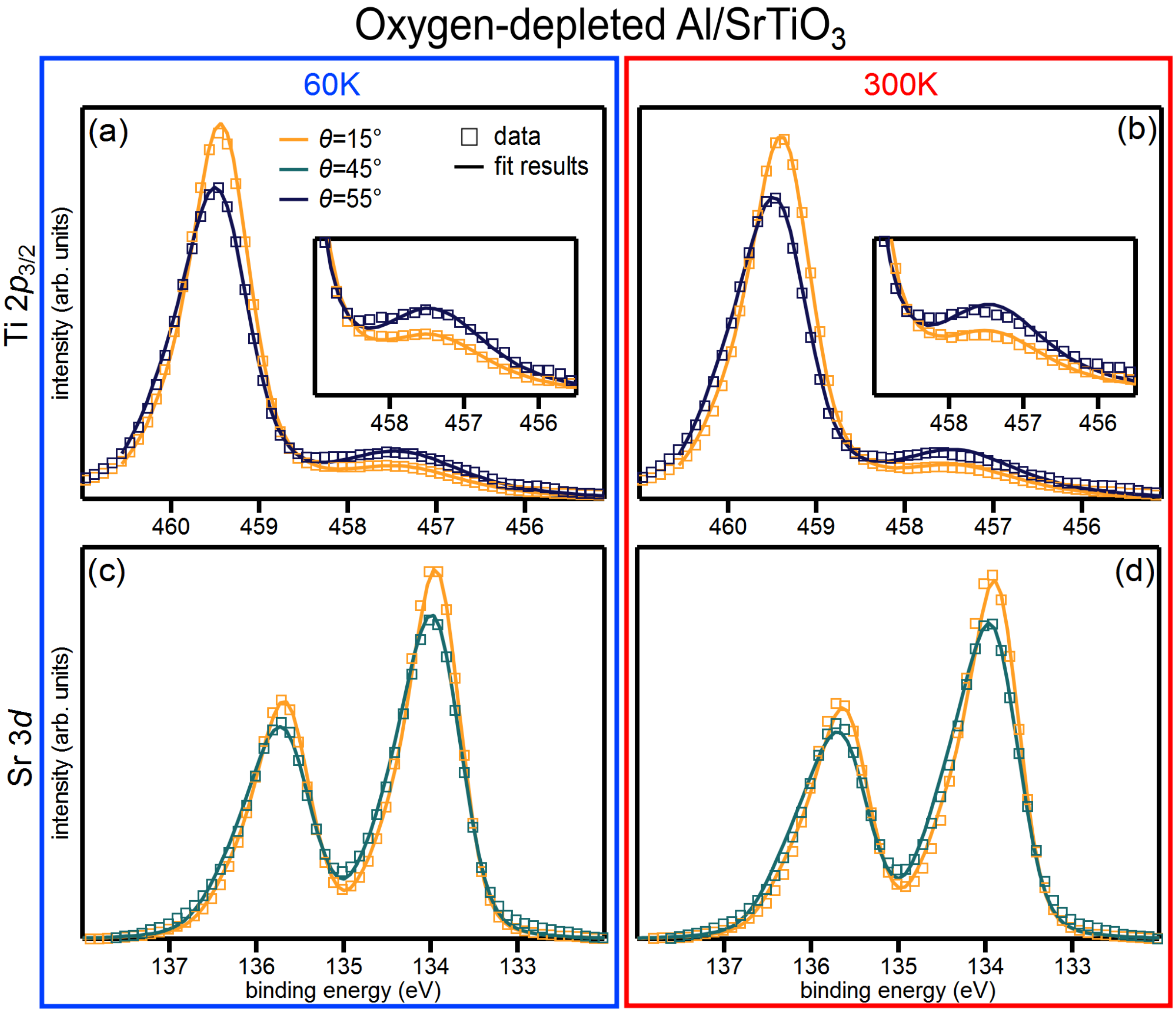

Fig. C.2: Fitting the Ti 2p and Sr 3d core level spectra of the oxygen-depleted (001)-oriented Al/SrTiO$_3$ heterostructure at different temperatures with the Poisson-Schrödinger ansatz: The Ti 2p spectra and the fits are compared at the extremal electron emission angles in (a) and (b) for $T = 60\,\mathrm{K}$ and $T = 300\,\mathrm{K}$, respectively. Corresponding figures for the Sr 3d core level are presented in (c) and (d). The fitted curves agree well with the measured data.

C.2 Analysis of O 1*s* spectra for the fully oxidized (111)-oriented $LaAlO_3/SrTiO_3$ heterostructure

Since oxygen atoms in the film as well as in the substrate contribute to the O 1*s* signal, we can test the band diagram in Fig. 5.5 by fitting the O 1*s* spectra. To model the O 1*s* spectra, we proceed as described in Sec. B.5. The electron-emission-angle-dependent O 1*s* spectra are depicted in Fig. C.3 (a), whereas the corresponding fits are shown in Fig. C.3 (b). For the sake of clarity, we only display the spectra recorded at the extremal electron emission angles. Although the differences between the spectra recorded at 60 K and 300 K are once again small, the fits can yet again reproduce the relevant differences between the spectra [compare Fig. C.3 (a) to Fig. C.3 (b)].

We only touch upon the one fit parameter which we can directly relate to the band diagram previously established: The fit reveals that the binding energy of the O 1*s* core level in the $LaAlO_3$ film shifts by (-0.24 ± 0.2) eV toward higher binding energy when the temperature increases. This value agrees, within error bars, with the binding energy shift of (-0.08 ± 0.2) eV specified in the band diagram in Fig. 5.5.

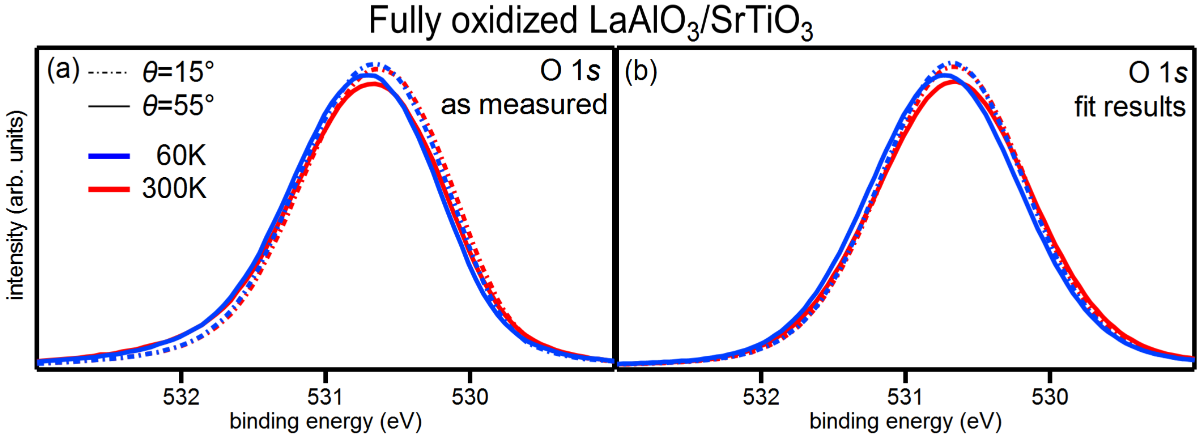

Fig. C.3: (a) Electron-emission-angle-dependent O 1*s* spectra of a fully oxidized (111)-oriented $LaAlO_3/SrTiO_3$ heterostructure at low and at room temperature. (b) Fits of the O 1*s* spectra. The fits reproduce the relevant differences between the spectra measured at low and room temperature.

D The two-dimensional electron system at the (111) $LaAlO_3/SrTiO_3$ interface

D.1 Preparation of the Ti-terminated $SrTiO_3$ (111) surface

The commercially available $SrTiO_3$ crystals are thoroughly cleaned in acetone and ethanol in an ultrasonic bath. Subsequently, they are immersed in deionized water for 30 min and soaked in a hydrofluoric acid solution for 30 s. Finally, the $SrTiO_3$ substrates are annealed under flowing oxygen at 950 °C for 2 h (for substrate miscut $0.05 - 0.1°$) to 3 h (for substrate miscut $< 0.05°$).

D.2 Tight binding model for slab of N Ti layers

In chapter 7 the tight binding model of a Ti honeycomb lattice is derived. In the following we derive a tight binding model for a slab of N triangular Ti layers in the (111)-oriented $SrTiO_3$ crystal.

As before, only hopping terms between orbitals of the same character are included. In consequence, the $(3N \times 3N)$ Hamiltonian decouples into three $(N \times N)$ matrices describing the hopping for the d_{xz}, d_{xy} and d_{yz} orbitals, respectively.

We only exemplarily solve the tight binding model for the d_{yz} orbital. Since we only allow hopping between adjacent Ti layers, the entries ϵ_c and $\tilde{\epsilon}_c$ in the new matrix H are the same as in the tight binding Hamiltonian of a Ti honeycomb lattice (see Sec. 7.5.1). The matrix H is, however, now larger

$$H = \begin{pmatrix} d_1^\dagger \\ d_2^\dagger \\ \vdots \\ \vdots \\ \vdots \\ d_N^\dagger \end{pmatrix}^T \begin{pmatrix} \epsilon_c & \tilde{\epsilon}_c & & & & \\ \tilde{\epsilon}_c^* & \epsilon_c & \tilde{\epsilon}_c & & & \\ & \tilde{\epsilon}_c^* & \epsilon_c & \ddots & & \\ & & \ddots & \ddots & \tilde{\epsilon}_c & \\ & & & \tilde{\epsilon}_c^* & \epsilon_c & \tilde{\epsilon}_c \\ & & & & \tilde{\epsilon}_c^* & \epsilon_c \end{pmatrix} \begin{pmatrix} d_1 \\ d_2 \\ \vdots \\ \vdots \\ \vdots \\ d_N \end{pmatrix}, \tag{8.1}$$

where the indices $1, ..., N$ label the atomic layer. A Hamiltonian with such a form is known as a tridiagonal Toeplitz matrix.[209] The eigenvalues E_j of a tridiagonal Toeplitz matrix with the dimension $N \times N$ are[209]

$$E_i = \epsilon_c + 2|\tilde{\epsilon}_c| \cos\left(\frac{j}{N+1}\pi\right) \text{ with } j{=}1, 2...N. \tag{8.2}$$

At low filling we are only interested in the lowest eigenvalue E_N

$$E_N = \epsilon_c + 2|\tilde{\epsilon}_c| \cos\left(\frac{N}{N+1}\pi\right) \tag{8.3}$$

and its corresponding eigenvector[209]

$$\begin{pmatrix} d_1 \\ d_2 \\ \vdots \\ d_N \end{pmatrix} = \begin{pmatrix} \sin\left(\frac{N}{N+1}\pi\right) \cdot e^{-i\alpha} \\ \sin\left(\frac{2N}{N+1}\pi\right) \cdot e^{-2i\alpha} \\ \vdots \\ \sin\left(\frac{N^2}{N+1}\pi\right) \cdot e^{-Ni\alpha} \end{pmatrix}, \tag{8.4}$$

where α denotes the argument of the complex number $\tilde{\epsilon}_c = |\tilde{\epsilon}_c| \cdot e^{i\alpha}$. Comparing the tight banding model for the Ti honeycomb lattice (see Sec. 7.5.1) and the slab with N Ti layers, we note that the lowest energy eigenvalue differs in its absolute value. Yet, the energy eigenvalue shows a characteristic band structure, i.e., a similar behavior as a function of **k**.

D.3 Photoemission structure factor for slab of *N* Ti layers

In chapter 7 the photoemission structure factor of a hexagonal lattice is computed. However, it could not explain the large intensity modulations observed in the measured Fermi surface. Here, we thus expand our model and derive an expression for the photoemission structure factor of a slab which is composed of N triangular layers in the following [see model in Fig. 7.10 (e)]. The photoemission structure factor is exemplarily determined for the d_{yz} orbitals. First we have to determine the unit cell vectors $\mathbf{a}_i$ and $\mathbf{b}_i$ characterizing the slab model in real and reciprocal space, respectively. The real space unit cell vectors $\mathbf{a}_i$ have to describe one entire slab containing N Ti layers as well as the vacuum separating two slabs. The vector $\mathbf{a}_1$ is set to point in the [111] direction, i.e., perpendicular to the single triangular layers, while the vectors $\mathbf{a}_2$ and $\mathbf{a}_3$ are oriented in the plane of the single layers. In his convention the real space unit cell vectors $\mathbf{a}_i$ read

$$\mathbf{a}_1 = c\begin{pmatrix}1\\1\\1\end{pmatrix}, \quad \mathbf{a}_2 = a\begin{pmatrix}1\\-1\\0\end{pmatrix}, \quad \mathbf{a}_3 = a\begin{pmatrix}0\\1\\-1\end{pmatrix}, \tag{8.5}$$

where c describes the distance between the slabs and a=3.905 Å denotes the lattice constant of SrTiO$_3$.

The corresponding reciprocal lattice vectors $\mathbf{b}_i$ read

$$\mathbf{b}_1 = \frac{2\pi}{3c}\begin{pmatrix}1\\1\\1\end{pmatrix}, \quad \mathbf{b}_2 = \frac{2\pi}{3a}\begin{pmatrix}2\\-1\\-1\end{pmatrix}, \quad \mathbf{b}_3 = \frac{2\pi}{3a}\begin{pmatrix}1\\1\\-2\end{pmatrix}. \tag{8.6}$$

Next, the basis atoms in the unit cell have to be described. Slabs are built of N triangular lattices with atoms m sitting at position $\boldsymbol{\tau}_1$ to $\boldsymbol{\tau}_N$

$$\boldsymbol{\tau}_1 = \begin{pmatrix}0\\0\\0\end{pmatrix}, \quad \boldsymbol{\tau}_2 = a\begin{pmatrix}1\\0\\0\end{pmatrix}, \quad \boldsymbol{\tau}_3 = a\begin{pmatrix}1\\1\\0\end{pmatrix}, \quad \boldsymbol{\tau}_4 = a\begin{pmatrix}1\\1\\1\end{pmatrix}, \tag{8.7}$$

$$\boldsymbol{\tau}_m = a\cdot\lfloor\frac{m}{3}\rfloor\cdot\begin{pmatrix}1\\1\\1\end{pmatrix} + \begin{cases}\boldsymbol{\tau}_1 & \text{for } m \bmod 3 = 1\\ \boldsymbol{\tau}_2 & \text{for } m \bmod 3 = 2\\ \boldsymbol{\tau}_3 & \text{for } m \bmod 3 = 0,\end{cases} \tag{8.8}$$

where $\lfloor\ \rfloor$ describes the floor function.

The photoemission structure factor is defined as described before[204]

$$F_N(\mathbf{k}) = \sum_{m=1}^{N}\exp(-i\mathbf{G}\boldsymbol{\tau}_m)c_m(\mathbf{q}). \tag{8.9}$$

An arbitrary reciprocal lattice vector $\mathbf{G}$ can be expressed as

$$\mathbf{G} = h\mathbf{b}_1 + k\mathbf{b}_2 + l\mathbf{b}_3, \tag{8.10}$$

where h, k and l are integers and specify which Brillouin zone we are looking at.

Exploiting the relation $\mathbf{a}_x\mathbf{b}_y$=$2\pi\delta_{xy}$, we calculate $\mathbf{G}\boldsymbol{\tau}_m$

$$\mathbf{G}\boldsymbol{\tau}_m = \begin{cases}2\pi\lfloor\frac{m}{3}\rfloor\frac{a}{c}h & \text{for } m \bmod 3 = 1\\ 2\pi\lfloor\frac{m}{3}\rfloor\frac{a}{c}h + \frac{2\pi}{3}\left(\frac{a}{c}h + 2k + l\right) & \text{for } m \bmod 3 = 2\\ 2\pi\lfloor\frac{m}{3}\rfloor\frac{a}{c}h + \frac{2\pi}{3}\left(2\frac{a}{c}h + k + 2l\right) & \text{for } m \bmod 3 = 0.\end{cases} \tag{8.11}$$

In the limit $\frac{a}{c} \to 0$ the term $\mathbf{G}\boldsymbol{\tau}_m$ can be further simplified

$$\mathbf{G}\boldsymbol{\tau}_m = \begin{cases} 0 & \text{for } m \bmod 3 = 1 \\ \frac{2\pi}{3}\,(2k+l) & \text{for } m \bmod 3 = 2 \\ \frac{2\pi}{3}\,(k+2l) & \text{for } m \bmod 3 = 0. \end{cases} \tag{8.12}$$

To facilitate the analysis, we again only examine the intensity modulation at the Γ points, i.e., $\mathbf{q} = \mathbf{0}$ in the following. The coefficients $c_m(\mathbf{q})$ describing the photoemission initial state are determined based on the tight binding model derived in Sec. D.2. $c_m(\mathbf{q} = \mathbf{0})$ are read from the eigenvector in equation (8.4)

$$\begin{pmatrix} c_1(\mathbf{0}) \\ c_2(\mathbf{0}) \\ \vdots \\ c_N(\mathbf{0}) \end{pmatrix} = \begin{pmatrix} d_1 \\ d_2 \\ \vdots \\ d_N \end{pmatrix} = \frac{1}{\sqrt{N}} \begin{pmatrix} \sin\left(\frac{N}{N+1}\pi\right) \cdot (-1)^1 \\ \sin\left(\frac{2N}{N+1}\pi\right) \cdot (-1)^2 \\ \vdots \\ \sin\left(\frac{N^2}{N+1}\pi\right) \cdot (-1)^N \end{pmatrix}. \tag{8.13}$$

Inserting these values we calculate $|F_N(\mathbf{k})|^2$

$$|F_N(\mathbf{k})|^2 = \left| \sum_{m=1}^{N} \exp(-i\mathbf{G}\boldsymbol{\tau}_m) \sin\left(\frac{mN}{N+1}\pi\right)(-1)^m \right|^2 . \tag{8.14}$$

At constant N, the results differ depending on the values that are chosen for k and l, which appear in the term $\mathbf{G}\boldsymbol{\tau}_m$ (see equation (8.12)). As before, $|F_N(\mathbf{k})|^2$ can only attain two values in the Fermi surface cut measured: For Γ_{00}, $\Gamma_{2\bar{1}}$ and Γ_{11} one obtains a high value for $|F_N(\mathbf{k})|^2$, while one obtains a small value for $|F_N(\mathbf{k})|^2$ for all other Γ points. This intensity pattern corresponds to the intensity pattern observed in experiment as well as to the intensity pattern attained for the honeycomb lattice model. However, the intensity ratio between dark and bright Γ points does depend on the number of layers included in the slab model as the list in Tab. D.1 shows. We note that the intensity ratio strongly decreases when the number of layers N in the slab model increases.

	N=2	N=3	N=4	N=5	N=6	N=7	N=8
intensity ratio $\frac{\textbf{dark } \boldsymbol{\Gamma} \textbf{ points}}{\textbf{bright } \boldsymbol{\Gamma} \textbf{ points}}$	0.25	0.015	0.005	0.010	0.001	0.001	0.002

Tab. D.1: Photoemission intensity ratio between the Γ points of bright and dark Brillouin zones estimated by the slab model. The intensity ratio strongly depends on the number N of Ti layers included in the slab.

Acknowledgements

An dieser Stelle möchte ich noch die Gelegenheit nutzen, all denen Dank zu sagen, die zum Gelingen dieser Arbeit beigetragen haben:

Zunächst möchte ich mich bei Prof. Dr. Ralph Claessen bedanken, dass ich meine Doktorarbeit an seinem Lehrstuhl anfertigen konnte. Danke für die Betreuung dieser Arbeit und die vielen wissenschaftlichen Diskussionen und Ratschläge. Bedanken möchte ich mich auch für die zahlreichen Möglichkeiten und Anregungen während dieser Zeit meinen Horizont zu erweitern: So konnte ich an internationalen Konferenzen, Schulen und Synchrotron-Strahlzeiten teilnehmen. Sehr lehrreich war es aber auch, bei der der Erstellung von Forschungsanträgen mitzuwirken oder meine Arbeit bei einem Science Slam zu präsentieren.

Prof. Dr. Michael Sing möchte ich für seine kompetente Unterstützung bei allen möglichen physikalischen Fragen und Problemen danken. Danke für viele aufschlussreiche Diskussionen, aber auch für das Korrekturlesen zahlreicher Strahlzeitanträge, Abstracts und Poster sowie für alle netten Gespräche, die den Arbeitsalltag stets auflockerten.

I would also like to thank Prof. Dr. Mark Golden for agreeing to be the second reviewer of this thesis and for an instructive joint beamtime at Diamond Light Source.

A large part of the data in this thesis has been recorded on various syhnchrotron beamtimes. These beamtimes would not have been successful without the support of the beamline personnel on site.
Thus I would like to thank Dr. Tien-Lin Lee, Dr. Christoph Schlueter, Dave McCue, Dr. Pardeep Kumar Thakur and Dr. David Duncan from Diamond Light Source for their superb support at numerous I09-beamtimes.
I would also like to acknowledge the help of Dr. Vladimir Strocov, Dr. Claudia Cancellieri, Dr. Victor Rogalev and Dr. Marius-Adrian Husanu from Swiss Light Source.

Gerade Strahlzeiten, aber auch die Laborarbeit sind nur in guter Teamarbeit zu bewältigen. Für die gute Zusammenarbeit möchte ich deshalb allen ehmaligen und aktiven Kollegen danken:
Danke an Dr. Götz Berner, Dr. Florian Pfaff und Ozan Kirilmaz, die mich in die Laborarbeit genauso wie in die Welt der Oxide eingeführt haben.
Danke an meine langjährigen Kollegen Michael Zapf, Philipp Scheiderer und Florian Adler, die mit mir zusammen die Zeit der Master- und Doktorarbeit durchgestanden haben. Danke für viele hilfreiche Diskussionen über, aber auch abseits der Physik auf Strahlzeiten, im Labor, aber auch auf dem Nachhauseweg, beim Bouldern oder auf Weinfesten.
Danke aber auch an Dr. Lenart Dudy, Philipp Schütz, Martin Stübinger, Berengar Leikert und Matthias Schmitt für viele Diskussionen, für unzählige Transfers im Labor und für die Übernahme zahlreicher (Nacht-)Schichten auf Strahlzeiten.

Ein besonderes Dankeschön auch an Berengar Leikert, der mich und diese Arbeit als Bachelor- und Masterstudent sowie als HiWi unterstützt hat.
I also want to thank my Canadian summer student Rory Cochrane for his help in accelerating many PPMS measurements.
Danken möchte ich auch Thomas Demarczyk für viele schöne AFM-Bilder, für das Bonden unzähliger Proben sowie die stetige Versorgung mit Helium und Stickstoff am PPMS.
Herzlich Danke sagen möchte ich auch Moni Seifer. Danke für Deine Hilfe in bürokratischen Angelegenheiten, aber auch für manches aufmunternde Gespräch.
Dem gesamten Team der EP4 möchte ich für die schöne, unvergesssliche Zeit am Lehrstuhl danken. Danke für die kollegiale Arbeitsatmosphäre und die vielen kurzweiligen Mittagessen und Kaffeepausen.

Bei meinen Kollaborationspartner aus der Technischen Physik, Dr. Patrick Maier, Dr. Fabian Hartmann, Silke Kuhn und Prof. Dr. Sven Höfling, möchte ich mich für die erfolgreiche Zusammenarbeit bedanken, die zum LAO/STO-Memristorpaper geführt hat. Danke für die Probenstrukturierung und die lehrreichen Einblicke in die Halbleitertechnologie.
Bei Prof. Dr. Jean Geurts, Sebastian Elsässer und Dr. Martin Kamp möchte ich mich für die Raman- bzw. TEM-Messungen an den (111)-orientierten $LaAlO_3/SrTiO_3$-Proben bedanken.

Danke sagen möchte ich auch allen, die geholfen haben, die Zahl der Fehler in dieser Arbeit zu minimieren. Hierbei sei insbesondere mein Vater genannt, der trotz seines fehlenden Fachwissens die komplette Arbeit gelesen hat. Danke aber auch an Florian Adler, Michael Zapf, Philipp Scheiderer, Dr. Louis Veyrat, Dr. Simon Moser, Dr. Victor Rogalev, Matthias Schmitt, Berengar Leikert, Martin Stübinger und Ozan Kirilmaz für das Korrekturlesen einzelner Kapitel.

Herzlich danken möchte ich auch meinen Freunden und all meinen Verwandten, die immer regen Anteil an meiner Doktorarbeit nahmen und mir durch manchen Tiefpunkt geholfen haben. Danke für Eure Unterstützung, den guten Zuspruch aber auch für manche Ablenkung von der Doktorarbeit und der Physik.
Hier seien inbesondere auch meine Großeltern genannt, die nicht dieselben Möglichkeiten wie ich hatten, zu studieren und sich zu bilden, die mich auf meinem Weg aber immer bedingungslos unterstützt haben.
Mein ganz besonderer Dank gilt zuletzt meinen Eltern und meinen Brüdern. Danke für Eure stete Unterstützung und Euren Rückhalt. Danke, dass ihr immer an mich glaubt (auch wenn ich das selbst mal nicht tue) und mir immer zur Seite steht.